SOLID STATE NMR INVESTIGATION OF ELECTROLYTE MATERIALS FOR HYDROGEN FUEL CELLS

SOLID STATE NMR INVESTIGATION OF ELECTROLYTE MATERIALS FOR HYDROGEN FUEL CELLS

BY

JASON W. TRAER, B.SC.

A Thesis

Submitted to the School of Graduate Studies

in Partial Fulfillment of the Requirements

for the Degree

Doctor of Philosophy

McMaster University

Doctor of Philosophy (2008)

Department of Chemistry
McMaster University
Hamilton, Ontario

TITLE: SOLID STATE NMR INVESTIGATION OF ELECTROLYTE MATERIALS FOR HYDROGEN FUEL CELLS

AUTHOR: Jason W. Traer, B.Sc.

SUPERVISOR: Professor G. R. Goward

NUMBER OF PAGES: xvii, 232

Abstract

Today's commercial proton exchange membranes for fuel cell applications use a liquid electrolyte such as water to facilitate the conduction process. The vapour pressure of water limits the operating temperature of a fuel cell, resulting in a decrease in efficiency as the electrolyte evaporates. Anhydrous electrolytes such as acidified polybenzimidazole or poly(vinyl-4-imidazole) are able to transport ions without using water as an electrolyte.

The mechanism of ion transport involves the structural diffusion of the ions through the solid-state lattice. Compounds modeling the basic modes of the ionic conductivity are used in the solid-state nuclear magnetic resonance (NMR) investigation. The hydrogen-bonding structures of model compounds are established using diffraction paired with ^{1}H solid-state double quantum NMR. The structural studies of the compounds reveal a continuous network of hydrogen bonded molecules. The structural motif is based on strong N-H••O and O-H••O hydrogen bonds between the ions of the material. The dynamics of the hydrogen bonds observed in the ^{1}H NMR and the multinuclear studies using the CODEX (**C**enterband **O**nly **D**etection of **EX**change) pulse sequence define the mechanism of ionic conductivity in these model compounds.

These solid-state NMR techniques are then applied to a novel electrolyte material consisting of a solid electrolyte inside the pores of a host polymer material. This new material is able to transport protons at high temperatures without the use of an aqueous electrolyte. The properties and mechanism of ion transport is investigated using solid-state NMR and impedance spectroscopy.

Acknowledgements

Throughout the course of my degree I have had the pleasure of working with many people. I am grateful for the all of the support and positive influences that has shaped this degree and my experience at McMaster to be what it is today.

I would like to thank my supervisor Gillian R. Goward for all the hard work and time that went into helping me succeed as a graduate student. Her kindness and support has made these achievements a reality. I would like to acknowledge the support and insight passed onto me by my committee members over the course of my degree.

I would like to thank all members of the departmental staff, beginning with the administrative, X-ray, BIMR, and the NMR staff for their help during my degree.

I would like to acknowledge all the friends I've made throughout the course of my degree, especially members of the Goward research group. Without them it wouldn't have been the same experience.

Lastly, I would like to offer my humble thanks to my father, brother and my girlfriend for their love, support and encouragement to start and finish my graduate studies.

Table of Contents

List of Figures

List of Tables

List of Abbreviations

Term	Abbreviation
Back-to-Back	BaBa
Benzimidazole Bis(trifluorosulfonyl) Imide	BITFSI
Benzimidazole Ethylphosphonate	Bi-ePA
Benzimidazole Methylphosphonate	Bi-mPA
Benzimidazole Phosphonate	Bi-PA
Centerband-Only Detection of Exchange	CODEX
Cesium Dihydrogen Phosphate	CDP
Chemical Shift Anisotropy	CSA
Differential Scanning Calorimetry	DSC
Double Quantum Correlation	DQC
Double Quantum Filter	DQF
Frequency Switched Lee-Goldburg	FSLG
Imidazole Methylphosphonate	Im-mPA
Imidazole Methylsulfonate	Im-SA
Magic Angle Spinning	MAS
Nuclear Magnetic Resonance	NMR
One-Dimensional	1D
Parts Per Million	ppm
Polybenzimidazole	PBI
Polytetrafluoroethylene	PTFE
Polyvinyldifluoride	PVDF
Potassium Dihydrogen Phosphate	KDP
Proton Electrolyte Membrane Fuel Cell	PEM-FC
Relaxation-Induced Dipolar Exchange with Recoupling	RIDER
Rotational Echo Double Resonance	REDOR
Rubidium Dihydrogen Phosphate	RDP
Small Angle X-ray Scattering	SAXS
Thallium Dihydrogen Phosphate	TDP
Thermogravic Analysis	TGA
Two-Dimensional	2D
Williams-Landel-Ferry	WLF

Chapter 1: Introduction - Fuel Cells

This chapter introduces the chemistry in a fuel cell and reviews the mechanism of ion conduction in several different types of electrolytes used in hydrogen based fuel cells. The main topics covered in this chapter are the operation and components of a hydrogen based fuel cell, aqueous electrolytes, acidic electrolytes, solid-state electrolytes, and new anhydrous electrolytes. This chapter intends to give an overview of the chemical concepts needed to support the research goals of this thesis, which is the study and development of new electrolytes and their methods of ion conduction.

1.0 - Fuel Cells

A hydrogen fuel cell converts stored chemical energy to electricity while producing water and heat as by-products.[1, 2] Fuel cells resemble engines more than batteries because they consume a fuel, much like the engine of an automobile. Hydrogen gas has a single chemical bond that stores the potential energy for later use in the fuel cell. A fuel cell is designed to harvest the energy stored in the chemical bond. When the chemical bond is broken, the energy is released via the electrons that are in the chemical bond. The hydrogen ions move through the fuel cell while the electrons carry the energy of the chemical bond through the electrical circuit of the fuel cell. Any device connected to the circuit is able to tap into the newly generated electricity.

Current research areas involve improving the lifetime and efficiency of the fuel cell components. This thesis investigates current materials and builds upon the basic understanding of the ion transport in a fuel cell. With a better understanding of ion transport, the synthesis of new materials with increased ion flow will improve the efficiency of the fuel cell. Improving the materials in a fuel cell will make them an even better choice for replacing internal combustion.

Fuel cells have many other features that make them attractive targets for replacing the internal combustion engine like having a higher efficiency, quiet operation, and no production of greenhouse gases.[3] The applications for a fuel cell could vary between powering an electric motor in an automobile as a mobile cell or as a stationary cell by providing electricity for a building. With renewable energy sources like solar, wind, or tidal generation, it is possible to use electrolysis to generate hydrogen and use that hydrogen in portable devices.

1.0.1 – Types of Fuel Cells

There are many applications for fuel cells and this has led to the evolution of many different types and configurations that are summarized in **Table 1**.[1, 4, 5]

Table 1 – Comparison of the operating temperatures of several types of fuel cells.

Fuel Cell Type	Solid Oxide	Aqueous Proton Exchange Membrane	Direct Methanol	Solid Acid
Temperature Range	600 ~ 1000°C	60-120 °C	60-120 °C	230-250 °C

The operating temperature of a fuel cell can range from ambient temperatures to 1000°C, the temperature regime defines the materials used for the various components.[3] Fuel cells that operate over 500°C transport oxygen anions between the electrodes instead of hydrogen ions and use ceramic ion conductors.[6, 7] In contrast, fuel cells operating at or near ambient temperatures allows for a more portable design for electronics or automobiles. These fuel cells use polymer membranes to transport hydrogen ions between the electrodes. The following section will outline the physical chemistry of a hydrogen fuel cell, each of the components, and materials used in the design of a fuel cell.

Proton electrolyte membrane fuel cell (PEM-FC) technology has made many gains since its first inception, however many problems still exist. One of the current limitations is the poisoning of the expensive platinum catalyst by carbon monoxide.[8, 9] This problem disappears at higher temperatures because the binding of carbon monoxide is less efficient. However, current polymer electrolytes cannot function at temperatures high enough to mitigate carbon monoxide poisoning. The development of new membranes for high temperature operation is a priority to reduce catalyst poisoning. With new materials, the method of ion conduction changes and provides an opportunity to investigate new methods of ion conduction. This thesis aims to understand the process of ion conduction in anhydrous electrolytes for high temperature operation in fuel cells.

1.1 - Thermodynamics and Kinetics

The internal combustion engine relies on the combustion of hydrocarbons to convert chemical energy to mechanical work. This process produces primarily heat and an explosive force that acts as mechanical work on a piston to provide locomotion. In contrast, a hydrogen fuel cell breaks the covalent bonding in a molecule of hydrogen gas at the anode (Eq. 1-1), liberating electrons that travel through an external circuit to power a device. The hydrogen ions generated in the initial reaction pass through an electrolyte to reform with the electrons and oxygen to create water at the cathode (Eq. 1-2). The two half reactions that occur at the anode and cathode are as follows:

$$2\,H_{2\,(g)} \rightarrow 4H^{+}_{(aq)} + 4e^{-} \qquad E^{0} = 0 \text{ (By definition)}^{10} \qquad (1\text{-}1)$$

$$4H^{+}_{(aq)} + O_{2\,(g)} + 4e^{-} \rightarrow 2\,H_2O\,(l) \qquad E^{0} = +1.23 \text{ V @ } 298 \text{ K} \qquad (1\text{-}2)$$

The theoretical voltage of the overall fuel cell reaction is 1.23 V but this potential is often not reached due to several limiting factors. Some of the largest drops in the cell voltage occur due to ohmic loss (cell resistance), mass transport problems, which occurs when the electrodes do not have enough reactants, and charge transfer reactions at the surface of the electrode.[2, 11] These forces dominate at different current densities or loads on the fuel cell and **Figure 1** shows the major losses of a fuel cell with increasing current density. However, practical efficiencies are usually 60-70% of the equilibrium voltage or open circuit voltage in a hydrogen/oxygen fuel cell, which translates to 0.75 to 0.85 V.[2]

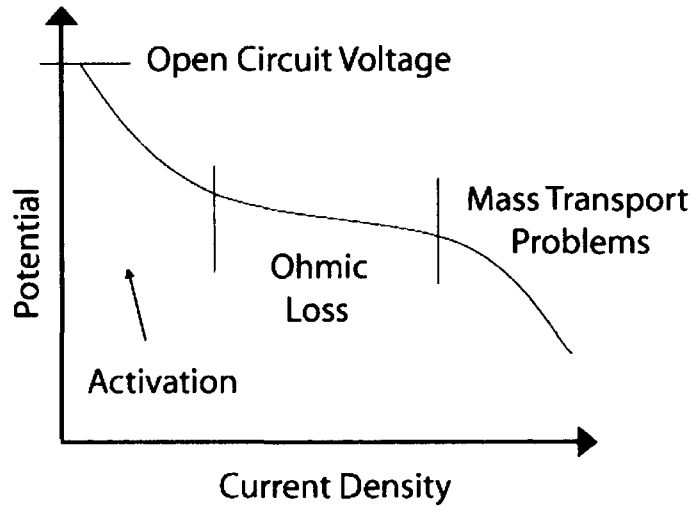

Figure 1 - The diagram of voltage losses as a function of increasing current density for a fuel cell. With a higher current density the fuel cell suffers primarily from poor ion mobility.

The theoretical potential from the electrochemical reaction for a hydrogen/oxygen fuel cell at 298 K is 1.23 V. The potential of the reaction represents the Gibbs free energy (ΔG^{o}) which is proportional to the output power of the fuel cell. The free energy of the reaction is related to the potential by Eq. 1-3 where n is the number of electrons involved in the reaction, F is Faraday's constant and E^{o} is the Nernst potential of the reaction at equilibrium, under standard conditions.

$$\Delta G^{\circ} = -nFE^{\circ} \qquad (1\text{-}3)$$

For a hydrogen/oxygen fuel cell the free energy of the reaction is ΔG^{o} = -235.76 kJ/mol. The energy of the reaction that is converted into heat is defined by the enthalpy of the

reaction which is ΔH^{o} = -285.15 kJ/mol. The entropy of the reaction is –163 J/K mol, which lowers the efficiency with temperature. The efficiency (ε) of the conversion from chemical energy to electrical energy is defined by Eq. 1-4

$$\varepsilon = {}^{w_E}\!/_{\Delta H^\circ} = {}^{\Delta G^\circ}\!/_{\Delta H^\circ} = 1 - \left({}^{T\Delta S^\circ}\!/_{\Delta H^\circ}\right) \qquad (1\text{-}4)$$

The efficiency of hydrogen/oxygen fuel cell reaction when only the electrical work is considered to be 83%. The open circuit voltage of a fuel cell is a direct measure of the performance of a cell while the thermodynamic efficiency relates to the overall performance of the chemistry involved in the process. When compared to the Carnot cycle of an internal combustion engine the efficiency of the thermodynamics reaches up to 50% in the most efficient engines.[1] A fuel cell assembly with an open circuit voltage of 0.8 V has an overall efficiency of 54%. The use of higher temperatures would increase the transport of ions in all components of the fuel cell. Increasing the kinetics of the fuel cell will increase the open circuit voltage of the fuel cell, improving the power output.

1.2 - Basic Components

A fuel cell consists of three primary components: an anode, electrolyte, and cathode, depicted in the diagram below of a hydrogen/oxygen fuel cell (**Figure 2**). The two catalyst layers (the anode and cathode) are separated by the solid-state electrolyte. The anode provides a site for the oxidation of hydrogen gas, and oxygen reduction occurs at the cathode. The anode and cathode are responsible for the transport of the ions towards the electrolyte and electrons through the circuit. The solid-state electrolyte is an

important component of the fuel cell since it transports the hydrogen ions between the electrodes, inhibits gas diffusion between layers, and acts an insulator to prevent short circuits. If the ionic conductivity of an electrolyte is poor then the power generation of the cell will suffer due to mass transport losses.

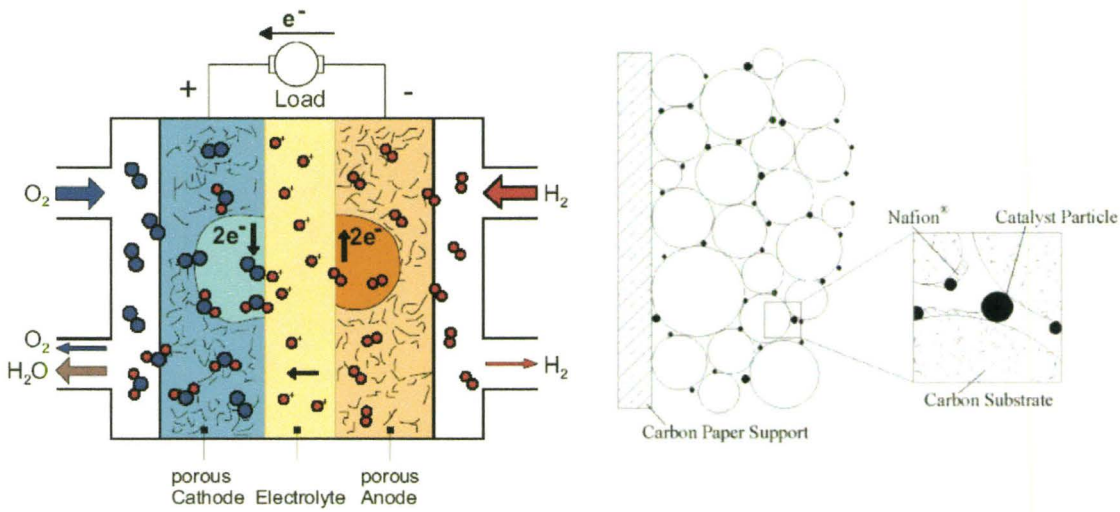

Figure 2 – (Left) A schematic diagram of a fuel cell, showing the flow of the gases and electrons. (Right) A closer view of the catalyst layer, good contact between the electrolyte, catalyst, and the incoming fuel is required for efficient operation. These figures were reproduced from Carrette *et al.* Fuel Cells, 2001, 1, 5-39.[1]

1.3 - Electrodes

The performance of an electrode in a fuel cell is dependent on the ability of the electrode to recreate the three phase boundary conditions between the fuel, electrolyte, and catalyst particles.[1] The first phase boundary occurs at the interface for the fuel and catalyst particles. The electrode in a fuel cell causes the production of ions which normally flow into the electrolyte and if the fuel passes through the electrode, voltage losses occur due to the fuel cell reaction occurring at the other electrode. Thus, it is

important that the hydrogen fuel does not crossover to the opposite electrode. The second phase boundary exists between the carbon and the catalyst. The role of the second phase boundary is to ensure that the electrode is able to conduct electrons. Due to the current price of Pt, catalyst particles are often mixed with carbon to reduce the overall price of the electrode. Mixing of the catalyst and carbon particles provides better ionic and electronic transport and limits the inclusion of the catalyst particles into the electrolyte. The third and final boundary created by the electrode exists between the catalyst layer and the electrolyte. Transport of unreacted fuel across the electrolyte creates activation losses at the electrodes. Ionic electrolytes are insulating materials which hinder electric currents, enforcing the third boundary condition. Integration of the electrolyte material into the catalyst layer (**Figure 2**) will provide good contact and will guarantee strong ion diffusion into the electrolyte. Poor contact at the surface between the electrode and the electrolyte will reduce the transport of ions into the electrolyte and in a fuel cell, the voltage will drop and result in a poor efficiency.

Advances in electrode design has led to binary or tertiary mixtures of other metals to reduce cost, adaptation for other fuels, and to avoid carbon monoxide poisoning.[11, 12] For example, mixing platinum and other transition metals creates a more resilient electrode and increases carbon monoxide tolerance of the cell.[3] Carbon monoxide impurities is created as a by-product of the fuel reformation. Fuel reformation is a process that modifies hydrocarbon fuel sources for use in a fuel cell. Carbon monoxide can bind strongly to the platinum, blocking any catalyst of the hydrogen gas. Very little

(10 ppm) carbon monoxide is required to cause a loss in performance of the catalyst. Over time the build-up of carbon monoxide degrades the performance of the electrodes.[11, 13] One method of reducing the amount of absorbed carbon monoxide on the surface of the catalyst particles is to operate the fuel cell assembly at temperatures above 100°C, this increases the kinetics and impedes the binding reaction of carbon monoxide to metal surfaces.[8, 14]

1.4 – Electrolytes

The focus of this thesis is to understand the movement of ions through current and new solid-state electrolytes. Solid-state electrolytes behave differently than liquid electrolytes and each electrolyte differs due to the factors contributing to the solid-state ionic conductivity.[4, 15-21] In the liquid state, ionic conductivity is the result of ions moving through a solvent, which leads to a net flux of ions across the electrolyte.[16, 22] The transport of ions in a liquid may occur through several mechanisms.[23] The most prominent mechanism is the translation of an ion or molecule through the liquid.[16] Another mechanism of ion transport involves ions hoping between molecules through hydrogen bonds.[24-26] The mobility of an ion in water depends on its hydrodynamic radius, which takes into account the solvation sphere of the ion.[10] Hydrogen ions are small and can produce large electric fields, which results in a large hydration sphere. The hydrogen ion in the hydration sphere exchanges very quickly between nearby water molecules, giving rise to the very high ionic mobility of the hydrogen ion in an aqueous

environment.[10] The high ionic mobility of the hydrogen ion contributes to the high ionic conductivity of aqueous based electrolytes.

The performance of the electrolyte in a fuel cell is important since the electrolyte is responsible for supplying the cathode with hydrogen ions. A greater ion transport capacity of the electrolyte would deliver more ions to the cathode increasing the power density of the fuel cell assembly. For this reason, maintaining a high ionic conductivity is extremely important for the operation of a fuel cell. In the liquid state, the majority of ion conduction occurs through a process known as the vehicle mechanism, where an ion is transported via a host molecule.[27, 28] The most common example of this method of ion transport is a H^+ ion in water, where the H^+ ion moves by diffusing with a carrier H_2O molecule. The vehicle mechanism of ion transport depends strongly on the molecular diffusion of the host molecule. The hydrogen bonding in water exists at room temperature. Proton transport through the hydrogen bonds is called structural diffusion.[10, 29, 30] The structural diffusion or Grotthuss model for ion transport occurs when a molecule rotates and allows the ion to be transported to a nearby ion acceptor. Once the rotation and the exchange process occur, the structure is free once again to pass the ion further along the solid-state structure. A well known example of the Grotthuss mechanism is the structural diffusion of a proton through solid state imidazole.[31] In the liquid state, the vehicle mechanism dominates due to the lack of restriction on the molecules translational motion.[10] In the solid state, where large molecules are bound, and

only access rotation modes, structural diffusion is essential for long-range proton transport.

1.4.1 - Nafion

The most successful electrolyte for hydrogen fuel cells is a perfluorinated polymer trademarked as Nafion by DuPont, the chemical structure of Nafion is shown as **Figure 3.** [32-41]

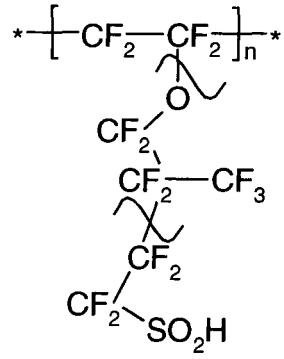

Figure 3 – The chemical structure of Nafion.

The high conductivity of Nafion is due to the strong electronegative pull of the fluoropolymer side chain, which increases the acidity of the sulfonate group. The increased acidity creates a strongly dissociated ion pair. This ensures that the number of charge carriers is high and depends on the mobility of the hydrogen ion in water. The mobility of the hydrogen ion, however, is contingent on the water content in the Nafion membrane. Dry conditions cause the ionic conductivity of Nafion to decrease.[41] The reduction in water content reduces the number of water molecules in the solvation sphere

of the hydrogen ion. This causes the ion to bind strongly to the sulfonate group, reducing the mobility of the hydrogen ion.

1.4.1.1 – The Importance of Water in Nafion

In the presence of water, the ionic conductivity of Nafion is reaches 0.1 S/cm but for dry Nafion the ionic conductivity drops to ~ 10^{-7} S/cm.[1, 41] For membranes with a high water content, the ratio of water to sulfonate molecules may reach over 20:1. A Nafion membrane with an abundance of water leads to the creation of large continuous pores that promote high ionic conductivity for they hydrogen ion.[5, 42, 43] The ability of the polymer membrane to retain large amounts of water and maintain long pathways for diffusion contribute to the success of this polymer. There are several models to explain the water content and the related ionic conductivity of Nafion based on the observed morphology from small angle X-ray scattering (SAXS).[43-53] Recent simulations and fitting to SAXS data sets suggest that when Nafion has a water content of 20% by volume, the water clusters orientate into long, parallel channels that are randomly packed within the polymer structure.[43]

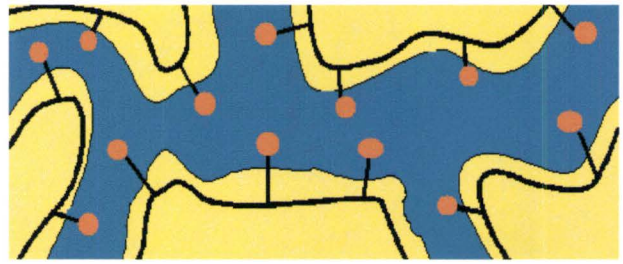

Figure 4 - The hydrated structure of Nafion with the partially solvated sulfonate groups shown inside the water channels that borders a hydrophobic component comprised of the perfluorinated backbone. Blue areas represent water, while the beige is for polymer domains.

Figure 4 shows a schematic of the possible structure of hydrated Nafion. The water channels inside the polymer membrane have a diameter between 1.5 to 3.5 nm and are partially surrounded by the hydrophilic side chains of the Nafion polymer. Evidence for the formation of the water channels even at room temperatures coincides with the high ionic conductivity of hydrated Nafion.

1.4.1.2 – Preventing Water Loss

Water loss causes these channels collapse and this drastically reduces the ion transport capacity of the membrane. The high temperature operation of a fuel cell above the vapor pressure of water will reduce the performance of the Nafion electrolyte. This dependency is the single most limiting factor of any polymer membranes that uses an aqueous environment to transport protons. The ionic conductivity of hydrated Nafion is 6×10^{-2} S/cm at 80°C, a further increase in temperature causes a loss in hydration and reduces the ionic conductivity.[54-56]

Hydrophilic particles such as SiO_2 will improve the water retention of Nafion in dry environments. The silica particles are formed inside the pores of Nafion using tetraethylorthosilicate with a sol-gel synthesis.[57-60] The total reaction time controls the particle size and longer reaction times produce large particles. Larger particles had unreacted ethyl sidechains.[61] Using solid-state nuclear magnetic resonance (NMR) it was determined that the residual ethyl resonances were immobile.[62] Smaller particles showed complete conversion to SiO_2 and higher ionic conductivity in low humidity environments.[63, 64] The surface of the smaller SiO_2 particles were fully hydrolyzed. The hydroxyl groups on the surface exhibited strong hydrogen bonding to the water molecules. The strong affinity of the particles for water helped prevent dehydrations. When the silicon particles are in excess they might block the proton channels and hinder proton movement.[64] Under dry conditions, the polymer membranes with the SiO_2 performed better than the pure Nafion.[62, 64] These studies showed that the SiO_2 particles do help the polymer to function under dry conditions.

1.4.1.3 – Ion Transport

The mechanism of proton diffusion in Nafion changes with hydration. Under wet conditions the vehicle mechanism dominates, while under dry conditions the ionic conductivity via structural diffusion increases.[65] The water channels in Nafion collapse with a decrease in water content. Additives like SiO_2 particles were able to retain water through the surface hydrogen bonding and slow the collapse. The network of hydrogen

bonds on the surface of the SiO_2 particles promotes diffusion of the hydrogen ion. The small size of the particles did not block the water channels at high or low hydration levels, this helps maintain a high ionic conductivity.

The ionic conductivity of the Nafion/SiO_2 composites under dry conditions is 5 x 10^{-4} S/cm. This is several orders of magnitude larger than pure Nafion under dry condition.[41] The inclusion of SiO_2 particles into the water channels of Nafion promotes a more resilient membrane to dehydration. The SiO_2 particles help prevent dehydration, which allows for the diffusion of ions through the membrane at lower hydration levels. However, the addition of SiO_2 particles does not completely make the polymer immune to water deficiencies.

1.4.2 – Acidified PolyBenzimidazole

One of the most successful strategies for replacing water-based electrolytes is using another electrolyte that has a boiling point that is much higher than 100°C. A higher boiling point for the liquid electrolyte will increase the operating range of the fuel cell, into a region where catalyst poisoning is minimized. Phosphoric acid is a weak triprotic acid (pKa = 2.12) that will form a hydrogen-bonding network by protonating a basic species. A fuel cell electrolyte comprised of pure phosphoric acid would suffer from acid leaching, corrosion of fuel cell components, and adsorption of phosphoric acid onto the catalyst.[66, 67] To reduce acid leaching, the anhydrous liquid electrolyte is

embedded into a basic polymer to ensure binding of the liquid electrolyte to the polymer backbone.

Polybenzimidazole (PBI) is a thermally and chemically stable polymer capable of surviving high temperature and acidic environments.[68, 69] Polybenzimidazole is a basic polymer (pKa = 5.5) that reacts with phosphoric acid creating N-H∘∘O hydrogen bonds. The chemical structure of PBI consists of two benzimidazole units, the chemical structure is shown in **Figure 5**. The nitrogen sites on the polymer have a high affinity for moisture and results in a uptake of up to 19% by weight and this relates to approximately 3.2 mol of water per repeat unit of PBI.[70]

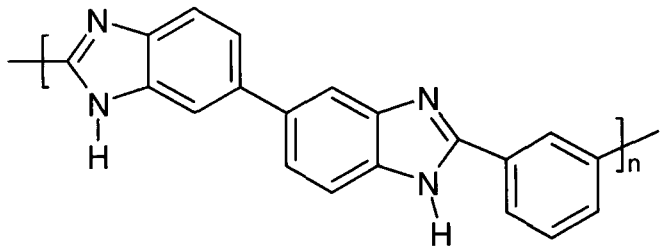

Figure 5 – The chemical structure of Polybenzimidazole, the benzimidazole groups provide the necessary hydrogen atom acceptor sites needed to complex phosphoric acid.

In comparison, Nafion is able to adsorb up to 34% by weight of water and results in a ratio of 21 mol of water per sulfonate group. The uptake of phosphoric acid in PBI occurs readily and using a 2M solution of H_3PO_4 resulted in a 2% uptake by weight. By increasing the concentration of the H_3PO_4 solution to 14 M the polymer was able to adsorb 10% of its weight in phosphoric acid.[70] The strong affinity of PBI for H_3PO_4 is promising for increased longevity of any fuel cell using H_3PO_4 as a liquid electrolyte.

However, the increase in H_3PO_4 is also related to an increase in water uptake that washes the acid molecules out of the electrolyte.[70]

Having a high concentration of acid inside the polymer membrane equates to having more acid molecules than basic sites on the polymer backbone. Using a high concentration stock acid solution, up to 4.7 units of H_3PO_4 per repeat unit of the polymer could be adsorbed.[71] This suggests that not all of the acid is bound to the polymer backbone via N-H∘∘O hydrogen bonding. The excess acid molecules interact together in the free volume of the polymer through strong intermolecular hydrogen bonding. Washing the acidified membrane with methanol removes any free acid leaving only the bound acid.[72] The amount of bound acid was studied by increasing the acid concentration in the membrane then washing it way. This study found that the amount of bound acid was constant at two units of $H_2PO_4^-$ per repeat unit of the polymer, while the free acid inside the polymer increased with the concentration of the stock solution. Infrared spectra of acidified PBI show that as the acid concentration increases, the bands corresponding to the free or hydrogen bonded N-H disappear. High concentrations of acid cause an onset of strong O-H vibrations, along with bands matching the $H_2PO_4^-$ anion. At higher acid levels, the infrared spectrum closely resembles the spectrum of pure phosphoric acid, implying the additional acid is acting as liquid phosphoric acid.

1.4.2.1 – Mechanism of Ion Conduction

The ionic conductivity of pristine PBI is extremely low and is below 10^{-5} S/cm without any acid.[71] The addition only two acid molecules per monomer unit causes an increase in ionic conductivity to 2.5 x 10^{-2} S/cm at 200°C.[73] Increasing the amount of acid creates free H_3PO_4 molecules that are not bound to the polymer backbone. By further increasing the acid content to 5.7 acid molecules per polymer unit, the conductivity increases to 6.8 x 10^{-2} S/cm at 200°C. The free acid in the polymer system contributes two thirds of the overall ionic conductivity. This shows that the ionic transport in acidified PBI originates from both the bound and the free acid molecules. Activation energies derived from the Arrhenius behavior of the ionic conductivity for strongly acidified samples are similar to that of concentrated phosphoric acid.

In phosphoric acid the mechanism of proton conduction depends on the viscosity of the solution.[74, 75] At high viscosity, the favoured mechanism involves a rotation of the phosphate, transferring a proton to a neighboring phosphate, this mechanism of proton transport is often referred to as the Grotthuss mechanism or structural diffusion and is illustrated in **Figure 6a**.[29, 30, 75] The second mechanism observed in phosphoric acid consists of bulk transport of the protons by a carrier molecule and is illustrated in **Figure 6b**. The strength of the second mechanism of ion transport in phosphoric acid is dependent on the amount of free acid.

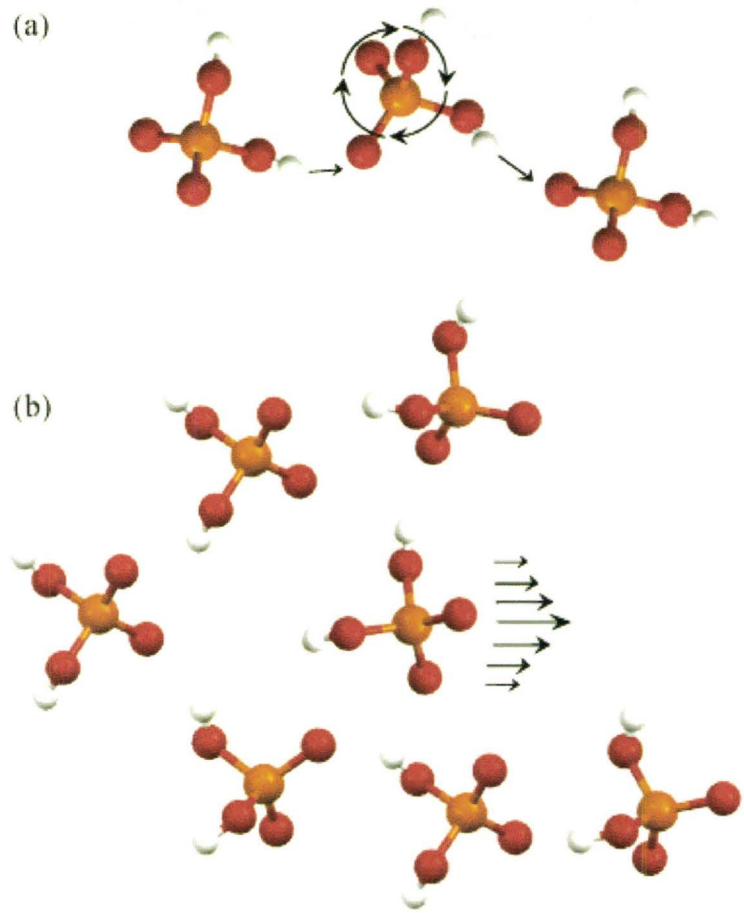

Figure 6 – (a) Proton transfer in phosphoric acid occurs through a hop of the proton between phosphates and a rotation of a phosphate. (b) Diffusion of the phosphate is the second mechanism of proton transport in phosphoric acid.

Knowing the mechanism of ion conduction for phosphoric acid simplifies the possible mechanisms for acidified PBI. The mechanism of proton conduction in acidified PBI was investigated through solid state NMR.[74, 75] NMR diffusion measurements on the ^{1}H and ^{31}P spins of acidified PBI show that the ^{1}H diffusion constants are more than two orders of magnitude larger than the phosphate. This confirms the presence of a structural diffusion mechanism of ion transport for acidified membranes.[74] The translation

diffusion of ions in acidified-PBI occurs via the unbound $H_2PO_4^-$ and H_3PO_4 and structural diffusion of protons through the hydrogen bonded protons of the system.[75] The mechanism of proton conduction in acidified-PBI varies due to the high dependence on the amount of bound, free acid, and the water content of the membrane.

1.4.2.2 – Drawbacks of a Liquid Electrolyte

The major drawback to acidified-PBI to being a successful ionic conductor is that the liquid electrolyte will escape the confines of the polymer membrane over time.[76, 77] As the temperature and loading of the catalyst increases, the amount of phosphoric acid lost from acidified-PBI membranes increases.[66] The increased load generates more water at the cathode, which at high temperatures quickly turns into steam. This leads to the steam distillation of phosphoric acid, which accelerates the escape of the acid from the membrane.[66] Loss of the liquid electrolyte in PBI is the primary factor in fuel cell degradation and is not reversible, unlike the dehydration process of Nafion membranes.

At temperatures above 100°C, the decay of the carbon support causes the Pt particles to agglomerate. This reduces the surface area of the particles, decreasing catalytic output for any fuel cell.[66] In acidified PBI, the phosphate anions also bind strongly to the Pt catalyst blocking any electrochemical reactions at the electrode.[78] The combination of agglomeration of the catalyst particles and binding of the phosphate molecules to the surface of the Pt particles severely hinders the electrochemical performance of the fuel cell. The breakdown of the carbon support at high temperature in

acidified PBI exacerbates the flooding of the electrodes by phosphoric acid due to the hydrophilic degradation products of the carbon support.[79, 80] This causes more water to flow into the electrolyte increasing the amount of steam generated, which removes the phosphoric acid from the membrane.

The operation of acidified-PBI at high temperature reduces the influence of carbon monoxide poisoning and eliminates the need for an aqueous electrolyte. However, the potential loss of the liquid electrolyte leads to decay of the catalyst and a reduction in ionic conductivity across the polymer. Introducing phosphoric acid to the polymer solves one mechanism of electrode degradation (carbon monoxide) but results in the generation of an alternative degradation mechanism.

1.4.3 – Protic Ionic Liquids

A new emerging area of fuel cell electrolytes focuses on the ionic transport properties of ionic liquids.[81-84] An ionic liquid or molten salt refers to an ionic salt that possesses a low melting point or the use of the material is above the melting temperature. The first reported ionic liquid was ethylammonium nitrate, discovered in 1914 by Paul Walden. The design of an ionic liquid involves the reduction of columbic forces that bind the ions by increasing the size of the cation or disrupting any periodic packing. The properties of ionic liquids opened new applications in catalysis, as green solvents, electrolytes and separation techniques.[85-90] An ionic liquid can be placed in one of two categories, an aprotic ionic liquid or protic. Aprotic ionic liquids do not have any

hydrogen atoms available for hydrogen bonding, unlike protic ionic liquids. Ionic liquids are known for the low vapour pressure, thermal and chemical stability, and as a reusable solvent for extracting metal ions or solvating organic compounds for reactions. Mixing a Brønsted acid (trifluoroacetic acid) and base (ethylamine) would create a protic ionic liquid, more examples are given in **Table 2**.

Table 2 – The properties of several protic ionic liquids.

Organic Base Mixed With Bis(trifluoromethanesulfonyl) amide	Melting Point of Complex (°C)	Ionic Conductivity at 130°C (10^{-2} S/cm)
Butylamine	16.2	1.04
Triethylamine	3.5	3.23
Imidazole	73.0	2.71
Benzimidazole	101.9	1.31
1,2,4 Triazole	22.8	2.20

The requirement to replace current aqueous systems with a protic ionic liquid would require the electrolyte to maintain ionic conductivity in temperature region above the boiling point of water. The low vapour pressures of an ionic liquid will ensure that the electrolyte will not evaporate at very high temperatures.

1.4.3.1 – Protic Ionic Liquids As Electrolytes

The high mobility and the strong ionic nature of protic ionic liquids makes them excellent candidates for proton electrolytes. Protic ionic liquids for use as fuel electrolytes was first tested using a series of protic ionic liquids based on the

bis(trifluorosulfonyl) imide anion.[91] The melting points of the salts varied between 3-170°C and notably the ionic conductivity of a number of the molten salts had ionic conductivities with a magnitude of 10^{-2} S/cm at 130°C. To prove that the ionic liquid transports hydrogen ions, a U-shaped tube with platinum electrodes would measure the polarization of the cell. Using N_2 gas at the anode, the cathode detected little to no current. Using H_2 gas at the anode however produced a much higher current density at the cathode, with an evolution of gas. The production of gas at the cathode confirms that the ionic liquid was indeed acting as a proton electrolyte transporting the hydrogen ion and reforming at the cathode. The same experiment except with an aprotic ionic liquid produced no current and no generation of gases at the cathode when switching between N_2 and H_2. This simple experiment showed that protic ionic liquids do indeed transport protons. A second test with oxygen and hydrogen at the electrodes converted enough fuel to power a calculator.[91] This shows that ionic liquids are capable electrolytes that can support the generation of electricity.

1.4.3.2 – Mechanism of Ion Transport

The mechanism of proton transport in ionic liquids depends on the flow of the ions or a structural diffusion mechanism. With ionic liquids, an imbalance in the stoichiometry creates a third mechanism of proton transport. The additional unprotonated cation molecules facilitate structural diffusion of the proton. Alternatively, in extremely fluid systems where the viscosity of the solution is very low, the amount of translational

diffusion would increase. The conditions and chemistry of the ionic liquid determines the overall method of ion conduction.

For benzimidazole bis(trifluorosulfonyl) imide (BITFSI), the contributions of each mechanism of proton diffusion was elucidated using NMR.[92] The measurement of the various diffusion constants for BITFSI through NMR yielded diffusion data for each resonance observed in the ^{1}H spectrum (cation) and ^{19}F spectrum (anion). Through the ^{1}H diffusion constant of the aromatic rings ($D_{Bz\text{-}H}$) the contribution of the vehicle mechanism was elucidated because those protons cannot be transferred by any other means. The diffusion of the nitrogen protons ($D_{N\text{-}H}$) was the sum of the unprotonated amide proton (in the case of excess benzimidazole) and the hydrogen ion attached to the free nitrogen site on the ring from the acid. The total diffusion of the hydrogen ions attached the benzimidazole ring (D_{H+}) represents the diffusion from the Grotthuss mechanism (D_G) and the contribution of the vehicle mechanism (D_V).[92] Any motion related to the vehicle mechanism is independently measured through the diffusion constant of the aromatic protons. The relationship between the diffusion of the hydrogen ions is

$$D_{H+} = D_V + D_G = D_G + D_{Bz\text{-}H} \qquad (1\text{-}5)$$

When the solution has an equimolar amount of both cation and anion, the diffusion constant of the hydrogen ions is equal to that of the diffusion constant of the nitrogen protons of the benzimidazole ring ($D_{N\text{-}H} = D_{H+}$). The diffusion constants allow for an in depth analysis of the mechanism of ion transport in ionic liquids.

1.4.3.3 – Fuel Cell Testing

The conductivity of the ionic liquid is comparable to any hydrated membrane in the solid-state. This shows that ionic liquids are viable electrolytes for hydrogen fuel cells. Operation of a BITFSI cell with hydrogen at the anode and oxygen at the cathode comparable power generation to other ionic liquids. [81, 91, 92] The current density of the ionic liquid was three times greater than anhydrous phosphoric acid at 150°C. Addition of water to the cathode had little effect on the power generation indicating that the fuel cell reaction will not affect the performance of the cell. However, the potential design of the electrode assembly to avoid leaching is incredibly difficult to imagine with current membrane plates. Using a glass tube in the shape of a U as used in solution electrochemistry does not provide a suitable means of operation for a mobile environment.[91, 92] Thus, the primary reason ionic liquids would be a bad electrolyte in fuel cells is that a cell requires a liquid electrolyte, negating any benefits such as a dry mechanism of ion conduction, the durability and mechanical properties of a solid, and similar processing requirements with a solid electrolyte membrane.

1.4.4 - Solid Acid Electrolytes

For a fuel cell electrolyte, the benefits of solid-state operation cannot be ignored. Pure ionic liquids have excellent ionic conductivity but suffer from the same fundamental problem as acidified PBI. Similar to ionic liquids or molten salts another class of solid state electrolytes exists, where the structure contains a metal cation (Cs^+, Rb^+, K^+, etc.)

and the anion of a protic acid ($H_2PO_4^-$, HSO_4^-, etc.).[17, 93-102] The name solid acid electrolyte was given to this family of salts due to their origins from strong acids and their solid-state ionic conductivity. The first occurrence of these simple salt compounds in the literature investigates the material's ferroelectric transition at low temperatures.[103] The search for another phase transition in cesium dihydrogen phosphate (CDP) led to the discovery of a high temperature transition at 230°C.[104] The phase transition of CDP at 230°C is accompanied by a 2-3 magnitude increase in ionic conductivity; the transition was dubbed 'superprotonic'. The ionic conductivity of CDP from three separate research groups is shown in **Figure 7**.[105] The discovery of the superprotonic phase transition inspired a search for other materials with a superprotonic phase transition.[106-108] However, reproducibility of the phase transition was the original problem with some researchers attributing the increase in conductivity to the water loss due to decomposition of the phosphate.[109, 110] A comprehensive investigation on the high temperature phase transition of CDP concluded that the transition is extremely sensitive to the preparation and local environment of the electrolyte.[105] Physical variables such as the high surface area, slow heating rates, and a lack of moisture will affect whether the thermal transition is superprotonic or a decomposition event. The superprotonic transition for CDP is temperature independent but the temperature of the dehydration can precede the superprotonic phase transition under certain heating conditions.[105] The superprotonic phase transition in CDP occurs primarily in high pressure or humid environments where the dehydration of the phosphate is unlikely. Measurement of a stable superprotonic

phase transition is achieved by using a single crystal of CDP rather than using finely ground powder.

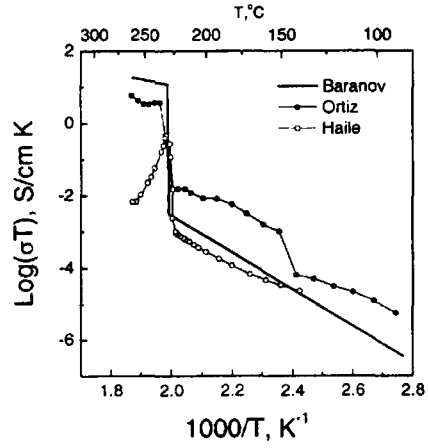

Figure 7 – The ionic conductivity of CDP from three separate research groups, reproduced from Boysen *et al.* Chem. Mater., 2003, 15, 727.

The superprotonic phase transition in CDP transforms the monoclinic cell into a structure with cubic symmetry.[111] In the lower temperature phase, the activation energy for the rotation of the phosphate via ^{31}P NMR is 71 kJ/mol as measured by Yamada *et al.*.[111] This value corresponds to the energy needed to increase the reorientation rate of the phosphate. As the thermal energy of the system increases, the increased motion of the phosphate leads to the rearrangement of the solid-state structure. The large barrier for rotation of the phosphate in the low temperature phase implies that the rotation of the phosphate plays an important role in the mechanism of ion conduction.

1.4.4.1 – Mechanism of Ion Transport

The exact mechanism of ion conduction in CDP at high temperatures is unknown, however a universal mechanism of proton transport in all solid acid electrolytes involves the reorientation of the anion.[112] Specifically the protons may hop or tunnel between the two potential minima near oxygen atoms of adjacent anions, molecular dynamics computations show nearly 2800 rotations of the -O-H group in 150 ps.[113] The next step involves the breaking of any hydrogen bonds, followed by a rotation of the anion. In the case of $CsHSO_4$, the anion reorientation is faster than the proton hopping, thus the proton hopping is the rate determining step.[114, 115] Since the reorientation rate is so fast once the proton hops, the transfer of a proton to an adjacent sulfate is guaranteed. However, a computational study shows that the barrier to proton hopping is much less for CDP, making the anion reorientation the slowest step in the conduction of protons.[116] This complicates the mechanism of proton transport because the proton could hop between the two potential minima and delay the phosphate reorientation.

A second mechanism of proton transport is possible in the solid acid electrolytes. A computational study on CDP suggested that the second mechanism does not require the phosphate to rotate.[116] In this mechanism, shown in **Figure 8**, the proton hops between the two minima of the hydrogen bond and eventually transfers to a second set of potential energy minima on the opposite side of the attached oxygen. This creates a hydrogen bond between the old oxygen atom and a completely different phosphate, and the proton would

then oscillate between the two oxygen atoms, repeating the process results in a net transfer of protons without the rotation of the anion.

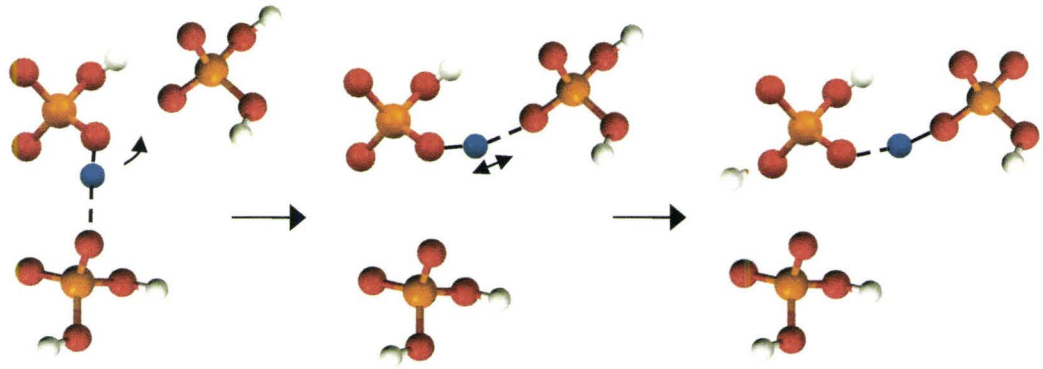

Figure 8 – The second possible mechanism of CDP begins with the flipping of the proton (shown in blue) to an empty adjacent hydrogen bond, followed by fast transfer between minima of the hydrogen bond, allowing for the overall transport of the proton.

In the computational study, the second mechanism without an anion reorientation is faster, due to the slow reorientation rate of the phosphate in CDP.[116] Both mechanisms are viable and could compete with each other in the superprotonic phase of CDP. The differences between $CsHSO_4$ and CDP show that the preferred mechanism of proton transport depends on the solid-state chemistry and symmetry of the solid acid structure.

1.4.4.2 – Solid Acid Fuel Cells

With a proton transport in CDP occurring readily above the stable superprotonic phase transition, the successful fabrication of a fuel cell comprised of a solid acid

electrolyte has great potential.[93] The first incarnation of a solid acid fuel cell did not produce a large enough current density to be competitive with polymer electrolytes. Ion transport in the cell was completely independent of any humidification and stable operation of the fuel cell lasted over 100 hours.[17] The high current density of the polymer electrolytes results from using thin electrolyte membranes, which minimizes the resistance of the electrolyte.

To improve the output of the fuel cell the thickness of the electrolyte layer was reduced. This caused the power density of the cell to increase to 415 mW/cm^2, which is comparable to a fuel cell using acidified-PBI as a electrolyte.[70] However, the thinner electrolyte caused irreversible instabilities in the operation of the fuel cell. The thin electrolyte membrane deformed due to mechanical stress as the cell operated. The formation of holes in the electrolyte prevented stable operation over a long period. The limiting factor for the power density in these fuel cells is the slow kinetics of the electrodes and not the mass transport of the electrolyte. Using a thin solid acid electrolyte layer produces a high power density but comes at the cost of stable operation. The major drawback is the deformation of the material at small electrolyte volumes, which causes a loss of contact between the electrode and the electrolyte. The approach of solid acid electrolytes towards hydrogen transport is a novel design but the structural decomposition contribute to the poor mechanical properties of the electrolyte. Increasing the ionic conductivity at a lower temperature and removing the decomposition of the

electrolyte by using other types organic salts would resolve the problems of a solid-acid fuel cell.

1.4.5 – Anhydrous Polymers

The main deficiency of acidified PBI was the removable acid medium used as a protic solvent. To counter the loss of the liquid acid, it was proposed by Kreuer to attach amphoteric nitrogen containing heterocycles to a polymer backbone.[117] The nitrogen heterocycles would replace the liquids and provide the necessary hydrogen bonding for proton conductivity. The goal of using the heterocycles is to remove the liquid state dependence of the ionic conductivity and rely on the solid-state conductivity of the polymer.

The first anhydrous polymer system incorporated vinyl imidazole blends with phosphoric acid and was later extended to include vinyl phosphonic acid instead of phosphoric acid into one copolymer.[118-121] Different ratios of the vinyl phosphonic acid and vinyl imidazole monomers units polymerized into one copolymer that was capable of anhydrous ion conduction. These new polymer systems are able to transport protons well above the boiling point of water. However, the ionic conductivity of the anhydrous vinyl imidazole vinyl phosphonic acid polymer at elevated temperatures did not exceed 10^{-6} S/cm. The low ionic conductivity is not sufficient for use in a fuel cell because it would create mass transport problems at the cathode. The low conductivity in a vinyl phosphonic polymer resulted from a condensation between neighboring phosphonates.

The condensation of the phosphonates limits the mobility of the phosphonate group reducing the number of charge carriers and blocking the pathway for ion conduction.[122]

To improve the ionic conductivity of the anhydrous polymer, a triazole ring replaced the imidazole ring in the monomer unit. Triazole has a cyclic structure that contains two basic nitrogen centers instead of the one of imidazole.[123] The maximum conductivity of the polymer electrolyte did increase by two orders of magnitude. The extra nitrogen center provides an additional location for the donation of a hydrogen atom, this increases the charge capacity of the heterocycle and as a result, the overall transport capability of the polymer. Other types of anhydrous polymer membranes comprised of poly(ethylene oxide) or poly (vinyl phosphonic acid) with triazole additives, or tethering a triazole ring to a long carbon chain attached to a siloxane polymer backbone have been studied.[124-127] Anhydrous electrolytes using triazoles is a new area of investigation and requires further understanding of the method of ion conduction and the performance in a fuel cell assembly.

1.4.5.1 – Mechanism of Ion Transport

The lack of any liquid in anhydrous polymer negates any ion conduction in the solid-state by translational diffusion. The diffusion of water in Nafion is possible because of the small size of the water molecule. The existence of nanoscale channels in Nafion aid water diffusion, these channels might not exist for other polymer membranes inhibiting diffusion of the additive electrolytes.[43] For additives larger than water, the

barrier to translational diffusion is high because the polymer lacks any solvent to facilitate the diffusion process. The overall ionic conductivity suffers from the lack of a vehicle mechanism for ion transport in anhydrous polymers. The only remaining mechanism of ion transport in a solid is structural diffusion. Structural diffusion requires high temperatures to provide the necessary thermal energy to drive the conduction process. For a heterocycle ring, transport of the hydrogen atoms occurs through a ring flip motion, exchanging hydrogen-bonded protons of the ring.[31, 128] The mechanism of ion conduction for a triazole-functionalized siloxane polymer (structure shown in

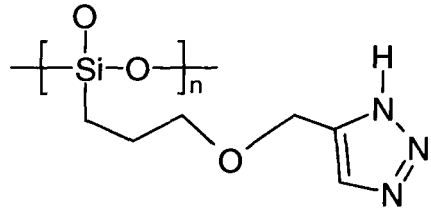

Figure 9 – The chemical structure of a triazole functionalized siloxane polymer for proton transport.

Figure 9) involves the breaking of the hydrogen bonds and the rotation of the triazole ring.[127] Solid-state NMR investigations show that the polymer backbone is very mobile above the glass transition temperature. Strong intermolecular couplings between the two aromatic rings and between triazole hydrogen bonds show that the packing of the triazole rings in the polymer avoids the silicon backbone and prefers to hydrogen bond. The hydrogen bonding in the polymer structure shows exceptional mobility near the glass transition temperature.[127] However, the increase in mobility of the polymer backbone is correlated to the change in activation energy for the ionic conductivity of the polymer,

implying that the dynamics of the polymer backbone is a necessary condition for the conduction of protons. The activation of the hydrogen bonding near the glass transition temperature is responsible for a two order of magnitude increase in the ionic conductivity, cooperatively the backbone and hydrogen bonding dynamics contribute to an overall conductivity of $5x10^{-6}$ S/cm at 140°C.[127] Linewidth measurements and the change in chemical shift of the ^{1}H hydrogen bonding resonances lead to the conclusion that the rate of hydrogen bonds in the structure breaking exceeds the rate of which they form at high temperatures. This suggests that the triazole ring is able to rotate freely and transport protons across the hydrogen-bonding network of triazole rings. The triazole ring rotates almost two orders of magnitude faster than the dynamics of the hydrogen bonds; implying that the limiting step in the conduction of protons for this polymer is the formation and deformation of the hydrogen bonds.[127] As the reorientation rate of the triazole ring increases, a decrease in activation energy occurs as the polymer begins to soften which allows for the cooperative rotation of the triazole rings.

The Arrhenius behavior of the hydrogen bonds in the triazole-functionalized polymer determines the overall conductivity and behavior of the polymer. The mobility of the hydrogen bonding determines the strength of the ionic conductivity. Further understandings of the role of hydrogen bonding in anhydrous polymers will allow for the optimization of structural diffusion and promote better ionic conductivity. The use of solid-state NMR to study the anhydrous polymer electrolyte revealed much about the

system at the molecular level and provided a mechanism of ion transport from the NMR data.

1.5 – Motivation and Goals

Nuclear magnetic resonance is a powerful tool for probing the structure and dynamics of solid-state materials. The tremendous amount of information available from NMR can contribute to a better understanding of solid-state materials. Particularly, in the case of solid-state electrolytes, solid-state NMR is able to investigate the local structure of a spin and the properties of the material that influence the nucleus. The mechanism of ion conduction in benzimidazole-based polymers is not completely understood and this thesis aims to determine the contribution of the phenyl functional groups of benzimidazole and the phosphate to the mechanism of ion exchange. The approach taken by this work is through the application of solid state NMR on a series of analogous electrolytes. The model compounds involve benzimidazole and different phosphate based anions to model the structure of acidified PBI. The model compounds simplify the system to its base factors, a benzimidazole cation and a phosphate based anion. Simplifying the structure will allow us to probe the role and contribution of each ion using solid state NMR. Based on the behavior of the ions, quantifying and mapping the mechanism for ion exchange in the model compounds is achievable. By modifying the model compounds, the changed structure will alter the mechanism and improve our understanding of mechanism of ion conduction for benzimidazole systems.

The design of new materials that avoid hydration dependent ion conduction is a necessary step forward. A new composite electrolyte is formed by inserting the model compounds into the pores of the host material. The new electrolyte will possess a solid-state mechanism and not require any liquids to conduct ions. This new electrolyte material will use a polymer as the host for the electrolyte material. Polytetrafluoroethylene (PTFE) is an excellent choice as support since the material is porous and chemically inert. The free volume of the polymer will determine the amount of electrolyte that the polymer may hold. If the polymer cannot support enough electrolyte material to form a continuous network, then the conducting ions will experience bottlenecks and dead ends that will reduce the ionic conductivity. The strong carbon-fluorine bonds contribute to the longevity and strength of the material, which is essential for fuel cell operation. The choice of polymer support is crucial because a weak polymer material could decompose and cause the migration of the electrolyte material into other areas of the fuel cell

The benefit to this approach is that the system is modular. If the electrolyte does not fit the desired specifications, then a new electrolyte is cast into the pores of the polymer. The electrolytes in this study are a combination of the acidified PBI polymer and the anhydrous organic phosphonate electrolytes. The electrolytes for the composite use the basicity of the imidazole ring to bind the phosphate-based acid groups together. The acidic and basic molecules react to form a hydrogen-bonding network. The ionic conductivity is investigated in the pure electrolyte and then as a composite material.

Characterizing the pure electrolyte first will provide insight into the mechanism of the more complex system. The study of these electrolytes will focus on fully understanding the mechanism of ion conduction in the pure material and the behavior of the electrolyte in the polymer support.

The combination of a high temperature anhydrous electrolyte and porous polymer membrane will fill the same role as anhydrous polymers while filling in the gap in the operating temperature range of a fuel cell and overcome the decomposition and deformation observed in solid acid electrolytes. Polymer composites proposed hope to fill the temperature gap between Nafion and acidified PBI in **Figure 10**. The study of these materials will improve our knowledge and understanding of ion conduction in the solid-state.

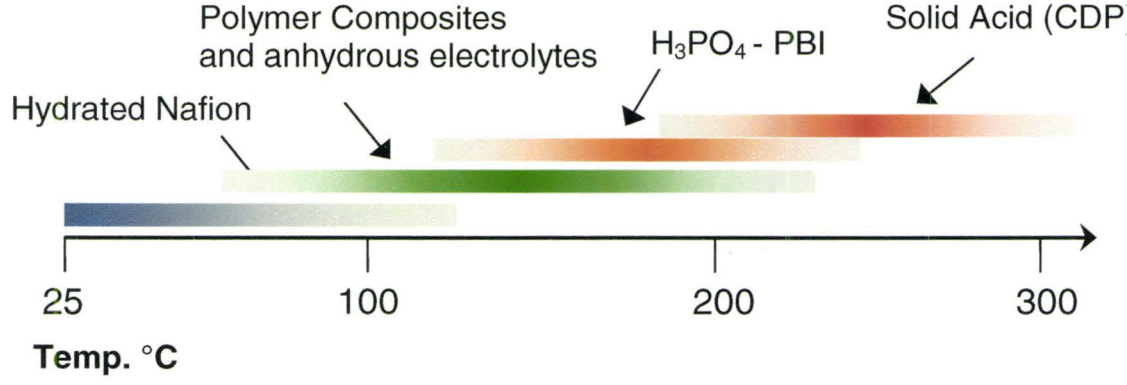

Figure 10 – The limited temperature range of Nafion, acidified PBI, the solid acid electrolyte (CDP) and the potential operating range of polymer composites and other anhydrous electrolytes.

1.6 - Thesis Outline

The first chapter introduces the background information on hydrogen fuel cells and several different types of electrolytes. The motivation and goals of this thesis are provided in the first chapter. In the second chapter, the NMR techniques used to study the different electrolyte materials are described in detail. The bulk techniques used in this thesis are introduced in the third chapter.

In the fourth chapter, the structure and dynamics of ion transport in several solid acid materials is investigated using solid-state NMR. Several different metal ions are investigated to understand their influence on the dynamics observed via solid-state NMR.

The fifth chapter is the study of polybenzimidazole using model compounds to depict the various types of transport in the polymer material. The types of reorientation and timescale of the dynamics in the model compounds have been characterized by solid-state NMR. The sixth chapter also uses a model compound to study how the imidazole ring flip influences the local dynamics.

The seventh chapter describes the union of the model compounds and a polymer host. This new material is intended to act as an anhydrous electrolyte for hydrogen fuel cells. The structure and dynamics of the material is characterized using solid-state NMR, scanning electron microscopy, and impedance spectroscopy. The last chapter provides a summary of the work completed and provides several avenues of future work.

1.7 - References

1. L. Carrette, K. A. Friedrich and U. Stimming, *Fuel Cells*, 2001, **1**, 5-39.
2. M. Winter and R. J. Brodd, *Chem. Rev.*, 2004, **104**, 4245-4269.
3. K. V. Kordesch and G. R. Simader, *Chem. Rev.*, 1995, **95**, 191-207.
4. K. D. Kreuer, *Annu. Rev. Mater. Res.*, 2003, **33**, 333-359.
5. K. D. Kreuer, *J. Membr. Sci.*, 2001, **185**, 29-39.
6. S. Koch, P. V. Hendriksen, M.Mogensen, Y.-L. Liu, N. Dekker, B. Rietveld, B. d. Haart and F. Tietz, *Fuel Cells*, 2006, **6**, 130-136.
7. M. C. Williams, *Fuel Cells*, 2007, **7**, 78-85.
8. C. W. Griffin, *J. Am. Chem. Soc.*, 1942, **64**, 2610-2613.
9. J. J. Baschuk and X. LI, *Int. J. Energy Res.* , 2001, **25**, 695-713.
10. P. Atkins, *Physical Chemistry*, W. H. Freeman & Co. and Sumanas, Inc., New York, NY, 1998.
11. V. Mehta and J. S. Cooper, *J. Power Sources*, 2003, **114**, 32-53.
12. J. Y. Tilquin, R. Cote, D. Guay, J. P. Dodelet and G. Denes, *J. Power Sources*, 1996, **61**, 193-200.
13. A. Rodrigues, J. C. Amphlett, R. F. Mann, B. A. Peppley and P. R. Roberge, Proceedings of the Intersociety Energy Engineering Conference, 1997.
14. S. J. Tauster, S. C. Fung and R. L. Garten, *J. Am. Chem. Soc.*, 1978, **100**, 170-175.
15. M. Yamada and I. Honma, *Polymer*, 2005, **46**, 2986-2992.
16. S. Tsushima, K. Teranishi and S. Hirai, *Energy (Amsterdam, Netherlands)*, 2004, **30**, 235-245.
17. D. A. Boysen, T. Uda, C. R. I. Chisholm and S. M. Haile, *Science*, 2004, **303**, 68-70.
18. Q. Li, R. He, J. O. Jensen and N. J. Bjerrum, *Chem. Mater.*, 2003, **15**, 4896-4915.
19. S. M. Haile, D. A. Boysen, C. R. I. Chisholm and R. B. Merle, *Nature*, 2001, **410**, 910-913.
20. A. Bozkurt, M. Ise, K. D. Kreuer, W. H. Meyer and G. Wegner, *Solid State Ionics*, 1999, **125**, 225-233.
21. T. A. Zawodzinski, Jr., T. E. Springer, F. Uribe and S. Gottesfeld, *Solid State Ionics*, 1993, **60**, 199-211.
22. J. Roziere and D. J. Jones, *Annu. Rev. Mater. Res.*, 2003, **33**, 503-555.
23. N. N. Greenwood and A. Thompson, *J. Chem. Soc.*, 1959, 3485-3492.
24. H. Steininger, M. Schuster, K. D. Kreuer, A. Kaltbeitzel, B. Bingol, W. H. Meyer, S. Schauff, G. Brunklaus, J. Maier and H. W. Spiess, *Phys. Chem. Chem. Phys.*, 2007, **9**, 1764-1773.
25. C. G. Densmore, P. G. Rasmussen and G. R. Goward, *Macromolecules*, 2005, **38**, 416-421.
26. Y. L. Ma, J. S. Wainright, M. H. Litt and R. F. Savinell, *J. Electrochem. Soc.*, 2004, **151**, A8-A16.

27. K. D. Kreuer, W. Weppner and A. Rabenau, *Solid State Ionics*, 1981, **3-4**, 353-358.
28. K. D. Kreuer, A. Rabenau and W. Weppner, *Angew. Chem.*, 1982, **94**, 224-225.
29. C. J. T. Grotthuss, *Ann. Chim. (Paris)*, 1806, **58**, 54-74.
30. N. Agmon, *Chem. Phys. Lett.*, 1995, **244**, 456-462.
31. W. Munch, K. D. Kreuer, W. Silvestri, J. Maier and G. Seifert, *Solid State Ionics*, 2001, **145**, 437-443.
32. A. J. Hopfinger and K. A. Mauritz, *Compr. Treatise Electrochem.*, 1981, **2**, 521-535.
33. K. A. Mauritz, *Proc. IUPAC, I. U. P. A. C., Macromol. Symp., 28th*, 1982, 879.
34. M. C. Wintersgill and J. J. Fontanella, *Electrochim. Acta*, 1998, **43**, 1533-1538.
35. B. S. Pivovar, M. Hickner, T. A. Zawodzinski, Jr., X. Ren, S. Gottesfeld and J. Neutzler, *Proc. - Electrochem. Soc.*, 2001, **2001-4**, 221-230.
36. Z. Siroma, T. Ioroi, N. Fujiwara and K. Yasuda, *Electrochem. Commun.*, 2002, **4**, 143-145.
37. Q. Chen and K. Schmidt-Rohr, *Macromolecules*, 2004, **37**, 5995-6003.
38. K. A. Mauritz and R. B. Moore, *Chem. Rev. (Washington, DC, U. S.)*, 2004, **104**, 4535-4585.
39. C. Zhou, T. A. Zawodzinski and D. A. Schiraldi, *Polym. Prepr. (Am. Chem. Soc., Div. Polym. Chem.)*, 2004, **45**, 760-761.
40. G. Ye, N. Janzen and G. R. Goward, *Macromolecules*, 2006, **39**, 3283-3290.
41. G. Ye, C. A. Hayden and G. R. Goward, *Macromolecules*, 2007, **40**, 1529-1537.
42. S. J. Paddison, R. Paul and T. A. Zawodzinski, Jr., *J. Chem. Phys.*, 2001, **115**, 7753-7761.
43. K. Schmidt-Rohr and Q. Chen, *Nat. Mater.*, 2008, **7**, 75-83.
44. T. D. Gierke, G. E. Munn and F. C. Wilson, *J. Polym. Sci. Pt. B-Polym. Phys.*, 1981, **19**, 1687-1704.
45. W. Y. Hsu and T. D. Gierke, *J. Membr. Sci.*, 1983, **13**, 307-326.
46. W. Y. Hsu, T. D. Gierke and C. J. Molnar, *Macromolecules*, 1983, **16**, 1945-1947.
47. T. D. Gierke, G. E. Munn and F. C. Wilson, *ACS Symp. Ser.*, 1982, **180**, 195-216.
48. W. Y. Hsu and T. D. Gierke, *Macromolecules*, 1982, **15**, 101-105.
49. W. Y. Hsu and T. D. Gierke, *J. Electrochem. Soc.*, 1982, **129**, C121-C121.
50. M. Fujimura, T. Hashimoto and H. Kawai, *Macromolecules*, 1982, **15**, 136-144.
51. M. Fujimura, T. Hashimoto and H. Kawai, *Macromolecules*, 1981, **14**, 1309-1315.
52. E. J. Roche, R. S. Stein and W. J. Macknight, *J. Polym. Sci. Pt. B-Polym. Phys.*, 1980, **18**, 1035-1045.
53. E. J. Roche, R. S. Stein, T. P. Russell and W. J. Macknight, *J. Polym. Sci. Pt. B-Polym. Phys.*, 1980, **18**, 1497-1512.
54. V. J. McBrierty, S. J. Martin and F. E. Karasz, *J. Mol. Liq.*, 1999, **80**, 179-205.
55. M. Ciureanu, *J. Appl. Electrochem.*, 2004, **34**, 705-714.

56. J. L. Zhang, Y. H. Tang, C. J. Song, J. J. Zhang and H. J. Wang, *J. Power Sources*, 2006, **163**, 532-537.
57. I. D. Stefanithis and K. A. Mauritz, *Macromolecules*, 1990, **23**, 2397-2402.
58. J. T. Payne and K. A. Mauritz, *Polym. Prepr. (Am. Chem. Soc., Div. Polym. Chem.)*, 1996, **37**, 520-521.
59. K. A. Mauritz, C. K. Jones and R. F. Storey, *Polym. Mater. Sci. Eng.*, 1988, **58**, 1079-1082.
60. S. Marzouk, F. Rachdi, M. Fourati and J. Bouaziz, *Colloids Surf., A*, 2004, **234**, 109-116.
61. L. Wang, D. Zhao, H. M. Zhang, D. M. Xing and B. L. Yi, *Electrochem. Solid State Lett.*, 2008, **11**, B201-B204.
62. G. Ye, C. A. Hayden and G. R. Goward, *Macromolecules*, 2007, **40**, 1529-1537.
63. Z. G. Shao, H. F. Xu, M. Q. Li and I. M. Hsing, *Solid State Ionics*, 2006, **177**, 779-785.
64. M. P. Rodgers, Z. Q. Shi and S. Holdcroft, *J. Membr. Sci.*, 2008, **325**, 346-356.
65. K.-D. Kreuer, *Chem. Mater.*, 1996, **8**, 610-641.
66. S. Yu, L. Xiao and B. C. Benicewicz, *Fuel Cells*, 2008, **8**, 165-174.
67. R. Devanathan, *Energy & Environmental Science*, 2008, **1**, 101-119.
68. H. Vogel and C. S. Marvel, *Journal of Polymer Science*, 1961, **50**, 511-539.
69. Y. Iwakura, K. Uno and Y. Imai, *Journal of Polymer Science Part A*, 1963, **2**, 2605-2615.
70. Q. Li, R. He, J. O. Jensen and N. J. Bjerrum, *Fuel Cells* 2004, **4**, 147-159.
71. X. Glipa, B. Bonnet, B. Mula, D. J. Jones and J. Roziere, *J. Mater. Chem.*, 1999, **9**, 3045-3049.
72. R. Bouchet and E. Siebert, *Solid State Ionics*, 1999, **118**, 287-299.
73. R. He, Q. Li, G. Xiao and N. J. Bjerrum, *J. Membr. Sci.*, 2003, **226**, 169-184.
74. J. R. P. Jayakody, S. H. Chung, L. Durantino, H. Zhang, L. Xiao, B. C. Benicewicz and S. G. Greenbaum, *J. Electrochem. Soc.*, 2007, **154**, B242-B246.
75. C. E. Hughes, S. Haufe, B. Angerstein, R. Kalim, U. Mahr, A. Reiche and M. Baldus, *J. Phys. Chem. B*, 2004, **1088**, 13626-13631.
76. G. Liu, H. M. Zhang, J. W. Hu, Y. F. Zhai, D. Y. Xu and Z. G. Shao, *J. Power Sources*, 2006, **162**, 547-552.
77. Y. F. Zhai, H. M. Zhang, G. Liu, J. W. Hu and B. L. Yi, *J. Electrochem. Soc.*, 2007, **154**, B72-B76.
78. Z. G. Qi and S. Buelte, *J. Power Sources*, 2006, **161**, 1126-1132.
79. T. Kinumoto, K. Takai, Y. Iriyama, T. Abe, M. Inaba and Z. Ogumi, *J. Electrochem. Soc.*, 2006, **153**, A58-A63.
80. J. Xie, D. L. Wood Iii, D. M. Wayne, T. A. Zawodzinski, P. Atanassov and R. L. Borup, *J. Electrochem. Soc.*, 2005, **152**, A104-A113.
81. A. Noda, A. B. Susan, K. Kudo, S. Mitsushima, K. Hayamizu and M. Watanabe, *J. Phys. Chem. B*, 2003, **107**, 4024-4033.
82. J.-P. Belieres and C. A. Angell, *J. Phys. Chem. B*, 2007, **111**, 4926-4937.

83. H. Nakamoto and M. Watanabe, *Chem. Commun.*, 2007, 2539-2541.
84. T. Yasuda, A. Ogawa, M. Kanno, K. Mori, K. Sakakibara and M. Watanabe, *Chem. Lett.*, 2009, **38**, 692-693.
85. T. Welton, *Coord. Chem. Rev.*, 2004, **248**, 2459-2477.
86. K. N. Marsh, J. A. Boxall and R. Lichtenthaler, *Fluid Phase Equilib.*, 2004, **219**, 93-98.
87. M. Galinski, A. Lewandowski and I. Stepniak, *Electrochim. Acta*, 2006, **51**, 5567-5580.
88. J. F. Liu, J. A. Jonsson and G. B. Jiang, *Trac-Trends in Analytical Chemistry*, 2005, **24**, 20-27.
89. O. A. El Seoud, A. Koschella, L. C. Fidale, S. Dorn and T. Heinze, *Biomacromolecules*, 2007, **8**, 2629-2647.
90. W. Xu and C. A. Angell, *Science*, 2003, **302**, 422-425.
91. M. A. B. H. Susan, A. Noda, S. Mitsushima and M. Watanabe, *Chem. Commun.*, 2003, 938-939.
92. H. Nakamoto, A. Noda, K. Hayamizu, S. Hayashi, H. O. Hamaguchi and M. Watanabe, *Journal of Physical Chemistry C*, 2007, **111**, 1541-1548.
93. T. Uda and S. M. Haile, *Electrochem. Solid-State Lett.*, 2005, **8**, A245-A246.
94. J. Otomo, T. Tamaki, S. Nishida, S. Q. Wang, M. Ogura, T. Kobayashi, C. J. Wen, H. Nagamoto and H. Takahashi, *J. Appl. Electrochem.*, 2005, **35**, 865-870.
95. T. Uda, D. A. Boysen and S. M. Haile, *Solid State Ionics*, 2004, **176**, 127-133.
96. C. R. I. Chisholm and S. M. Haile, *Solid State Ionics*, 2000, **136-137**, 229-241.
97. S. M. Haile and P. M. Calkins, *J. Solid State Chem.*, 1998, **140**, 251-265.
98. S. M. Haile, G. Lentz, K.-D. Kreuer and J. Maier, *Solid State Ionics*, 1995, **77**, 128-134.
99. K. R. Jeffrey and R. E. Wasylishen, *Can. J. Phys.*, 1986, **64**, 833-838.
100. R. Blinc, J. Dolinsek, G. Lahajnar, I. Zupancic, L.A.Shuvalov and A. I. Baranov, *Physica Status Solidi (b)*, 1984, **123**, K83-K87.
101. H. Matsunaga, I. Kazuyuki and E. Nakamura, *J. Phys. Soc. Jpn.*, 1980, **48**, 2011-2014.
102. Y. Uesu and J. Kobayashi, *Phys. Status Solidi A*, 1976, **34**, 475-481.
103. A. Levstik, R. Blinc, P. Kadaba, S. Cizikov, I. Levstik and C. Filipic, *Solid State Commun.*, 1975, **16**, 1339-1341.
104. A. I. Baranov, V. P. Khiznichenko and L. A. Shuvalov, *Ferroelectrics*, 1989, **100**, 135 - 141.
105. D. A. Boysen, S. M. Haile, H. Liu and R. A. Secco, *Chem. Mater.*, 2003, **15**, 727-736.
106. A. I. Baranov, L. A. Shuvalov and N. M. Schagina, *J. Exp. Theor. Phys.*, 1982, **36**, 459-462.
107. A. I. Baranov, V. P. Khiznichenko and L. A. Shuvalov, *Ferroelectrics*, 1989, **100**, 135-141.

108. M. Vijayakumar, J. W. Traer, J. F. Britten and G. R. Goward, *The Journal of Physical Chemistry C*, 2008, **112**, 5221-5231.
109. E. Ortiz, R. A. Vargas and B. E. Mellander, *J. Chem. Phys.*, 1999, **110**, 4847.
110. K. S. Lee, *J. Phys. Chem. Solids*, 1996, **57**, 333.
111. K. Yamada, T. Sagara, Y. Yamane, h. Ohki and T. Okuda, *Solid State Ionics*, 2004, **175**, 557-562.
112. A. I. Baranov, *Crystallogr. Rep.*, 2003, **48**, 1012-1037.
113. C. R. I. Chisholm, Y. H. Jang, S. M. Haile and W. A. Goddard(III), *Phys. Rev. B: Condens. Matter Mater. Phys.*, 2005, **72**, 134103-134101-134103-134120.
114. A. V. Belushkin, C. J. Carlile and L. A. Shuvalov, *journal of condensed matter*, 1992, **4**, 389.
115. J. C. Badot and P. Colomban, *Solid State Ionics*, 1989, **35**, 143.
116. H.-S. Lee and M. E. Tuckerman, *Journal of Physical Chemistry C*, 2008, **112**, 9917-9930.
117. K. D. Kreuer, *Solid State Ionics*, 1997, **94**, 55-62.
118. A. Bozkurt and W. H. Meyer, *Journal of Polymer Science*, 2001, **39**, 1987-1994.
119. A. Bozkurt and W. H. Meyer, *Solid State Ionics*, 2001, **138**, 259-265.
120. H. Pu, W. H. Meyer and G. Wegner, *Macromol. Chem. Phys.*, 2001, **202**, 1478-1482.
121. A. Bozkurt, W. H. Meyer, J. Gutmann and G. Wegner, *Solid State Ionics*, 2003, **164**, 169-176.
122. Y. J. Lee, B. Bingol, T. Murakhtina, D. Sebastiani, W. H. Meyer, G. Wegner and H. W. Spiess, *J. Phys. Chem. B*, 2007, **111**, 9711--9721.
123. S. U. Celik, U. Akbey, R. Graf, A. Bozkurt and H. W. Spiess, *Phys. Chem. Chem. Phys.*, 2008, **10**, 6058-6066.
124. C. A. Alabi, Z. Chen, Y. S. Yan and M. E. Davis, *Chem. Mater.*, 2009, **21**, 4645-4652.
125. S. T. Günday, A. Bozkurt, W. H. Meyer and G. Wegner, *J. Polym. Sci. Pt. B: Polym. Phys.*, 2006, **44**, 3315-3322.
126. U. Akbey, R. Graf, Y. G. Peng, P. P. Chu and H. W. Spiess, *J. Polym. Sci., Part B: Polym. Phys.*, 2009, **47**, 138-155.
127. U. Akbey, S. Granados-Focil, E. B. Coughlin, R. Graf and H. W. Spiess, *J. Phys. Chem. B*, 2009, **113**, 9151-9160.
128. K. D. Kreuer, A. Fuchs, M. Ise, M. Spaeth and J. Maier, *Electrochim. Acta*, 1998, **43**, 1281-1288.

Chapter 2: Methodology – Nuclear Magnetic Resonance

2.0 – Introduction

This chapter introduces the background and implementation for several key methods utilized in this thesis. The study of solid-state electrolytes often requires a multi-disciplinary approach to understand the proton transport properties of the material, and each technique yields specific information. The description of these techniques is split into two chapters one dealing with nuclear magnetic resonance (NMR) and the other with bulk techniques. Magnetic resonance experiments probe the local environment of the nuclear spin, observing changes on the molecular level. The following section outlines the theory and implementation of magnetic resonance in the solid state.

2.1 – The Origins of Spin

There are four intrinsic properties of a nucleus: mass, charge, magnetism and spin.[1] The first three properties are more tangible and easily related to everyday experiences. However, the spin of a nucleus is not. Spin, much like charge and mass, originate from the quarks that comprise the nucleus. The three elementary particles (proton, neutron, electron) are all fermions, possessing spin. The spin of a nucleus is like a rotation, which creates angular momentum. The spin angular momentum is quantized using the quantum number, I, and differs from the orbital angular momentum of an

electron. The spin quantum number may take whole integer or half integer values, and follows the same conventions as orbital angular momentum quantum numbers. Thus, the total number of spin states for an isolated nuclear spin in a magnetic field is 2I + 1. For example, a hydrogen nucleus has a nuclear spin of I = ½, and the two orientations of the spin in a magnetic field are m_I = ½, -½. For some nuclei, the spin quantum number for the naturally abundant nucleus is zero. Nuclei with a spin of zero do not possess a magnetic moment and are not NMR active isotopes.

Angular momentum, or spin, is only quantized along the z-axis of the magnetic field. The spin does not perfectly align along the magnetic field but rotates around the field in a cone due to the Heisenberg uncertainty principle. The magnetic moment of a nucleus is proportional to the spin through the gyromagnetic ratio, γ. The value of the gyromagnetic ratio is unique to every isotope and can vary greatly with respect to the number of protons and neutrons within the nucleus. The rate of the precession around the magnetic field is defined as,

$$\omega = -\gamma B_O \tag{2-1}$$

where ω is the rate of precession, γ is the gyromagnetic ratio, and B_O is the strength of the magnetic field in Tesla (T).[2-4] In the context of NMR discussions, the rate of precession for spin in a magnetic field is referred to as the Larmor frequency. A common magnetic field strength of an NMR spectrometer is 11.74 T; the Larmor frequency of a proton in this magnetic field is 500.12 MHz.

In a sample with many spins, the overall magnetization in the absence of a magnetic field is zero, as all the spin states are randomly oriented. For an ensemble of nuclear spins in an external magnetic field, a small population difference is generated as the spins orient along the field, creating a bulk magnetization according to the Boltzmann distribution. The bulk magnetization serves as the starting point for all NMR experiments and the amount of magnetization is directly proportional to the strength of the observed signal.

2.2 – Radiofrequency Pulses

The manipulation of spins occurs through a short burst of radio frequency radiation at or near the resonance frequency of the spin, called a pulse. The magnetic field component of the pulse at a given phase has a specific direction, defined by the rotation axis and rotates the magnetization around the axis according to the "right-hand rule" from classical physics.[1] A series of pulses and/or delays followed by a detection period is called a pulse sequence. A pulse sequence may vary the pulse length, phase, field strength, spacing, or number of pulses to probe a specific NMR interaction. Most modern pulse sequences include phase cycles, which cycle the phases of the pulses by ninety degrees to remove any pulse errors, artefacts, or unwanted transitions. The phase cycle of more complicated pulse sequences can use non ninety degree phase cycles.[14] A description of several important and reoccurring pulse sequences follows at the end of this chapter.

2.3 – Relaxation

2.3.1 – Longitudinal Relaxation

The magnetic field causes the spins to align with or against the magnetic field according to their current spin state. The process of the spins aligning along the magnetic field is called relaxation. Longitudinal relaxation of a spin is along the axis of the magnetic field, while transverse relaxation of the spins occurs in the plane perpendicular to the magnetic field. The relaxation of the magnetization in the magnetic field continues until the magnetic equilibrium is reached. The exponential build-up of the magnetization along the axis of the magnetic field is described by the Bloch equation,

$$M_Z(t) = M_z^0(1-\exp\{-(t-t_O)/T_1\}) \qquad (2\text{-}2)$$

This equation measures the change in magnetization along the z-axis (M_Z) against its original magnetization and time (M_Z^0, t_0) at given time (t).[2, 5] The T_1 parameter in Equation (2-2) is a time constant and it determines the rate of relaxation. The time required to reach magnetic equilibrium may range from very long (hours, even days) to very short (μs). For ^1H and most organic compounds, the relaxation times are on the timescale of seconds. The magnitude of the T_1 parameter is governed by time dependent variations in the local magnetic fields of the spin. For molecular motions to have an effect on the variations of the magnetic field at the spin, the correlation time of the motion has to match the Larmor frequency of the spin. The spectral density function, J (ω), defines the overlap of the magnetic fluctuation and the Larmor frequency

$$J(\omega) = 2 < B_X^2 > \frac{\tau_C}{1+\omega^2 \tau_C{}^2} \qquad (2\text{-}3)$$

where $<B_x^2>$ represents the average magnitude of the fluctuating field, τ_c is the correlation time of the fluctuating field and ω is the frequency of the spin.[1] A large correlation time yields a narrow spectral density function. The correlation time is required to overlap with the Larmor frequency to generate relaxation. Without these fluctuations in the local field, the nuclear spins would not relax.

2.3.2 – Relaxation in the Transverse Plane

Relaxation is anisotropic meaning that relaxation perpendicular to the static magnetic field occurs at a different rate than the longitudinal relaxation. Transverse relaxation causes polarization perpendicular to the magnetic field to decay over time. The detection of the NMR signal occurs in the transverse plane and decays according to equations (2-4) and (2-5) following a radiofrequency pulse which rotates the bulk magnetization into the transverse plane.

$$M_y(t) = -M_y^0 \cos(\omega t) \exp\{-t/T_2\} \qquad (2\text{-}4)$$

$$M_x(t) = M_x^0 \sin(\omega t) \exp\{-t/T_2\} \qquad (2\text{-}5)$$

The parameters describing the transverse relaxation are the starting magnetization along the axis (M_x^0 and M_y^0), the Larmor frequency (ω), and the transverse relaxation time constant (T_2). Any magnetization in the transverse plan undergoes precession around the magnetic field according to the Larmor frequency of the spin.[2, 5] Slight fluctuations in

the local magnetic field of a spin due to flip-flop transitions of the M_z state causes variations in the magnetic field experienced by the nucleus. This gives rise to a distribution of Larmor frequencies over a group of spins. Over time, the variation in local magnetic field causes dephasing of the magnetization, shown in **Figure 1**. This is the origin of transverse relaxation and the relaxation constant (T_2) describes how quickly the spins relax, or lose coherence, in the xy-plane.

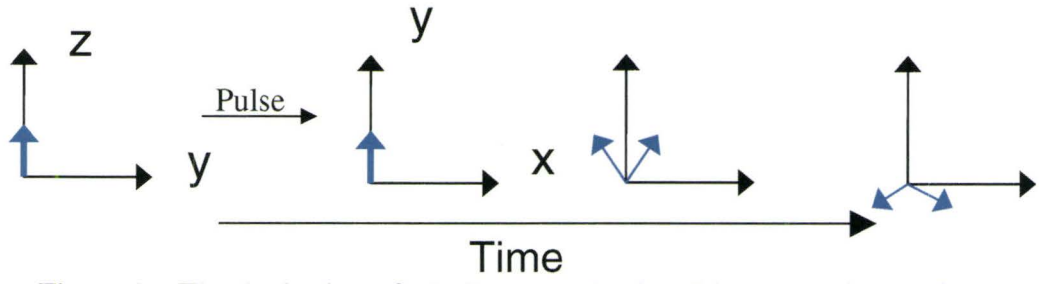

Figure 1 – The dephasing of a bulk magnetization (blue arrows) over time.

2.3.3 – Detection of the Nuclear Spin

The rotation of the nuclear spins in the transverse plane creates a measurable oscillation in the coil of the spectrometer. The decay of the spins in the time domain is referred to as the free induction decay (FID). A sample FID is presented as **Figure 2**. The relaxation of each spin sums to form a single FID representing the whole sample. The Fourier transform of the time dependent NMR signal is a spectrum.[6] The decay in the time domain controls the linewidth of the resonance in the spectrum. The Fourier transform of a very fast relaxing spin (short T_2) creates a very broad resonance.[6] There are two major types of line broadening: homogenous and inhomogeneous.

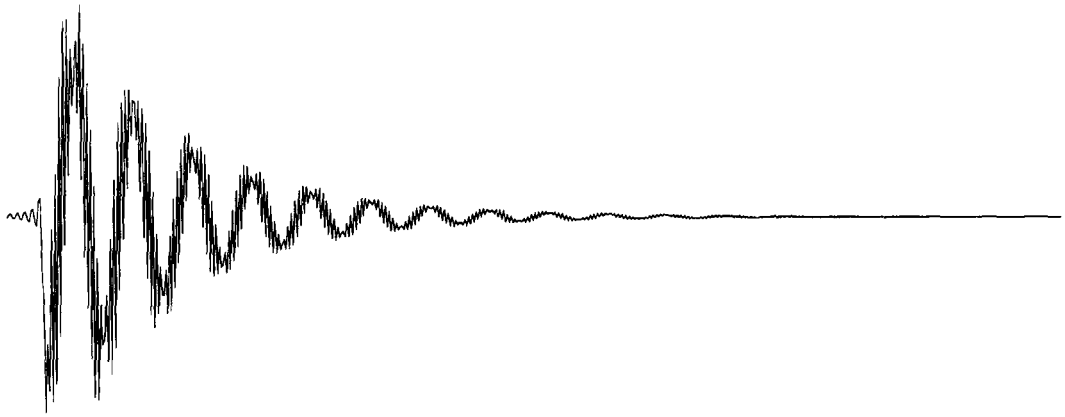

Figure 2 – An example of the relaxation acquired in the transverse plane, the observed relaxation is an NMR signal.

Homogenously broadened lines result from coherent multibody processes like the interaction of several strong dipolar couplings between protons.[7] Incoherent homogenous broadening results from the interaction of the spin with several incoherent fluctuating fields causing irreversible T_2 relaxation as described in the previous section.[7] Inhomogeneous broadening is due to many parallel coherent processes.[7] The overlap of the lineshapes could originate from an inhomogenity in the large static field, chemical shift dispersion, or anisotropy in the spins interactions.

2.4 - Nuclear Spin Interactions

The treatment of the spins using a classical approach like in **Figure 1** to predict the effect of pulses, breaks down for coupled systems. To treat coupled and more advanced systems the 'product operator' treatment was introduced.[15] The product operator formulism uses operators to label the spins and predict their rotation by pulses and delays. A mathematical operator describes the direction of the spin polarization

using Cartesian components of the form $\hat{I}_Z$, $\hat{I}_X$, $\hat{I}_Y$. The Hamiltonian is an operator that describes the total energy of the system. The contribution to the modulation by the spatial components of the Hamiltonian are summarized into one frequency term, ω, for each particular interaction. The modulation of the spins is described by sine and cosine functions oscillating at the frequency of the interaction. The application of 'product operator' is very accurate for spin systems in liquid state NMR. Any visual representation or vector model breaks down when treating a pulse sequence with any correlated spin state.[15] Thus, a more complex description of a spin dynamics involving a matrix representation for all the operators, pulses, and spin states is more applicable for advanced solid-state NMR techniques.[10, 13, 16, 17] The matrix representations accurately describe the evolution and time dependence of an ensemble of coupled nuclear spins. The density of states, $\rho(t)$, describes the current state of the spin system in the form of a matrix, the trace of $\rho(t)$ leads to the observable. The application of the density matrix approach leads to a better understanding of the pulse sequence and promotes the design and implementation of new sequences.

Using spherical tensors is an acceptable approach for describing coupled spin states of a system undergoing evolution or pulse. The spherical tensors for the spins have the form $\hat{T}_{l,m}$, where l is the rank of the total angular momentum of the coupled spins and m is the z-component of the spin state. The spatial portion of the Hamiltonian is given by a similar formalism, $\hat{A}_{l,m}$. For example, prior to a pulse the spin state is $\hat{I}_Z$ or

$\hat{T}_{1,0}$ and immediately after the pulse the spin state is $\hat{I}_X$ or $2^{-½}(-\hat{T}_{1,1}+\hat{T}_{1,-1})$.[10] This method quickly shows the number of coupled spins and their coherence. The last spherical harmonic of interest is the $\hat{T}_{2,\pm2}$ which refers to two coupled spins that have the spin state $I_\pm I_\pm$. The spherical tensors only describe the spin operators while $\rho(t)$ represents the current state of the system.

2.4.1 – Zeeman

The presence of a magnetic field influences the nuclear spin significantly. The largest interaction for a spin half nucleus is the Zeeman interaction, which correlates the static magnetic field with the gyromagnetic ratio and the spin. The Hamiltonian for the Zeeman interaction dictates the energy levels of the spins.[8]

$$H = -\gamma B_0 I_Z \qquad (2\text{-}6)$$

The Zeeman term scales directly with an increase in magnetic field, increasing the energy spacing between spin states. The energy gap between two energy levels corresponds to the Larmor frequency of the spin. On the general scale of the electromagnetic spectrum, the transition energy of NMR is small and is on the radiofrequency scale. In NMR, the thermal energy (at ambient temperatures) of the system is larger by a few orders of magnitude than the Zeeman interaction. This creates a very small population difference between the spin states. The population of the spin states are controlled by the Boltzmann equations.[9] The low population difference causes only a tiny fraction of the population contribute to the overall polarization of the sample. For this reason, NMR falls behind

other spectroscopic techniques in terms of sensitivity. Larger magnetic fields increase the Larmor frequency and improve the amount of signal detected.

2.4.2 – Quadrupolar Interactions

The charge distribution of the nucleus may not be symmetric and thus has a quadrupole moment which interacts with local electric field gradients from the surrounding chemical environment. The interaction of the nucleus with the electric field is the quadrupolar interaction. This interaction exists for spins with I > ½. The Hamiltonian of the quadrupolar interaction is,

$$H_Q^{(ij)} = -\frac{eQeq}{2I(2I-1)\bullet\hbar}\bullet\frac{1}{2}(1-3\cos^2\theta)\bullet(3I_Z^{(i)}I_Z^{(j)} - I^{(i)}I^{(i)}) \qquad (2\text{-}7)$$

where e is the elementary charge, Q is the quadrupole moment, and eq corresponds to the electric field-gradient tensor.[10] The quadrupolar moment is different for each atom and each isotope has a unique quadrupolar moment. The quadrupolar interaction is sensitive to changes in the local environment of the spin through the direction and the magnitude of the electric field gradient at the nucleus. These are the two main contributing factors to the magnitude of the quadrupolar coupling constant (C_Q). The quadrupolar constant in Hertz is defined as,

$$C_Q = \frac{eQeq}{h} \qquad (2\text{-}8)$$

For spins with I = ½, there is no quadrupolar interaction because the nucleus is symmetric. For this body of work, the quadrupolar interaction is largely disregarded as

the majority of the work is performed on hydrogen, carbon, and phosphorus, which are all $I = ½$ nuclei.

2.4.3 – Chemical Shift

The circulating electrons surrounding the nucleus decrease the strength of the magnetic field at nucleus, reducing the Zeeman interaction. The effect of the electrons on the magnetic field at the nucleus is illustrated in **Figure 3**, which describes the chemical shift tensor, σ.

$$\vec{B}_i = \sigma\vec{B}_O \qquad (2\text{-}9)$$

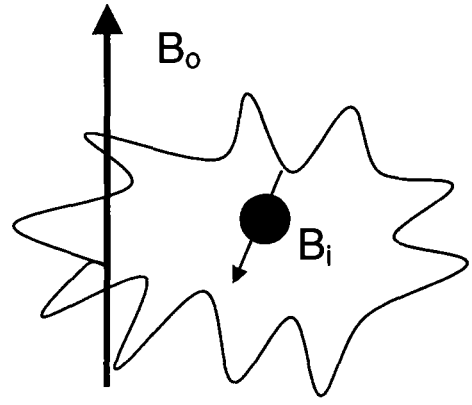

Figure 3 – The circulating electrons reduce the strength of the magnetic field at the nucleus, B_i.

The shielding a nucleus experiences depends greatly on the surrounding electron density. The isotropic chemical shift, σ_{iso}, is the orientation independent component of the shielding tensor from the trace of the tensor matrix,

$$\sigma_{iso} = \frac{1}{3}(\sigma_{11} + \sigma_{22} + \sigma_{33}) \qquad (2\text{-}10)$$

The local magnetic field at the nucleus, B_i, differs along the axis of a bond versus being perpendicular to a bond and with the direction of the external magnetic field, giving rise to the overall shielding experienced by each nucleus. The three diagonal elements are referred to as the principal values.[7] When the matrix is diagonalized, only the σ_{11}, σ_{22}, and σ_{33} components remain. These three components are averaged to give the isotropic chemical shift. The shielding tensor describes the shielding in three dimensions making the shielding of a nuclear spin very sensitive to changes in the chemical environment. The chemical shielding is sensitive to electronic structure of the chemical environment and the perturbation to the Zeeman Hamiltonian is given as,

$$H_{CS,iso} = \sigma_{iso}\gamma B_O I_Z \qquad (2\text{-}11)$$

where the contribution of the isotropic shielding is σ_{iso}.[1] The range of the chemical shift for a nucleus scales with field and the axis is normalized to the Larmor frequency of the spin, making it independent of the field. The units of the chemical shift are given in part per million (ppm) of the resonance frequency and is referenced to a specific compound.

In the liquid state, rapid isotropic tumbling causes the molecule to sample every orientation with respect to the magnetic field, causing the chemical shift to be averaged to σ_{iso}. In the solid-state, the orientation dependence is preserved and retains important information on the local electronic environment of the nucleus and is referred to as the chemical shift anisotropy (CSA). A single crystal may only produce one resonance as it is highly ordered system where all the nuclei have the same orientation with respect to the magnetic field. In a powder sample, all possible orientations for the electron cloud

surrounding the nucleus occur, giving a distribution in frequency. The frequency distribution results in a power pattern An example powder is shown in **Figure 4**. The three defining features of the powder pattern are defined by using the following equality,

$$|\sigma_{33} - \sigma_{iso}| \geq |\sigma_{22} - \sigma_{iso}| \geq |\sigma_{11} - \sigma_{iso}| \quad (2\text{-}12)$$

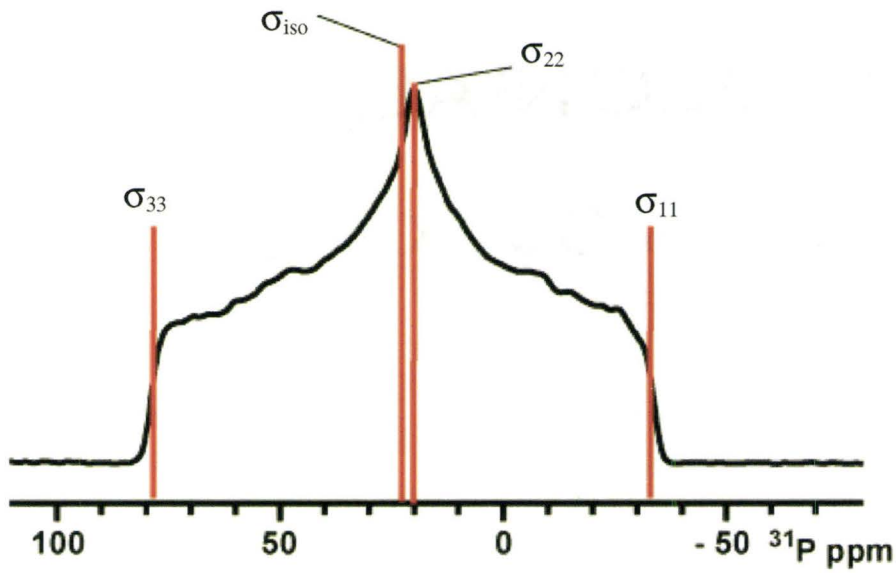

Figure 4 – The CSA pattern for single ^{31}P spin in a methyl phosphonate. The span of the interaction is 112 ppm wide.

Using these rules, it is possible to assign the CSA parameters to the spectrum in **Figure 4**. The edge with the highest frequency is σ_{33}, the lowest edge is defined by σ_{11} and the discontinuity in the middle is σ_{22}.[7] With the assignment of the three components of the chemical shift tensor, the calculation of the asymmetry (η) and span (δ) characterize the powder pattern and are useful when comparing different chemical environments. The span is the difference between the two edges of the pattern and gives the total width. The asymmetry of the CSA defines the general shape and type of environment that the spin

occupies. The CSA of an isolated molecule with tetrahedral symmetry would collapse into a single resonance. The asymmetry and span are defined by the following set of equations,[7]

$$\eta = \frac{\sigma_{22} - \sigma_{11}}{\sigma_{33} - \sigma_{iso}} \tag{2-13}$$

$$\delta = \sigma_{33} - \sigma_{11} \tag{2-14}$$

The CSA holds valuable information on the chemical shift of the spin and its surrounding environment. Changes to the shape of the CSA reflect variations in the chemical environment.

2.4.4 – Scalar Coupling

The most common coupling in liquid state NMR is the scalar coupling. The coupling describes the scalar product of two interacting spins with a proportionality constant, J.[9] A scalar coupling occurs between two nuclei and is mediated by the electrons in the chemical bonds between the coupled nuclei. The strength of a scalar coupling depends on the σ and π bonding between the coupled nuclei. The strength of the scalar coupling will decay with an increase in the number of chemical bonds between the coupled nuclei. A J-coupling between two protons is very small and the typical proton-proton J-coupling is only a few Hertz. This body of work focuses on solid-state electrolytes where J-couplings are present, but are obscured due to the strength of other interactions.

2.4.5 – Dipole-Dipole Coupling

Dipolar couplings are direct couplings, while J couplings are indirect couplings.[1] For spin half nuclei with a high gyromagnetic ratio, the largest interaction is the dipolar coupling. A J-coupling occurs by the interaction of the nuclear spin with the spin of the nearby electrons in the chemical bonds. The influence of the nuclear spin on the spin of the electron is propagated to the second electron of the bond to the nearby nucleus, the resultant perturbation is the scalar coupling depicted in **Figure 5**. The dipolar coupling between two nuclei occurs through space. Both couplings diminish with distance.

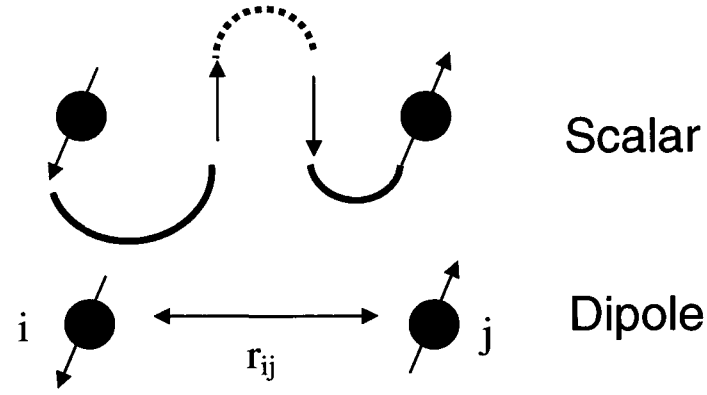

Figure 5 – The scalar coupling is mediated through the spin of the electron, while the dipolar coupling occurs directly through space.

The dipolar coupling originates from the magnetic field of the nucleus. As the influence of the nuclear magnetic field diminishes the strength of the coupling decreases. The magnitude of the dipolar coupling depends strongly on the gyromagnetic ratios of the spin pair and the distance between them. The terms of the complete dipolar Hamiltonian that commute with the Zeeman interaction form the secular equation below, where μ_0 is

the permeability of free space and θ is the angle between the vector connecting the spins and the magnetic field.

$$H_D^{(ij)} = -\frac{\mu_o \hbar \gamma_i \gamma_j}{8\pi \cdot r_{ij}^3}(1-3\cos^2\theta)(3I_Z^{(i)}I_Z^{(j)} - I^{(i)}I^{(i)}) \qquad (2\text{-}15)$$

The homonuclear dipolar Hamiltonian scales with the square of the gyromagnetic ratio and inverse cube of the internuclear distance. In ^{1}H NMR, the dominant form of line broadening due to coherent and incoherent dipolar interactions due to its large gyromagnetic ratio and high natural abundance of the ^{1}H spins. The dipolar couplings are so strong that they broaden the resonance to such an extent that no information about the individual spin interactions remain. For example, the sum of all the homonuclear dipolar couplings for a single aromatic proton in benzimidazole in the solid state could reach 30 kHz by just considering only the nearest neighboring protons. The dipolar Hamiltonian for homonuclear spins presented above differs from the heteronuclear Hamiltonian. The scalar product **I**·**S** is not present because the difference between the precession frequencies for the heteronuclear spins is so much larger than the magnitude of the coupling those terms are suppressed.[10] Thus, the heteronuclear Hamiltonian for a dipolar coupling is much simpler and contains only the terms relating to the I_Z and S_Z states.[7]

$$H_D^{(ij)} = -\frac{\mu_o \hbar \gamma_i \gamma_j}{4\pi \cdot r_{ij}^3} \bullet \frac{1}{2}(1-3\cos^2\theta) \bullet (3I_Z^{(i)}S_Z^{(j)}) \qquad (2\text{-}16)$$

The strength of the heteronuclear Hamiltonian is generally lower than that of proton homonuclear case due to the change in gyromagnetic ratios. Heteronuclear dipolar couplings are approximately several hundred Hertz, while a homonuclear coupling involving protons may go above ten thousand Hertz.

The dipolar Hamiltonian has two dependencies, space and spin. The spatial dependence of the Hamiltonian includes the distance dependence and the angle dependence. Physical changes such as movement of the atoms and their position relative to the magnetic field affect the space portion of the Hamiltonian, while magnetic fields interact with the spin portion of the Hamiltonian. For homonuclear spin pairs, the I_Z states of the Hamiltonian describe the interaction of the dipolar fields of the nuclear spins.[10] The $\mathbf{I}\cdot\mathbf{I}$ term in the dipolar Hamiltonian describes interaction of spins with different polarization. If the difference in transition energy between the two spins is small, then the dipolar field of one spin may flip the polarization of the other. This causes both spins to change polarization and exchange their spin states.[10] The process of spin exchange occurs for spins in the $\mathbf{I_Z}$ state, and is called spin diffusion. The process is negligible for a spin pair with a chemical shift difference that exceeds the strength of the dipolar coupling.[10] For a heteronuclear spin pair, the difference in Larmor frequencies is large and the exchange terms are dropped from the Hamiltonian. Homonuclear spin pairs produce the strongest examples of spin diffusion.

2.5 – Magic Angle Spinning

In the solid state, assuming little molecular motion, the spectra for spin ½ nuclei are dominated by the dipolar couplings and the chemical shift anisotropy. The two interactions have different effects on a spectrum, as seen in **Figure 4**, where the CSA for a single ^{31}P site spans over 100 ppm. A strong dipolar coupling will lead to a broad resonance. For nuclei with strong dipolar couplings and a small chemical shift range, all the resonances tend to overlap. In the case of protons, the chemical shift scale is small, < 20 ppm, and those spins experience the strongest dipolar broadening, 10 to 100 kHz. This would undermine any chemical shift resolution in the spectrum. The overlap of the resonances occurs when two or more spins occupy the same region of the spectrum. In contrast, the CSA pattern of **Figure 4** collapses in the liquid state into a single narrow line at the isotropic chemical shift. The broadening from the dipolar couplings is negligible due to the fast molecular reorientation in the liquid state. Without effective reduction in broadening effects, ^{1}H solid-state NMR would be rendered useless with overlapping resonances.

The Hamiltonians of anisotropic interactions provide an insight to how the samples maybe manipulated to achieve high resolution in the solid-state. The principal axis system with polar coordinates (θ, ϕ, γ) defines the frame of reference for the spin (**Figure 6**) with respect to the rotor axis. The angular dependence of the chemical shift Hamiltonian in the principal axis system is,[7]

$$H = \{\sigma_{iso}\gamma B_O + \frac{1}{2}\delta_{CS}(3\cos^2\theta - 1 - \eta\sin^2\theta\cos 2\phi)\}I_Z \qquad (2\text{-}17)$$

The anisotropic portion of the chemical shift Hamiltonian contains an angular dependence on $(3\cos^2\theta\text{-}1)$. This feature also manifests itself in the dipolar Hamiltonian. For any interaction along the magic angle, 54.7° will have a reduction in the dipolar coupling strength or the anisotropy of the chemical shift. For any interaction not along the magic angle, the strength of the interaction is scaled. However, rotating the sample around the magic angle will average the interactions onto that axis, if the rate of rotation is significantly larger than the interaction. Rotation of the sample at the magic angle is illustrated in **Figure 6** and the manipulation of the space terms in the Hamiltonian through rotation of the sample is referred to as magic angle spinning (MAS).[11]

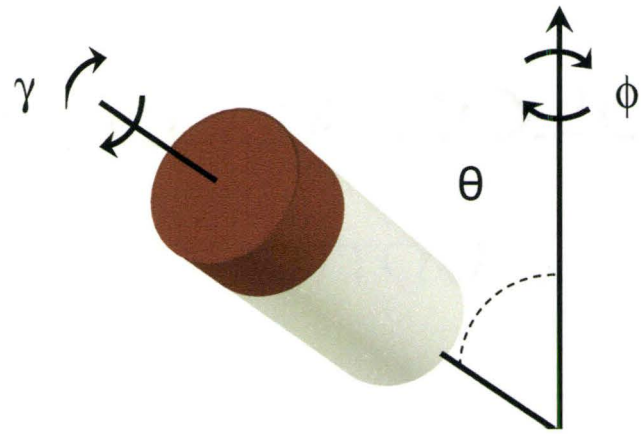

Figure 6 – The illustration of a sample rotating at the magic angle. The rotation causes a decrease in line broadening in the solid-state spectrum.

Rotation around the magic angle creates high-resolution spectra, free of any significant line broadening. Magic angle spinning in part has promoted the growth of an entire research field based on the investigation of solid-state materials using NMR.

The rotation of the sample around the magic angle introduces a dependence of the Hamiltonian on the frequency of the sample rotation. The Hamiltonian is now time dependent and does not commute with itself at different points in the rotation causing the time-dependent spatial part of NMR Hamiltonian to be,

$$\Omega(t_0,t_1) = \frac{\omega_\lambda}{2\omega_R} \bullet [\frac{1}{2}\sin^2\theta(\sin(2\omega_R t_1 - 2\gamma) - \sin(2\omega_R t_0 - 2\gamma)) - \sqrt{2}\sin\theta(\sin(\omega_R t_1 - \gamma) - \sin(\omega_R t_o - \gamma))] \quad (2\text{-}18)$$

where ω_R is the frequency of the sample rotation, t is the time, ω_λ is the spatial portion of the Hamiltonian, the angles γ and θ are polar coordinates referring to the rotor axis.[10] The spin terms of the Hamiltonian are unaffected by the sample rotation and need not be considered. The time dependence of the rotation creates modulations in the observed spectrum, refocusing at intervals of the rotation frequency, there by generating rotational echoes in the FID. This causes the appearance of spinning side bands that mimic the linewidth of the isotropic resonance at intervals of the rotor period. Spinning side bands occur when the MAS frequency does not exceed the strength of the interaction by several fold. In **Figure 7**, the MAS frequency is purposely set to a low value to demonstrate the number of the sidebands that might occur in a spectrum. Sample rotation creates many orders of sidebands spreading out the intensity of the isotropic resonance with a pattern resembling the power pattern. Determining CSA parameters for a multi-spin system with sample rotation is difficult but using the intensity and number of the sidebands for each resonance it is possible to fit the CSA parameters for many sites.[12]

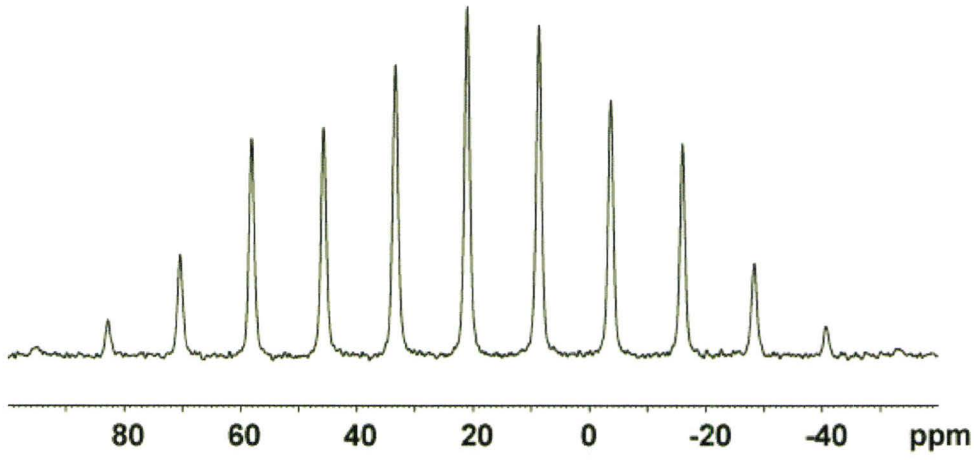

Figure 7 – The ^{31}P MAS spectrum of Figure 4 using a rotation frequency of 2400 Hz, with the isotropic resonance is at 21 ppm.

Sidebands from dipolar coupling do appear in the spectrum for strongly coupled spins.[10] The number of dipolar couplings and their strengths all contribute to the intensity and number of sidebands. Homonuclear dipolar couplings of a spin increase the linewidth of the resonance by slightly perturbing the energy of the spin state. With fast MAS, it is possible to narrow the resonance and remove the effect of the strong dipolar couplings. Without fast MAS frequencies (~25kHz MAS) the proton resolution in a spectrum of a polymer system is incredibly poor and only systems without a network of strong dipolar couplings could be studied. The effect of strong MAS on a resonance that experiences homogeneous broadening due to the dipolar couplings is shown as **Figure 8**. Once the MAS frequency is significantly above the strength of the space term in the dipolar Hamiltonian (D_{ij}), further increases to the MAS frequency would have little effect on the linewidth of the resonance.[13] The dipolar coupling strength does not scale with the

magnetic field; hence increasing the Larmor frequency would increase the separation between resonances, increasing resolution.

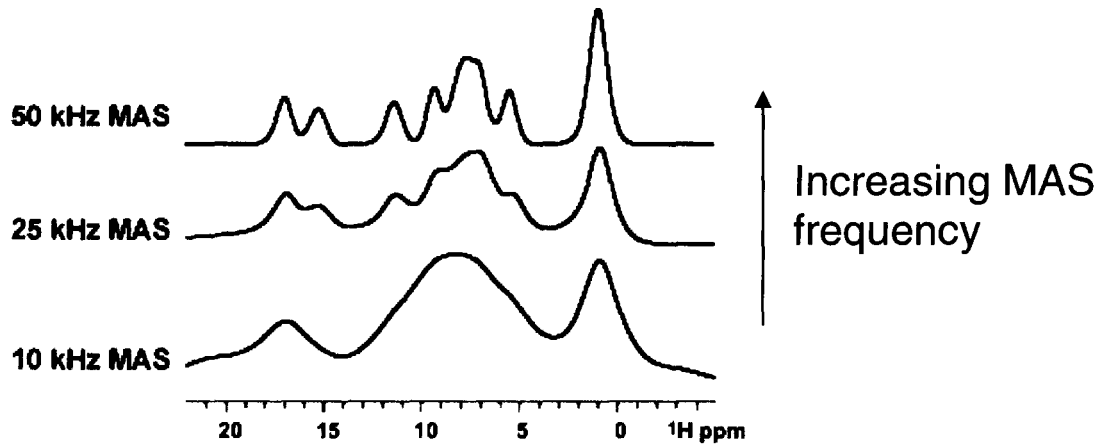

Figure 8 – As MAS frequency increases, the linewidth of a dipolar broadened line decreases. Once $\omega_R >>> D_{ij}$, then increases in the MAS frequency will have little effect on the linewidth of the resonance.

2.6 - Dynamics

Solid-state NMR is able to probe the local atomic structure of a spin using homo and heteronuclear correlation spectra. The second key component of solid-state NMR is the ability to observe effect of molecular motions on the spectrum.[18] There are three different regimes of motion in NMR and they are demonstrated in **Figure 9** and defined by the separation of the exchanging resonances in frequency with respect to the exchange rate.[1] The slow motion regime occurs when the rate of chemical exchange is less than the frequency difference between the exchanging spins and is shown at the lower temperatures in **Figure 9**.

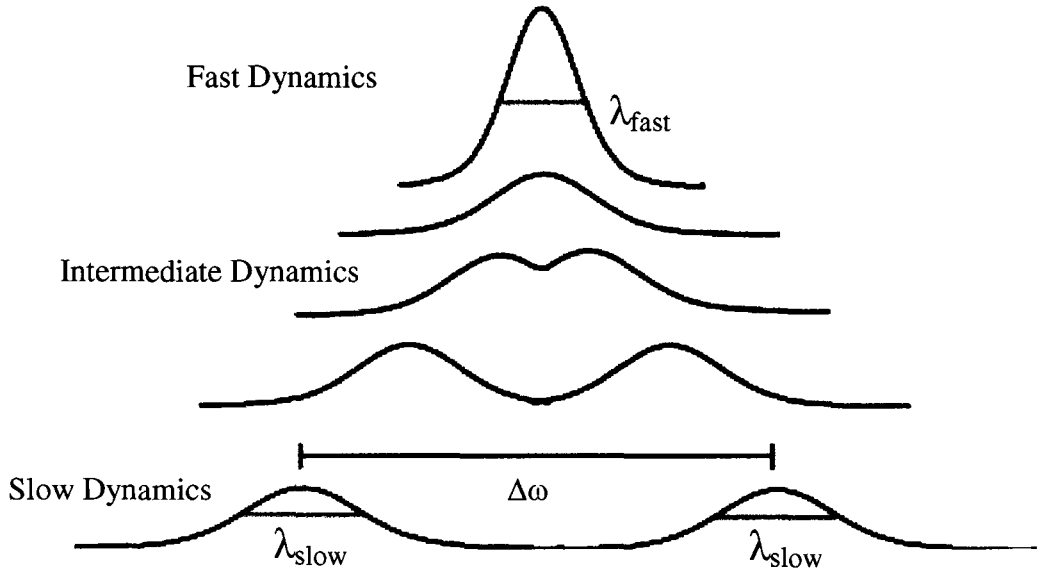

Figure 9 – The coalescence of two resonances shows the exchange between two different locations in the crystal structure.

In the intermediate exchange regime, the exchange rate is close to or equal to the difference in frequency of the two resonances. As the exchange rate increases, the frequency difference between the two resonances starts to decrease; this is the coalescence process. When the spins enter the intermediate motional regime in **Figure 9**, the two resonances broaden and combine to form only one resonance at the average of the two chemical shifts. The average of the two chemical shifts is only observed if the process is undergoing symmetric exchange, which occurs when the two exchange rates are equal between the two sites.[1] In some cases, unsymmetrical exchange occurs causing the coalescence to shift to the resonance with the larger population.

With fast dynamics, an increase in temperature results in quicker motions that reduce the linewidth of the resonance. The definition of the fast motion regime is when

the rate of chemical exchange (Ω) is faster than the frequency difference between the exchanging resonances. The linewidth change measured by NMR is proportional to a change in correlation time in the fast motion regime. For exchange in the fast motion regime, an Arrhenius analysis applies to the linewidth. The T_2 or linewidth of the resonance changes according to the following Arrhenius expression for motion,

$$\frac{1}{\tau_c} \propto \Omega(T) = \frac{1}{\pi T_2} = \Omega_O \exp[-E_A / k_b T] \qquad (2\text{-}19)$$

where the activation energy of the process is E_A, T is for temperature, and k_b represents the Boltzmann constant.[19, 20] For motions in the slow exchange regime the linewidth of the resonance is given as

$$\lambda_{slow} = 1/T_2 + k \qquad (2\text{-}20)$$

where k is the rate and T_2 is the transverse relaxation time.[18] In the limit of fast exchange the linewidth of the two resonances becomes

$$\lambda_{fast} = 1/T_2 + k[1 \pm \sqrt{1 - \frac{(\Delta\omega)^2}{4k^2}}] \qquad (2\text{-}21)$$

where $\Delta\omega$ was the separation between the two resonances. In the limit of large exchange rates the linewidth of one resonance becomes the transverse relaxation time. The other resonance becomes broader and decreases in integrated intensity and disappears in the limit of fast exchange rates.[18] Motions in the slow exchange regime are hard to detect and often go unnoticed if the resonances are broad or if there is no second resonance for chemical exchange. For systems with only one resonance in a spectrum, quantification of

the slow dynamics is incredibly difficult and in some cases, only advanced NMR techniques can access the dynamic information.

2.7 – Double Quantum Excitation

Knowing the atomic structure of a solid-state material is an important step in determining and understanding the behavior of the material. With crystalline materials, the X-ray diffraction pattern easily yields high quality structures. However, with noncrystalline materials the packing of the molecules is disordered and difficult to determine. The strength of a dipolar coupling is distance dependent and the presence and absence of a specific dipolar coupling in the spectrum provides a glimpse of the spins local environment. Generally speaking, a simple single pulse experiment does not allow for the quantification of the dipolar coupling or its specific dipolar partners. To observe the dipolar couplings, a pulse sequence that correlates the dipolar interactions is required. Akin to the COSY (correlated spectroscopy) spectrum in liquid-state NMR, the dipolar recoupling experiments create correlations entirely based on the dipolar coupling. The dipolar recoupling sequences are a significant improvement over INADEQUATE homonuclear correlation experiment, which only correlates off-diagonal elements and couplings between identical spins do not occur in the spectrum.

There are many different versions of dipolar recoupling experiment, one popular class of dipolar experiment uses continuous radiation of the sample with non-ninety pulse angles and variable pulse width.[21-23] The parent pulse sequence in this family, known as

C7, uses seven consecutive pulses over the rotor period to create the dipolar correlation. A second class of dipolar correlation experiment uses pulses and delays to evolve the magnetization under an effective dipolar Hamiltonian.[13, 24] Both methods produce spectra that correlate specific resonances with their dipolar partners, however C7 type experiments require irradiation times that spans over the rotor period, which requires recalibration with a change in MAS frequency. At long recoupling times the constant irradiation over many rotor periods increases the load on the spectrometer. The dipolar recoupling method implemented in this thesis is the Back-to-Back (BaBa) pulse sequence, shown in **Figure 10**. It was chosen due to the low power requirements, its robustness under fast MAS and the simple calibration. The sequence earned the Back-to-Back name from the consecutive 90° pulses at every half-rotor period.

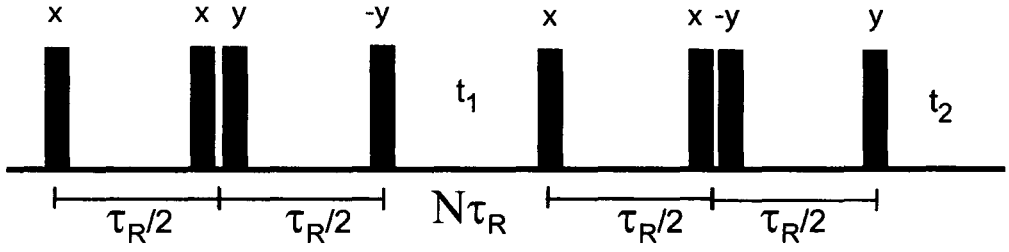

Figure 10 – The Back-to-Back pulse sequence for the excitation of a double quantum coherence that correlates a dipolar spin pair.

The spectrum obtained from the BaBa pulse sequence is referred to as a double quantum correlation (DQC) spectrum. A coherence is the quantum mechanical description of the spin polarization. For a spin half, the single quantum transition is from $m_I = 1/2$ to $m_I = -1/2$, this transition referred to as single quantum coherence. The value of the coherence

for this transition is $\Delta m = -1$. For double quantum coherences (DQC), the two spins have parallel spin states and both flip simultaneously. The spherical tensor for DQC is $\hat{T}_{2,\pm 2}$, this operator has two spins which are acting as a single entity with a coherence of +2 or -2, **Figure 11** shows the coherence pathway transfer diagram for the BaBa pulse sequence.

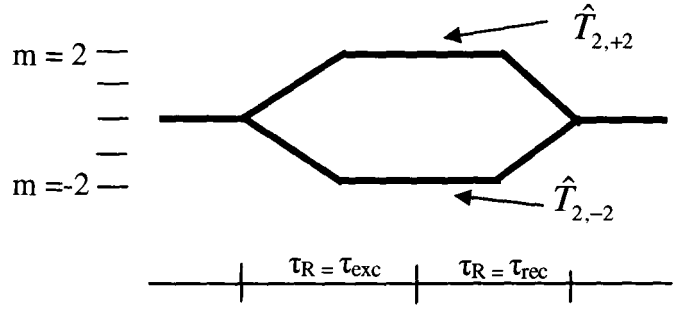

Figure 11 – The coherence pathway for the BaBa sequence over two rotor periods, showing both excitation and reconversion blocks and the generation of the double quantum coherences.

In a typical MAS experiment, the dipolar Hamiltonian is refocused every rotor period. The density of states after the first pulse is

$$\rho(t) \propto (\hat{I}_X^i + \hat{I}_X^j)\cos(\omega_D t) + i(\hat{T}_{2,1}^{(ij)} + \hat{T}_{2,-1}^{(ij)})\sin(\omega_D t) \qquad (2\text{-}22)$$

The propagator evolves under the dipolar Hamiltonian and switches between the transverse ($\hat{I}_X$) and antiphase states (states containing a mix of transverse and longitudinal states, $\hat{I}_Y\hat{I}_Z$) according to the cosine and sine of the dipolar coupling strength (ω_D).[10] The spin states after the first pulse does not describe the double quantum coherence rather a correlation between spins that possesses an $\hat{I}^i_Z\,\hat{I}^j_Y + \hat{I}^i_Y\,\hat{I}^j_Z$ spin state. These spin states

represent the $\hat{T}_{2,\pm1}$, and the single quantum coherence. The evolution of the $\hat{T}_{2,\pm1}$ specifically yields after the next pulse[10]

$$\rho(t) = \begin{matrix} -i\sqrt{3/8}(\hat{T}_{-2,0}\sin(2\theta) + (\hat{T}_{2,1}^{(ij)} + \hat{T}_{2,-1}^{(ij)})\cos(2\theta) \\ -\frac{i}{2}(\hat{T}_{2,2}^{(ij)} + \hat{T}_{2,-2}^{(ij)})\sin(2\theta) \end{matrix} \qquad (2\text{-}23)$$

The two-spin correlation from equation (2-19) transforms into $\hat{T}_{2,\pm2}$ term, which represents the DQC. This treatment of the spins to create a DQC only accounts for the spin portion of the Hamiltonian and neglects the time-dependent spatial terms. Including MAS creates a time dependence for the spatial term in the dipolar Hamiltonian, which then becomes equation (2-17). The spatial term at the half rotor period mark in the pulse sequence is

$$\Omega(0,\frac{1}{2}\tau_R) = -\frac{\omega_\lambda}{\omega_R}\sqrt{2}\sin 2\theta(\sin(\gamma) = -\Omega(\frac{1}{2}\tau_R,\tau_R) \qquad (2\text{-}24)$$

The rotation by MAS causes the spatial terms to invert and prevents the refocusing of the chemical shift terms in the Hamiltonian. Thus, to cancel the effect of MAS on the spatial terms and cancel any dephasing of the chemical shift terms, the spins undergo a counter-rotation from the phase of the pulse, which acts as a composite pulse.[10] The first half rotor period of the BaBa sequence is a pulse along the x-axis followed by a delay and then another pulse along the x-axis. The second half of the rotor period repeats this but is phase shifted by $\pi/2$. Both halves rotor periods build up DQC and MAS inverts only the spatial component every half-rotor period. By shifting the phase of the pulses in the latter half of the rotor period, the sign of the DQC build up is negative and cancels out the sign

inversion created by MAS. This method negates the averaging of the spatial term and creates DQC, allowing for the continuous dephasing of the DQC according to the strength of the dipolar coupling. Further recoupling periods create DQC out of weaker dipolar couplings while continuously dephasing the DQC that are already present.[13] Following the excitation period for the pulse sequence is a series of pulses and delays that reconvert the DQC to a zero quantum coherence, that is then transferred to a single quantum coherence for detection. The reconversion period undoes the excitation and without a proper phase cycle, the spins would return to their original state. The phase cycle of the pulse program allows for the subtraction of the higher order coherences that do not contribute to the DQC.

The example dipolar recoupling curve of **Figure 12**, shows the relationship between the signal intensity of a rigid spin pair and the amount of recoupling applied.[10] Weak dipolar couplings do not dephase quickly or as intensely as stronger dipolar couplings and require longer excitation and recoupling periods. The recoupling of the double quantum coherences recreates the original zero-quantum coherence and is followed by a read-out pulse that converts the coherence into detectable magnetization. The intensity of the recoupled DQC is

$$I_{DQ}^{(ij)} \propto \sin(\Omega_{D,EXC}^{(ij)})\sin(\Omega_{D,REC}^{(ij)}) \qquad (2\text{-}25)$$

When using long recoupling times, it is possible in large spin systems to excite higher order coherences but the design of the phase cycle will select only double quantum coherences and remove any other coherence from the final signal.

Without any modulation of the coherences after the initial excitation, the recoupling creates a one-dimensional (1D) spectrum. The 1D spectrum retains the chemical shift information of the spin and the resonance of a spin represents recoupled intensity of all the dipolar spin pairs for each resonance. The intensity of a resonance is

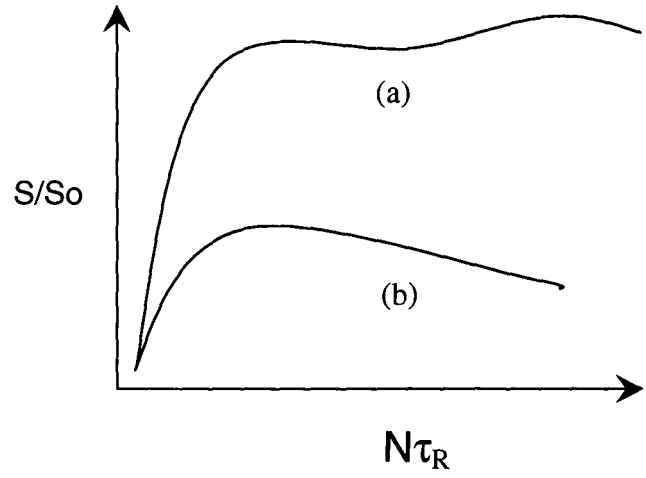

Figure 12 – An example dipolar recoupling curve for a (a) rigid and (b) weak dipolar coupling from a spin pair The intensity of the signal is strongly related to the strength of the dipolar coupling.

directly proportional to the strength and number of dipolar couplings relating to that particular spin.

In the case of a multi-spin system, a two-dimensional (2D) spectrum is able to correlate all of the dipolar couplings of a resonance through the evolution of the DQC during the t_1 period in the pulse sequence. The t_1 period in the pulse sequence occurs

between the excitation and reconversion blocks of the pulse sequence. During the t_1 period, the DQC evolves under the dipolar and chemical shift Hamiltonian in integer increments of the rotor period. This ensures that the modulation created by the Hamiltonians do not give rise to any spinning sidebands. Evolution of the magnetization under the chemical shift Hamiltonian creates a state where the DQC evolves at the sum of the two frequencies and the position of the resonances in the indirect dimension is the sum of those single quantum chemical shifts. The Fourier transform of the time dependent signal in both dimensions is the 2D double quantum correlation spectrum that is shown in **Figure 13**. The single quantum projection in a 2D DQC represents the 1D DQC spectrum of the same recoupling period, while the resonances in the double quantum dimension represent specific spin pairs. Spin pairs that have the same chemical shift (AA, BB) will occur on the diagonal of the 2D spectrum. Off-diagonal spin pairs occur at the sum of the single quantum resonant frequencies for the spin pair (AB).

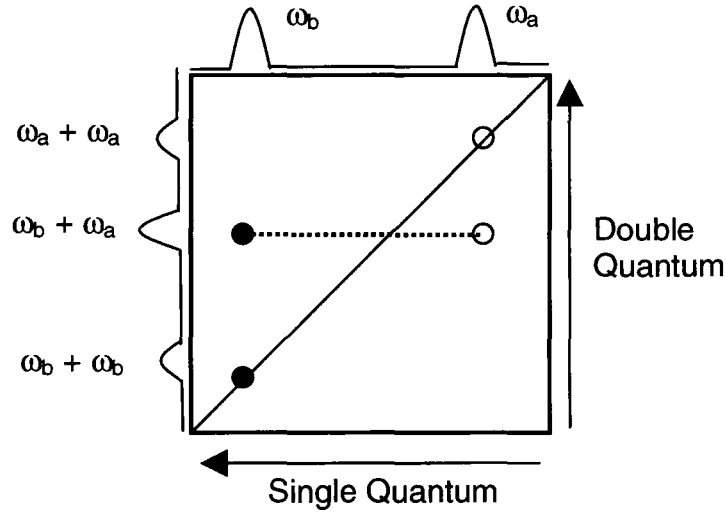

Figure 13 – An example of a double quantum correlation spectrum. In this example, there are three couplings.

Molecular motions change the spin's location in space and this alters the strength of the dipolar coupling. With fast isotropic motion, the dipolar coupling will disappear if the correlation time of the motion is significant. Molecular motions destructively remove the dipolar coupling, reducing the efficiency of the pulse sequence. The intensity of the resonance in a DQ correlation spectrum depends on strength of the dipolar coupling, with an increase in motion the intensity of the resonance will decrease it. For a spin with strong motional averaging of the dipolar couplings, the resonance may completely disappear. The DQ spectra of a sample with a mobile species will only show the rigid resonance and by comparing the DQ spectrum to a single pulse experiment, it is possible to identify which resonances have a mobile component.

2.8 –Centerband-Only Detection of Exchange

A pulse sequence termed the centerband-only detection of exchange (CODEX) is uniquely able to sense the reorientations of a spin in the slow motion regime and measure the correlation time of the slow solid state motions.[25, 26] The pulse sequence is shown as **Figure 14**. The CODEX pulse sequence measures the reorientation of a molecule by observing the changes in the CSA of the nuclei (^{13}C or ^{31}P) before and after a mixing time. The 180° pulses every half-rotor period do not let the CSA refocus, causing a continuous dephasing of the CSA. During the mixing time (t_m) any rotation or fluctuation in the local structure that causes a change in the CSA will influence the dephased magnetization. Thus, the magnetization will not be in the same position as at the start of the mixing time and therefore the magnetization will not be entirely refocused during the reconversion portion of the pulse sequence, attenuating the CODEX signal.

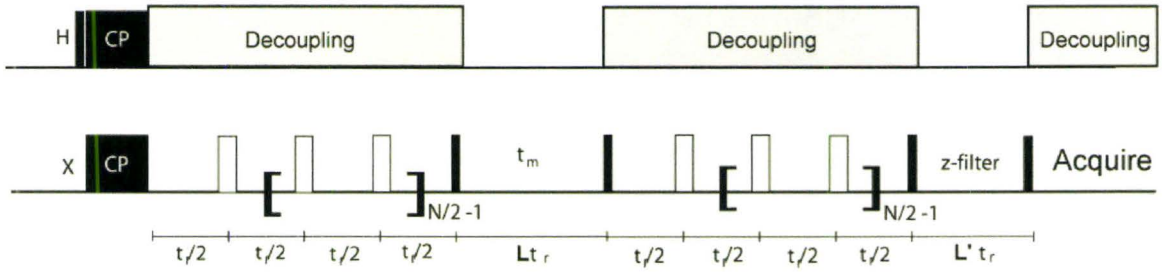

Figure 14 - The centerband-only detection of exchange pulse sequence. Rotor synchronization is required to ensure the recoupling of the CSA is successful.

The total attenuation of the CODEX signal (E) is proportional to the length of the dephasing applied. The dephasing is controlled by the number of rotor periods (Ntr) of

excitation applied to the sample and the span of the CSA (δ). After sufficient dephasing and long mixing times, the CODEX signal cannot attenuate any further and the total number of sites involved in the reorientation controls the final value of the attenuated signal.

$$E_{\infty}(t_m, \delta N\tau_R) = \frac{(M-1)}{M} f_m \qquad (2\text{-}26)$$

The number of sites (M) involved in the exchange is related to the signal where f_m is the fraction of mobile sites involved in the exchange. For example, a ring flip should produce a final signal attenuated to 50%, since the ring flip is a two-site exchange. To find the correct amount of dephasing, a long mixing time is chosen with a short z-filter to provide adequate exchange to provide "infinite time" time conditions for the exchange. The number of recoupling loops is increased until the intensity of the exchange signal reaches a constant value versus a reference spectrum (short mixing time, long z-filter) at the same number of recoupling loops. The combination of the delay periods (t_m and z-filter) are always held at constant time to account for any relaxation that might have occurred. A reference spectrum is required at each iteration of the recoupling loop due to magnetization loss with the growth of the pulse train. To measure the time scale of the exchange, the normalized signal intensity, which is a function of the dephasing (Ntr) is plotted against the mixing time for a given amount of dephasing. The exchange curve is built by measuring the intensity of the resonance at an assortment of mixing times that fully characterizes the signal decay. This analysis is similar to how the rate of exchange is extracted from a series of 2D exchange spectra. The CODEX exchange curves are

fitted to a single exponential to find the correlation time, τ_c, of the exchange process that causes the attenuation of the CODEX signal.

$$E_\infty(t_m, \delta N \tau_R) = A(1 - \exp(-t_m / \tau_c)) \qquad (2\text{-}27)$$

The correlation time represents the period of the motion that occurs during the mixing time. The correlation time provides valuable information on the rates of critical exchange processes.

The recoupling pulses used to probe the changes in the CSA also recouple an interaction called the relaxation-induced dipolar exchange with recoupling (RIDER) and spin diffusion.[27] The RIDER effect is the consequence of a fast relaxing spin exchanging magnetization through a dipolar coupling with the observed nucleus. The 2nd set of recoupling pulses refocus coherence changes from the RIDER effect that were active during the mixing time. The RIDER effect is a form of heteronuclear spin diffusion since it requires a dipolar coupling and is controlled by the spin flip of the other nucleus. The RIDER effect is more prevalent with quadrupolar nuclei due to their fast relaxation. Both the RIDER effect and homonuclear spin diffusion phenomena attenuate the observed echo. This is problematic since any combination of these factors may produce attenuation of the echo. The combination of the molecular motion with either of the exchange mechanisms increases the plateau beyond what the geometry of the reorientation would predict. Multi-exponential fits of the exchange data typically produce weightings and correlation times that are ambiguous as to their origins.

The three mechanisms of exchange are dependent on various factors, which make differentiating between them possible. For example, the RIDER effect is dependent on the strength of the dipolar coupling and the relaxation time of the passive nucleus. Thus, all the factors that contribute to a strong dipolar coupling will affect the exchange during the recoupling. The fast longitudinal relaxation of most quadrupolar nuclei ($I > 1/2$) make them ideal candidates for inducing relaxation based exchange.

The three exchange mechanisms scale differently with temperature and magnetic field. The physical motion of the phosphate in a lattice is temperature dependent and the correlation time would decrease with the increase in thermal energy. The correlation time of the molecular motion, is controlled by the hydrogen bonding and the ionic interactions, does not scale with magnetic field. However, since the recoupling of the molecular motion is based on the dephasing CSA (which is proportional to the magnetic field) the amount of recoupling needed to observe physical motion would increase with a decrease in magnetic field. The correlation times for a spin diffusion constant is related the strength of the dipolar couplings and are not affected by a change in temperature or magnetic field. The total amount of dephasing needed to observe spin diffusion would change with magnetic field.[27] The dipolar coupling portion of the RIDER effect does not scale with field or temperature, however, the relaxation of a nucleus is altered by both. Thus, changing the magnetic field would alter the observed correlation time for the RIDER effect but would not change the amount of recoupling needed to observe the effect. Through multiple measurements using different temperatures and magnetic fields,

the contribution of each exchange mechanism will be shown to be separable in a particular solid.

2.9 - Summary

Solid state NMR is a versatile technique that is able to measure the dynamics or sense the local structure of a material through the nuclei of the material. The combination of MAS and advanced pulse sequences will allow for the discovery and understanding of the mechanism of ion conduction in ionic electrolytes. Future sections will make extensive use of the ^{1}H-^{1}H DQ correlation spectra, multinuclear CODEX NMR, variable temperature NMR. The dipolar coupling contacts observed in the homonuclear correlation spectra are essential to assignment of the ^{1}H NMR spectra. This allows for the prediction of the mechanism of ionic conductivity from the variable temperature NMR. Multinuclear CODEX NMR is able to probe the dynamics and geometry of the molecules through the CSA. The unique information gained through solid-state NMR is incredibly valuable and provides supports other solid state techniques.

2.10 – References

1. M. H. Levitt, *Spin Dynamics: Bacis of Nuclear Magnetic Resonance*, John Wiley & sons, Ltd, New York, NY, 2001.
2. F. Bloch, W. W. Hansen and M. Packard, *Phys. Rev.*, 1946, **69**, 127.
3. F. Bloch, *Phys. Rev.*, 1946, **70**, 460-474.
4. F. Bloch, W. W. Hansen and M. Packard, *Phys. Rev.*, 1946, **70**, 474.
5. H. C. Torrey, *Phys. Rev.*, 1956, **104**, 563-565.
6. R. R. Ernst, *Biosci. Rep.*, 1992, **12**, 143-187.
7. K. Schmidt-Rohr and H. W. Spiess, *Multidimensional Solid-State NMR and Polymers*, Academic Press Limited, San Diego, CA, 1994.
8. M. Bak, J. T. Rasmussen and N. C. Nielsen, *J. Magn. Reson.*, 2000, **147**, 296-330.
9. P. Atkins, *Physical Chemistry*, W. H. Freeman & Co. and Sumanas, Inc., New York, NY, 1998.
10. I. Schnell and H. W. Spiess, *J. Magn. Reson.*, 2001, **151**, 153-227.
11. J. S. Waugh, L. M. Huber and U. Haeberlen, *Phys. Rev. Lett.*, 1968, **20**, 180-182.
12. J. Herzfeld and A. E. Berger, *J. Chem. Phys.*, 1980, **73**, 6021-6030.
13. S. P. Brown and H. W. Spiess, *Chem. Rev.*, 2001, **101**, 4125 -4155.
14. G. Bodenhausen, H. Kogler and R. R. Ernst, *Journal of Magnetic Resonance (1969-1992)*, 1984, **58**, 370-388.
15. O. W. Sorensen, G. W. Eich, M. H. Levitt, G. Bodenhausen and R. R. Ernst, *Prog. Nucl. Magn. Reson. Spectrosc.*, 1983, **16**, 163-192.
16. A. D. Bain, *J. Magn. Reson.*, 1980, **37**, 209-216.
17. A. D. Bain, *J. Magn. Reson.*, 1980, **39**, 335-342.
18. A. D. Bain, *Prog. Nucl. Magn. Reson. Spectrosc.*, 2003, **43**, 63-103.
19. H. W. Spiess, *Adv. Polym. Sci.*, 1985, **66**, 23-58.
20. G. R. Goward, M. F. H. Schuster, D. Sebastiani, I. Schnell and H. W. Spiess, *J. Phys. Chem. B*, 2002, **106**, 9322-9334.
21. Y. K. Lee, N. D. Kurur, M. Helmle, O. G. Johannessen, N. C. Nielsen and M. H. Levitt, *Chem. Phys. Lett.*, 1995, **242**, 304-309.
22. M. Hohwy, H. J. Jakobsen, M. Eden, M. H. Levitt and N. C. Nielsen, *J. Chem. Phys.*, 1998, **108**, 2686-2694.
23. D. H. Brouwer, P. E. Kristiansen, C. A. Fyfe and M. H. Levitt, *J. Am. Ceram. Soc.*, 2005, **127**, 542-543.
24. M. Feike, D. E. Demco, R. Graf, J. Gottwald, S. Hafner and H. W. Spiess, *J. Magn. Reson., Ser. A*, 1996, **122**, 214-221.
25. E. R. de Azevedo, W. G. Hu, T. J. Bonagamba and K. Schmidt-Rohr, *J. Am. Chem. Soc.*, 1999, **121**, 8411-8412.
26. E. R. de Azevedo, W. G. Hu, T. J. Bonagamba and K. Schmidt-Rohr, *J. Chem. Phys.*, 2000, **112**, 8988-9001.
27. K. Saalwachter and K. Schmidt-Rohr, *J. Magn. Reson.*, 2000, **145**, 161-172.

Chapter 3: Methodology – Bulk Techniques

3.0 – Introduction

The study of electrolyte materials through solid-state nuclear magnetic resonance does not probe the macroscopic scale. This includes long-range behavior of the ions or thermal properties. This chapter describes the important experiments needed to characterize the materials chemistry of an electrolyte system.

When trying to understand the dynamics or more specifically, the mechanism of ion conduction in a solid, two methods stand out above the rest; solid-state nuclear magnetic resonance (NMR) and impedance spectroscopy. Impedance spectroscopy is a technique that measures the ionic conductivity of a material.[1-5] Impedance spectroscopy is able to measure the change in ionic conductivity with temperature. Characterization of the conductivity with temperature yields an activation energy that should be comparable to those determined by NMR. There often are multiple mechanisms of ion exchange, impedance spectroscopy cannot readily differentiate between them. In contrast, impedance spectroscopy does measure the long-range motion of ions making it a very important tool for characterizing the conduction of ions.

Techniques such as differential scanning calorimetry (DSC) are useful for investigating phase changes on the macroscopic scale, which include melting points,

glass transitions, or a bulk physical reorientation of the structure. These two techniques are discussed below.

3.1 - Impedance Spectroscopy

Monitoring the motion of ions in the solid-state is vital to characterizing the performance of a solid-state electrolyte. The ionic conductivity of a sample is the inverse of the resistance to the flow of ions. In an ideal case where the voltage (v) and current (I) applied is proportional to the resistance,

$$R = V / I \tag{3-1}$$

Ohms law applies. However, the response of a system is not ideal and the response to the applied voltage and current is complex and greatly depends on the system. Applying Ohm's law to the alternating voltage and current yields the impedance of the system (Z), as shown in equation (3-2), where frequency is ω, and is θ the phase difference between the voltage and the current.

$$Z(\omega) = \frac{V \exp(i\omega t)}{I \exp(i\omega t - i\theta)} \tag{3-2}$$

The expression of the impedance as a complex number allows for the representation of the experimental impedance data in a Nyquist plot. A Nyquist plot, (**Figure 1a**) has the imaginary impedance on the y-axis and the real impedance on the x-axis. The drawback to the Nyquist plot is that the frequency of the response does not appear on the graph. A Bode plot summarizes the system's response by showing the dependence of the

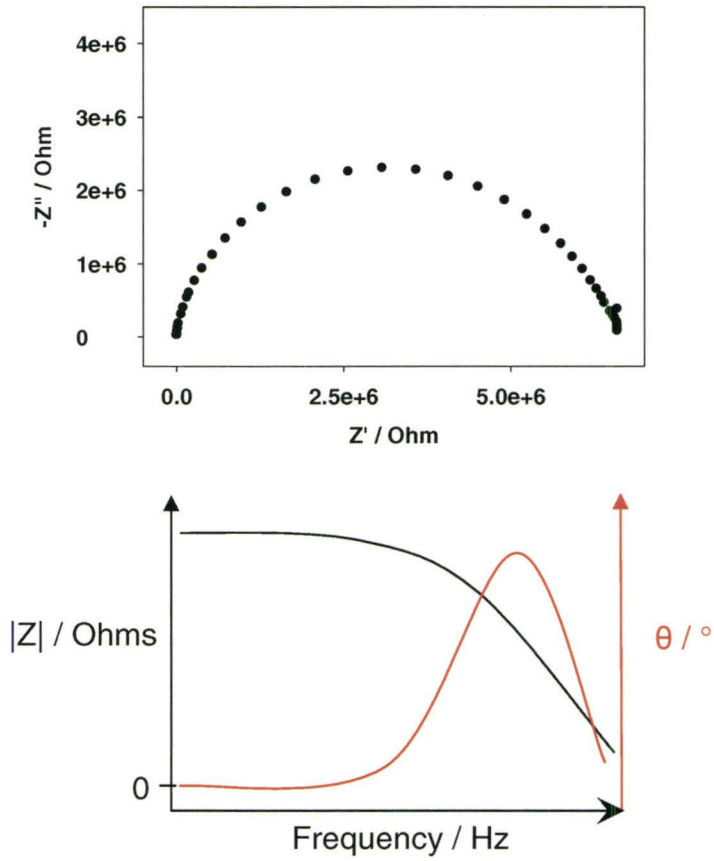

Figure 1 - An example of a (a) Nyquist Plot and (b) a Bode plot. A Nyquist plot has the imaginary impedance on the y-axis with the real impedance on the x-axis. (b) A Bode plot has the impedance on the left axis and phase angle on the right. When the phase angle is zero, the impedance has no imaginary component.

impedance and the phase angle on the frequency of the applied voltage and an example Bode plot is shown as **Figure 1b**. The impedance of a system is a complex property and the real resistance of the system occurs when the phase angle is zero, implying no imaginary impedance.

Impedance spectroscopy is an important technique and has applications in many areas of research where the ionic conductivity is important such as ion conduction in fuel cells or solar cells.[2, 5-10] For polymer systems, four-probe geometry is the main setup for determining the impedance of a sample. The four-probe geometry has two voltage and two current electrodes, one electrode for excitation and another for detection. The geometry of the sample cell has four electrodes in a single plane and is shown in **Figure 2**. The outer two electrodes apply a constant current across the sample, while the inner voltage electrodes measure the voltage drop across the sample as a function of frequency.[11]

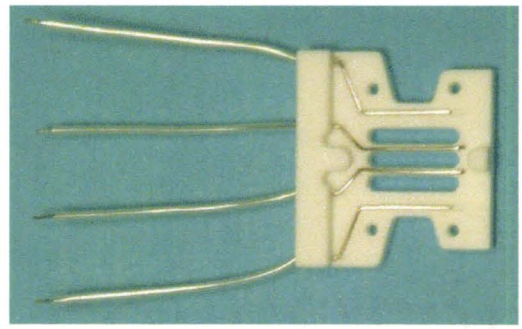

Figure 2 – The four probe impedance spectroscopy sample cell. The cell has four electrical contacts that are composed of platinum wire.

The benefits in using a four-probe measurement is that the cell excludes the impedance of the system by measuring the voltage and current through different electrodes. This is not important for systems with high resistance since the contribution from the electrodes to the overall resistance is negligible. However, for fuel cells or any system with low impedance where the electrodes might contribute a significant portion of the impedance,

the choice of electrode geometry is extremely important for measuring the impedance. The impedance of the system is found from the Bode plot when the measured impedance becomes independent of frequency according to the Jonscher Power Law.[12] The ionic conductivity (σ) of the system is found by using

$$\sigma = L/(ZWH) \qquad (2\text{-}3)$$

where L is the distance that the ions travel between the electrodes, Z is the real component of the impedance, W is the width, and H is the thickness of the polymer membrane. The macroscopic motion of the ions is dependent on temperature and the Arrhenius describes the activation energy for the macroscopic transportation of ions.

A second type of cell is used to measure the impedance of crystalline solids that can not form thin film membranes. The sample for this cell is a cylindrical pellet that will have an electrode on either face of the disc forming a two-electrode geometry, known as the blocking electrode geometry. The two electrodes must apply a constant current and detect the voltage drop across the sample. Due to the simplicity of the design, any inductance, resistance of the leads or capacitance of the system is measured.[11] Due to these factors, the total contribution from the impedance spectrometer is kept to a minimum by decreasing the length of the wires. The impedance of the two cell geometry might reach several kΩ. Most solid systems requiring the two-electrode method have rather high resistance in the MΩ region where a kΩ contribution is less than 0.1% of the total resistance measured.

Impedance spectroscopy is a valuable tool for determining the ionic conductivity of a sample and often the strength of the conductivity is a measure of the material's success. Thus, being able to measure and compare the impedance of the system to hydrated Nafion gives the reader a point of reference. When compared to NMR the activation energy from impedance spectroscopy is greater or equal due to macroscopic bottlenecks or grain boundaries that block the flow of ions. Impedance spectroscopy is able to measure the flow of ions in a material, which makes the technique an important part in determining the usefulness of a sample.

3.2 – Thermal analysis

Thermal analysis of an electrolyte material provides information about the characteristics of the material and its response to a change in temperature.[13-15] The most prominent thermal analysis techniques in this thesis are differential scanning calorimetry (DSC) and thermogravic analysis (TGA).[13, 15-17] Both techniques measure the response of the material with a constant increase in temperature, the difference is in the measured quantity. A DSC measures the amount of heat needed to increase the temperature of a sample with respect to a reference.[18] When the material undergoes a phase transition between states of matter the temperature stays constant until the phase change is complete. The heat flow from the DSC into the sample at the phase transition must increase to match the constant rate of temperature increase of the reference compound. An example DSC trace is plotted as **Figure 3** and the transition shows the heat required

to flow into the sample. This is an example of a endothermic transition, such as a melting point. The DSC trace of a material reveals when the electrolyte will melt or undergo any other phase transition and the total energy for the phase transition is the area of the peak in the DSC trace. The timescale of the transition measured depends on the thermal conductivity and response time of the instrument.[19-21] The measured rate of a polymer initiation reaction ranges in the 40 – 150 ms timescale to the curing process of a dental cement, that occurs within seconds.[19-21] For DSC to measure the motion or any process (motion of a long polymer chain), the absorption of thermal energy must cause a thermal transition to occur. The thermal transition must occur over a timescale that is slower than the scanning rate of the device.[22]

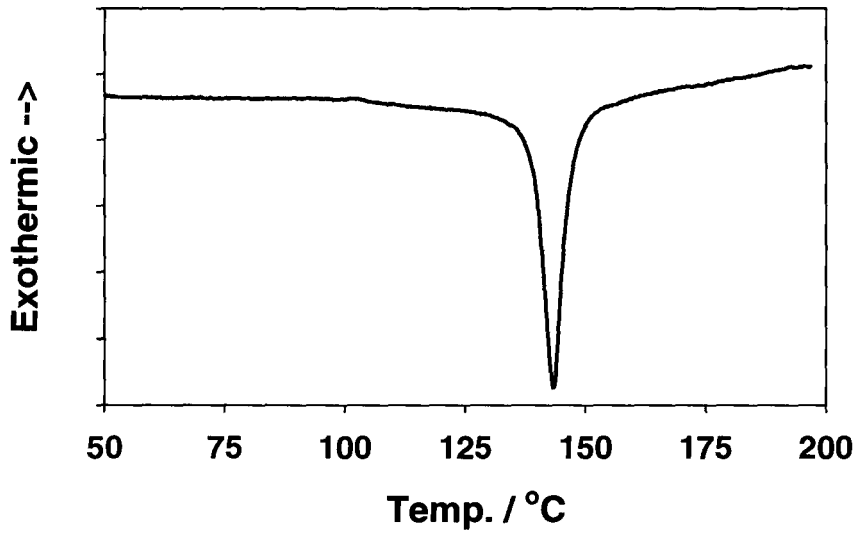

Figure 3 – A typical DSC trace showing the melting transition of an organic molecule. The y-axis measures the heated needed to retain a constant increase in temperature.

Operation above the melting point for a solid electrolyte would cause the material to become a liquid and contaminate the electrodes. A DSC trace is not a direct probe of the

microscopic structure of a solid, none the less, DSC is very valuable and practical tool for understanding the thermodynamics of the bulk material.

The second technique involving the thermal properties of the material is thermogravic analysis (TGA). This technique is similar to DSC but the measured quantity is mass loss versus temperature. TGA does not measure phase transitions but rather the mass loss resulting from a phase transition or reaction. The temperature range of a TGA is much greater than a DSC as higher temperatures are needed to decompose most materials. TGA has several applications such as determining the decomposition products from the mass loss, the temperature of safe operation, or finding how much electrolyte is present in an inert host.

3.3 – Summary

Nuclear magnetic resonance probes only the local environment of the spin and requires some additional techniques to supplement the analysis. The long-range transport of ions and thermal behavior of a material are important properties that determine many factors and conditions for a fuel cell. Impedance spectroscopy is perhaps the closest macroscopic probe that compares directly to the dynamics of a spin. The short-range motion of ions will lead to long-range motion and the activation energy of both techniques should overlap. Thermal analysis of a material provides much information on behavior of the material with temperature and provides insight on the trends of the chemical structure.

3.4 – References

1. T. E. Springer, T. A. Zawodzinski, M. S. Wilson and S. Gottesfeld, *J. Electrochem. Soc.*, 1996, **143**, 587-599.
2. B. D. Cahan and J. S. Wainright, *J. Electrochem. Soc.*, 1993, **140**, L185-L186.
3. G. Fafilek, *Solid State Ionics*, 2005, **176**, 2023-2029.
4. G. Alberti, C. Bastioli, M. Casciola, F. Marmottini, G. Capannelli and S. Munari, *J. Membr. Sci.*, 1983, **16**, 121-135.
5. J. J. Fontanella, M. G. McLin, M. C. Wintersgill, J. P. Calame and S. G. Greenbaum, *Solid State Ionics*, 1993, **66**, 1-4.
6. J. O. Besenhard, M. Hess and P. Komenda, *Solid State Ionics*, 1990, **40-41**, 525-529.
7. B. E. Conway, *J. Electrochem. Soc.*, 1991, **138**, 1539-1548.
8. S. M. Haile, G. Lentz, K.-D. Kreuer and J. Maier, *Solid State Ionics*, 1995, **77**, 128-134.
9. E. Iguchi, Y. Tokuda, H. Nakatsugawa and F. Munakata, *J. Appl. Phys.*, 2002, **91**, 2149-2154.
10. L. Wang, Z. Li, H. Xu and K. Zhang, *J. Phys. Chem. C*, 2008, **112**, 308-312.
11. C. H. Lee, H. B. Park, Y. M. Lee and R. D. Lee, *Ind. Eng. Chem. Res.*, 2005, **44**, 7617-7626.
12. A. K. Jonscher, *Nature*, 1977, **267**, 673-679.
13. I. D. Stefanithis and K. A. Mauritz, *Macromolecules*, 1990, **23**, 2397-2402.
14. D. A. Reuschle, D. A. Mountz, L. B. Brister, C. L. Curry, K. A. Shoemake, R. F. Storey and K. A. Mauritz, *Polym. Prepr. (Am. Chem. Soc., Div. Polym. Chem.)*, 1998, **39**, 381-382.
15. S. Su and K. A. Mauritz, *Polym. Prepr. (Am. Chem. Soc., Div. Polym. Chem.)*, 1994, **35**, 795-796.
16. S. Su and K. A. Mauritz, *Macromolecules*, 1994, **27**, 2079-2086.
17. W. Gao, L. Dickinson, F. G. Morin and L. Reven, *Chem. Mater.*, 1997, **9**, 3113-3120.
18. A. Bozkurt, M. Ise, K. D. Kreuer, W. H. Meyer and G. Wegner, *Solid State Ionics*, 1999, **125**, 225-233.
19. D. C. Watts and A. J. Cash, *Meas. Sci. Technol.*, 1991, **2**, 788-794.
20. R. L. Sakaguchi, M. Peters, S. R. Nelson, W. H. Douglas and H. W. Poort, *J. Dent.*, 1992, **20**, 178-182.
21. S. C. Clark, C. E. Hoyle, S. Jonsson, F. Morel and C. Decker, *Polymer*, 1999, **40**, 5063-5072.
22. K. Akabori, H. Atarashi, M. Ozawa, T. Kondo, T. Nagamura and K. Tanaka, *Polymer*, 2009, **50**, 4868-4875.

Chapter 4: Solid Acid Electrolytes

In this chapter, the investigation of the mechanism of ion conduction for an array of solid-acid electrolytes provides insight into the mechanism of ion conduction in the phosphonate based electrolytes. In these simple ion conductors, the ionic conductivity is the result of proton and phosphate dynamics and this chapter explores the ion dynamics through solid-state NMR. The characterization of the solid acid materials proves to be nontrivial and requires an depth analysis of the multinuclear spin systems involved to understand the results.

This chapter summarized the work on understanding contributions to the mechanism of ion conduction in a series of solid-acid electrolytes. This chapter is under preparation as a manuscript for the Journal of Physical Chemistry, with co-authors Kristen J. Soo, Murugesan Vijayakumar and Gillian R. Goward. My contributions to this chapter include the synthesis, data collection, processing, interpretation of the spectra for this series of solid-acid electrolytes and the preparation of the manuscript. My co-authors contributions to the manuscript included the growth of the cesium dihydrogen phosphate crystals for our X-ray diffraction data by an undergraduate summer student Kristen J. Soo, and the ^{31}P nuclear magnetic resonance (NMR) and synthesis of rubidium dihydrogen phosphate by Dr. Murugesan Vijayakumar.

4.0 – Introduction

Polymer membranes as electrolytes in fuel cells have little to no ion transport under dry conditions, which creates a dependency on a liquid electrolyte to operate at peak efficiency.[1-5] The benefit of replacing protic electrolytes with a solid electrolyte is that in the latter, the ionic conductivity occurs in the absence of a highly mobile liquid phase. The loss of the liquid phase in many polymer membranes leads to poor ionic conductivity; these factors contribute to the overall decay of efficiency for a fuel cell.[6, 7] One class of solid state electrolytes uses the conjugate base of a polyprotic acid as the proton carrier. This family of solid-state ion conductors has been termed solid acid electrolytes. The high ionic conductivity of the solid acid electrolytes occurs following a high temperature phase transition.[8] The phase transition facilitates the dramatic increase in the ionic conductivity of the compound, thus this type of phase transition was termed superprotonic.[8-10]

The temperature at which the transition occurs varies with choice of cation and anion. For example, the superprotonic phase transition of $CsHSO_4$ is at 141°C, while CsH_2PO_4 (CDP) is reported to occur at 238°C.[11] For the solid acid electrolytes, structural diffusion is the only mechanism that promotes conductivity.[12] Proton conduction occurs through a collective series of rotations by hydrogen bonded anions, analogous to the proton transfer mechanism of solid state imidazole.[12, 13] At elevated temperatures, the thermal energy available to the system will activate the long-range structural diffusion. The superprotonic phase transition changes the space group and thereby increases the

ability of the material to transport ions. In cesium dihydrogen phosphate this transition occurs from a monoclinic symmetry to a cubic symmetry[8].

The solid-acid family of electrolytes is structurally similar to the organic electrolytes. Solid electrolytes are ionic salts that use (phosphorous or sulfur-based) anions. However, in the solid acid materials the cation (cesium) does not participate in the hydrogen bonding, while organic heterocycles such as imidazole form a cation that is able to form multiple hydrogen bonds. This causes the mechanism in solid acid electrolytes to depend on the hydrogen bonding of the anion.

The solid acid electrolytes investigated in this chapter use a phosphate-based anion. Phosphate based materials have been shown capable of high temperature operation in a fuel cell.[14] However, the deformation of the electrolyte layer with usage of the fuel cell causes an eventual drop in performance. To improve the stability of the electrolyte material a new solid acid, cesium methyl phosphonate (CMP) was prepared. The goal of reducing the critical temperature at which the dynamics occurs, would help reduce the decomposition of the electrolyte material. The chemical structure of CMP removes one hydroxyl from the phosphate and replaces it with a methyl group, hence reducing the total number of hydrogen bonding protons in the structure. The reduction in the number of hydrogen bonds should reduce the critical temperature needed to promote dynamics.

Solid-state nuclear magnetic resonance (NMR) is able to probe molecular motions of materials on the atomic scale. This allows for the direct observation of the chemical

environment of the nuclear spins to determine their local structure and behavior with temperature. This chapter uses an advanced solid-state NMR technique called Center-band Only Detection of EXchange (CODEX) to characterize the dynamics of the anion.[15-17] As described in Chapter 2, the pulse sequence uses fluctuations of the anisotropic chemical shift to obtain structure information about the anion.[18] The total decay of the echo is limited to number of sites and the timescale of the reorientation dictates the decay. The total decay for molecular motion when fully dephased in the limit of long mixing times is (M-1)/M where M is the number of sites involved in the motion.[16] A complete description of this pulse sequence is given in Chapter 2 and only a brief outline is given here.

The CODEX pulse sequence is a valuable tool that can be used to determine the correlation time of slow solid-state motions.[15-17, 19, 20] However, the 180° recoupling pulses used to probe the changes in the CSA also recouples other anisotropic interactions like relaxation-induced dipolar exchange with recoupling (RIDER) and spin diffusion.[21] The RIDER effect is the consequence of a fast relaxing spin exchanging magnetization through a dipolar coupling with the observed nucleus. The RIDER effect is a form of heteronuclear spin diffusion, which is more prevalent in quadrupolar nuclei due to their fast relaxation. Both the RIDER effect and homonuclear spin diffusion phenomena attenuate the observed echo, and have to be taken into account interpret the data.

4.1 - Experimental

The starting carbonate compounds where purchased from Sigma Aldrich. Adding the carbonate salt (Cs_2CO_3, Rb_2CO_3, K_2CO_3, $TlCO_3$)of the solid acid of interest to a stoichiometeric amount of phosphoric acid liberated carbon dioxide and produced the metal cation dihydrogen phosphate and water. These solutions were then saturated to produce crystals, and then ground into a fine powder. Any excess humidity was removed by drying above 100°C under a strong vacuum. Exceptional care was taken to avoid exposure to any humidity in the atmosphere once the solid material was dried.

All of the solid-state NMR experiments were collected using a Bruker Avance console with an 11.74 T magnet. The chemical shifts were referenced to adamantane at 1.63 ppm for ^{1}H chemical shifts and concentrated phosphoric acid at 0.0 ppm for ^{31}P chemical shifts. The ^{31}P CODEX experiments were acquired using a double resonance probe and rotors with an outer diameter of 4 mm and a magic angle spinning (MAS) frequency of 10 kHz. The recoupling pulses had a strength of 62.5 kHz and a contact time of 3000 μs was used for the cross polarization in the ^{31}P CODEX NMR experiments to ensure the best signal intensity. The double quantum experiments for CDP use ^{1}H RF fields of 83.3 kHz with a MAS frequency of 10 kHz. The temperature of the sample in the NMR experiments was calibrated using samarium stannate.[22]

4.2 – Results and Discussion

4.2.1 – Structure

The solid-state structure of the acid electrolytes forms from an aqueous solution. The solid obtained is an ionic salt with anions bridged through hydrogen bonding. This describes the synthesis and structure of all the solid acid materials. The crystal structure of CDP is presented in **Figure 1** with the phosphate anions as tetrahedrons, the Cs ions as yellow spheres, and the hydrogen atoms as the white spheres. The solid state structure of CDP was determined through single crystal X-ray and powder neutron diffraction. The structure presented here was recorded using single crystal X-ray diffraction, and is in agreement with the literature results.[8, 23] The structure solution from X-ray has two distinct hydrogen bonds. Those hydrogen atoms in **Figure 1** are labeled as A and B.

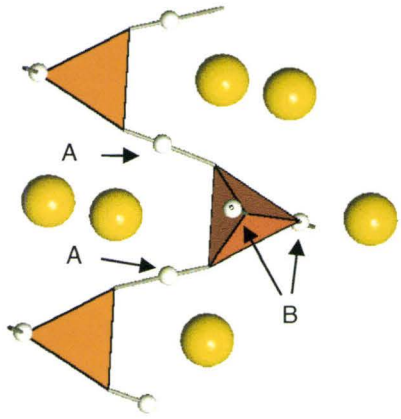

Monoclinic
Space Group:
$P2_1/m$
a = 4.87980 Å
b = 6.38780 Å
c = 7.9079 Å
β = 107.7180°

Figure 1 - A portion of the crystal structure of CsH_2PO_4 (CDP), which depicts the hydrogen bonding. The crystallographic data from our data set collected at 273 K is summarized next to the structure.

The two types of hydrogen bonds in the structure are perpendicular to each other. The A hydrogen bond always occurs in the plane of **Figure 1**, while the B hydrogen bonds always move out of the plane. The A hydrogen bond are shorter than the B hydrogen bonds by 0.067 Å.

The structure of CMP by diffraction is not available because the material is extremely hydroscopic. This prevented the growth of a single crystal and the collection of any data that did not have a sealed sample vessel but CMP is analogous with $CsHSO_4$, which also has only one hydrogen bond.

4.2.2 – ^{1}H Characterization

Proton conduction in the solid state for anhydrous materials occurs through structural diffusion. For solid acid materials, the bulk ionic conductivity occurs through the hydrogen bonding of the lattice. Breaking of the O-H···O hydrogen bonds allow for the rotation of the phosphate anions. The rotation of the anion repositions the hydrogen atoms and promotes long-range ion conduction.

The ^{1}H MAS NMR spectrum of CDP in **Figure 2a** has only two resonances, that represent the two hydrogen bonded protons. The lack of aromatic or alkyl protons in the structure reduces the amount of ^{1}H-^{1}H dipolar couplings and results in relatively narrow lines for the two CDP protons even at a MAS frequency of 10 kHz.

The solid-state structure of CDP in **Figure 1** will help in the assignment of the two hydrogen bonds because the strength and distance between the two electronegative atoms would affect the chemical shift.[24-27] The distance between the two oxygens for the A (2.467 Å) and B (2.534 Å) hydrogen bonds differ by 0.067 Å. A stronger the hydrogen bond pulls the proton further towards the second electronegative atom, further deshielding the proton.[24-27] The smaller distance in the A hydrogen bond is due to the strong interaction between the three atoms. The strong hydrogen bonding of the A proton pulls the hydrogen atom away from the oxygen atom. This strongly deshields the proton creating a higher chemical shift in the process. The longer hydrogen bond of proton B would not deshield the proton as strongly as in the A hydrogen bond and would cause a lower chemical shift.

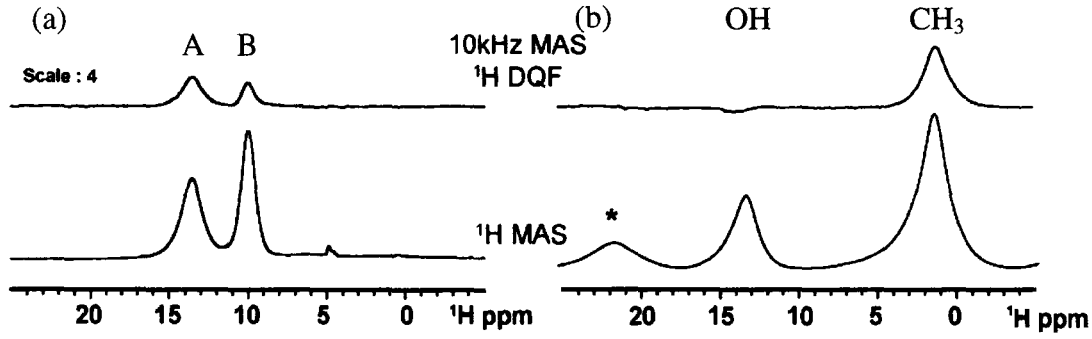

Figure 2 – (a) The ^{1}H MAS spectrum of Cesium Dihydrogen Phosphate (left, lower), and the corresponding ^{1}H-^{1}H DQF spectrum (left top) showing the reduced efficiency of the dipolar recoupling indicating the mobility of the spins. In the spectrum of CDP a small amount of water is absorbed onto the structure while packing. (b) The similar spectra for CMP are shown to the right, the CMP spectra have been expanded to show the spinning sidebands marked with an asterisk.

The ^1H MAS spectrum of CMP in **Figure 2b** has only two resonances that correspond to the hydrogen bonded proton and the methyl group of the phosphonate. The major difference between the two ^1H MAS spectra is the amount of broadening from methyl group. The proximity of the methyl group to the hydrogen bond increases the number and strength of the homonuclear dipolar couplings felt by the hydrogen bonded proton. Any additional dipolar couplings would create broader resonances, which would require faster MAS frequencies to maintain the resolution. The simplicity of these spectra is a direct result of their simple chemical structures.

The spectra above the ^1H MAS NMR in **Figure 2** are the ^1H-^1H DQF spectra observed at 100 μs of recoupling. The motion of the spin pair on the timescale of the rotor period causes the decay of the dipolar recoupling. In the structure of CDP the A protons are very close (~3.1 Å) to the next set of A protons while the B protons are further apart and are separated by 4.9 Å. The strength of a dipolar coupling for two protons is determined by the inverse of the distance between the two spins to the third power (see eq. 2-14 in chapter 2). The ^1H-^1H DQF spectra of **Figure 2** show a reduced signal intensity for both resonances, which implies that the ^1H-^1H spin pairs are dynamic on the time scale of rotor period (τ_R=100us). The motion of the hydrogen-bonded protons could arise from the jumping between the two potential energy minima of the hydrogen bond or the rotation of the phosphate.

Exchange spectroscopy (EXSY) produces a 2D spectrum that shows if chemical or magnetic exchange occurs between two resonances. The off-diagonal resonances in an

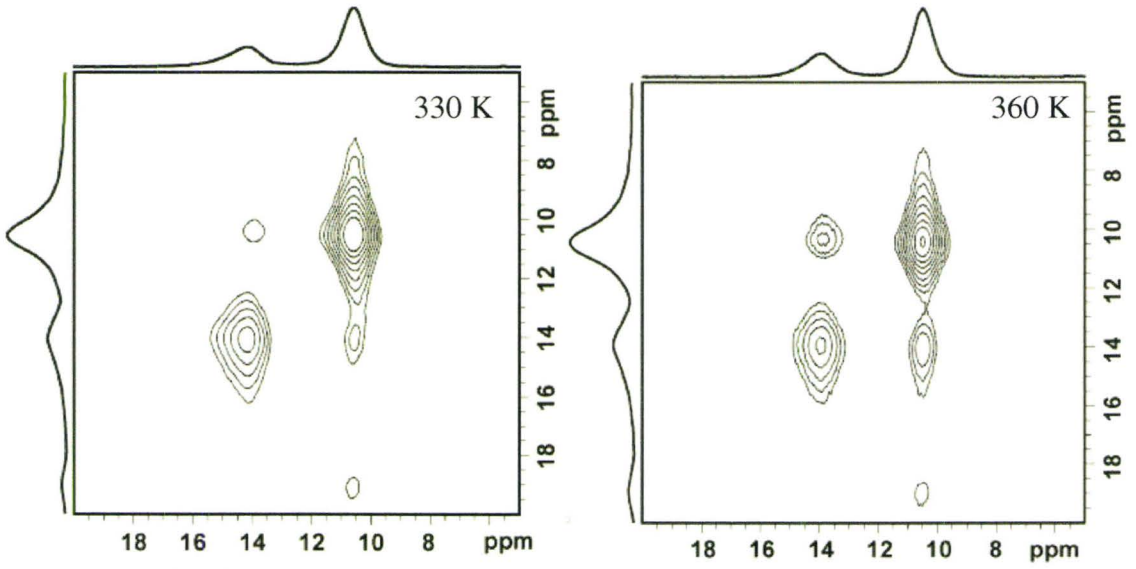

Figure 3 – ^{1}H-^{1}H EXSY spectra of CDP at 330 K (left) and 360 K (right), acquired using a mixing time of 40 ms and 10kHz MAS. The increase in off-diagonal resonances indicates chemical exchange.

EXSY spectrum represent exchange of the two nuclei. However, in strongly dipolar coupled systems, magnetic exchange through the dipolar coupling will give rise to off-diagonal elements, producing the same result as chemical exchange. Two EXSY spectra are presented in **Figure 3** for CDP. The mixing time in the experiments was set to 40 ms and off-diagonal resonances are present if the two spin states are indistinguishable by the end of the mixing time, indicating exchange. It is possible to distinguish chemical from magnetic exchange by raising the temperature. At a given mixing time, the amount of magnetic exchange is constant with temperature, while the rate of chemical exchange changes with temperature according to the activation energy of the exchange process.[16, 21] The plots show the increase in off-diagonal intensity with temperature with a constant mixing time, indicating that the off-diagonal elements originate at least partially from chemical exchange. This yields a rough estimate of the timescale for the exchange. The

40 ms mixing time in these experiments show that exchange between the two spins at the two temperatures plotted occurs faster or close to the mixing time. This could imply that the exchange of the protons could occur through the reorientation of the phosphate anion. By sampling the intensity of the off-diagonal resonances over a range of mixing times and fitting the exponential curve yields a rate constant representing the exchange and the spin diffusion. To separate the two processes, a double exponential fit would be required, which would add an additional degree of complexity. Due to the long T_1 of the ^1H nucleus in CDP, the 2D exchange study was not our preferred method of quantifying the dynamics. Determining rate of exchange from the EXSY is an inefficient path and a much simpler approach exist using multinuclear techniques.

4.2.3 – Anion Dynamics

Based on the ^1H-^1H DQF and EXSY data the hopping motion of the protons in CDP is rapid and the timescale for the motion is between length of the rotor period and the mixing time of the EXSY experiment. The estimate for the timescale of the phosphate reorientation is on the millisecond timescale. The two timescales differ by several orders of magnitude, implying that the proton hopping detected in the ^1H-^1H DQF experiments, preceeds the rotation of the phosphate. The correlation time of the phosphate rotation was determined using ^{31}P CODEX NMR.[18] The ^{31}P CODEX pure exchange curve for CDP at room temperature is shown as **Figure 4**, where each point represents the echo intensity at a given a mixing time. The ^{31}P CODEX NMR data offer

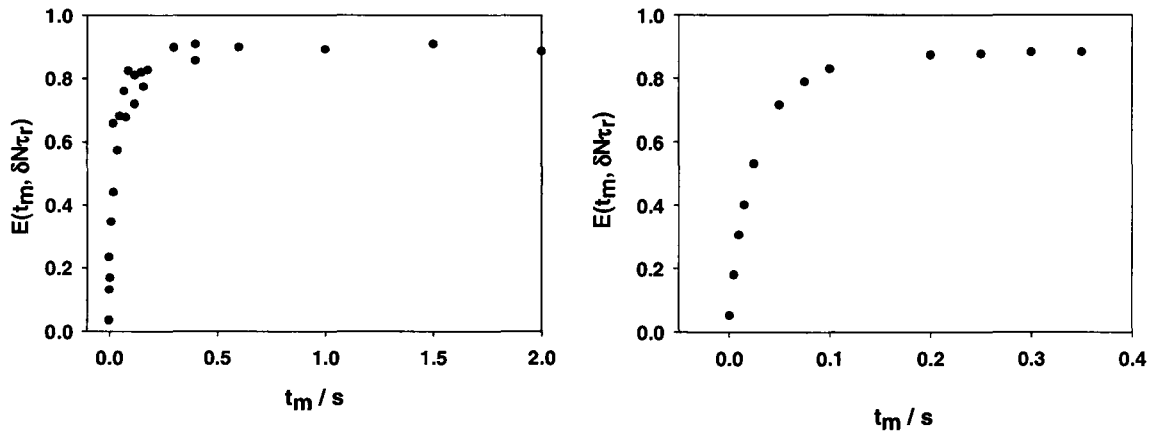

Figure 4 - The ^{31}P CODEX exchange curve for CDP (left) and RDP (right). The plateau from the CDP exchange curve is 87% which is over the expected 75%, indicating a secondary effect is dephasing the magnetization.

two important pieces of information; the geometry and the timescale for an reorientation process. The plateau in **Figure 4** is at 87%, which suggests if only physical motion is contributing to the exchange then the phosphate is undergoing a nine-fold reorientation. Chemically this plateau is nonsensical and therefore the CODEX pulse sequence is also recoupling other interactions with neighboring spins.[21] Both the RIDER effect and spin diffusion can influence the observed plateau and correlation time. A double exponential fit in this case would be justified due to the quadrupole moment at the cesium nucleus.[21, 28] The nuclear spin of ^{133}Cs is 7/2 and strong quadrupole moments contribute to fast relaxation in solid-state NMR. Additionally, the NMR active spin of cesium is 100% naturally abundant with a Larmor frequency of 65.6 MHz at 11.74 T. The high natural abundance of the nuclear spin would create strong dipolar couplings making it conspicuous nucleus for the RIDER effect. The high gyromagnetic ratio of the ^{31}P nucleus could also lead to exchange through homonuclear spin diffusion.

Rubidium dihydrogen phosphate (RDP) is an analogous solid acid with a strong quadrupolar nucleus as the cation. Rubidium has two active NMR isotopes that have strong quadrupole moments and one of the isotopes has gyromagnetic ratio that is twice as strong as cesium. The same factors that may influence the ^{31}P CODEX exchange of the phosphate exist between RDP and CDP. The ^{31}P CODEX NMR pure exchange curve for RDP is presented as **Figure 4b**. The plateau in **Figure 4b** peaks at 88%, similar to the results obtained for CDP. The plateau in both cases suggests an additional mechanism of exchange influencing the level of the plateau in **Figure 4b**. To further the investigation into the rotation of the phosphate using ^{31}P CODEX NMR, it is essential to determine the origin of the two correlation times.

To address this conflict, we turn to the analogous solid acid potassium dihydrogen phosphate (KDP) and attempt to understand how the nuclear properties of the other solid acids compare with CDP and RDP. Potassium has two active isotopes with a nuclear spin of 3/2, the quadrupole moments of potassium nuclei are larger than that of cesium but the overall NMR sensitivity of the potassium nucleus is poor due to the low gyromagnetic ratio. The values for the gyromagnetic ratio, quadrupolar moment, spin, and natural abundance of the alkali metal cations of interest are given in **Table 1**.

Table 1 – The various nuclear spin properties of the solid acid cations.

	Gyromagnetic Ratio Relative to ^{1}H	Quadrupole moment 10^{-30} m^2	Spin	Natural Abundance
^{1}H	1.00	0	½	99.98
^{133}Cs	-0.1311	-0.343	7/2	100
^{85}Rb & ^{87}Rb	0.097 & 0.327	27.6 & 12.4	5/2 & 3/2	72 & 28
^{39}K & ^{41}K	0.046 & 0.026	5.85 & 7.11	3/2 & 3/2	93 & 7
^{203}Tl & ^{205}Tl	0.541 & 0.577	0	½ & ½	29.5 & 70.5

The gyromagnetic ratio of the highest natural abundance isotope of potassium is twenty times weaker than that of a hydrogen nucleus, while the second is approximately forty times weaker. The reduction in the gyromagnetic ratio will reduce the strength of any dipolar couplings to a potassium spin and this will ease the relaxation induced dipolar exchange (RIDER) in the ^{31}P CODEX NMR signal for KDP. The reduction in the unwanted interactions will cause the recoupled signal of the phosphate to consist of primarily of dynamic information, if present. However, the ionic conductivity of KDP is much lower than its cesium and rubidium counterparts. KDP is reported to have a conductivity of 6×10^{-9} S/cm at 50°C, whereas other solid acids like CDP have a general conductivity of 10^{-7} S/cm.[10] The variable temperature plot of ^{31}P MAS NMR in **Figure 5** for KDP shows only a single resonance. The total change in linewidth for this resonance from room temperature to 360 K of only 30 Hz, this suggests that there is little dynamics from the anion, namely that the phosphate rotation is either very slow or nonexistent.

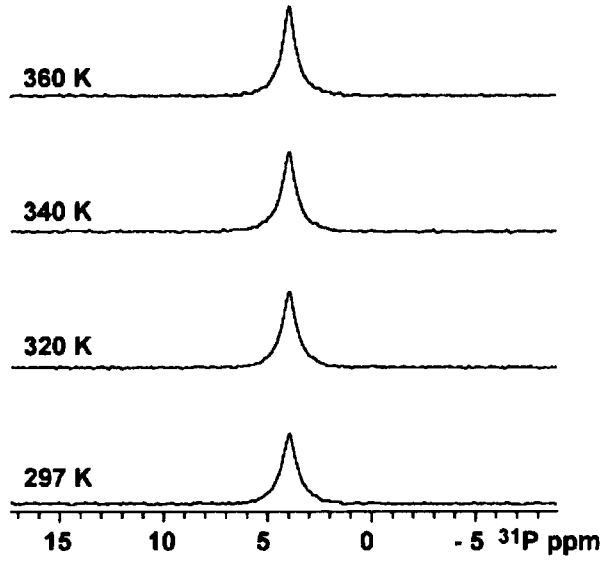

Figure 5 - The ^{31}P MAS variable temperature spectra of KH_2PO_4 show little linewidth change indicating that the material has little dynamics within our temperature range.

The lack of phosphate dynamics and the low gyromagnetic ratio of the potassium nucleus make KDP an excellent choice for testing the sensitivity of the CODEX sequence to homonuclear spin diffusion. These two factors will lessen the contribution of the RIDER effect and dynamics to the attenuation of the ^{31}P spin during the CODEX experiment. If the ^{31}P CODEX NMR signal for KDP attenuates significantly, then the ^{31}P-^{31}P homonuclear interactions must be responsible for a portion of the dephasing in CDP. A summary of the dephasing for KDP is shown in **Figure 6a**. The lack of attenuation of the ^{31}P CODEX NMR signal implies that there is neither ^{31}P-^{31}P spin diffusion, nor exchange due to the RIDER effect, nor dynamics for KDP. The slow linenarrowing of ^{31}P spectra with temperature in **Figure 5** and the lack of observable

motion in the ^{31}P CODEX NMR experiments supports that the phosphate in KDP is dynamically inactive and therefore a poor ion conductor.

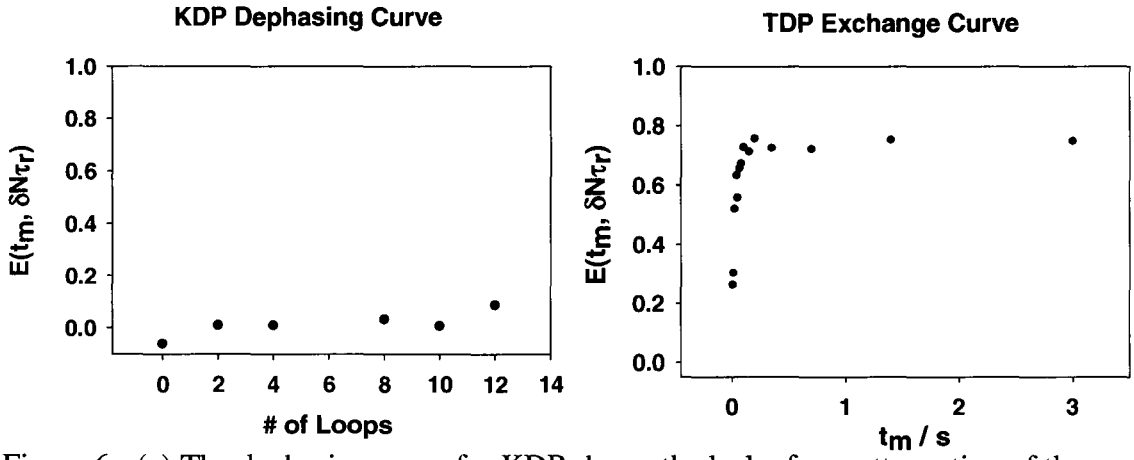

Figure 6 - (a) The dephasing curve for KDP shows the lack of any attenuation of the echo over twelve loops of recoupling. (b) The exchange curve of thallium dihydrogen phosphate (TDP) which exhibits a characteristic 72% plateau which corresponds to the four site reorientation of the phosphate.

For CDP, the nine loops of recoupling were sufficient to attenuate the ^{31}P CODEX signal to 87%; whereas little to no attenuation was recorded for KDP using these parameters. Homonuclear exchange during the mixing time between ^{31}P spins could be present in any of the phosphate based solid acids but does not affect the dephasing of the ^{31}P CODEX NMR signal in KDP. Additionally, the smaller cation size would decrease the distance between phosphates, thereby increasing the strength of the homonuclear ^{31}P dipolar couplings. With a stronger dipolar coupling, the effectiveness of the homonuclear spin diffusion is increased. The shortest ^{31}P-^{31}P contact in the solid-state structure of KDP is 4.114 Å and the shortest contacts for CDP and RDP are 4.5 Å and 4.8 Å.[29] In the room temperature structure of thallium dihydrogen phosphate (TDP) the closest ^{31}P-^{31}P

contact is 4.5 Å, similar to the contacts present in CDP.[30] The shorter contact in KDP means that if spin diffusion were present in any of the solid acid materials then the material with the shortest contact would have the strongest homonuclear spin diffusion. However, this is not the case and no attenuation from any of the exchange mechanisms affects the echo during the mixing time. This suggests that the second mechanism for exchange in CDP is unlikely to be homonuclear spin diffusion between phosphates and is a combination of heteronuclear exchange and dynamics.

The best choice for probing phosphate dynamics in the absence of a quadrupolar nucleus with CODEX within the solid acid family is thallium dihydrogen phosphate (TDP).[31-33] Thallium is spin half and has a high gyromagnetic ratio, the high gyromagnetic ratio could disrupt the ^{31}P CODEX measurements, through a strong dipolar coupling. However, the nuclear spin of both thallium isotopes are spin ½ which rules out fast relaxation in the solid state by the thallium nucleus. Slow relaxation would have a negative influence on the ability of the RIDER effect to exhibit itself in this system.[28] The ^{31}P CODEX NMR exchange curve for TDP in **Figure 6b** shows the plateau of 72 ± 2%, which correctly corresponds to a four-fold reorientation. The correlation time measured for TDP is 19 ± 2 ms corresponds to the estimated timescale for phosphate reorientation in solid acids. Observation of a plausible plateau and correlation time for a strongly dynamic solid suggest that the measurement of a correlation time is possible for the solid acid family of electrolytes, when all the variables are carefully evaluated. Clearly, ^{31}P-^{31}P spin diffusion does not obscure the dynamic information.

The ^{31}P CODEX NMR signal of CDP is combination of the phosphate rotation and a second mechanism of exchange, therefore the use of a double exponential fitting function applies to this case. Due to the additional interaction influencing the plateau of **Figure 4a**, the weighing of the exponential functions will not be representative of the geometry involved in the reorientation since the spin diffusion could potentially contribute to any amount depending on the magnitude of the interaction. The fitting of the CDP ^{31}P CODEX NMR data converged to two different exponentials with a weighting of 54 and 35 % with correlation times of 10 and 99 ms, respectively, the equation used is shown below. With a single data set, it is impossible to determine which correlation time corresponds to the motion of the phosphonate.

To determine which correlation time corresponds to the physical motion of the phosphate, a series of variable temperature ^{31}P CODEX NMR experiments were recorded on CDP on an 11.74 T magnet. Increasing the temperature would decrease the correlation time of the physical motion. The correlation time of a spin diffusion constant as measured by the CODEX experiments will stay the same since the ^{31}P anions are localized in the crystal structure, thus the dipolar couplings between phosphates are relatively independent of temperature. The correlation time for the RIDER effect is dependent on the relaxation of the other spin. The results from the variable temperature analysis of the ^{31}P CODEX data are summarized in **Table 2**.

$$E_{\infty}(t_m, \delta N \tau_R) = a(1-\exp(-t_m/b)) + c(1-\exp(-t_m/d)) \qquad (4\text{-}1)$$

Table 2 – The two exponential fits for the ^{31}P CODEX NMR data from the various solid acid electrolytes.

CDP	Weight a ± 10 %	Time Constant b ± 2 ms	Weight c ± 10 %	Time Constant d ± 5-7 ms
300 K	53	10	35	99
310 K	40	9	40	42
320 K	52	9	21	23
RDP				
296 K	26	10	62	38
CMP				
260 K	59	10	29	55
265 K	47	9	39	56
270 K	50	8	38	52
275 K	14	8	69	45
285 K	20	8	61	31
296 K	49	4	38	34

The results from **Table 2** confirm that the 10 ms correlation time does not vary significantly beyond the error of the experiment and that the introduction of a quadrupolar nuclei to the system creates a second exchange mechanism that was previously absent in other CODEX investigations. This suggest that the 10 ms correlation time in CDP is related to the dipolar exchange between heteronuclear spins of the quadrupolar nucleus.

The correlation time that ranges from 10 to 9 ms (fit as a for CDP) does change significantly with temperature. The change in correlation time with temperature is consistent with an increase in the ^{1}H-^{1}H exchange observed qualitatively in the 2D EXSY spectra from **Figure 3**. The activation energy of the correlation times ranging from 99 to 23 ms for CDP is 74 ± 1 kJ/mol, this value is below the ionic conductivity presented in the literature, which is ~ 95 kJ/mol recorded from impedance spectroscopy.[11, 34] The activation energy from ionic conductivity is larger than the one observed by NMR because NMR only measures the local dynamics of the phosphate. Impedance spectroscopy is a macroscopic technique and is affected by material defects like grain boundaries. Grain boundaries are void spaces in the solid-state structure that inhibit the flow of ions and this increases the activation energy. The activation energy from the ^{31}P CODEX NMR on CDP supports the hypothesis that that the major barrier for proton conductivity for the phosphate solid acids prior to the superprotonic phase is the rotation of the phosphate.[35] The gain in ionic conductivity from the superprotonic phase transition in solid acid materials must reduce the barrier for rotation of the phosphate, leading to an increase in ionic conductivity. For RDP, the weighting of the two exponentials is 26 and 62%, with correlation times of 10 and 38 ms, respectively. It is surmised that the 10 ms correlation time originates from a RIDER style of exchange and the 38 ms correlation time is a measurement of the four-fold motion of the phosphate, which is similar to the rate observed in CDP at the same temperature.

The modification of the phosphate to a phosphonate would immensely change the hydrogen bonding around the phosphonate. The dynamics of the methyl phosphonic acid analogue is observable through the ^{31}P CODEX NMR. The plateau of the exchange curve of CMP in **Figure 7** has a maximum value of 89% for the three-fold rotation, whereas the theoretical value for a C_{3v} rotation is only 66%. The high plateau of the exponential in CDP is also present in the ^{31}P CODEX NMR exchange curve for CMP. Since the cesium cation is present in both CDP & CMP, dipolar exchange from the cesium cation could affect the phosphorous spins during the ^{31}P CODEX mixing times in CMP. This justifies using a double exponential to fit the additional dephasing in **Figure 7**.

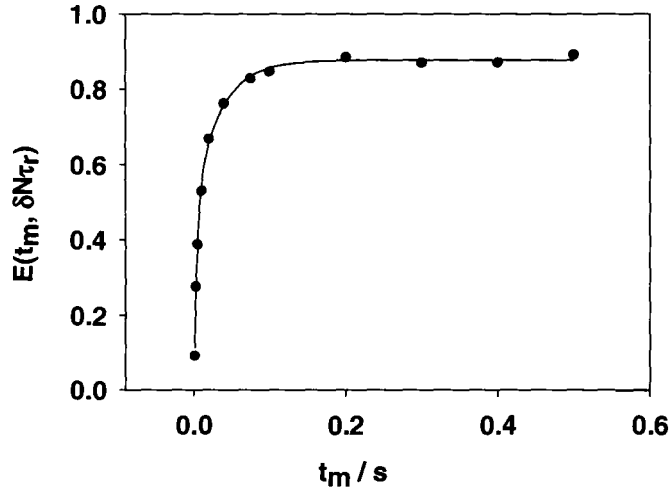

Figure 7 – ^{31}P CODEX NMR exchange curve for CMP using 16 loops of recoupling. The double expontential fit resulted in correlation times of 4 ± 2 and 34 ± 2 ms with weighting of 0.49 ± 10 and 0.38 ± 10, respectively.

The double exponential fit of the exchange curve for CMP yielded two correlation times of 4 ± 2 ms and 34 ± 2 ms with weights of 0.49 ± 10 and 0.38 ± 10, respectively. These

values are reminiscent of the constants from CDP where the faster correlation time due to heteronuclear spin diffusion and had the larger contribution to the exchange. A plot of the correlation times obtained from a series of variable temperature ^{31}P CODEX NMR experiments is plotted as **Figure 8**. The activation energy of the temperature dependent correlation times are 11 ± 3 kJ/mol. The activation energy for CMP is smaller than the activation energy obtained for CDP and is the result of changing the fourth oxygen atom to a methyl group on the phosphate.

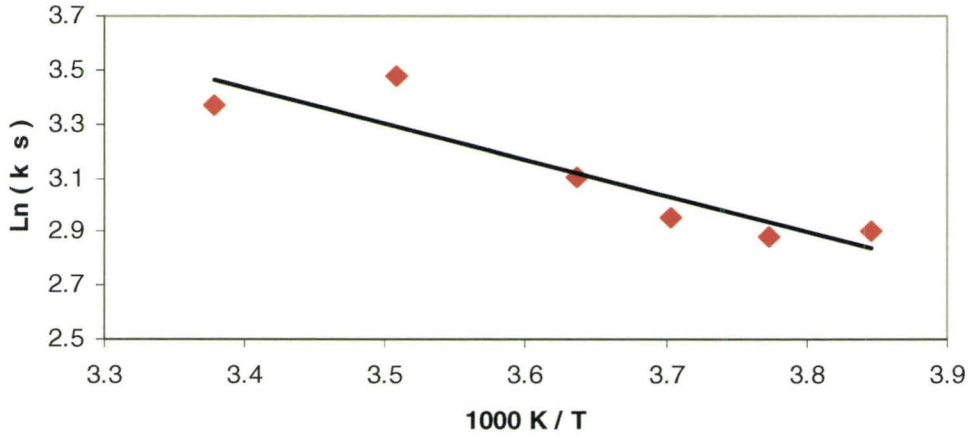

Figure 8 – A variable temperature plot of the correlation times obtained from ^{31}P CODEX NMR on CMP. The activation energy of the correlation time for CMP is 11 ± 3 kJ/mol.

The four-fold motion of the phosphate is strongly dependent on thermal energy to promote the reorientation of the entire phosphate anion. The three-fold motion of the methane phosphonate is only bound by two hydrogen bonds and requires less energy to become active. Since the phosphonates require less energy to rotate, the observation of the onset of dynamics should occur at lower temperatures.

A molecular dynamics study on $CsHSO_4$ calculated the barrier for the three-fold rotation of the sulfate in the crystal structure to be 6.7 to 7.5 kJ/mol.[12] The calculation of the rotational barrier in $CsHSO_4$, supports the conclusion that the correlation time giving a low activation energy for CMP originates from the rotation of the phosphonate.

For CMP, the rotational barrier in the solid acid electrolytes was reduced from 74 kJ/mol in CDP to 11 ± 3 kJ/mol. This structural change promotes a faster reorientation of the anion and increases the low temperature ionic conductivity. It was observed that the methyl group of the phosphonate in an analogous rubidium hydrogen methyl phosphonate that the alkyl groups experiences the onset of dynamics prior to any superprotonic transition. As well, the alkyl group on the phosphonate reduces and delays the onset of the thermal decomposition, by transferring thermal energy into the rotation of the alkyl group. The thermal decomposition of CDP under dry conditions releases water and creates a pyrophosphate. The decomposition of CDP under these conditions occurs at the same temperature as the superprotonic phase transition preventing the material from providing a sustained ionic conductivity. The ability of the alkyl group to rotate removes energy from the system that would normally cause the decomposition of the bridging hydrogen bond into water.[36]

A fuel cell using CDP as an electrolyte can operate above the superprotonic phase transition but requires thin layers and high pressures to ensure that the material does not decompose immediately.[14] The creation of solid acid fuel cells holds much promise if the decomposition of the electrolyte is avoided. A similar trend for CMP exists where under

dry and humid conditions, a phase transition for CMP was observed in the differential scanning calorimetry trace at 205°C. However, if the material maintains the fast reorientation rate prior to this transition and this material has the potential to be used in fuel cells with high temperature operation up to 205°C, yielding large temperature range for the operation of the fuel cell that does not require a superprotonic phase transition to for the electrolyte to function.

4.3 - Summary

Solid state NMR was able to determine the rate and temperature dependence of the rotation of two types of anions in several solid acid electrolytes, the phosphate having the largest barrier for rotation at 74 ± 1 kJ/mol. Through ^{31}P CODEX NMR and comparing the distances of ^{31}P-^{31}P contacts, it was possible to determine that the RIDER effect is present in the CODEX analysis of CDP, RDP, and CMP materials. With CDP and CMP, multiple temperatures provided the necessary information to determine the dependence of the correlation time with temperature for each type of anion. The change from a four-fold rotation of the phosphate to the three fold transition of the methyl phosphonate reduced the energy barrier for rotation from 74 ± 1 kJ/mol to 11 ± 3 kJ/mol. The high activation energy for the phosphate creates a strong dependence of the rotation on temperature, requiring high temperatures for operation. The activation energy from the ^{31}P CODEX NMR suggests that the rotation of the phosphate in CDP is the major barrier for proton conduction in the solid-state for CDP. By lowering the activation

energy, the methyl analogue does not experience the same barrier for rotation as the phosphate.

This analysis is unique, provides valuable information on the processes involved in the mechanism of proton transport, and applies to other materials in the solid-state with slow dynamics. The addition of a methyl group to the phosphate holds great promise because of the increased rate of reorientation, from 99 ms in CDP to 34 ms in CMP and the reduction in the barrier for the rotation, will promote the conduction of ions at lower temperatures. The onset of fast dynamics in the alkyl phosphonate supports the creation and further study of a solid acid electrolyte that conducts ions in a temperature range that precedes the phase transition. This new type of electrolyte would have characteristics of an anhydrous ionic electrolyte.

4.4 - References

1. R. Bouchet and E. Siebert, *Solid State Ionics*, 1999, **118**, 287-299.
2. H. T. Pu, W. H. Meyer and G. Wegner, *J. Polym. Sci. Pt. B-Polym. Phys.*, 2002, **40**, 663-669.
3. J. Xie, D. L. Wood Iii, D. M. Wayne, T. A. Zawodzinski, P. Atanassov and R. L. Borup, *J. Electrochem. Soc.*, 2005, **152**, A104-A113.
4. K. A. Mauritz and R. B. Moore, *Chem. Rev. (Washington, DC, U. S.)*, 2004, **104**, 4535-4585.
5. G. Gebel, *Polymer*, 2000, **41**, 5829-5838.
6. Z. G. Qi and S. Buelte, *J. Power Sources*, 2006, **161**, 1126-1132.
7. G. Ye, C. A. Hayden and G. R. Goward, *Macromolecules*, 2007, **40**, 1529-1537.
8. A. Preisinger, K. Mereiter and W. Bronowska, *Mater. Sci. Forum*, 1994, **166-169**, 511-516.
9. A. I. Baranov, L. A. Shuvalov and N. M. Shchagina, *J. Exp. Theor. Phys.*, 1982, **36**, 459-462.
10. C. R. I. Chisholm, R. B. Merle, D. A. Boysen and S. M. Haile, *Chem. Mater.*, 2002, **14**, 3889-3893.
11. D. A. Boysen, S. M. Haile, H. Liu and R. A. Secco, *Chem. Mater.*, 2003, **15**, 727-736.
12. C. R. I. Chisholm, Y. H. Jang, S. M. Haile and W. A. Goddard(III), *Phys. Rev. B*, 2005, **72**, 134103.
13. M. Iannuzzi and M. Parrinello, *Phys. Rev. Lett.*, 2004, **93**, 025901-025901.
14. T. Uda and S. M. Haile, *Electrochem. Solid-State Lett.*, 2005, **8**, A245-A246.
15. K. Schmidt-Rohr, E. R. de Azevedo and T. J. Bonagamba, *Encyclopedia of Nuclear Magnetic Resonance*, 2002, **9**, 633-642.
16. E. R. de Azevedo, W. G. Hu, T. J. Bonagamba and K. Schmidt-Rohr, *J. Am. Chem. Soc.*, 1999, **121**, 8411-8412.
17. E. R. de Azevedo, W. G. Hu, T. J. Bonagamba and K. Schmidt-Rohr, *J. Chem. Phys.*, 2000, **112**, 8988-9001.
18. E. R. deAzevedo, W. G. Hu, T. J. Bonagamba and K. Schmidt-Rohr, *J. Am. Chem. Soc.*, 1999, **121**, 8411-8412.
19. D. J. Harris, T. J. Bonagamba, M. Hong and K. Schmidt-Rohr, *Macromolecules*, 2000, **33**, 3375-3381.
20. Ingrid Fischbach, T. Pakula, P. Minkin, A. Fechtenkotter, K. Mullen, H. W. Spiess and S. Kay, *J. Phys. Chem. B*, 2002, **106**, 6408-6418.
21. K. Saalwachter and K. Schmidt-Rohr, *J. Magn. Reson.*, 2000, **145**, 161-172.
22. G. J. M. P. van Moorsel, E. R. H. Vaneck and C. P. Grey, *J. Magn. Reson., Ser. A*, 1995, **113**, 159-163.
23. R. J. Nelmes and R. N. P. Choudhary, *Solid State Commun.*, 1978, **26**, 823-826.
24. D. Sebastiani, G. Goward, I. Schnell and H. W. Spiess, *THEOCHEM*, 2003, **625**, 283-288.

25. D. Sebastiani, G. Goward, I. Schnell and M. Parrinello, *Comput. Phys. Commun.*, 2002, **147**, 707-710.
26. K. Yamauchi, S. Kuroki, K. Fujii and I. Ando, *Chem. Phys. Lett.*, 2000, **324**, 435-439.
27. B. Berglund and R. W. Vaughan, *J. Chem. Phys.*, 1980, **73**, 2037-2043.
28. D. Cuc, S. Bouguet-Bonnet, N. Morel-Desrosiers, J.-P. Morel, P. Mutzenhardt and D. Canet, *J. Phys. Chem. B*, 2009, **113**, 10800-10807.
29. Z. Tun, R. J. Nelmes, W. F. Kuhs and R. F. D. Stansfield, *J. Phys. C: Sol. Sta. Phys.*, 1988, **21**, 245-258.
30. I. H. Oh, M. Merz, S. Mattauch and G. Heger, *Acta Crystallogr., Sect. B: Struct. Sci.*, 2006, **62**, 719-728.
31. R. J. Nelmes and R. N. P. Choudhary, *Solid State Commun.*, 1981, **38**, 321-324.
32. K. S. Lee, J. H. Park, K. B. Kim, J. B. Kim and J. N. Kim, *J. Phys. Soc. Jpn.*, 1998, **66**, 1268-1271.
33. S. Rios, W. Paulus, A. Cousson, M. Quilichini and G. Heger, *Acta Crystallogr., Sect. B: Struct. Sci.*, 1998, **54**, 790-797.
34. A. I. Baranov, V. P. Khiznichenko and L. A. Shuvalov, *Ferroelectrics*, 1989, **100**, 135 - 141.
35. H.-S. Lee and M. E. Tuckerman, *J. Phys. Chem. C*, 2008, **112**, 9917-9930.
36. P. Foley, R. DiCosimo and G. M. Whitesides, *J. Am. Chem. Soc.*, 1980, **102**, 6713-6725.

Chapter 5: Solid Organic Electrolytes: Benzimidazole

This chapter introduces the solid organic electrolytes based on acidified polybenzimidazole. This body of work is from a series of papers that were published in the Journal of Physical Chemistry B and a special topics issue of Magnetic Resonance in Chemistry. The co-authors on the papers are James F. Britten for the collection and solution of the X-ray structures and Gillian R. Goward who revised the work. My contributions to this chapter are the synthesis, collection, and interpretation of all of the data relating to the solid organic electrolytes. The exact mechanism of conduction in polybenzimidazole is only currently understood through modification of the membrane and interpretation of macroscopic techniques. Solid organic electrolytes model the ionic conductivity of the polymer with a benzimidazole cation and phosphorus based anion. The implications of tethering the anion to the polymer backbone are explored through the model compounds and a range of techniques, with a focus on using solid-state nuclear magnetic resonance (NMR) to discover the mechanism of ion conduction.

5.0 – Introduction

Polybenzimdiazole (PBI) like Nafion is a poor electrolyte without a liquid electrolyte to facilitate the conduction of ions.[1, 2] Adding phosphoric acid to the PBI, increases the ionic conductivity of the polymer membrane. The ion conduction and

properties of PBI are fully outlined in Chapter 1. The major drawback is the eventual loss of the liquid phosphoric acid that is not replenished as the fuel cell operates and causes the membrane to become inactive.[3] To retain the transport properties of acidified PBI, other imidazole polymers have the phosphonate group attached to the backbone of the polymer.[2, 4-7] The new anhydrous polymers, however, do not have an impressive conductivity as the original membrane.

The mechanism of ion exchange in acidified PBI is dependent on the phosphoric acid with assistance from the backbone dynamics.[8, 9] The contribution of ring dynamics is unknown for benzimidazole. Hydrogen bonding anchors the phosphates to the backbone. Reducing the amount of acid in the polymer backbone and binding it to the polymer backbone will hinder the mechanisms of ion transport that depend on free phosphoric acid. Thus, tethering the anion to the polymer backbone will promote a different mechanism of ion transport. The role and mechanism of the benzimidazole cations and tethered phosphonate anions in new electrolytes has yet to be understood. The three model compounds of **Figure 1** are derivates of acidified PBI and tethered phosphonates and depict the modes of transport available in these polymer membranes. The model compounds are benzimidazole phosphate (Bi-PA), Benzimidazole methylphosphonate (Bi-mPA), and benzimidazole ethylphosphonate (Bi-ePA).

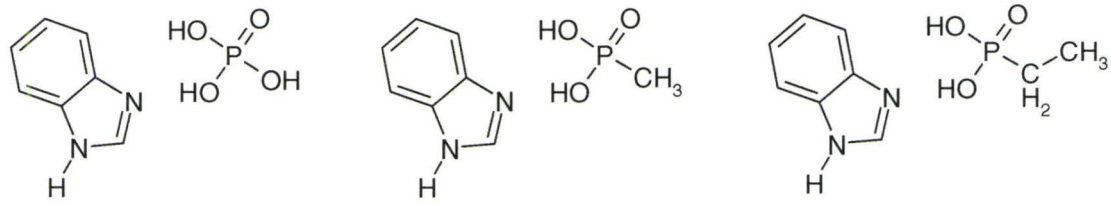

Figure 1 – The chemical structure of the three model compounds of benzimidazole based polymers. (Left) Benzimidazole phosphate, (Middle) Benzimidazole methylphosphonate, (Right) Benzimidazole ethylphosphonate.

Studies involving the mechanism of acidified PBI have indirectly observed the changes via macroscopic techniques.[9-12] These techniques depend on our chemical intuition to understand the data. On the other hand, solid-state nuclear magnetic resonance (NMR) is a method that directly probes the system on a molecular level. In this chapter, the mechanism of ion conduction involving benzimidazole model compounds is studied using the techniques outlined in Chapter 2. In particular, the ^{1}H-^{1}H double quantum correlation (DQC) spectra, provides homonuclear correlations through the dipolar couplings. The multinuclear CODEX NMR that is able to detect motion that influences the chemical shift anisotropy of the material. These techniques will help improve our understanding of ion transport in anhydrous polymers.

5.1 - Experimental

Crystals of the Bi-mPA, Bi-PA, and Bi-ePA compounds were obtained by saturating a solution in dimethylsulfoxide with the components in a 1:1 ratio. Leaving the solutions in a closed environment, both solutions produced good quality crystals that were transparent and colourless. Trace amounts of dimethylsulfoxide found in the ^{1}H

MAS spectra were removed by heating the powders to 100-120°C. The single crystal X-ray diffraction data for the Bi-mPA was recorded using Cu K-α radiation with a wavelength of 1.54178 Å. The final R-factor for the structure solution was 3.21% with a space group of $P2_1/c$. The crystal structure for Bi-ePA gave a structure solution of 3.62% and occupied the same space group as Bi-mPA. The crystal structure of Bi-PA has been previously reported in the literature and therefore no further diffraction data was acquired.[13] Powder X-ray diffraction data of the materials were acquired, in both cases this confirming the high degree of crystallinity in the materials.

The high field ^1H NMR work was conducted at the National Ultrahigh Field NMR Facility for Solids in Ottawa, Canada. The magnet used had a proton Larmor frequency of 900.20 MHz with ^1H pulse lengths of 2.5 μs. Rotors of 2.5mm outer diameter, with a sample volume of 10μl were used to obtain MAS frequencies of 30 kHz.

An 11.74 T magnet was used for the ^{31}P and ^{13}C CODEX studies. The CODEX data was acquired with a MAS frequency of 10 kHz with a double resonance probe using rotors with a 4 mm outer diameter. For Bi-mPA a 3.5 s ^1H T_1 was measured and 53 s ^1H T_1 was measured for Bi-PA. These long relaxation times imposed long acquisition times on the experiments, with an average CODEX build-up curve requiring 72 h. A contact time of 3000 μs was used for the CODEX experiments.

The double quantum filter spectrum of Bi-mPA was acquired using a Bruker AMX 600 system with a proton Larmor frequency of 600.16 MHz. The 50.3 kHz MAS spectrum was acquired using an proto-type probe with rotors of an outer diameter of

1.8 mm. The double quantum filter spectrum was acquired using $\tau_{exc} = \tau_r$. The two dimensional DQC spectrum was acquired with 64 scans and 64 slices in the indirect dimension using 1.8 μs ^{1}H pulse lengths. A separate cooling line is used to compensate for the frictional heating in this probe.

The temperatures used to describe the variable temperature MAS spectra have been corrected for the frictional heating of the MAS rotor with the bearing gas using samarium stannate.[14, 15]

5.2 – Results and Discussion

5.2.1 – ^{1}H Characterization

The mechanism of proton transport in the doped PBI system has been proposed based on impedance spectroscopy.[8] The drawback of using ionic conductivity for justification of a mechanism is that the measurement directly observes only the resistance of the material across the electrodes. Only the flow of ions through the material at the electrode determines the ionic conductivity. Therefore, data interpretation must rely on our chemical intuition to rationalize the mechanism of proton transport. The application of solid state NMR to characterize the molecular-level local dynamics in other systems has proved valuable for understanding the structure and reorientations of molecules in the solid state.[16-18] By investigating the interactions of the spins on a molecular level, discovering the exact mechanism of ion exchange is possible.

The three model compounds will help illustrate the structure and mobility of each functional group in acidified PBI and other anhydrous polymer systems that use benzimidazole. The three model compounds form a series of ionic salts that use benzimidazole for the cation and vary the alkyl chain length on the anion. The compounds of **Figure 1** form two types of hydrogen bonds, N-H∞O and O-H∞O, between the nitrogen atoms of benzimidazole ring to the oxygen on the phosphate and another hydrogen bond between two phosphates. The number and organization of hydrogen bonds differs between the structures due to the alkyl group on the phosphonic acid. This change in chemical structure leads to a different organization of the hydrogen bonds in the solid-state. The model compounds form crystalline salts that produce high quality X-ray diffraction data sets, the hydrogen bonding around the benzimidazole from the structure solutions are shown as **Figure 2**. The ethyl analogue is not shown because the structure strongly resembles the methyl analogue.

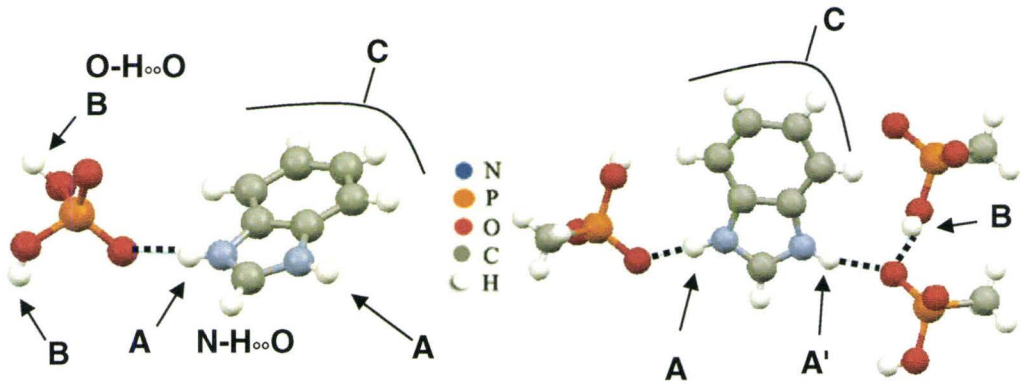

Figure 2 – The hydrogen bonding around the benzimidazole cation for the phosphate (left) and the methyl analogues (right). The A protons are in N-H∞O hydrogen bonds and B protons are in O-H∞O bonds, aromatic protons are labeled C, while aliphatic protons are labeled as D.

The differences in the two structures result from exchanging a hydroxyl (which acts as a hydrogen bonding donor group) for a methyl group. The methyl group does not participate in any of the hydrogen bonding. This switch changes the number of hydrogen bonds linked to each anion; the methyl phosphonate has four hydrogen bonds while the phosphate has six.

This distinction leads to a decrease in lattice energy for the alkyl phosphonates and lowers the melting point of the material. This effect is observed in the differential scanning calorimetry (DSC) traces of the three benzimidazole compounds shown in **Figure 3**. The DSC trace of the benzimidazole phosphate in **Figure 3a**, shows the melting point of the powder material at 156°C. Similarly, for the methyl and ethyl analogues the melting points decrease to 143°C and 120°C, respectively. The DSC trace for the phosphate shows a strong exothermic behavior after the phase transition,

attributed to phosphate dehydration.[19] The DSC traces of the methyl and ethyl analogues both have a stable liquid region at high temperatures above the melting point while the phosphate compound does not.

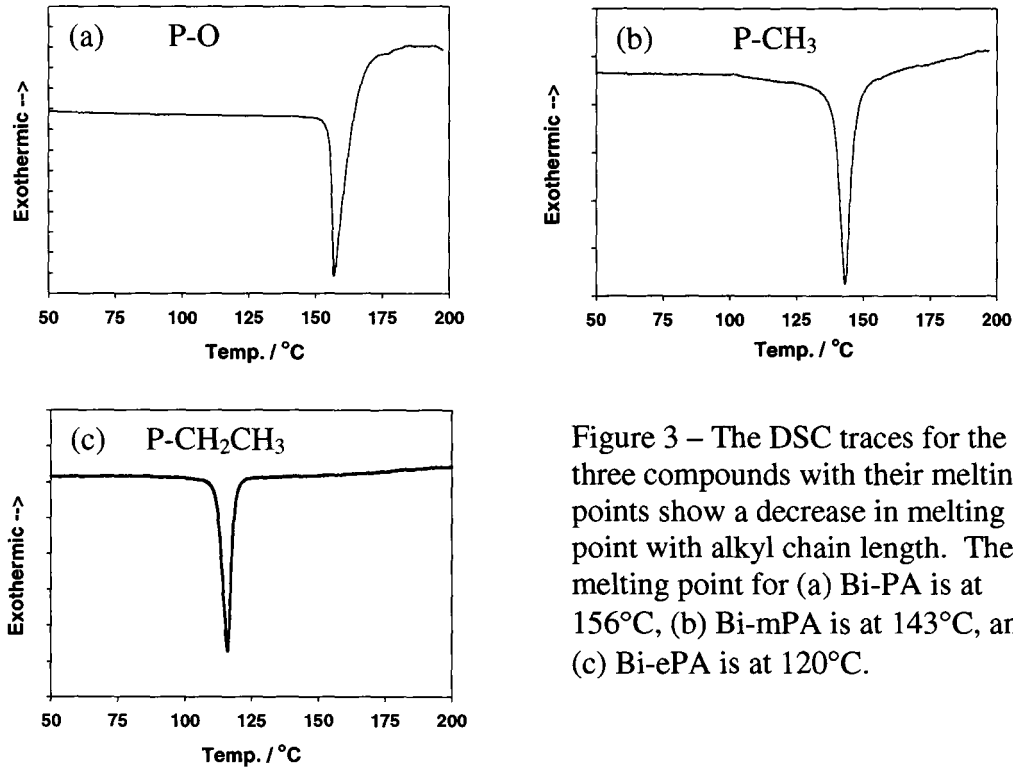

Figure 3 – The DSC traces for the three compounds with their melting points show a decrease in melting point with alkyl chain length. The melting point for (a) Bi-PA is at 156°C, (b) Bi-mPA is at 143°C, and (c) Bi-ePA is at 120°C.

The lower melting point of the methyl and ethyl analogues suggests that the solid-state packing is the strongest in the phosphate due to the increased number of hydrogen bonds. The increased alkyl chain length of the ethyl analogue lowers the temperature of the melting point of the compound drastically over the methyl phosphonate by disrupting the packing of the ions. A lower melting point suggests that the ions will experience the onset of liquid-like dynamics in the solid-state at an lower temperature. However, DSC

traces do not provide information on the strength of the individual hydrogen bonds, while the relative strength of these hydrogen bonds can be inferred from their ^{1}H NMR resonances.

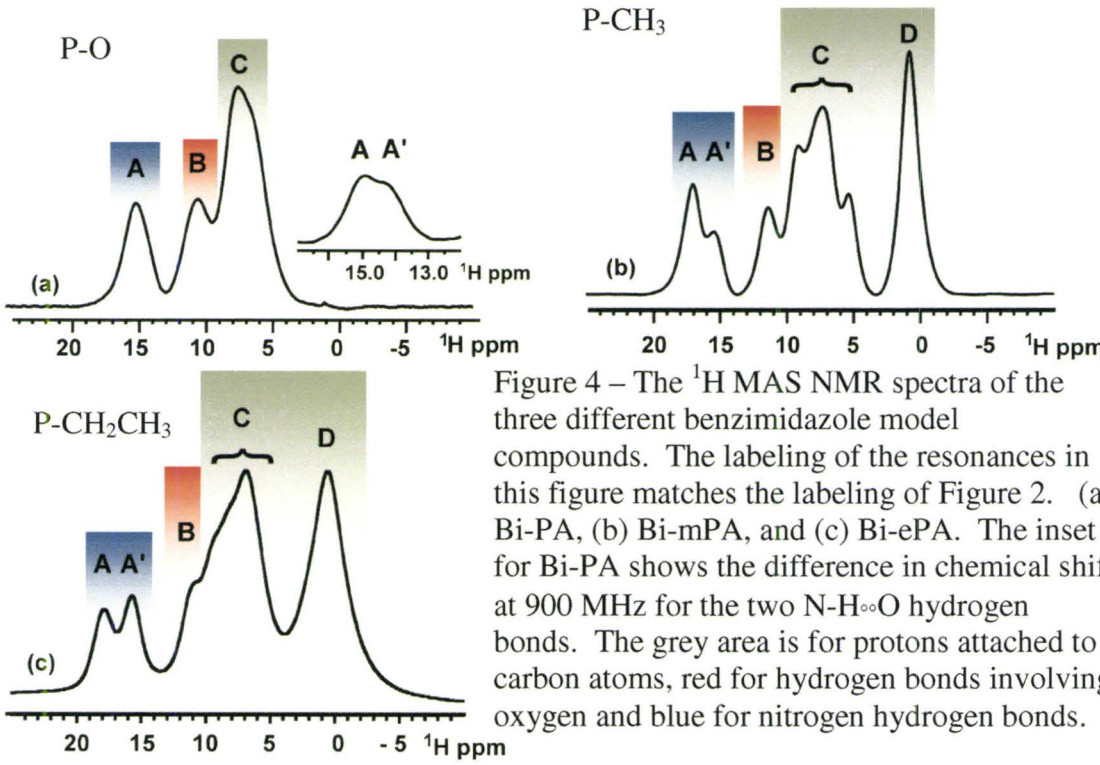

Figure 4 – The ^{1}H MAS NMR spectra of the three different benzimidazole model compounds. The labeling of the resonances in this figure matches the labeling of Figure 2. (a) Bi-PA, (b) Bi-mPA, and (c) Bi-ePA. The inset for Bi-PA shows the difference in chemical shift at 900 MHz for the two N-H◦◦O hydrogen bonds. The grey area is for protons attached to carbon atoms, red for hydrogen bonds involving oxygen and blue for nitrogen hydrogen bonds.

The influence of the different hydrogen bonding environments is observed in the ^{1}H MAS NMR spectra that are shown in **Figure 4**. The N-H◦◦O hydrogen bonds have the higher chemical shift (17-15 ppm) because they are stronger hydrogen bonds, while the O-H◦◦O hydrogen bonds are weaker and have a lower chemical shift (12-10 ppm). All N-H◦◦O hydrogen bonds are labeled as A or A' and O-H◦◦O hydrogen bonds are given the designation B. The resonances at 9-6 ppm in **Figure 4** are assigned to the aromatic protons of the benzimidazole ring, and are labeled C. The resonances near

0 ppm in **Figure 4** are assigned to the alkyl group of the phosphonate, and are referred to as resonance D. Since the number of hydrogen-bonding protons available in Bi-ePA is the same as Bi-mPA, the structure adopts a similar organization and this is reflected in the similar appearance of their ^{1}H MAS NMR spectra. The major difference between the spectra of Bi-mPA and Bi-ePA is that the ^{1}H spins of Bi-ePA have strong dipolar couplings to the extra methylene group of the ethylphosphonate; this causes dipolar broadening of the spectrum and blends the resonances of the ethyl into one resonance.

The assignment of hydrogen bonded resonances cannot be accounted for solely by the different heteroatomic distances or the type of electronegative atoms surrounding the proton. These factors impact the chemical shift but do not absolutely control them. Additional factors like the presence of electronegative neighbors and style of hydrogen bonding will all contribute to the overall chemical shift of the ^{1}H NMR resonance.[20, 21]

For a hydrogen bond, the distance between electronegative atoms helps determine the chemical shift of the proton.[22, 23] A short hydrogen bonding distance implies a strong hydrogen bond and this pulls the proton away from the shielding of the electronegative nucleus of the donor atom. This causes the total electron shielding of the proton to decrease, producing an increase in chemical shift, while the opposite is true for weaker hydrogen bonds.

In Bi-PA, the N-H$\circ\circ$O heteroatomic distances differ by 0.083 Å and the chemical shift difference of the two resonances is only 0.7 ppm. The Bi-mPA analogue has similar heteroatomic distances, which differ by 0.073 Å. However, in Bi-mPA the two N-H$\circ\circ$O

hydrogen bonded protons are separated by 1.7 ppm. This illustrates that the difference in the distance between two electronegative atoms does not necessary form a direct correlation. If they did then the chemical shift difference between the two protons in Bi-mPA would be much smaller than 1.7 ppm. From the chemical structures, it is apparent that the number of hydrogen bonding donor atoms and acceptor sites does not match. To match all the hydrogen bonding donors to hydrogen bonding acceptor sites, the structures require that of the one oxygen atoms participate in a second hydrogen bond becoming bifurcated. This causes an oxygen atom in Bi-mPA and Bi-ePA to participate in two hydrogen bonds. The bifurcation of the oxygen atoms changes the strength of the surrounding hydrogen bonds and alters the chemical shift of the hydrogen-bonded protons. A ^{15}N CPMAS spectrum of Bi-mPA (not shown) has two different resonances, this confirms that there are different environments for the two nitrogen atoms of the benzimidazole ring. The two ^{15}N resonances are separated by 8.3 ppm for Bi-mPA and this proves that the two sites are similar but not are equivalent.

In Bi-mPA, the $N\text{-}H_A\cdots O$ hydrogen bond that is not bifurcated is referred to as the hydrogen bond A, the bifurcated $N\text{-}H_{A'}\cdots O$ hydrogen bond is referred to as hydrogen bond A', and the $O\text{-}H_B\cdots O$ is labeled hydrogen bond B. The chemical shifts related to the two $N\text{-}H\cdots O$ hydrogen bonded protons in Bi-mPA do not correlate directly to the distances in the structure, but rather the **type** of hydrogen bonding (bifurcated or not). In order for Bi-PA to have a complete set of hydrogen bonds then two of the oxygen atoms on the phosphate would have to accept an additional proton. The third hydroxyl group of

the phosphate causes both N-H∘∘O protons in Bi-PA to hydrogen bond to a bifurcated oxygen atom.

Although the hydrogen bonding distances are important to the chemical shift, the bifurcation of the oxygen atoms has a greater effect on the chemical shift of the hydrogen atoms. On a spectrometer with a proton frequency of 500 MHz, the two N-H∘∘O protons in the Bi-PA structure are unresolved. Only by increasing the field to 900 MHz does the difference between the two sites start to manifest itself in the ^{1}H NMR spectrum (shown as an inset for **Figure 4a**. The small difference in the two chemical shifts is attributed to the small difference in heteroatom distances (0.083 Å).

The deconvolution of the 30 kHz ^{1}H MAS spectrum of Bi-mPA at 900 MHz using Gaussian lineshapes gives a 1:1:1 ratio for the three hydrogen bonded resonances within experimental error. This ratio matches the crystal structure, which has two N-H∘∘O protons and one O-H∘∘O proton. Similarly, the deconvolution of the 30 kHz ^{1}H MAS spectrum of Bi-PA yielded two resonances at 15.1 & 14.3 ppm which corresponds to the two N-H∘∘O protons and two resonances at 10.9 & 10.2 ppm which corresponds to the two O-H∘∘O protons.

The three highest chemical shift resonances are identified as the three unique hydrogen bonded protons in the Bi-mPA and Bi-ePA crystal structure.. The 2D ^{31}P-^{1}H correlation spectrum is able to identify which protons are close to the ^{31}P spin by detecting only spins with a strong dipolar coupling to the spin of the phosphorus. The strongest dipolar couplings will have a high intensity at low excitation times. The proton

in the O-H∘∘O hydrogen bond is the closest spin to the phosphonate and will have the strongest dipolar coupling to the ^{31}P spin. In **Figure 5**, the resonance that has the strongest intensity is at 11.3 ppm, this resonance corresponds to the proton in the O-H∘∘O hydrogen bond and has significantly grown versus the 1D experiment in **Figure 4b**. The intensity of the other hydrogen-bonded and the methyl resonances are also strong, due to their proximity of their spins to the phosphate. The lowered intensity of the aromatic protons suggests that they are the furthest away from the phosphate.

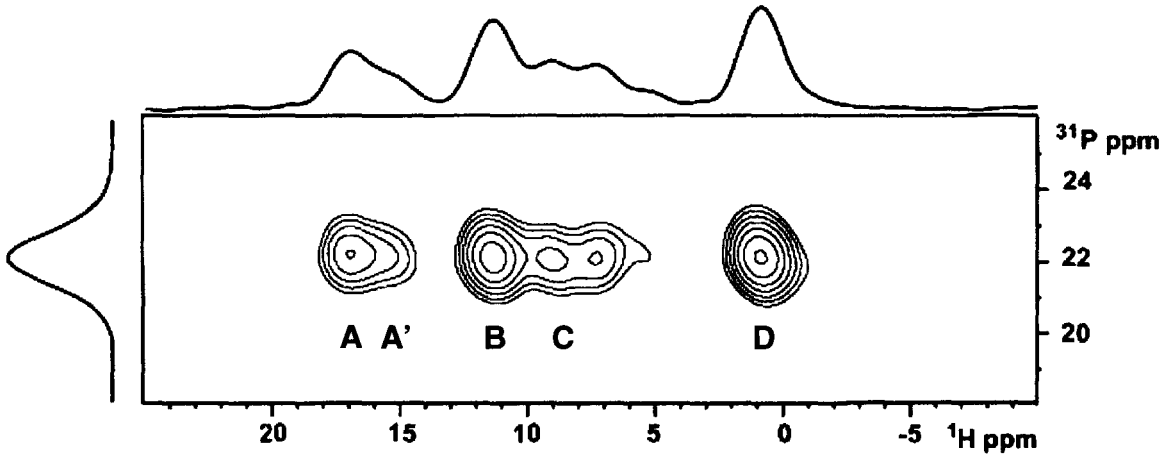

Figure 5 – The ^{31}P-^{1}H heteronuclear correlation spectrum of Bi-mPA. Only the spins near the phosphonate will have a strong correlation. The contact time for this heteronuclear correlation experiment was set to 500 μs and used 25 kHz MAS.

The exact assignment of the three hydrogen bonded protons is established by using the ^{1}H-^{1}H two dimensional DQC spectrum, shown in **Figure 6**. It is important to note that all of the ^{1}H resonances in the three model compounds pass through the ^{1}H double quantum filter. This is a clear indicator that there are no highly mobile protons with correlation times shorter than a rotor period and that any motion that are present are

slower than 40 μs. The 2D DQC spectrum allows us to determine the local packing environment of the hydrogen spins based on their homonuclear dipolar couplings. This approach, of utilizing the 2D DQC spectroscopy under fast MAS is a well-established tool that can be applied to crystalline or amorphous solids and does not require any complex crystallographic techniques to probe the local environment of the spins.[24-26] Using the 2D DQC spectrum interesting and unique packing motifs can be readily determined. The description of the pulse program and the interpretation of the data is provided in Chapter 2 of this thesis.

In **Figure 6**, the three DQC spectra show the local contacts of all the surrounding protons for each spin. The DQC spectrum becomes increasingly complex with the introduction of more resonances. In tightly packed organic solids, such as the benzimidazole model compounds where many strong dipolar exist it is common to observe all of the possible contacts. However, the intensity of the recoupled resonance is an indication of the strength of the dipolar coupling. For example, the AA dipolar coupling appears strongly in the Bi-PA spectrum and decreases in intensity as the alkyl chain length increases. This decrease is an effect of the alkyl group not packing efficiently and putting more space between layers of the benzimidazole.

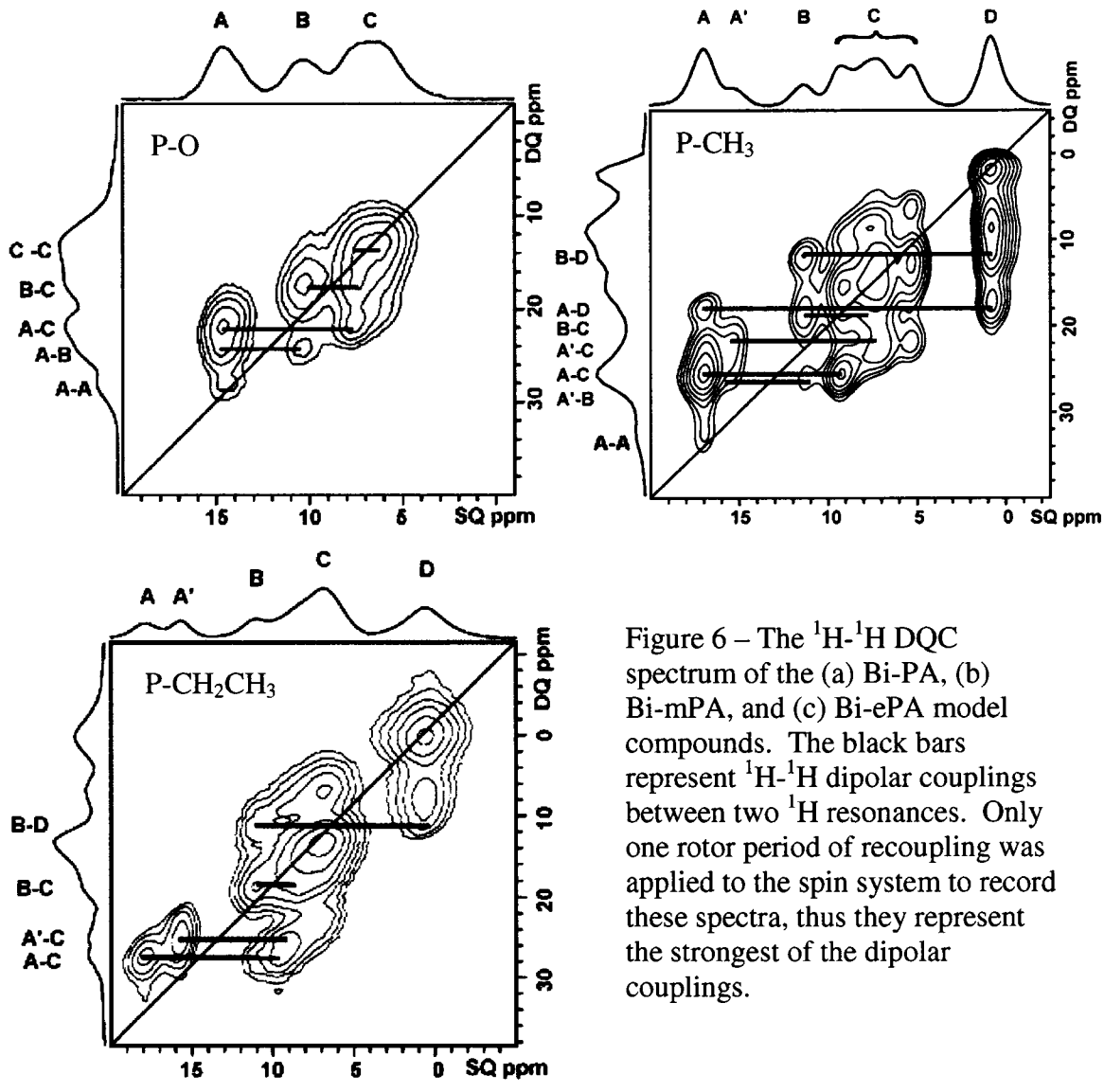

Figure 6 – The ^{1}H-^{1}H DQC spectrum of the (a) Bi-PA, (b) Bi-mPA, and (c) Bi-ePA model compounds. The black bars represent ^{1}H-^{1}H dipolar couplings between two ^{1}H resonances. Only one rotor period of recoupling was applied to the spin system to record these spectra, thus they represent the strongest of the dipolar couplings.

From the ^{1}H-^{31}P correlation spectrum, it was determined that the B resonance originates from the proton in the O-H∘∘O hydrogen bond, while the A and A' resonances originate from spins that are in N-H∘∘O hydrogen bonds. However, in Bi-ePA and Bi-mPA the two N-H∘∘O protons have significantly different chemical shifts. From the crystal structure, the two hydrogen bonded protons (a O-H∘∘O and N-H∘∘O hydrogen bond) that

share the same oxygen in **Figure 2** would have a stronger dipolar coupling to each other than to the third hydrogen bond N-H∘∘O. This A-B dipolar coupling appears between the two proton resonances of 15 & 11 ppm, thus the proton resonance at 17 ppm must be the proton in the N-H∘∘O hydrogen bond that does not share an oxygen atom. Further evidence for the assignment of the two lower hydrogen bonded resonances at 15 & 11 ppm comes from a second dipolar coupling. The resonance at 11 ppm in the DQC spectrum of Bi-mPA shows a dipolar coupling to the methyl group, labeled D in the spectrum, while a similar coupling is not observed between the resonance at 15 ppm and the methyl group. In the crystal structure of Bi-mPA, the proton of the O-H∘∘O hydrogen bond is 1.4 Å closer to the center of the methyl group than the proton in the adjacent N-H∘∘O hydrogen bond, which translates to a stronger dipolar coupling for O-H∘∘O hydrogen bonded proton to the methyl group. Therefore, the proton in the O-H∘∘O hydrogen bond is at 11 ppm and the resonance at 15 ppm must be the proton in the N-H∘∘O hydrogen bond since that resonance does not have a similar B-D coupling. This assignment holds for both Bi-mPA and Bi-ePA compounds due to their similar hydrogen bonding motifs and 2D DQC spectra. A table summarizing the contacts in the DQC spectra are presented in **Table 1**. With the complete assignment based on both the crystal structures and ^{1}H NMR data for the model compounds, the dynamics processes may now be characterized by NMR methods that probe the site-specific mobility.

Table 1 – Table of DQC contacts for Bi-PA, Bi-mPA, and Bi-ePA.

Contact	Bi-PA		Bi-mPA		Bi-ePA	
	SQ/SQ	DQ	SQ/SQ	DQ	SQ/SQ	DQ
AA	14.2/14.2	28.3	16.8/16.8	33.1		
AB	14.2/10.4	24.6				
AC	14.0/7.5	21.5	16.8/9.2 16.9/5.3	26.0 22.1	18.1/9.6	27.7
AD			16.9/1.0	18.0		
A'B			15.2/11.2	26.4	16.0/11.3	27.3
A'C			15.4/6.6	22.0	15.7/7.4	23.1
BC	10.3/7.0	17.3	11.3/7.5	18.8	11.1/7.9	19.0
BD			11.4/0.8	12.2	11.0/0.3	11.4
CC	6.9/6.9	13.8	7.3/7.4 5.3/6.7 9/6.9	14.8 13.0 15.9	7.2/7.4	13.6
CD			7.5/1.1 5.3/1.1	8.6 6.4	6.8/0.3	7.1
DD			0.8/0.8	2.0	0.5/0.5	1

5.3 – Dynamics

5.3.1 – ^{1}H Variable Temperature

The decreasing melting point with an increase in alkyl chain length in this series of compounds should cause an onset of fast dynamics for the hydrogen bonded protons at a lower temperature. Highly mobile hydrogen bonded protons will increase the ionic

conductivity of the electrolyte and at higher temperatures the mechanism of ion exchange becomes easier to observe. The response of the benzimidazole compounds with temperature is summarized in **Figure 7**.

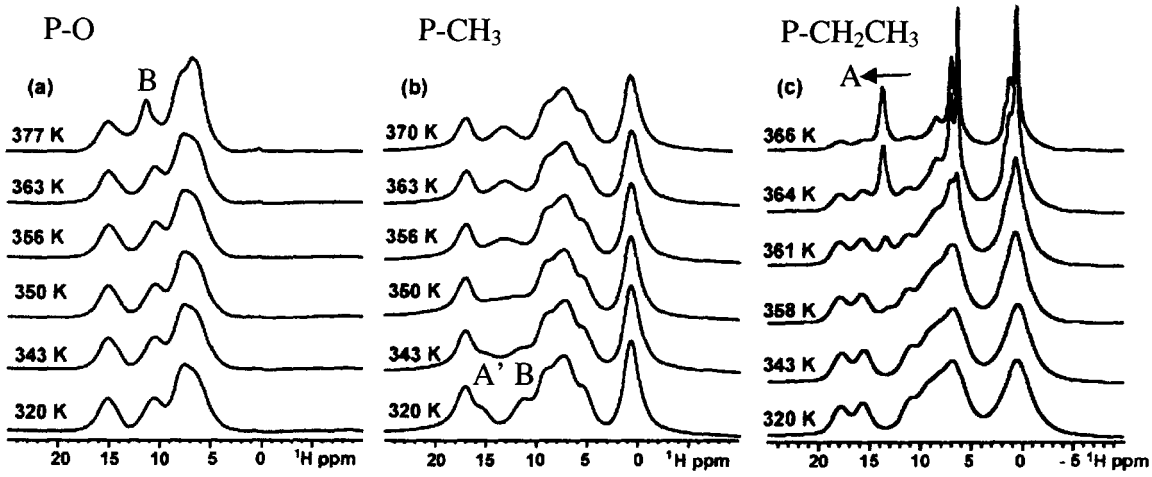

Figure 7 – The ^{1}H variable temperature NMR spectra of the three different benzimidazole compounds arranged with increasing alkyl chain length: (a) Bi-PA, (b) Bi-mPA, (c) Bi-ePA. The spectra show dynamics for Bi-PA only at very high temperatures, a coalescence process for Bi-mPA and Bi-ePA.

The local mobility within these compounds is clearly related to the length of the material's alkyl substitution. For Bi-PA, the maximum temperature of the spectrometer limits the system and the onset of observable local dynamics begins at the O-H∘∘O hydrogen bond in **Figure 7a**. As the temperature increases, the intensity of the spectrum between the hydrogen bonded resonances increases. The onset of coalescence with temperature represents slow (or intermediate) exchange between the two types of hydrogen bonds. However, at higher temperatures a narrow resonance appears at the chemical shift of the O-H∘∘O hydrogen bond. This new resonance indicates that fast exchange occurs between those hydrogen bonds at the elevated temperatures. The strong

hydrogen bonding slows the exchange of the spins between the different hydrogen bonding sites.

In the methyl analogue, the coalescence of the A' and B protons occurs near 356 K, the protons are from the two hydrogen bonds that share the same oxygen atom, as shown in **Figure 7b**. This coalescence shows that the interchange of these two protons is favored in the alkyl analogue. The reorientation of the methyl phosphonate indicates that Grotthuss style transport of protons in these or similar materials is facilitated, via the hydrogen bonding network of the material. The mechanism of ion exchange will involve the exchange between the A' and B hydrogen bonds. From the frequency separation (3.5 kHz) between the A' and B resonances at ambient temperature, we can conclude that the dynamics of the protons have a rate that is greater than the frequency difference between the resonances ($1/\Delta\omega = \tau_c \sim 280\ \mu s$) once coalescence occurs. The absence of the coalescence with resonance A in the observed temperature range for Bi-mPA indicates that there is no motion occurring that would exchange the two N-H$\circ\circ$O hydrogen bonded protons on the benzimidazolium ring. This preliminary data indicates that the dynamics in these salts are dominated by anion motion.

This trend is further reinforced by the variable temperature spectra of the ethyl analogue, shown in **Figure 7c.** Deconvolutions of the ^{1}H NMR spectra show that the new resonance begins near the chemical shift of the O-H$\circ\circ$O hydrogen bond, prior to any narrowing in the aromatic region. As the temperature increases, the resonance shifts towards a higher chemical shift and gains intensity. By 358 K, the new resonance occurs

at the average chemical shift of resonances **A'** and **B**. This implies that the new resonance originates from exchange of spins located in those two sites. At this temperature only a fraction of the anions produce a successful jump which interchanges the spins, represented in the spectrum as the appearance of the new resonance. If only the **A'** and **B** sites were exchanging the coalescence would follow the same pattern as the methyl phosphonate. However, if all three hydrogen bonding resonances were under going coalescence, the new resonance would reach the average chemical shift of all three hydrogen bonded sites. As the chemical shift increases, the contribution of the **A** hydrogen bond to the exchange increases. As the temperature increases past 358 K the new resonance shifts from 13.07 to 13.81 ppm at the temperature of 366 K. By 366 K, the material is nearing its melting point, however, full isotropic rotation is not yet achieved, as the ^{1}H MAS NMR spectrum does not differ significantly from the spectrum at 364 K. At higher temperatures, the resonances narrow considerably, as a result of the fast molecular motions. NMR observes the onset of local dynamics well below the melt transition observed by DSC, at 393 K. This is consistent with the ability of NMR to probe molecular level process before the onset of macroscopic behavior. This is due to either the low thermal barrier of the process or that the motion is too fast to be sampled via a DSC trace.[27, 28] Upon cooling, the material returns to its earlier state and reproduces the spectrum shown in **Figure 4c**. The onset of phosphonate dynamics, followed by the benzimidazole ring reorientation at higher temperatures, gives evidence that the ionic conduction by structural diffusion is present in these compounds.

At higher temperatures the DQ MAS NMR spectrum has only resonances with dipolar couplings that have a lifetime that is longer than the rotor period. Any resonance that does not meet this specification is removed from the DQ MAS NMR spectrum. The new resonance at ~13 ppm in the high temperature Bi-ePA spectra is not present in the 1D ^{1}H-^{1}H DQ MAS NMR spectrum at temperatures above 358 K. Given the MAS frequency of 25 kHz, and a recoupling period of one rotor period, this implies a jump rate between sites of equal to or greater that 40 μs. As the temperature increases beyond 358 K, the benzimidazole ring becomes mobile, which causes the narrowing of the aromatic resonances. The mobility of the aromatic ring at higher temperatures contributes to the exchange of all three hydrogen bonded protons in Bi-ePA.

5.3.2 – Variable Temperature REDOR

The rotational echo double resonance (REDOR) pulse sequence is able to measure the distance between heteronuclear spins. The REDOR signal attenuates with the number of rotor periods. The REDOR exchange curve in **Figure 8** is for the A' and B protons of Bi-mPA and it shows an increased decay of the dipolar coupling with temperature. Fitting of the room temperature REDOR dephasing patterns of protons A' and B suggests that the spins experience dipolar dephasing from more than one coupling partner. The dephasing of the B resonances at room temperature does not fit reliably to a single dipolar coupling and CSA or any combination from multiple sites. This shows that the dephasing required to match the B resonance have more than one dipolar coupling

influencing the REDOR attenuation. The dephasing of the A' resonance at room temperature fit to a single ^{1}H-^{13}P dipolar coupling and CSA. However, the best fit values exceeded the parameters obtained from the static ^{31}P CSA spectrum by 10% and strength of the dipolar coupling by 200Hz (1550 Hz from the X-ray structure). This suggests that the A' proton might be closer to the benzimidazole ring than what the crystallographic data suggests.

At higher temperatures, the amount of dephasing for each spin has increased. The reduced dipolar couplings at 343 K between the A' or B protons and the ^{31}P spin are now identical. After the coalescence process, the REDOR dephasing pattern of the new resonance (A'B) matches the earlier phasing curve of the A' and B protons prior to coalescence of the two resonances. The REDOR sequence is therefore, sensitive to their exchange. Attempts at fitting the dephasing curved proved difficult. No realistic match could be found for the data corresponding to the higher temperature dephasing curves.

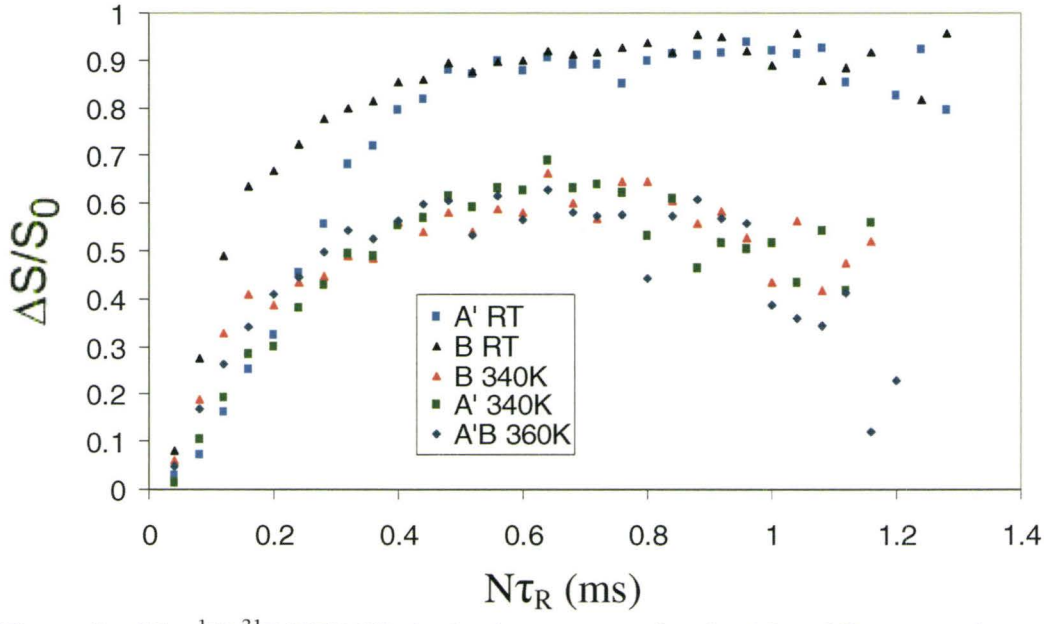

Figure 8 – The ^{1}H-^{31}P REDOR dephasing patterns for the A' and B protons in Bi-mPA at room temperature and 340 K show the decrease in the strength of the dipolar coupling. At room temperature the REDOR dephasing patterns fits to a 95% of the static dipolar coupling. When the temperature is increased the dipolar coupling is reduced. The REDOR dephasing pattern for the coalesced A'B resonance at 356 K show an averaged proton dipolar coupling that is the same as the uncoalesced resonances at 343 K.

5.3.3 - Ionic Conductivity

The overall ionic conductivity depends on many factors and contributions that might not be present in the ^{1}H NMR spectra. The ionic conductivity of the Bi-mPA compound reaches 6.5 x 10^{-7} S/cm by 125°C. This value represents the bulk ionic conductivity and the total contribution from macroscopic defects in the crystallites. The transport of ions in the crystallites face resistance from the space between the particles (grain boundaries) and will decrease the overall conductivity. The Nyquist and the

activation energy data from Bi-mPA in **Figure 9** show an example data set and the increase in the ionic conductivity with temperature for the salt.

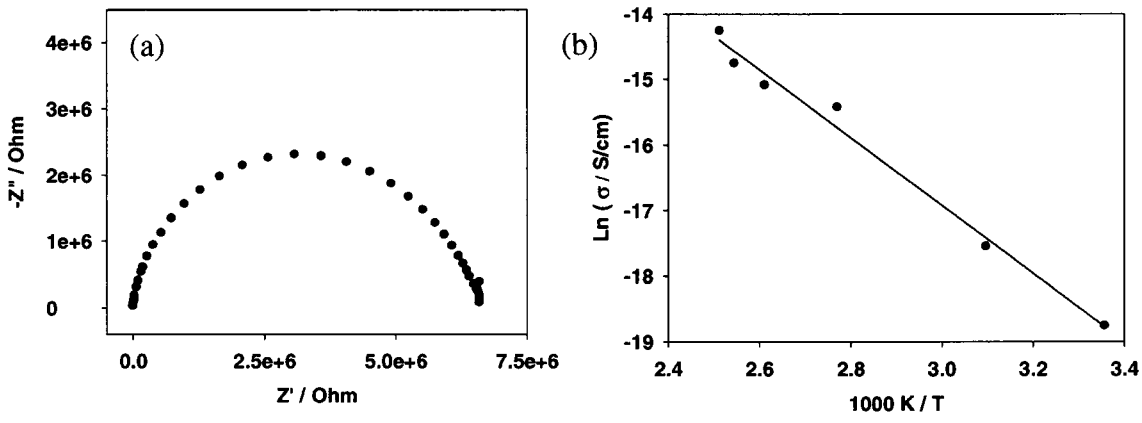

Figure 9 – (a) The Nyquist plot of the conductivity data for Bi-mPA at room temperature. (b) The Arrhenius plot of the ionic conductivity for Bi-mPA up to 125C, the activation energy is 42 ± 2 kJ/mol.

The Nyquist plot shows the total resistance of the cell and the data points on the semi-circle of the plot represents the frequency needed to sample the ionic conductivity. The frequency where the resistance of the cell becomes independent of frequency is near 8 ± 1 Hz. The frequency independence of the impedance signifies the movement of ions through the material.[29] The correlation time for the flow ions at this rate through the bulk material is 125 ms. The activation energy for the ionic conductivity is 42 ± 2 kJ/mol for Bi-mPA and this information does not directly provide any insight on the mechanism of ion conduction. Additionally, the contribution of the resistance from the grain boundary increases the activation energy of the solid and reduces the ionic conductivity. Due to the grain boundary, the activation energy of the bulk conductivity is generally higher than the value obtained by solid-state NMR methods, which only measures the local hindrances to

the movement of ions. The dynamics observed in the ^{1}H variable temperature NMR spectra only give the proton's perspective of the processes involved in the conduction of ions in the solid state. To further investigate the transport of ions in the solid-state, the dynamics of the ions is investigated using multinuclear NMR.

5.3.4 – Cation Dynamics

Having considered the dynamics of the protons in these salts, we now move to quantifying the participation of the benzimidazolium cations. Our preliminary data showed that the benzimidazolium ring flip of was not observed in the variable temperature ^{1}H NMR study due to the lack of coalescence of resonances A with the other hydrogen bonded resonances in Bi-mPA. In comparison the imidazole ring flip in a previous study of imidazolium methane sulfonate occurs with a correlation time of several milliseconds.[16] Here we investigate the cation dynamics using ^{13}C CODEX NMR at ambient temperature, a more complex description of the pulse sequence is given in Chapter 2. The benzimidazolium ring flip is expected to be slower than imidazolium itself because of the attached phenyl ring. The ^{13}C resonance that represents the two carbon atoms that adjoin the imidazole ring to the phenyl was chosen for the data analysis, since these carbon atoms do not have a directly bonded proton and should be least affected by spin diffusion. The ^{13}C CODEX exchange curves of Bi-PA and Bi-mPA are shown in **Figure 10**, respectively. The ^{13}C CODEX exchange curves use six rotor periods to provide adequate dephasing. Further dephasing of the signal resulted in poor

quality spectra. Thus, a small number of rotor periods of dephasing was chosen to determine a correlation time. This limits our ability to determine the number of sites involved in the exchange but it is reasonable to assume that if a reorientation of the ring was occurring, the two-site ring flip of the benzimidazole is the most likely mechanism.

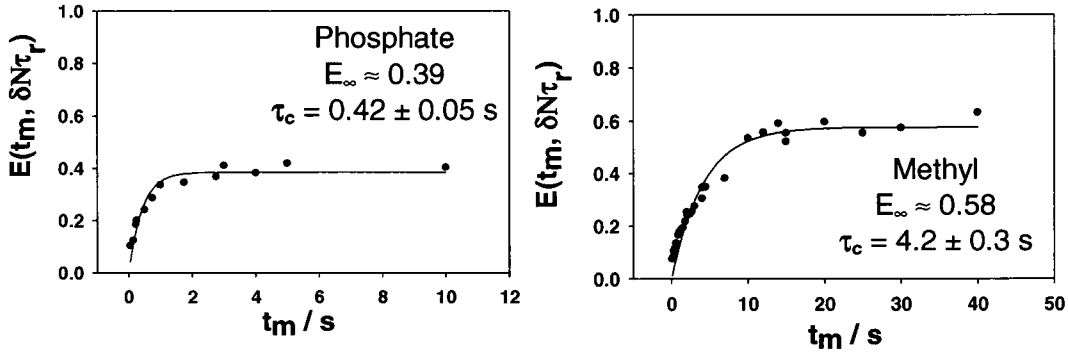

Figure 10 – The ^{13}C CODEX exchanges curves for (a) Bi-PA and (b) Bi-mPA. The single exponential fit for the two data sets yielded time constants of 0.42 ± 0.05 s for Bi-PA and 4.2 ± 0.3 s for Bi-mPA.

The exchange curves of the two compounds show a very slow build up and the attenuation only reaches the plateau for Bi-mPA near a mixing time of 12 s. The correlation time of the two exchange curves are 0.42 ± 0.05 s for Bi-PA and 4.2 ± 0.3 s for Bi-mPA. The correlation times are not attributed to the benzimidazole ring flip but instead the observed dephasing is due to spin diffusion due to the magnitude of the correlation times. Spin diffusion is a type of exchange that occurs when two dipolar coupled spins possess a I_Z state during the mixing time. Spin diffusion is when the magnetization of one spin influences a neighboring spin through flip-flop term of the dipolar Hamiltonian and causes the magnetization to relax. This type of exchange

mechanism is different from the rotation of the ring as it involves no motion of the benzimidazole ring. The presence of an earlier plateau is not observed for either compound, implying that the benzimidazolium ring does not flip on this timescale. If the ring flip does occur, it is on the same time scale as the spin diffusion, which is on the order of seconds.

The presence of spin diffusion in these samples also explains the plateau values of the exchange curves. The spins decay to an equilibrium state during the mixing time due to spin diffusion and this is measured as the correlation time. The value of the plateau in either case would then be dependent on magnitude of the spin diffusion. Several factors like the number of spins and their distance from the ^{13}C resonance will affect the decay measured by ^{13}C CODEX NMR. The long correlation time for the measured ^{13}C CODEX data for both benzimidazole model compounds are in dramatic contrast of the imidazole methane sulfonate compound which was reported to have a correlation time of 29 ± 1 ms at 274 K.[16] Therefore, the addition of the phenyl group to the imidazole ring serves to immobilize the cation in the benzimidazole compounds. Hence, we are able to surmise that the benzimidazole based polymers do not utilize the benzimidazole ring reorientation in their proton transfer process. The slow correlation times of the benzimidazole rings imply that the major contributor to the ionic conductivity in a benzimidazole based polymer is exclusively the phosphoric acid electrolyte. Further, these experiments show that reduction in hydrogen bonding at the anion or tethering the anion to the polymer backbone will not substantially impede proton transport. For

imidazole based polymers (as will be seen in the next Chapter), proton diffusion through the structure by the two-site ring flip is a significant mechanistic step, with a timescale appropriate for contributing to long-range transport, whereas this is not the case for the benzimidazole-based polymers.

5.3.5 – Anion Dynamics

The CODEX experiment indirectly confirmed that the benzimidazole rings did not rotate, and the second application of the pulse sequence is to look at the dynamics of the anion itself. The ^{31}P CODEX signal for Bi-PA (**Figure 11a**) attenuates to 74% after five rotor periods of dephasing. This attenuation corresponds to a four site reorientation of the phosphate tetrahedra. This motion is illustrated in **Figure 12a**. The reorientation of the phosphate anion involves an exchange of the two non-equivalent sites, and a three-dimensional rotation. The amount of dephasing needed to reach a plateau is determined by the structures themselves, and the amplitudes of the reorientational motion involved. Significant changes in the orientation of the CSA are known to rapidly dephase the CODEX signal, while small or large motions (via symmetry) that do not significantly change the orientation of the CSA, and therefore require long dephasing periods.[30] Thus, only five rotor periods of attenuation are required to reach the plateau for the phosphate exchange, consistent with the large amplitude of the reorientation involved.

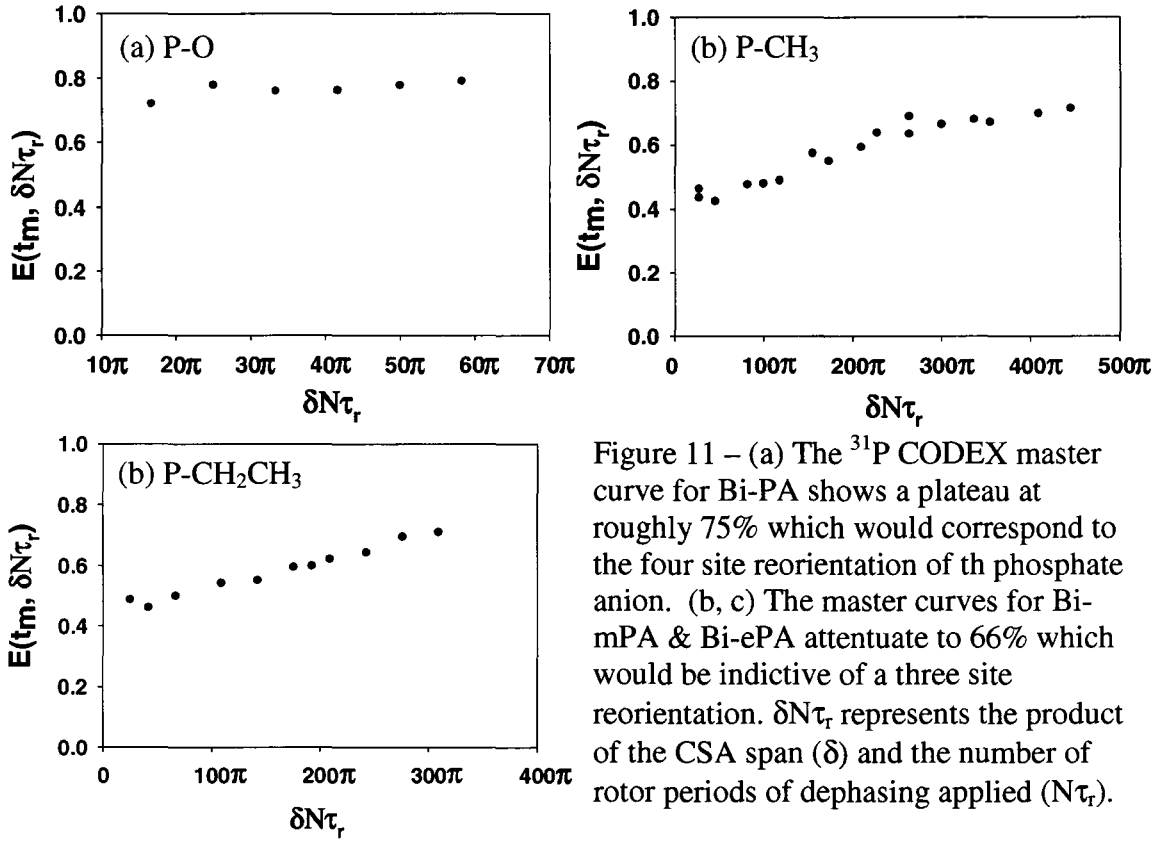

Figure 11 – (a) The ^{31}P CODEX master curve for Bi-PA shows a plateau at roughly 75% which would correspond to the four site reorientation of th phosphate anion. (b, c) The master curves for Bi-mPA & Bi-ePA attentuate to 66% which would be indictive of a three site reorientation. $\delta N\tau_r$ represents the product of the CSA span (δ) and the number of rotor periods of dephasing applied ($N\tau_r$).

The master curve for the Bi-mPA (**Figure 11b**) shows the attenuation of the ^{31}P CODEX signal to 63% after 25 rotor periods of dephasing, which can be attributed to the three site rotation of the methyl phosphonate. The restricted motion of the ^{31}P site for Bi-mPA indicates that the CSA rotates only about the C_{3v} axis, as shown in **Figure 12b**. The Bi-ePA compound also requires many rotor periods of dephasing to observe a significant amount of dephasing, shown in **Figure 11c.** The dephasing plot for the ^{31}P CODEX NMR of Bi-ePA reaches 70% after 26 rotor periods, just above the 66% required for a three-site reorientation. The ethylphosphonate has a three-site motion like the methylphosphonate, in **Figure 12b** and rotates on the C_{3v} axis of the phosphonate.

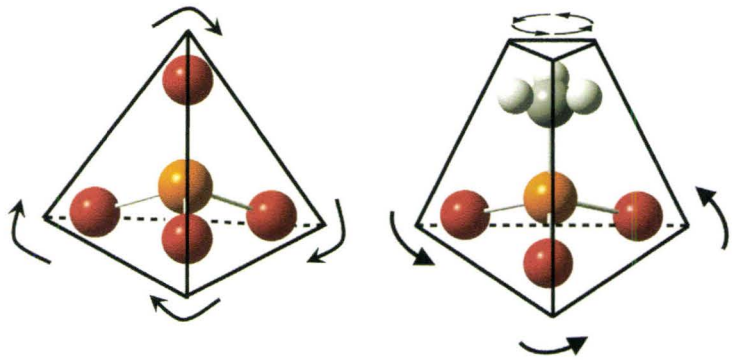

Figure 12 - The rotation of the phosphorus groups are different due to the hydrogen bonds and the structure of the two anions. The phosphate of Bi-PA (a) can be considered a tetrahedron rotating at the center, while the phosphonate of Bi-mPA (b) can be viewed like a tetrahedron rotating along the C_{3v} axis of the methylphosphonate.

The hydrogen bonding for the methyl phosphonate anion occurs in a single plane perpendicular to the rotation axis; when switching between these similar environments, the apparent change of the ^{31}P CSA is small and thus a large amount of dephasing is required to reach the defined plateau. For the three model compounds studied here, the ambient temperature static powder patterns for the ^{31}P sites produce nearly symmetrical CSAs, with the Bi-mPA salt having a larger asymmetry parameter than its Bi-PA counterpart, the powder patterns are shown as **Figure 13**. The ethylphosphonate requires more rotor periods of dephasing than the methylphosphonate because the width of the ^{31}P power pattern is less for the ethylphosphonate.

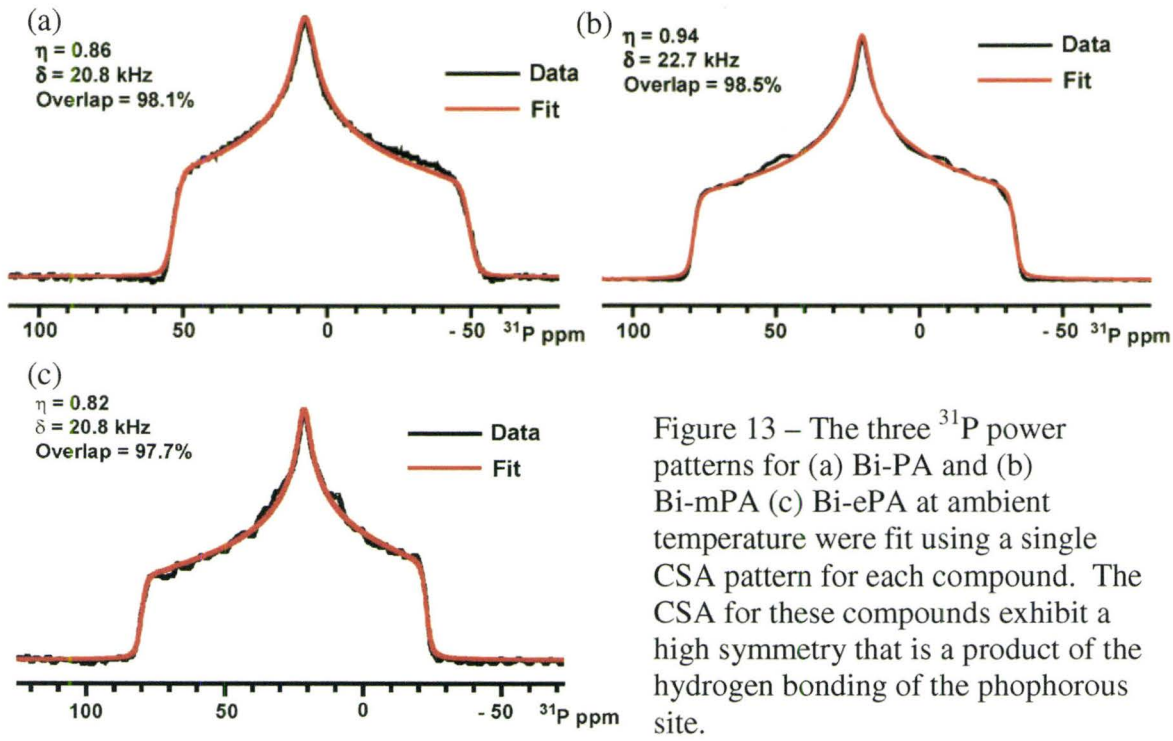

Figure 13 – The three ^{31}P power patterns for (a) Bi-PA and (b) Bi-mPA (c) Bi-ePA at ambient temperature were fit using a single CSA pattern for each compound. The CSA for these compounds exhibit a high symmetry that is a product of the hydrogen bonding of the phophorous site.

The CSA parameters are η = 0.86 and a δ = 20.8 kHz for Bi-PA and η = 0.94 and a δ = 22.7 kHz for Bi-mPA and η = 0.82 and a δ = 20.8 kHz for Bi-ePA. These CSA values are used to determine the x-axis of the data in **Figure 11**, where $\delta N\tau_r$ represents the product of the CSA span (δ) and the number of rotor periods of dephasing applied ($N\tau_r$).

To measure the reorientation rates of the different anions the ^{31}P CODEX exchanges curves were constructed by varying the mixing time while holding the amount of dephasing constant, at the values established in the preceding section. The ^{31}P CODEX exchange curves of the three types of phosphonates are shown as **Figure 14**, respectively. The exchanges curves have been fitted to single exponentials to produce a

correlation time for each reorientation. The room temperature correlation time for Bi-PA is 56 ± 3 ms while the correlation time for Bi-mPA is 75 ± 6 ms and 101 ± 5 ms for Bi-ePA. The decrease in correlation time for the methyl phosphonate is somewhat surprising, since this anion has two fewer hydrogen bonds than the phosphate analogue. From this, we conclude that the bifurcated hydrogen bonds are somewhat weaker than their single hydrogen-bonding counterpart and are therefore more easily broken and reformed. This is also seen in the relative chemical shifts of the hydrogen bonded protons, where the single hydrogen bond, A, in Bi-mPA is observed at the highest frequency shift of 17 ppm.

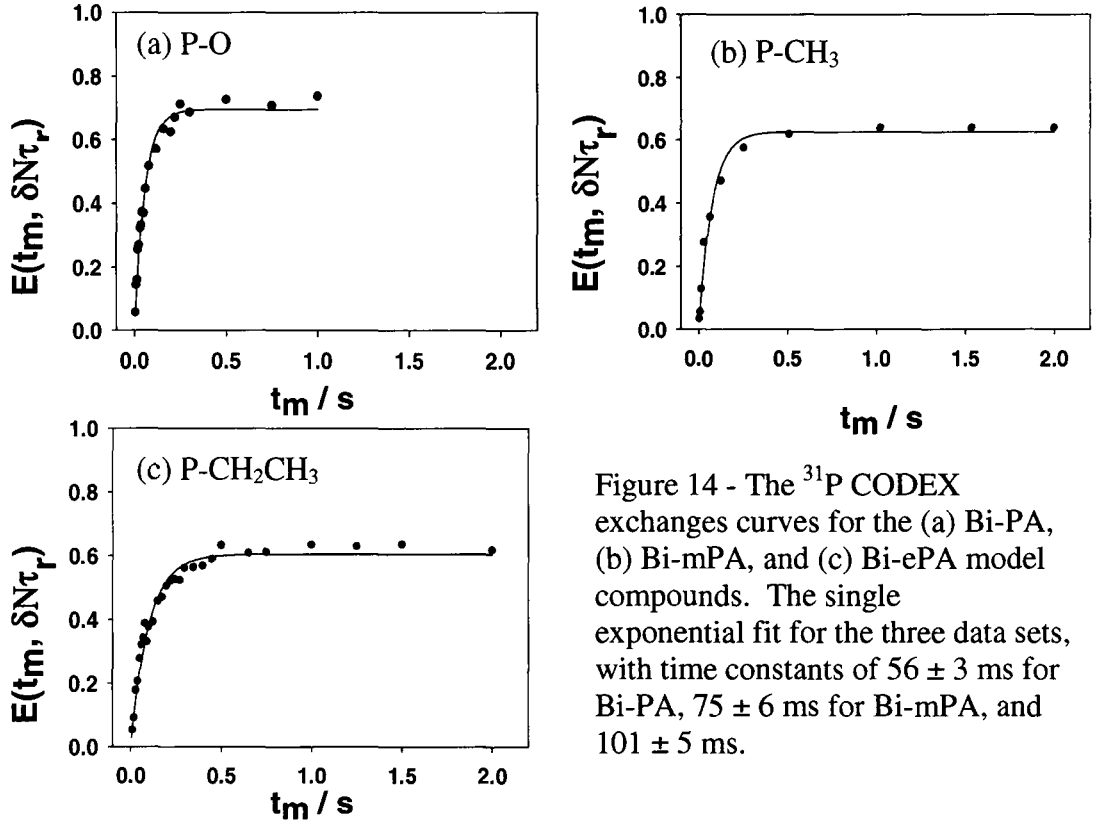

Figure 14 - The ^{31}P CODEX exchanges curves for the (a) Bi-PA, (b) Bi-mPA, and (c) Bi-ePA model compounds. The single exponential fit for the three data sets, with time constants of 56 ± 3 ms for Bi-PA, 75 ± 6 ms for Bi-mPA, and 101 ± 5 ms.

The CODEX data shows that the methyl phosphonate anion and phosphate itself are very similar in the timescales of their molecular level dynamics. This anion reorientation is proposed to be a key step in the proton transport mechanism. The mechanism is explored further below. The correlation times from the fits reveal that, as the length of the chain increases, the rotation of the phosphate is slowed. The phosphate, having no constraints on the type or direction of the isotropic reorientation of the tetrahedron, has the quickest reorientation time, while the restriction to an anisotropic three-fold motion slows the alkyl phosphonates. Variable temperature data supports the conclusion that the motion of the ethyl phosphonate possess the lowest activation energy. The phosphate will have the highest of the materials studied here, as evident from their variable temperature response observed in **Figure 7**. In **Figure 15**, the trend of the ^{31}P CODEX NMR for Bi-mPA and Bi-ePA follows the predicted trend. The activation energy for Bi-ePA is 3.2 ± 0.3 kJ/mol, while Bi-mPA is 7 ± 1 kJ/mol. The low activation energy for the ethylphosphonate shows that the motion of the phosphonate has little restriction to the rotation, while the methylphosphonate will have a higher barrier for the rotation. This shows that the methylphosphonate will require higher temperatures to activate the rotation.

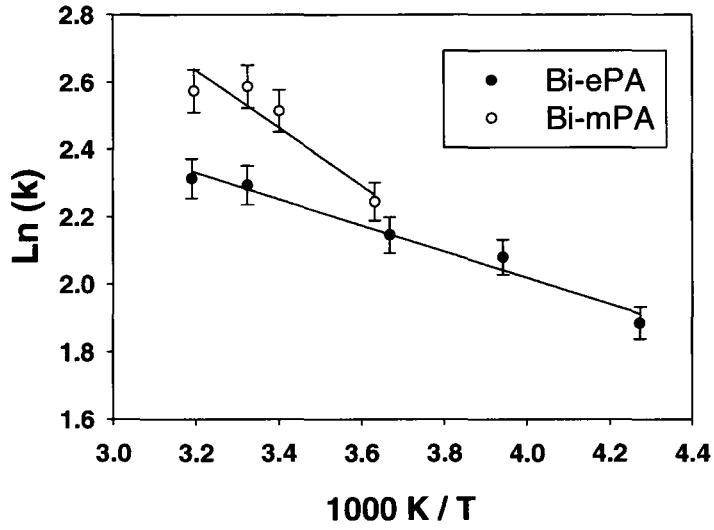

Figure 15 – The Arrhenius activation energy plot of the ^{31}P CODEX NMR data for Bi-mPA and Bi-ePA. The activation energy for Bi-mPA is 7 ± 1 kJ/mol and 3.2 ± 0.3 kJ/mol for Bi-ePA.

The ^{31}P variable temperature CODEX NMR data implies that the tethered phosphonate will not inhibit structural diffusion driven conductivity mechanisms of the polymer by any significant amount. The increased dynamics of the alkyl phosphonates at higher temperatures may lead to higher ionic conductivity and would mean that any polymer membrane based on the phosphonate may have increased performance at higher temperatures relative to the acid salt. Tethering the phosphate does limit the group's ability to provide a second mechanism of conductivity by vehicle transport, however, increasing the chain length may improve this mode of conductivity.

5.4 – Mechanism of Ion Conduction

The mechanism of proton transport for crystalline Bi-mPA is developed based on the combination of the ^{1}H NMR and multinuclear CODEX data and is shown in **Figure 16**. A 2D excerpt of the crystal structure is used to illustrate the transport process. From the ^{1}H NMR variable temperature spectra we know that the mechanism involves exchange between protons A' and B, leaving proton A unchanged. From the ^{31}P CODEX data, the rotation of the phosphonate must be three-fold. The mechanism described here gives the elementary steps involved in anion reorientation, which altogether (a-e) total the correlation time measured by ^{31}P CODEX, or similarly, ^{1}H coalescence, as observed at elevated temperatures. **Figure 16a** shows the static crystal structure before any proton migration begins. The view presented is looking down the C_{3v} axis of the phosphonate groups, where the methyl groups are not shown for simplicity. For proton transfer to occur proton A' (shown in white) moves to its nearest oxygen atom, as in **Figure 16b**. Subsequently, the adjacent phosphonate anions counter-rotate in an interlocking cogwheel fashion, to provide a free oxygen center for the A' proton. This proton transfer between the phosphonates is paused in mid-rotation in **Figure 16c**. The phosphonate anions rotate such that the protons zig-zag through the structure; this pathway is highlighted by the green arrows. In **Figure 16d** proton B (shown in green) is nearing the benzimidazole ring and proton A' begins to form the O-H$\circ\circ$O hydrogen bond. The final step returns the system to its equilibrium state, shown in **Figure 16e** where proton A' and B have exchanged places. Thus, **Figure 16a** and **Figure 16e** represent identical

structures, where the color coding of the protons simply allows us to follow the proton path through the structure. The mechanism of proton conduction for Bi-ePA follows the same general description until higher temperatures where the ring flip motion would start to participate and exchange the A and A' protons.

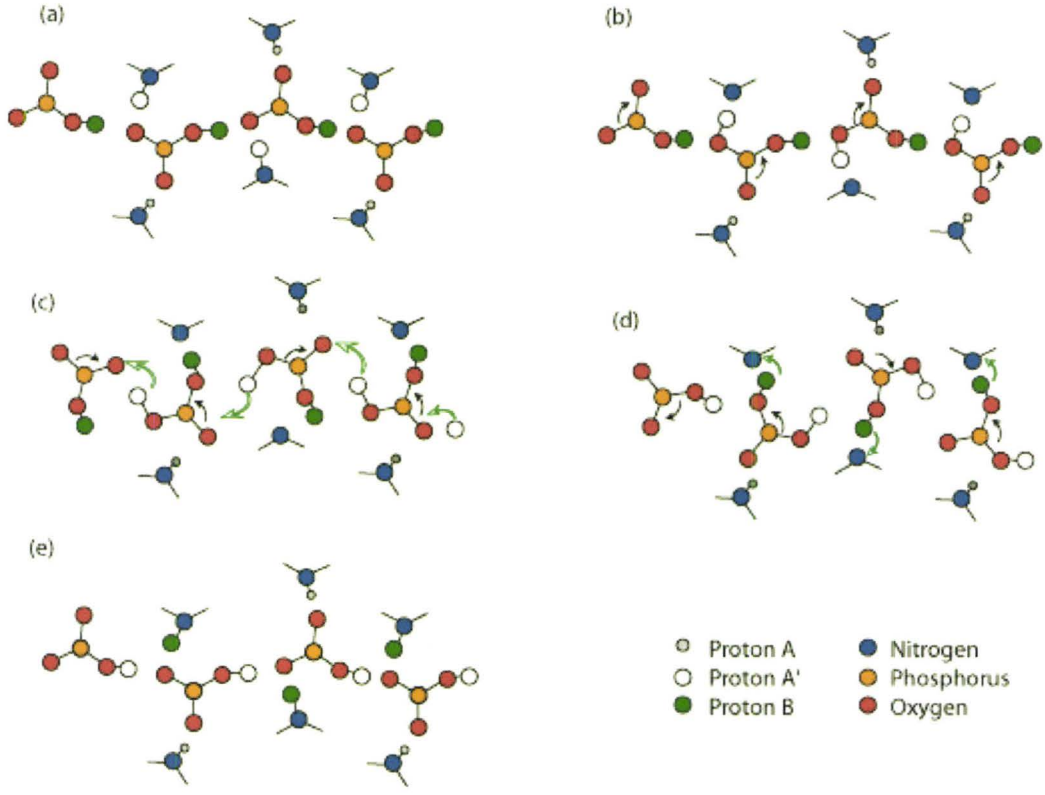

Figure 16 - The mechanism of proton transport for Bi-mPA is based on the ^{1}H MAS variable temperature data and multinuclear CODEX data. Black Arrows represent rotation of the phosphonate anion and green arrows represent protons jumping from one anion to another.

5.5 - Summary

The three model compounds, Bi-PA, Bi-mPA, and Bi-ePA have unique hydrogen bonding structures, which are determined through the combination of X-ray diffraction and high-resolution solid-state ^{1}H MAS NMR. The ^{31}P CODEX studies of these model compounds showed that the phosphate undergoes four-site reorientation whereas the alkyl phosphonate showed only a three-site reorientation. This rotation allows two dimensional diffusion of the protons along a zig-zag pathway, as illustrated in the model. In contrast, the free phosphate facilitates a more isotropic motion of the protons in three dimensions. The ^{31}P CODEX results conclude that the effect of binding the phosphonate group to the backbone of a polymer slows down the rotational diffusion of the protons, but allows significant local dynamics, as observed in the phosphonate model salts. Attaching the acid group to the backbone prevents any translational diffusion of the group but does not impede the ability of the phosphonate to undergo a reorientation. The rotational motion of the anions greatly outpaces any contribution of backbone dynamics by the benzimidazole ring, and therefore the former is the dominant mechanism of proton transport and is supported by the relative correlation times of benzimidazole versus imidazole, characterized by ^{13}C CODEX NMR. To increase the ionic conductivity of the tethered phosphonates and anyhydrous polymers, the mobility of the ionic species has to offset the loss of the translational mechanism of from the liquid electrolyte.

5.7 – References

1. R. Bouchet and E. Siebert, *Solid State Ionics*, 1999, **118**, 287-299.
2. M. E. Schuster and W. H. Meyer, *Annu. Rev. Mater. Res.*, 2003, **33**, 233-261.
3. Q. Li, R. He, J. O. Jensen and N. J. Bjerrum, *Fuel Cells* 2004, **4**, 147-159.
4. Y. J. Lee, B. Bingol, T. Murakhtina, D. Sebastiani, W. H. Meyer, G. Wegner and H. W. Spiess, *J. Phys. Chem. B*, 2007, **111**, 9711-9721.
5. H. Pu, W. H. Meyer and G. Wegner, *Macromol. Chem. Phys.*, 2001, **202**, 1478-1482.
6. A. Bozkurt and W. H. Meyer, *Solid State Ionics*, 2001, **138**, 259-265.
7. A. Bozkurt and W. H. Meyer, *J. Polym. Sci.*, 2001, **39**, 1987-1994.
8. Y. L. Ma, J. S. Wainright, M. H. Litt and R. F. Savinell, *J. Electrochem. Soc.*, 2004, **151**, A8-A16.
9. R. H. He, Q. F. Li, J. O. Jensen and N. J. Bjerrum, *J. Polym. Sci., Part A: Polym. Chem.*, 2007, **45**, 2989-2997.
10. S. K. Kim, T. H. Kim, J. W. Jung and J. C. Lee, *Polymer*, 2009, **50**, 3495-3502.
11. Z. G. Qi and S. Buelte, *J. Power Sources*, 2006, **161**, 1126-1132.
12. R. H. He, Q. T. Che and B. Y. Sun, *Fiber. Polym.*, 2008, **9**, 679-684.
13. J. Emsley, N. M. Reza, H. M. Dawes, M. B. Hursthouse and R. Kuroda, *Phosphorus and sulfur and the related elements*, 1988, **35**, 141.
14. A.-R. Grimmer, A. Kretschmer and V. B. Cajipe, *Magnetic Resonance in Chemistry*, 1997, **35**, 86-90.
15. G. J. M. P. van Moorsel, E. R. H. Vaneck and C. P. Grey, *J. Magn. Reson., Ser. A*, 1995, **113**, 159-163.
16. I. Fischbach, H. W. Spiess, K. Saalwaechter and G. R. Goward, *J. Phys. Chem. B*, 2004, **108**, 18500-18508.
17. K. Schmidt-Rohr, E. R. de Azevedo and T. J. Bonagamba, *Encyclopedia of Nuclear Magnetic Resonance*, 2002, **9**, 633-642.
18. D. Reichert, T. J. Bonagamba and K. Schmidt-Rohr, *J. Magn. Reson.*, 2001, **151**, 129-135.
19. D. A. Boysen, S. M. Haile, H. Liu and R. A. Secco, *Chem. Mater.*, 2003, **15**, 727-736.
20. I. Schnell, S. P. Brown, H. Y. Low, H. Ishida and H. W. Spiess, *J. Am. Chem. Soc.*, 1998, **120**, 11784-11795.
21. J. Dunkers, E. A. Zarate and H. Ishida, *J. Phys. Chem.*, 1996, **100**, 13514-13520.
22. B. Berglund and R. W. Vaughan, *J. Chem. Phys.*, 1980, **73**, 2037-2043.
23. D. Sebastiani, G. Goward, I. Schnell and H. W. Spiess, *THEOCHEM*, 2003, **625**, 283-288.
24. S. P. Brown, I. Schnell, J. D. Brand, K. Mullen and H. W. Spiess, *J. Mol. Struct.*, 2000, **521**, 179-195.
25. G. Ye, N. Janzen and G. R. Goward, *Macromolecules*, 2006, **39**, 3283-3290.

26. T. M. Alam, M. Nyman and S. K. McIntyre, *J. Phys. Chem. A*, 2007, **111**, 1792-1799.
27. D. C. Watts and A. J. Cash, *Meas. Sci. Technol.*, 1991, **2**, 788-794.
28. S. C. Clark, C. E. Hoyle, S. Jonsson, F. Morel and C. Decker, *Polymer*, 1999, **40**, 5063-5072.
29. F. E. Salman, N. Shash, H. Abou El-Haded and M. K. El-Mansy, *J. Phys. Chem. Solids*, 2002, **63**, 1957-1966.
30. E. R. de Azevedo, W. G. Hu, T. J. Bonagamba and K. Schmidt-Rohr, *J. Am. Chem. Soc.*, 1999, **121**, 8411-8412.

Chapter 6: Solid Organic Electrolytes: Imidazole

This chapter continues to investigate the solid organic electrolytes based on acidified polybenzimidazole and attempts to understand the effect of replacing benzimidazole with imidazole. This body of work is from a publication that was featured in Physical Chemistry Chemical Physics. The second author of the paper was Gillian R. Goward who revised and edited the final text. My contributions to this chapter are the synthesis, collection, and interpretation of all of the data relating to the solid organic electrolytes. The rotation of the benzimidazole ring only occurs at the onset of liquid like dynamics near the melting point of a material. To increase this mode of ion transport a smaller imidazole ring replaces the benzimidazole ring to improve the kinetics of the ring. This should improve the ionic conductivity of the complex and introduce a second pathway for ion transport. The dynamics of the cation and anion are a priority with a focus on using solid-state nuclear magnetic resonance (NMR) to discover the mechanism of ion conduction.

6.0 – Introduction

Proton exchange membrane based fuel cells would benefit from higher operating temperatures, as this would reduce catalyst poisoning.[1-3] Deviation from the heavily humidified environment results in a loss in performance, particularly if a significant

amount of hydration is lost.[4, 5] However, operation of a PEM fuel cell above 120°C increases catalyst longevity by mitigating the binding of carbon monoxide to the platinum catalyst at high temperatures.[6, 7]

A proposed approach to eliminating the liquid electrolyte is to attach the protic groups of the liquid electrolyte to the backbone of the polymer, such that only chemical decomposition would result in a loss of ion carriers.[8-16] The chemical structures of several successful copolymer electrolytes are shown in **Figure 1**.

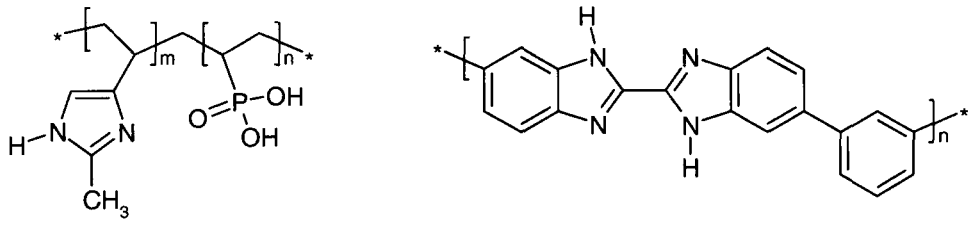

Figure 1 - The chemical structures of vinylphosphonic acid and 4-vinylimidazole copolymer (left) and poly benzimidazole (right).

The large benzimidazole ring of polybenzimdiazole (PBI) does not contribute to the dynamics of the polymer and the trend in the literature is towards smaller ring sizes. The combination of vinylphosphonic acid and 4-vinylimidazole produced a copolymer (VPA-co-4-VIm) with the protogenic groups tethered to the backbone of the polymer.[10] The anhydrous copolymer membrane VPA-co-4-VIm achieved ionic conductivities ranging from 10^{-6} to 10^{-12} S/cm over the temperature range of 5-140°C using different ratios of vinyl phosphonate and vinyl imidazole.[10] Another example of a dry polymer electrolyte is a copolymer of vinyl triazole and vinyl phosphonic acid which had a dry ionic

conductivity ranging from 10^{-3} to 10^{-4} S/cm.[17] The dry conductivities of these polymer electrolytes are lower than the fully acid-doped PBI at equivalent temperatures. More recently, a similar approach using a tethered triazole ring to a polysiloxane backbone yielded ionic conductivities reaching 10^{-5} S/cm at 140°C.[16] Dry polymer electrolytes require significant thermal energy to produce molecular motion, which facilitates long-range transport through the membrane. Thus, the dry polymer electrolytes are particularly favourable for high-temperature applications.

The disparity in the ionic conductivity between the wet and dry polymer material occurs due to the differences in the mechanisms of ionic conductivity. In PBI, the liquid electrolyte is able to diffuse through the polymer with ease as the phosphoric acid provides an exchange mechanism between molecules of the liquid electrolyte for the conduction of protons.[18-20] In contrast, in the dry copolymer membranes, the mechanism of the ionic conductivity is limited to structural diffusion.[8, 21] The protogenic groups of the dry copolymers form a network of hydrogen bonds that are the pathways for the conduction of protons.[17] Transport of the protons therefore must occur via backbone motion of the polymer or rotation of the protogenic groups. The lack of a liquid phase in VPA-co-4-VIm reduces the ionic conductivity, presumably due to the lack of a vehicular transport process and forces the polymer to use a structural mechanism of ionic conductivity.[10] The mechanism of proton conduction in phosphoric acid impregnated PBI was investigated by NMR using model compounds in the previous chapter, benzimidazole phosphate (Bi-PA), benzimidazole methylphosphonate (Bi-mPA), and

benzimidazole ethylphosphonate (Bi-ePA) to represent the polymer system.[22] For these compounds it was found that the ring does not rotate at room temperature, while the anion does. This chapter will investigate the mechanism of proton conductivity in imidazole methylphosphonate, a model salt of the VPA-co-4-VIm polymer. The application of solid state NMR to the model salts will distinguish the contributions of the hydrogen bonding motifs, and identify the role of the anion and cation participants in the proton transport of various polymer electrolytes. Hydrogen bonding plays a crucial role in the anhydrous conductivity of a phosphorous based polymer, thus ^{1}H solid-state NMR is well suited to study a strongly hydrogen bonded polymer system.[9, 23] Solid state NMR is a technique that can probe the local environment of the hydrogen nucleus and provide information on the dynamics and structure of the material on a molecular level.[24] The majority of the methods employed in this chapter are described in Chapter 2.

In the case of ^{1}H resonances, the major contribution to the linewidth is homonuclear dipolar couplings. Frequency switched Lee-Goldburg (FSLG) homonuclear decoupling schemes reduce the effect of dipolar broadening in the spectrum.[25, 26] When applied during the t_1 evolution period of a heteronuclear correlation, a high resolution ^{1}H NMR spectrum is observed in the indirect dimension. In many cases, improved chemical shift resolution is achieved. In the case of a disordered material, heterogeneous broadening caused by a chemical shift distribution limits the degree to which the resolution of the spectrum is enhanced by FSLG decoupling. Thus, this pulse sequence is

used in the present study to distinguish broadening due to strong couplings from chemical shift dispersion as a result of structural inhomogeneity.

6.1 - Experimental

^{15}N labeled imidazole, natural abundance imidazole, and methylphosphonic acid were purchased from Sigma Aldrich. The imidazolium methylphosphonate powder was prepared by mixing stoichiometric amounts of each ion in the minimum amount of methanol needed to dissolve each component. Evaporation of the solvent yielded clear crystals that were subsequently ground and further dried at 70-80°C to remove trace amounts of methanol.

The NMR experiments were conducted on an Bruker 500 MHz Avance system using double resonance probes that support rotors with an outer diameter of 2.5 mm or 4 mm at 25 kHz and 10 kHz MAS, respectively. All high-resolution ^{1}H NMR was carried out using a 90° pulse width of 2.5 μs on the 2.5 mm probe. The ^{13}C & ^{31}P CODEX experiments were acquired using 8 μs recoupling pulses and 3000 μs contact pulses to ensure saturation of the desired nucleus. ^{13}C CODEX analysis of the ^{15}N labeled sample required long acquisition times of ~ 3-6 hours per mixing time, due to the limited amount of ^{15}N labeled sample. Isotropic enrichment of the nitrogen atoms in imidazole was used to reduce any additional dephasing caused by dipolar-induced relaxation.[27] Additional dephasing could alter the observed correlation time and plateau of the exchange curve.

The on-resonance field for the FSLG decoupling was set to 83.3 kHz while the off-resonance fields were ± 58.9 kHz with a 2 kHz asymmetric offset. The scaling factor for the indirect dimension was set to 0.578. Contact pulses of 3000 μs were used to acquire the 1D CPMAS experiments. Temperature calibration of the MAS probes was performed using a sample of samarium stannate.[28]

An Autolab PGSTAT 30 was used to measure the AC impedance of a two-electrode cell, frequency range used was 500 kHz down to 0.1 Hz. The pellet had a thickness of 0.175 cm with a radius of 0.476 cm. The sample was allowed to equilibrate at a given temperature for a minimum of 4 hours between impedance measurements.

6.2 – Results and Discussion

6.2.1 - Structure

Imidazole methylphosphonate was chosen to model the hydrogen bonding donor and acceptor sites of the copolymer vinyl imidazole vinyl phosphonate to gain insight into the relative ionic conductivity of the polymer when compared to other proton exchange membranes. In a previous study, Fischbach *et al.* investigated the ring flip motion of the imidazole methylsulfonate (Im-SA) analogue of imidazole methylphosphonate (Im-mPA).[29] The structural similarity of the two compounds suggests the ring flip mechanism is likely present in the phosphonate derivative, and the ring flip was verified by ^{13}C & ^{15}N variable temperature NMR for Im-SA.[29] However, the number of hydrogen bond acceptor sites is known to play a significant role in the

crystal packing. The two salts differ in their hydrogen bonding motifs (**Figure 2**), with an additional hydrogen bonding donor atom in the methylphosphonate anion compared to a single hydrogen bonding donor atom in methylsulfonate. This results in shared hydrogen bonding protons between multiple sites, and influences the dynamics of the two salts, as seen below.

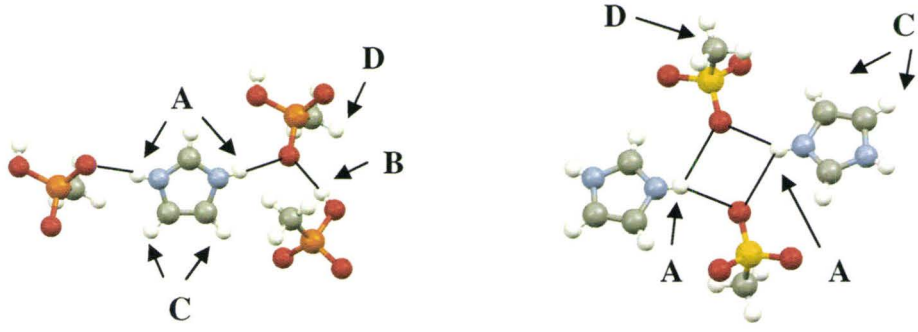

Figure 2 - The hydrogen bonding in the structures of Imidazole methylphosphonate (Im-mPA) (left) and imidazole methylsulfonate (Im-SA) (right).

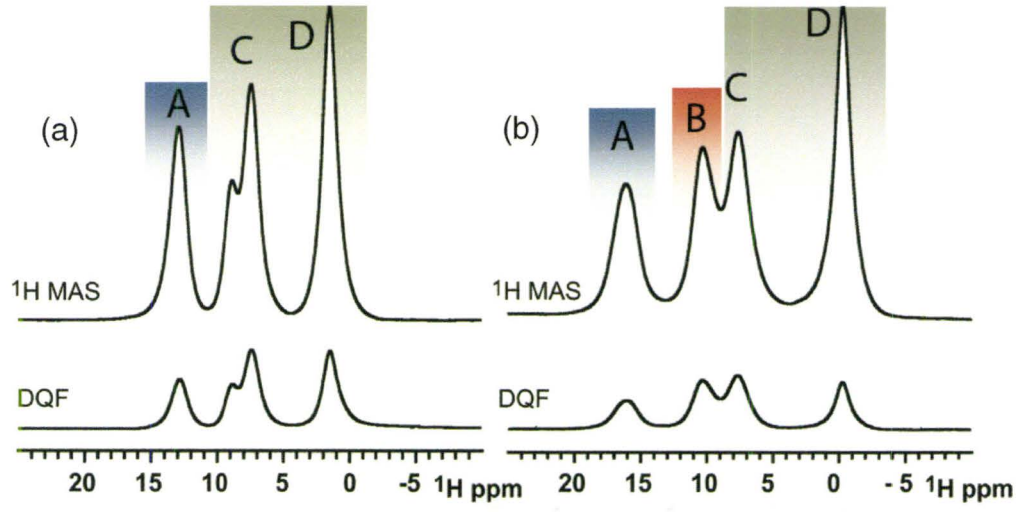

Figure 3 - (a) The ^{1}H MAS NMR spectrum of Im-mPA (above) and the corresponding ^{1}H-^{1}H DQF NMR spectrum (below). (b) The corresponding ^{1}H MAS NMR and ^{1}H-^{1}H DQF NMR spectrum for Im-SA. All spectra were acquired at 25 kHz MAS.

The ^{1}H MAS spectra (above) and DQF spectra (below) are shown in **Figure 3** for the two compounds. The ^{1}H MAS NMR spectra reveal the different proton chemical environments of the salts, Im-mPA and Im-SA. The chemical shift of the two N-H∘∘O hydrogen bonded protons occur at the same position since similar nitrogen to oxygen distances are found in the crystal structures. The chemical shift of a hydrogen bond is determined primarily by the two electronegative atoms, which control the bond lengths and local packing of the imidazole ring.[30] The O-H∘∘O hydrogen bond has a lower chemical shift compared to N-H∘∘O hydrogen bonds, which arises from reduced hydrogen bond strength.[31] Furthermore, the chemical shift assignment is similar to the Bi-PA analogue compound due to their similar number of hydrogen bonding donor and acceptor sites.

Resonances in the ^{1}H-^{1}H DQF spectra arise from double quantum coherence between spins with homonuclear dipolar couplings on the time scale of the MAS frequency. If a spin experiences an attenuated dipolar coupling due to mobility, the reduction in the strength of the dipolar coupling lowers the intensity of the recoupled resonance. For mobile protons, which experience motionally averaged dipolar couplings, the BABA pulse sequence cannot successfully recouple any intensity due to the poor excitation efficiency for weakly coupled species. In **Figure 3,** the DQF spectrum closely resemble the ^{1}H MAS spectrum of each compound respectively. The degree of signal attenuation in the DQF spectra which were recoupled for one rotor period, at 25 kHz MAS, is equivalent. Additional rotor periods of recoupling show a collective decrease in

signal suggesting molecular dynamics, which lead to attenuated dipolar couplings. Further consideration of the dynamics in these materials is provided below.

The 2D ^{1}H-^{1}H DQC spectrum correlates homonuclear spin pairs and separates the couplings based on the chemical shift of the resonances (**Figure 4**). It is not uncommon to observe all possible spin pairs in densely packed organic salts. In this case, Im-mPA is a tightly packed lattice, and the observed spin pairs are summarized in **Table 1**.

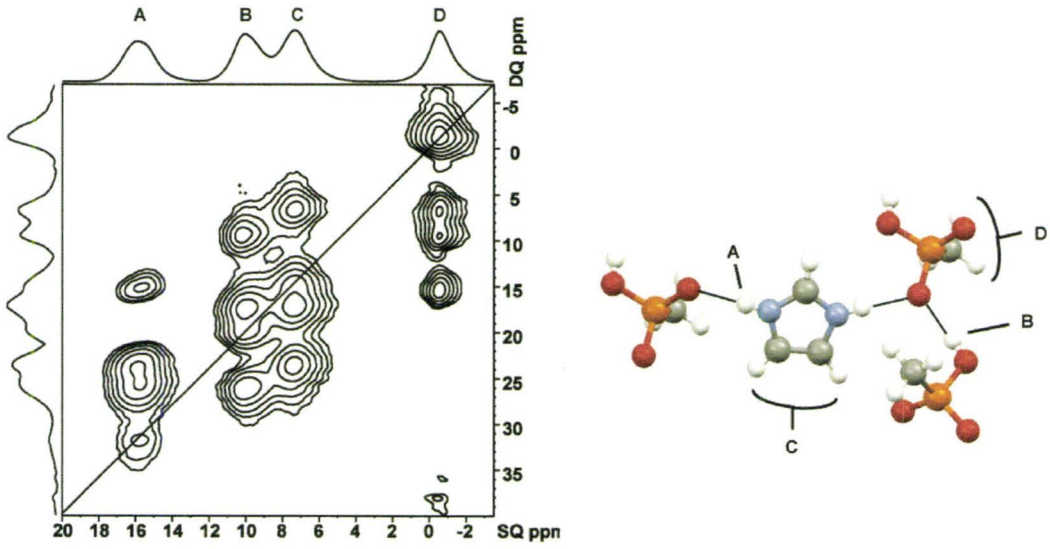

Figure 4 - The 2D ^{1}H-^{1}H DQC NMR spectrum shows the dipolar connectivity of the protons in the solid state structure (left). The protons in the structure are labeled from A to D, A & B being hydrogen bonded protons, C are aromatic protons, D are methyl protons (right).

Table 1 - Table of observed dipolar coupling partners in a ^1H-^1H 2D DQC NMR spectrum.

Dipolar Coupling Pair	1st Single Quantum Chemical Shift	2nd Single Quantum Chemical Shift	Double Quantum Chemical Shift
AA	15.9	15.9	31.7
AB	15.8	9.8	25.4
AC	16.0	7.5	23.9
AD	15.8	-0.4	15.2
BB	10.1	10.1	19.8
BC	10.1	7.4	17.4
BD	10.2	-0.5	9.5
CC	7.4	7.4	14.8
CD	7.4	-0.5	6.6
DD	-0.5	-0.5	-1.2

The table lists the two single quantum chemical shifts that sum to the double quantum chemical shift in the indirect dimension of **Figure 4**. A vertical slice taken through the 16 ppm frequency (A resonance) in the single quantum dimension of **Figure 4** corresponds to the two protons on either side of the imidazole ring. Although the hydrogen bonding on either side of the imidazole ring is different, the change in chemical shift for those protons is very small. The small difference in hydrogen bond distances (2.653 versus 2.673 Å, as measured by x-ray diffraction at 173 K) results in nearly identical chemical shifts for these protons, which are not resolved in the 1D ^1H MAS spectrum (**Figure 3b**) at this field strength. However, in the single quantum projection of the DQC spectrum, **Figure 4**, the broad, flattened A resonance reveals that this resonance is in fact comprised of two closely overlapping lineshapes, which suggests two different

chemical shifts for the N-H protons. Only one of the A protons is expected to have a strong dipolar coupling to the O-H∘∘O hydrogen bond, due to the crystallographic packing. This is confirmed and assigned by examining the 2D ^{1}H DQC spectrum. The intense **AB** cross-peak correlation has single quantum chemical shifts of 15.8 (**A'**) and 9.8 (**B**) ppm and a double quantum frequency of 25.4 ppm. The **A'** frequency is offset from the middle of the broad **A** resonance to a lower chemical shift ($\Delta \cong 0.3$ ppm). The oxygen atoms involved in the N-H_A, ∘∘**O** hydrogen bonding also participate in a second O-H_B∘∘**O** hydrogen bond, this results in a lengthening of the N-**O** distance. The oxygen atom in the N-H_A∘∘O hydrogen bond on the side of the imidazole ring is not bifurcated and causes the hydrogen to be pulled further from the nitrogen which results in a higher ^{1}H chemical shift. This change in chemical shift is small and is only visible through the contours and the projections at this resolution. If both protons experienced the same coupling then the contour would appear as an oval stretched in the single quantum dimension, as is the case for **AA'** and **AD**. The **AA'** dipolar coupling at 15.9 ppm in the single quantum dimension or the **AD** coupling at 15.8 ppm in the single quantum dimension have an oval shape indicating that the dipolar coupling is recoupled for both A protons on either side of the imidazole ring. The lower intensity of the weak **AA'** dipolar coupling likely arises due to the long-range packing contact between the two protons.

The small difference in the hydrogen bond distance and the strong homonuclear dipolar couplings both greatly decrease our ability to resolve these two resonances in a simple ^{1}H MAS spectrum. Moreover, even in the case of the 2D DQC spectra, much of

the interpretation is based on distinguishing subtle differences in contour shape among strongly overlapping resonances in the complex hydrogen-bonded structure. Frequency-switched Lee-Goldburg is a homonuclear decoupling scheme that attenuates the strong dipolar couplings between the protons based on a combination of both sample spinning and pulses applied at the magic angle.[32] Application of FSLG during the t_1-evolution period of a pulse sequence will produce a 2D spectrum with narrow resonances in the indirect dimension that compete and surpass the resolution provided by MAS alone. The heteronuclear 2D ^{31}P-^{1}H FSLG-CPMAS spectrum was acquired, and the sum over the ^{31}P resonance in the direct dimension creates a spectrum, the benefit of FSLG decoupling over standard MAS is shown as **Figure 5**.

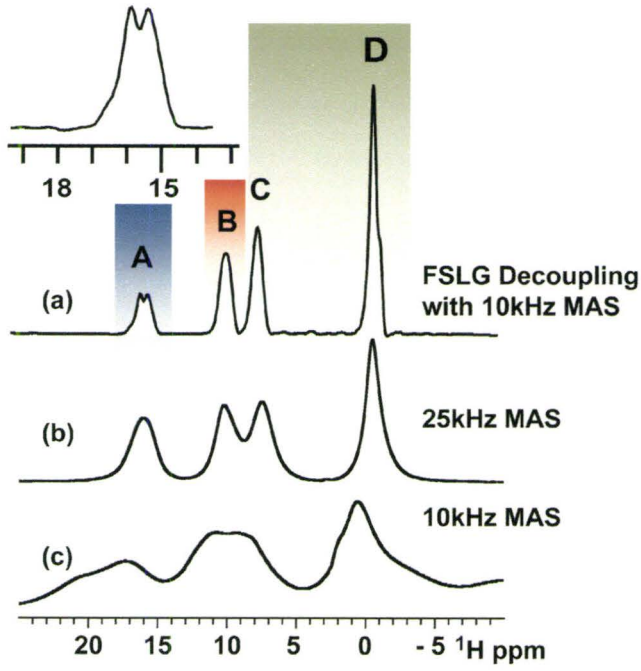

Figure 5 – (a) A sum over the ^{31}P resonance in the 2D ^{31}P-^{1}H FSLG-CPMAS spectrum results in a ^{1}H-^{1}H decoupled ^{1}H MAS spectrum. The inset shows that the A resonance is resolved as two protons with nearly identical chemical shifts. The spectrum in (a) shows the reduction in linewidth of the resonances over traditional MAS at (b) 25 kHz or (c) 10 kHz MAS.

The inset in **Figure 5** shows the increase in resolution achieved using FSLG decoupling under 10 kHz MAS. The overlapping two resonances shown in the inset correspond to the protons in the N-H$^{\circ\circ}$O hydrogen bonds, A and A', as above. The linewidths of the A and A' resonances are 250 Hz each, while the A and A' resonances extracted from the projection of the DQC spectrum are 900 and 1100 Hz. The A' proton has a larger linewidth because that proton has an extra dipolar coupling to the nearby proton in the O-$H_B$$^{\circ\circ}$O hydrogen bond. The FSLG data implies that the timescale of a ring flip in Im-mPA that would exchange these two protons is slower than the separation between these two resonances. The separation of 0.48 ± 0.05 ppm (240 Hz) provides an upper limit for the timescale of dynamics, at 4.2 ± 0.4 ms. If the rotation of the imidazole cation had a correlation time below this, a single coalesced resonance for the A protons would be observed. In comparison to Im-SA where ring dynamics have been observed, the correlation time was 3.6 ± 0.3 ms at ambient temperature, which was derived from ^{13}C CODEX NMR.[29] Since the local dynamics of the imidazole ring in Im-mPA cannot average these two resonances, the imidazole ring rotation contributes negligibly to proton transport at this temperature.

6.2.2 - Proton Dynamics by ^{1}H NMR

The macroscopic ionic conductivity of Im-mPA was measured using impedance spectroscopy from room temperature to 115°C. The room temperature conductivity of Im-mPA is 2.0×10^{-9} S/cm, which is significantly lower than competing hydrated

membrane technologies. However, this strongly thermally activated system responds to increased temperature with a substantial increase in conductivity to 1.8×10^{-5} S/cm at 115°C, as shown in **Figure 6**.

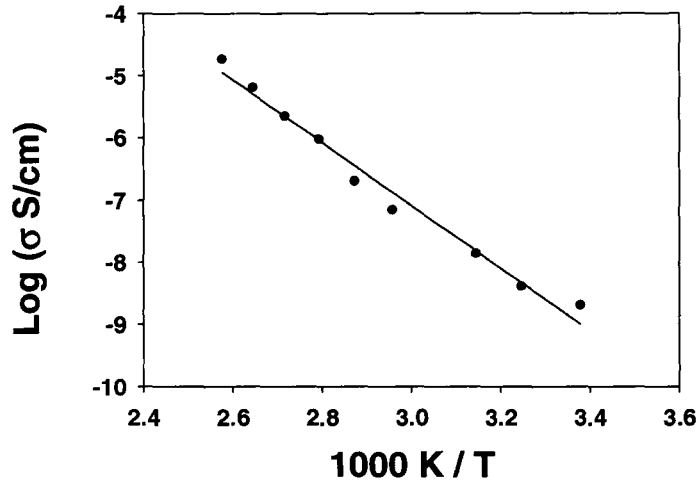

Figure 6 - A plot of ionic conductivity measured by impedance spectroscopy versus temperature, showing a steady increase in conductivity. The activation energy for the conduction process is 42 ± 2 kJ/mol.

The large change in ionic conductivity correlates to a large activation energy (42 ± 2 kJ/mol) for the overall process of ion conduction. The modest ionic conductivity observed at ambient temperature suggests that the material conducts protons, although the slow dynamics responsible for this are not evident in the 1D ^{1}H MAS NMR spectrum. Nevertheless, an indication of these dynamics is provided by the comparison to the DQF spectra shown in **Figure 4**, where the attenuated signal as a function of recoupling time is consistent with a degree of molecular motion at ambient temperature. The benzimidazole analogue has higher room temperature conductivity but Im-mPA has a higher ionic

conductivity when the temperature increases. This might imply that the Im-mPA compound is a better conductor of ions at elevated temperatures.

Solid-state ^{1}H MAS NMR acquired as a function of temperature is used to probe the mobility of the protons in hydrogen bonds. **Figure 7a** shows a series of ^{1}H MAS NMR spectra acquired between 310 and 370 K. The dynamics of the methylphosphonate begin to influence the lineshape of the ^{1}H NMR spectrum at approximately 363 K. Increasing ionic conductivity is proportional to the increasing number of charge carriers. Thus, in light of the conductivity data the new proton resonance in the 1D NMR spectra is assigned to a mobile component, based on both its chemical shift and lineshape, as well as its response to the DQF. These spectra (**Figure 7b**) show that the new peak at $\delta = 11.4$ ppm is removed by the DQF sequence, consistent with this species arising from mobile hydrogen-bonded protons within the salt. The chemical shift trend of this proton resonance is also consistent with the mobility of the associated protons, as the increasing frequency represents the changing weighting of an active chemical exchange process (**Figure 8**).

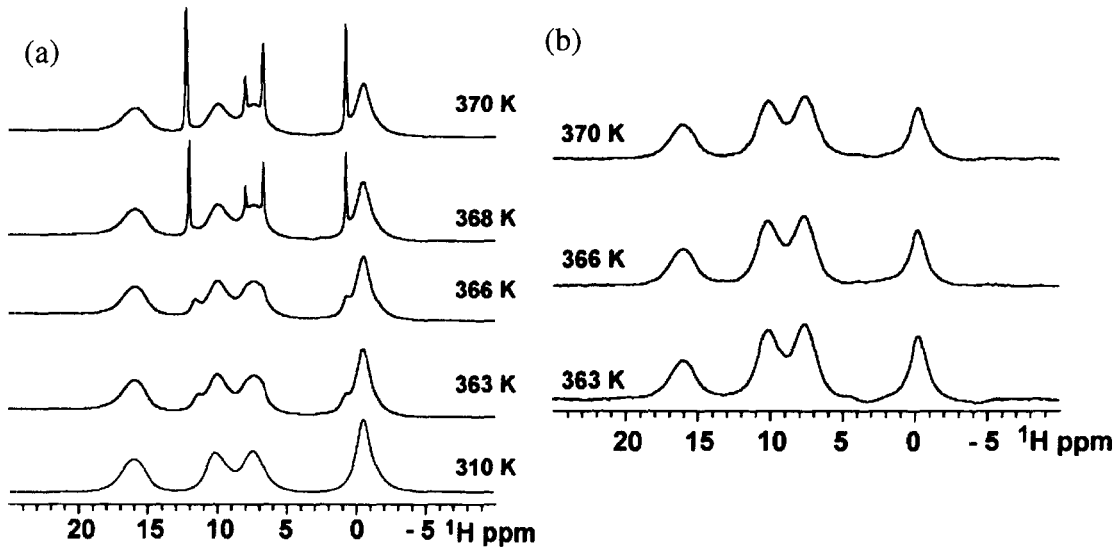

Figure 7 - (a) The variable temperature stack plot of the ^{1}H MAS NMR spectra of Im-mPA and (b) the corresponding ^{1}H-^{1}H DQF spectra, acquired at 25 kHz MAS, with one rotor periods of recoupling.

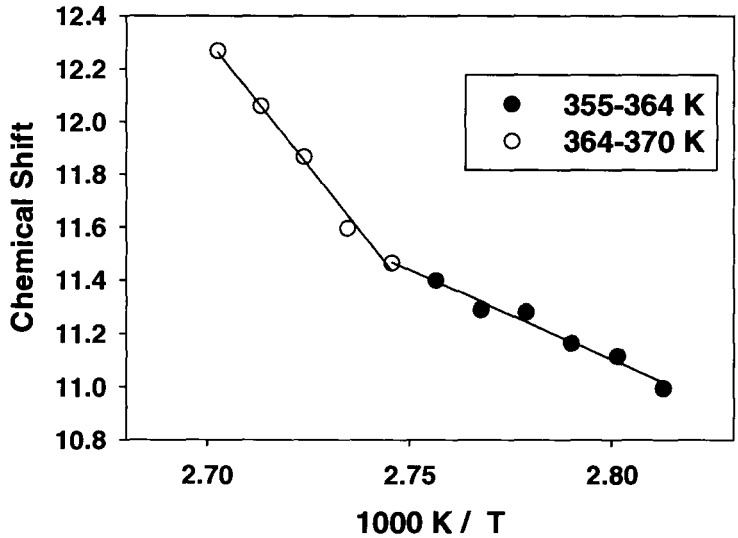

Figure 8 - The plot of ^{1}H chemical shift versus temperature for the hydrogen-bonded protons shows a distinct change in slope at 370 K.

Thermal analysis of Im-mPA by the differential scanning calorimetry is presented as **Figure 9**. In the range of 50 to 150°C a single only thermal transition is observed which corresponds to a melting point at 132°C.

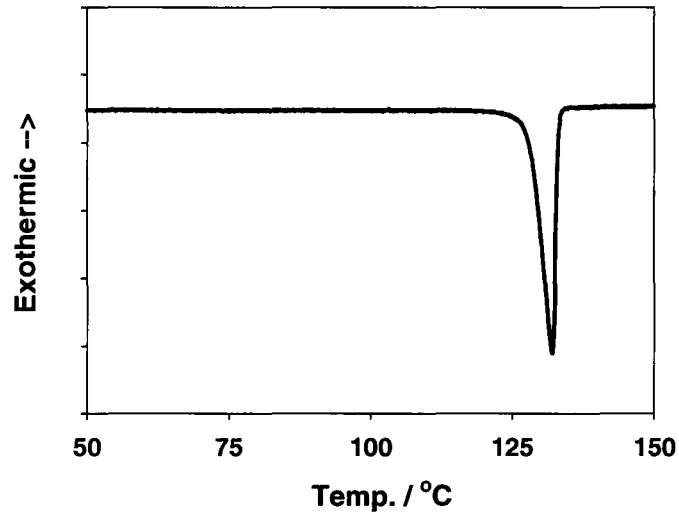

Figure 9 - The Differential scanning calorimetry trace for Im-mPA, a single transition occurs at 132°C and corresponds to the melting point.

The thermal analysis of Im-mPA does not show evidence of any secondary phase transitions prior to melting. This is in contrast to the solid acids such as CsH_2PO_4, where solid-state phase transitions have been shown to enable sudden increases in ionic conductivity.[33] The lack of any transition prior to the melt indicates that structural transitions leading to dynamics within Im-mPA are not observable by this method. From this, it is concluded that a constant increase in thermal energy allows faster dynamics within the original crystalline phase, rather than permitting a reorganization of new solid phase at a particular temperature. The onset of the melting transition observed by DSC begins near 120°C, well above any of the NMR spectra in **Figure 7a**.

The rapid line narrowing occurs over a narrow temperature range, and corresponds to a large activation energy for the onset of local proton dynamics. Several new resonances are observed upon increasing the temperature. The most significant of these is the resonance initially 11.2 ppm at 357 K. This is an intermediate resonance between the chemical shifts of the N-H∘∘O and O-H∘∘O hydrogen bonds. Based on the comparatively low frequency of this new peak, proton dynamics in Im-mPA begins between the O-H∘∘O and N-H∘∘O hydrogen bonds via the rotation of the phosphonate group, similar to the dynamics observed in Bi-mPA. As the temperature increases, the rate of exchange increases, thereby averaging the chemical shift of the exchanging protons.[34] The average chemical shift between one N-H∘∘O and one O-H∘∘O is 13.1 ppm, whereas the new resonance in **Figure 7a** begins at 11.1 ppm. As the temperature increases, the chance of a successful exchange increases, causing the chemical shift to trend to higher frequency. A plot of chemical shift change versus temperature in **Figure 8** illustrates the movement of the emerging resonance of **Figure 7a** with temperature. The change in slope at 364 K suggests that another process is contributing to the coalescence of the resonances above this temperature. As well, above 364 K the narrowing of the aromatic resonances increases, signifying increased mobility of the imidazole ring. Prior to the ring flip motion, the exchange between the bifurcated hydrogen bonds is the only allowed pathway for a proton to cross the solid state structure. Since the hydrogen bonding in Im-mPA is similar to its benzimidazole analogue, Bi-mPA, the conduction of protons was expected to follow the previous example.

However, with both the ring flip and the rotation of the phosphonate available, exchange between all three hydrogen bonds is possible. This ring flip mechanism is not available in the Bi-mPA salt, due to the greater steric bulk of the cation. In Im-mPA, while ring reorientation does take place, the complete coalescence of the three hydrogen bonded resonances is postulated to occur at the average of the three protons chemical shifts at 14.1 ppm. The largest observed chemical shift in the variable temperature data set was 12.3 ppm, which is well below the average of the three hydrogen bonded resonances. Therefore, equally weighted population exchange is not observed at the temperatures of these experiments, and is presumed to only be achieved once the salt is molten. Nevertheless, these data provide strong evidence for solid-state proton transport involving contributions of both cation and anion dynamics. This case is similar to the triazole heterocycle case studied by Akbey *et al.,* where triazole dynamics were elucidated by lineshape analysis providing of insight on the equilbria of the hydrogen bonding motif.[16] Chemical shift trends in Im-mPA indicate a comparable result, where the hydrogen bonding behavior at higher temperatures facilitates the rotation of the phosphonate then the imidazole ring.[16] In the case of Im-mPA the hydrogen bonding surrounding the phosphonate breaks first, allowing the motion of the phosphonate to occur readily, suggesting that the limiting step in the rotation of the phosphonate is the breaking of the A hydrogen bond. The proton transport mechanism includes, but does not rely on the rotation of the imidazole ring, while in Bi-mPA the cation dynamics are

prohibited. Further evidence for this mechanism is provided by the heteronuclear studies of the cations and anions individually.

6.2.3 – Heteronuclear NMR Studies of Ion Dynamics

There are two basic mechanisms for proton conduction available for vinyl imidazole and vinyl phosphonate co-polymers: the ring flip motion of imidazole and the rotation of the phosphonate group, both of which are examples of a Grotthuss (structural) diffusion mechanism of ion conduction.[35] To support the ^{1}H NMR results, heteronuclear studies can be applied. In the 1D ^{13}C CPMAS spectrum of imidazole methyl phosphonate, the 4/5 carbon atoms of the imidazole ring share the same chemical shift due to either having equivalent structure or undergoing chemical exchange. In Im-SA the resonances of the 4/5 carbon atoms of the ring coalesce as the correlation time for ring dynamics is shortened.[36] In the case of Im-mPA, in particular, lowering the temperature did not cause any significant change in the 1D ^{13}C CPMAS in **Figure 10**. It did not resolve the overlapping 4/5 ^{13}C resonances. This implies that the overlap is due to a similar chemical shifts and not ring dynamics. This is consistent with a lack of observable ring rotation at ambient temperature, as seen in the ^{1}H NMR data above.

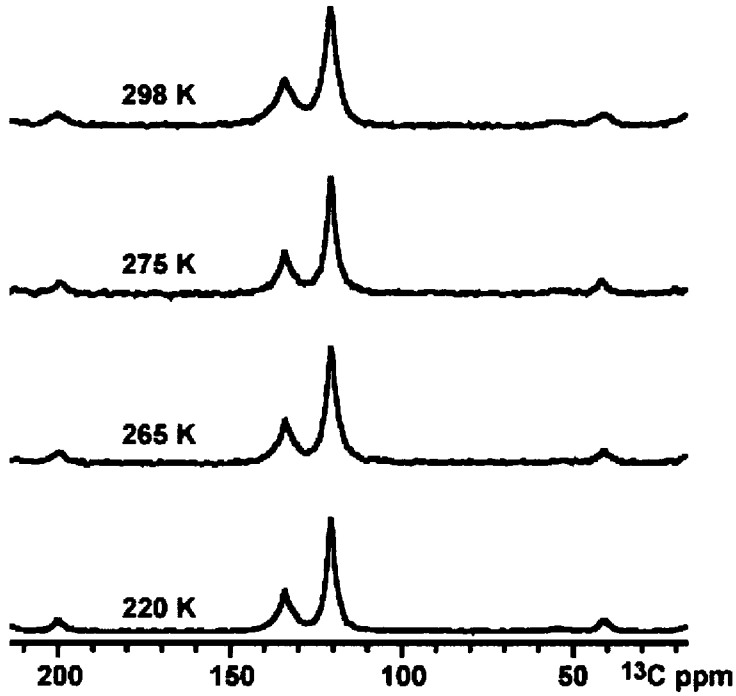

Figure 10 – The ^{13}C CPMAS spectra of Im-mPA below room temperature, no change in the chemical shift was observed in the spectra.

The slow reorientations of solid state materials has been monitored by using the fluctuations in the reorientation of the CSA.[37,38, 39] CODEX is a specialized pulse sequence that determines the timescale and the mode of motion that is accessible to a functional group or molecule.[40, 41] Multinuclear CODEX can be used to confirm and quantify both of these mechanisms of solid-state dynamics, since both mechanisms produces a change in the chemical shift anisotropy (^{31}P or ^{13}C) from the variations in the hydrogen bonding environment. For a three-site motion, the expected plateau would be 66%, whereas for a ring flip of either an imidazole or a benzimidazole ring, the expected plateau is 50%.

^{13}C CODEX NMR is used here to characterize dynamics of the imidazole cations. The cation ring flip in Im-SA and Bi-mPA occur on very different time scales; in Im-SA the imidazole ring rotation has a timescale of tens of milliseconds while the benzimidazole ring flip cannot be detected using ^{13}C CODEX NMR.[29] For Im-mPA the imidazole ring flip does occur but is slower than the sulfate analogue. The ^{13}C exchange curve is plotted in **Figure 11**.

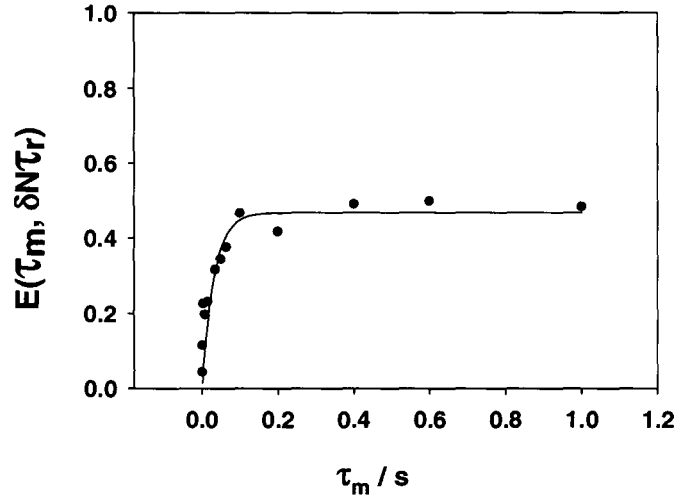

Figure 11 - The ^{13}C normalized pure exchange curve for Im-mPA, which shows a plateau at 0.5, or 50% intensity, consistent with a two-site rotation around the C_{2v} axis of the imidazole ring. The correlation time for the ring flip is 31 ± 9 ms.

The correlation time of the imidazole ring in Im-SA is 3.6 ± 0.3 ms at 23°C while the correlation time for Im-mPA is 31 ± 9 ms at 23°C with a 50% plateau, again consistent with observations from the ^{1}H NMR spectra shown above. Selectively labeling this material with the spin half ^{15}N isotope, reduced the probability for any additional dephasing due to the fast relaxation of the quadrupolar nucleus.[27] Additional dephasing

would obscure any geometry information obtained from the plateau of the exchange curve in **Figure 11**. The hydrogen bonding in Im-SA has one more oxygen atom from the sulfonate to which the hydrogen atoms may bind. This leads to longer hydrogen bonding distances in the crystal structure, **Figure 2**. The longer hydrogen bonds in Im-SA result in weaker hydrogen bonding around the imidazole ring that allows it to rotate more freely, as evidenced in the relative ^{13}C correlation times for the imidazole cation. The change in hydrogen bonding motif due to the extra hydrogen bonding donor in Im-mPA plays a significant role in increasing the strength of the hydrogen bonding and thereby limiting the dynamics of the imidazole ring in this compound. A plot of the ^{31}P normalized pure exchange CODEX NMR signal versus mixing time is shown in **Figure 12a**

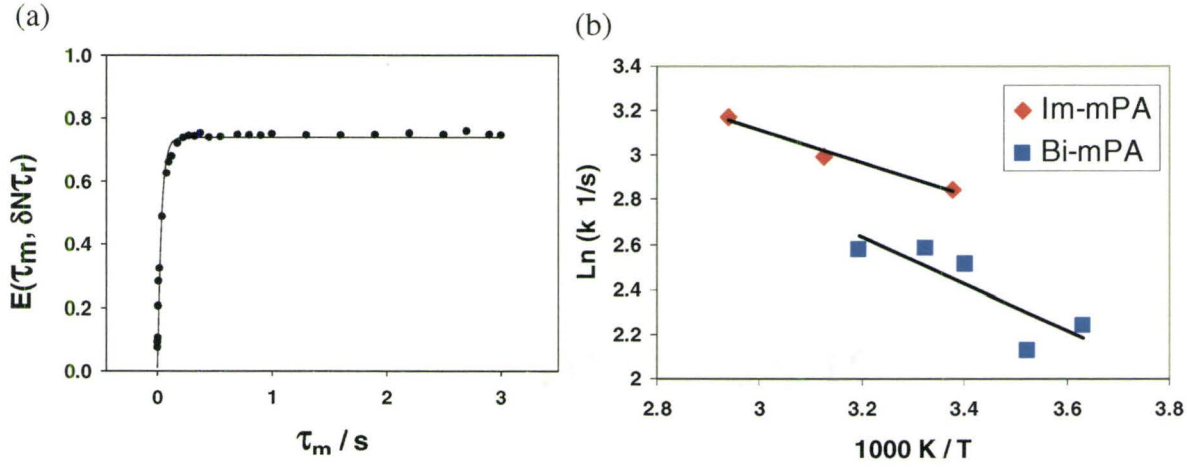

Figure 12 – (a) The ^{31}P normalized pure exchange curve for Im-mPA and (b) the variable temperate plot of the different rate constants. The exchange curve is used to obtain a correlation time, which is shown to change with temperature indicating that the process observed is related to the motion of the phosphonate.

Fitting the attenuation of the ^{31}P CODEX NMR signal to an exponential function yields a correlation time for the rotation of the phosphonate. The plateau of the ^{31}P CODEX NMR is 10% higher than the expected 66% due to longitude relaxation transmitted through a dipolar coupling.[27] By using a double exponential, the motion of the phosphonate and the spin relaxation of the ^{31}P spin were fitted. **Table 2** shows the correlation times of the exponentials representing the motion of the phosphonate. For room temperature the correlation time is 58 ± 4 ms with a plateau of 53 ± 6 % for the exponential representing the motion of the phosphonate. The relaxation portion of the data set is 21 ± 6% with a correlation time of 7 ± 3 ms and when the results are renormalized to include only exchange, the weighting for the second exponential is (52% / (100% - 21%) = 66% which corresponds to a three-fold motion, as expected for this anion.

Table 2 - ^{31}P Correlation times related to the motions of the phosphonate in Im-mPA. Times were obtained from two-component fits, where the second correlation time was constant, at 7 ± 2 ms.

Temperature (K)	Weight (%)	Correlation Time (ms)
296	52 ± 3	58 ± 4
320	55 ±4	50 ± 4
340	67 ± 4	42 ± 4

To justify the weighting of the dynamic process and the spin-diffusion process, the same experiment was performed at different temperatures. The correlation time for the dynamic process changes with temperature, whereas spin-diffusion is relatively temperature independent.[27] Using analogous data processing to that above, a temperature increase to 320 K resulted in a correlation time for the phosphonate reorientation of 50 ± 5 ms with a plateau of 55 ± 6 %, again with a spin diffusion of 22 ± 6 % and time of 7 ± 3 ms. This implies that the correlation time is sensitive to temperature change indicating that the dynamics of the phosphonate is increasing with temperature. **Figure 12b** shows a plot of two sets of ^{31}P CODEX correlation times, for the methyl phosphonate anion paired with a benzimidazole and with an imidazole cation respectively. The activation energy for the rotation of the methyl phosphonate rotation is quite low at 9 ± 3 kJ/mol for the Bi-mPA while for Im-mPA the activation energy is 6 ± 3 kJ/mol for the phosphonate dynamics. These activation energies are similar to the values obtained from a molecular dynamics study run on $CsHSO_4$ which found an activation energy of 7.5 kJ/mol for a rotation of the sulfate around one S-O bond.[42] The solid acid family, to which $CsHSO_4$ belongs, is a series of small molecule ion conductors.[42-46] The ion conduction in solid acid materials occurs through the hydrogen bonding of the material and is facilitated by the rotation of the anion. The previously reported activation energy is for the rotation of the sulfate in $CsHSO_4$ and matches the magnitude of the activation energy measured for the rotation of the phosphonate in Im-mPA. This strongly suggests that the ^{31}P CODEX

NMR experiments are probing the reorientation of the methylphosphonate, a slow reorientation in the solid state on the millisecond timescale at room temperatures.

The rotation of the imidazole ring in imidazole methyl sulfonate has an activation energy of 63.7 kJ/mol.[29] This study shows that the rotation of the imidazole ring is strongly activated by temperature. The results presented here suggest that the phosphonate anion is weakly activated by temperature. The ^{1}H variable temperature experiments confirm that the dynamics begins at the hydrogen bonds between phosphonates and is followed by the narrowing of the protons attached to the imidazole ring. The dynamics of the phosphonate shown in **Figure 13** depict the types of motion observed though solid-state NMR measurements. The local dynamics transport the ions and create a measurable ionic conductivity. The combination of phosphonate and imidazole rotation creates a higher ionic conductivity at elevated temperatures.

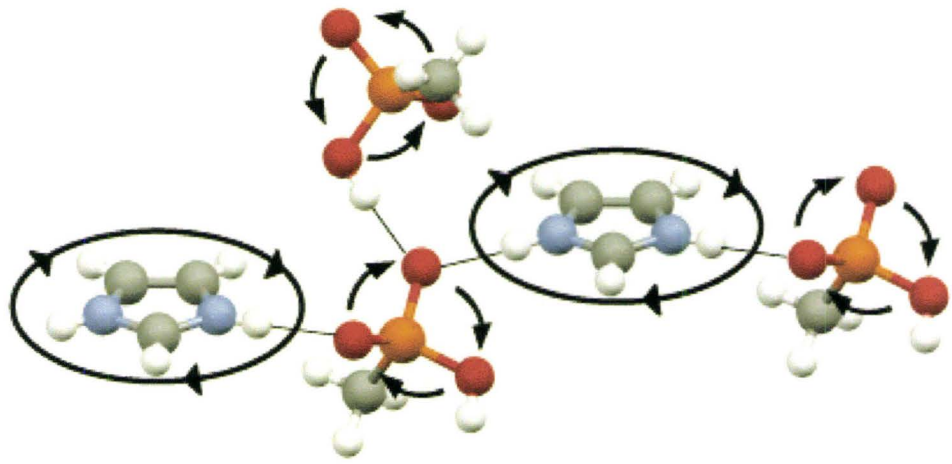

Figure 13 – The types of motion in Im-mPA observed through solid-state NMR.

6.3 - Summary

Anhydrous ionic conductivity in the solid state for fuel cell electrolytes is a new topic that requires further development. Ion conduction in anhydrous materials follows a different motif than hydrated electrolytes. The ionic conductivity of an anhydrous electrolyte depends more on the solid-state hydrogen bonding and the dynamic range of the ions. For Im-mPA, the local mobility of the methylphosphonate is a key component to the ionic conductivity. The ^{31}P CODEX NMR shows that the rotation of the methylphosphonate has a low activation energy and this implies that the motion of the anion is not impeded by the solid-state structure. The smaller imidazole ring exhibits faster reorientation than a benzimidazole cation, but this motion does not yield significant line narrowing in the ^{1}H variable temperature NMR experiments until higher temperatures (>363 K). Chemical exchange, observed through the appearance of a new resonance in the hydrogen bonding region, appears to occur first between phosphonate groups suggesting that proton transport between anions is the preferred pathway at lower temperatures until the imidazole ring dynamics are activated. When the imidazole ring starts to rotate it exchanges both N-H∞O hydrogen bonded protons. With the rotation of both the cation and anion, a beneficial cooperative mechanism of ion conduction exists. This is supported by the increase in ^{1}H chemical shift of the mobile hydrogen bonded resonance, as well as temperature-dependent heteronuclear CODEX studies of the cations and anions individually.

6.4 – References

1. A. Rodrigues, J. C. Amphlett, R. F. Mann, B. A. Peppley and P. R. Roberge, Proceedings of the Intersociety Energy Engineering Conference, 1997.
2. L. Ghassemadeh, M. Marrony, R. Barrera, K. D. Kreuer, J. Maier and K. Muller, *J. Power Sources*, 2009, **186**, 334-338.
3. A. Kabasawa, J. Saito, K. Miyatake, H. Uchida and M. Watanabe, *Electrochim. Acta*, 2009, **54**, 2754-2760.
4. P. D. Beattie, F. P. Orfino, V. I. Basura, K. Zychowska, J. Ding, C. Chuy, J. Schmeisser and S. Holdcroft, *J. Electroanal. Chem.*, 2001, **503**, 45-56.
5. A. V. Anantaraman and C. L. Gardner, *J. Electroanal. Chem.*, 1996, **414**, 115-120.
6. J. J. Baschuk and X. LI, *Int. J. Energy Res.* , 2001, **25**, 695-713.
7. K. S. Hwang, M. Yang, Z. Ji, J. Grunes and G. A. Somorjai, *J. Mol. Catal. A: Chem.*, 2003, **204-05**, 499-507.
8. U. Akbey, R. Graf, Y. G. Peng, P. P. Chu and H. W. Spiess, *J. Polym. Sci. Pt. B-Polym. Phys.*, 2009, **47**, 138-155.
9. Y. J. Lee, B. Bingol, T. Murakhtina, D. Sebastiani, W. H. Meyer, G. Wegner and H. W. Spiess, *J. Phys. Chem. B*, 2007, **111**, 9711-9721.
10. A. Bozkurt, W. H. Meyer, J. Gutmann and G. Wegner, *Solid State Ionics*, 2003, **164**, 169-176.
11. M. F. H. Schuster, W. H. Meyer, M. Schuster and K. D. Kreuer, *Chem. Mater.*, 2004, **16**, 329-337.
12. C. C. de Araujo, K. D. Kreuer, M. Schuster, G. Portale, H. Mendil-Jakani, G. Gebel and J. Maier, *Phys. Chem. Chem. Phys.*, 2009, **11**, 3305-3312.
13. M. Schuster, K. D. Kreuer, H. Steininger and J. Maier, *Solid State Ionics*, 2008, **179**, 523-528.
14. S. Beyazyildirim, K. D. Kreuer, M. Schuster, A. J. Bhattacharyya and J. Maier, *Adv. Mater.*, 2008, **20**, 1274-1278.
15. H. Steininger, M. Schuster, K. D. Kreuer, A. Kaltbeitzel, B. Bingol, W. H. Meyer, S. Schauff, G. Brunklaus, J. Maier and H. W. Spiess, *Phys. Chem. Chem. Phys.*, 2007, **9**, 1764-1773.
16. U. Akbey, S. Granados-Focil, E. B. Coughlin, R. Graf and H. W. Spiess, *J. Phys. Chem. B*, 2009, **113**, 9151-9160.
17. S. U. Celik, U. Akbey, R. Graf, A. Bozkurt and H. W. Spiess, *Phys. Chem. Chem. Phys.*, 2008, **10**, 6058–6066.
18. R. H. He, Q. T. Che and B. Y. Sun, *Fiber. Polym.*, 2008, **9**, 679-684.
19. J. R. P. Jayakody, S. H. Chung, L. Durantino, H. Zhang, L. Xiao, B. C. Benicewicz and S. G. Greenbaum, *J. Electrochem. Soc.*, 2007, **154**, B242-B246.
20. R. H. He, Q. F. Li, J. O. Jensen and N. J. Bjerrum, *J. Polym. Sci., Part A: Polym. Chem.*, 2007, **45**, 2989-2997.

21. S. U. Celik, U. Akbey, R. Graf, A. Bozkurt and H. W. Spiess, *Phys. Chem. Chem. Phys.*, 2008, **10**, 6058-6066.
22. C. E. Hughes, S. Haufe, B. Angerstein, R. Kalim, U. Mahr, A. Reiche and M. Baldus, *J. Phys. Chem. B*, 2004, **1088**, 13626-13631.
23. N. N. Greenwood and A. Thompson, *J. Chem. Soc.*, 1959, 3485-3492.
24. S. P. Brown and H. W. Spiess, *Chem. Rev.*, 2001, **101**, 4125 -4155.
25. M. Lee and W. I. Goldburg, *Phys. Rev.*, 1965, **140**, A1265-A1271.
26. C. Coelho, J. Rocha, P. K. Madhu and L. Mafra, *J. Magn. Reson.*, 2008, **194**, 264-282.
27. K. Saalwachter and K. Schmidt-Rohr, *J. Magn. Reson.*, 2000, **145**, 161-172.
28. G. J. M. P. van Moorsel, E. R. H. Vaneck and C. P. Grey, *J. Magn. Reson., Ser. A*, 1995, **113**, 159-163.
29. I. Fischbach, H. W. Spiess, K. Saalwaechter and G. R. Goward, *J. Phys. Chem. B*, 2004, **108**, 18500-18508.
30. C. F. Julio, *Concepts Magn. Reson. A*, 2004, **20A**, 42-69.
31. G. A. Kumar and M. A. McAllister, *J. Org. Chem.*, 1998, **63**, 6968-6972.
32. M. Lee and W. I. Goldburg, *Phys. Rev.*, 1965, **140**, A1261-A1271.
33. D. A. Boysen, S. M. Haile, H. Liu and R. A. Secco, *Chem. Mater.*, 2003, **15**, 727-736.
34. H. W. Spiess, *Adv. Polym. Sci.*, 1985, **66**, 23-58.
35. C. J. T. Grotthuss, *Ann. Chim. (Paris)*, 1806, **58**, 54-74.
36. G. R. Goward, K. Saalwachter, I. Fischbach and H. W. Spiess, *Solid State Nucl. Magn. Reson.*, 2003, **24**, 150-162.
37. S. P. Brown, *Macromol. Rapid Commun.*, 2009, **30**, 688-716.
38. Ingrid Fischbach, T. Pakula, P. Minkin, A. Fechtenkotter, K. Mullen, H. W. Spiess and S. Kay, *J. Phys. Chem. B*, 2002, **106**, 6408-6418.
39. C. Gervais, C. Coelho, T. Azais, J. Maquet, G. Laurent, F. Pourpoint, C. Bonhomme, P. Florian, B. Alonso, G. Guerrero, P. H. Mutin and F. Mauri, *J. Magn. Reson.*, 2007, **187**, 131-140.
40. E. R. deAzevedo, W. G. Hu, T. J. Bonagamba and K. Schmidt-Rohr, *J. Am. Chem. Soc.*, 1999, **121**, 8411-8412.
41. D. J. Harris, T. J. Bonagamba, M. Hong and K. Schmidt-Rohr, *Macromolecules*, 2000, **33**, 3375-3381.
42. C. R. I. Chisholm, Y. H. Jang, S. M. Haile and W. A. Goddard(III), *Phys. Rev. B*, 2005, **72**, 134103.
43. W. Muench, K. D. Kreuer, U. Traub and J. Maier, *Solid State Ionics*, 1995, **77**, 10-14.
44. T. Norby, M. Friesel and B. E. Mellander, *Solid State Ionics*, 1995, **77**, 105-110.
45. A. I. Baranov, L. A. Shuvalov and N. M. Schagina, *J. Exp. Theor. Phys.*, 1982, **36**, 459-462.
46. T. Uda, D. A. Boysen and S. M. Haile, *Solid State Ionics*, 2004, **176**, 127-133.

Chapter 7: Polymer Composites

This chapter introduces the polymer composite materials, which are a potential anhydrous electrolyte for a hydrogen fuel cell. This section of the thesis is comprised of unpublished work and was revised by Gillian R. Goward. My contributions to this chapter are the synthesis, data collection, processing, and interpretation of the spectra for this series of solid-acid electrolytes. The thermogravimetric analysis (TGA) experiments were performed by Frank Gibbs at the Brockhouse Institute for Materials Research. The scanning electron micrographs were recorded at the Brockhouse Institute for Materials Research with the assistance of Mark Ma, a graduate student in Gillian R. Goward's research group. In this chapter, the choice of a suitable polymer host material is outlined, and the combination of several ionic electrolytes and polymer materials are investigated for their structure and temperature dependent dynamic properties.

7.0 – Introduction

The most successful aqueous polymer electrolyte is the perfluorinated ionomer, Nafion, that requires substantial amounts of hydration to be effective.[1, 2] The loss of water reduces the number of charge carriers resulting in a loss of ionic conductivity. Many alternative polymer electrolytes improve upon the original design of Nafion. Examples include liquid acid based polymers, solid acid, and anhydrous polymer

electrolytes. These electrolytes are outlined in Chapter 1.[3-13] The goal of the previous chapters was to investigate the ion transport behavior of several small molecule electrolyte models to provide a basis for understanding the more complex mechanism of ion exchange in polymer systems. The imidazole methylphosphonate (Im-mPA), benzimidazole methylphosphonate (Bi-mPA), and benzimidazole ethylphosphonate (Bi-ePA) showed that the phosphonate was a key component in the transport of ions in the solid state. Rotation of the phosphonate provided a method of ion transport at room temperature while the rotation of the imidazole ring could participate in the ionic conductivity if the thermal energy was sufficient. The hydrogen bonding characteristics of the model compounds allowed them to transport ions in the solid state. The model compounds most resemble the solid-acid electrolytes that undergo a superprotonic phase transition at high temperatures. However, the organic nature of the model compounds cause them to melt, rather than to reorganize into a different proton conducting phase upon heating.

The model compounds studied in the previous chapters would act as high temperature electrolytes, similar to the solid acid family of electrolytes and the anhydrous polymer electrolytes and would not require any liquid electrolyte to transport ions. The ability of the solid acid electrolytes to transport protons without a liquid electrolyte reduces the complexity of the fuel cell design by removing the need for humidification of the fuel. However, for solid acid fuel cells a different set of problems exist, namely, the issue observed by Uda *et al.*, where the solid acid fuel cell ceases to function due to the

mechanical failure of the electrolyte layer.[7] This primarily occurred in electrolyte layers that were purposely made with minimized thickness to reduce the resistance across the electrolyte layer, thus, improving the current density of the fuel cell. The deformation of the electrolyte layer caused a loss of contact between the electrode and electrolyte, resulting in the malfunction of the cell. Thus, to improve the mechanical strength of the new electrolyte, a support material is required to give strength to the electrolyte layer while maintaining the thin electrolyte layer to improve the current density. This technique is often seen in materials engineering, and has appeared in solar cell research.[14-16] For example, where poly ethylene oxide acts as a support for titanium dioxide, ionic liquids, or other functional materials. The combination of electrolyte with polymer support creates entirely new area of electrolytes that does not belong to the solid acid or anhydrous electrolyte category. A more apt name for these new electrolytes are polymer composites.

The research goal of this study is to maximize the ionic conductivity of the polymer composite through understanding the factors that contribute to the transport of ions. This involves determining how the polymer support material will alter the onset of ion dynamics in the electrolyte material and the mechanism of ion transport, the factors that will maximize the ion transport, and how the polymer and electrolyte materials interact on the molecular level. The main focus of this study is the transportation of ions across the electrolyte and this is best accomplished using a molecular-level probe such as solid state NMR.

7.1 – Experimental

The imidazole, benzimidazole, ethylphosphonic acid and methylphosphonic acid were purchased from Sigma Aldrich while the poly tetrafluorethylene (PTFE) films were purchased from Millipore. The pore size of the PTFE films were given to be 0.45 μm and the thickness was near 50 μm. The synthesis of the electrolyte material followed the scheme outlined in Chapters 5 & 6. The polymer composites were obtained by wetting the PTFE films with dry methanol then placing the polymer into a methanol solution of the electrolyte (1 M) for 24 hours. The polymer composite was dried at 80°C for at least 24 hours to ensure that all of the methanol was removed from the structure.

The NMR experiments were conducted on an Bruker 500 MHz Avance system using double resonance probes that support rotors with an outer diameter of 2.5 mm or 4 mm at 25 kHz and 10 kHz MAS, respectively. All high-resolution ^{1}H NMR was carried out using a 90° pulse width of 2.5 μs on the 2.5 mm probe. The on-resonance field for the FSLG decoupling was set to 83.3 kHz while the off-resonance fields were ± 58.9 kHz with a 2 kHz asymmetric offset. The scaling factor for the indirect dimension was set to 0.578. Contact pulses of 3000 μs were used to acquire the 1D CPMAS experiments. Temperature calibration of the MAS probes was performed using a sample of samarium stannate.[17]

An Autolab PGSTAT 30 was used to measure the AC impedance of a two-electrode cell, frequency range used was 500 kHz down to 0.1 Hz. The pellet had a

thickness of 0.175 cm with a radius of 0.476 cm. The sample was allowed to equilibrate at a given temperature for a minimum of 4 hours between impedance measurements.

7.2 – Polymer Material

The polymer composite material has two major parts, first, an inert polymer host and secondly, an electrolyte material. The polymer material needs to adsorb and host the electrolyte material. Additional benefits such as chemical resistivity, low cost, and low spectra background are all desired properties but are not essential for the conduction of protons. For example, a chemical resistivity of the polymer material is necessary to ensure that the material does not breakdown or decay while in the operating environment of the fuel cell. Additionally, the polymer material must not hinder the conduction of protons, but simply provides an appropriate mechanical support for the electrolyte. The two polymers selected as the host material in this study are polyvinyl difluoride and poly tetrafluoroethylene, the chemical structure of each polymer is in **Figure 1**.

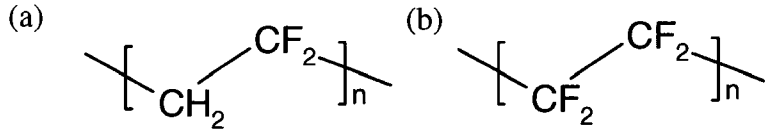

Figure 1 - The chemical structure of the polymer host material (a) polyvinyl difluoride (PVDF) and (b) polytetrafluoroethylene (PTFE). These two polymers will not bind the to the electrolyte through ionic interactions.

These two polymers are similar to the backbone of the Nafion polymer without the side chain. The strength and simplicity of the two structures begins with the C-H or C-F

bonding. Carbon fluorine bonding provides strong chemical resistance and strong mechanical strength for a polymer.[18] The non-polar bonding of the backbone prevents the hydrogen bonding centers of the electrolyte from interacting with the polymer, making them inert to the electrolyte or any other ionic species that may enter the polymer. The opposite case exists for acidified PBI where phosphoric acid molecules would bind to the basic sites of the polymer backbone and anchor the liquid state electrolyte to the backbone of the polymer to prevent the liquid from leaching from the polymer material. Anchoring the electrolyte is not required for these new polymer composites because the electrolyte is designed to conduct in the solid state, and therefore does not need to coordinate to the polymer backbone via hydrogen bonding. In the absence of any liquid and by preventing the melting of the electrolyte, little movement of the solid-state electrolyte will occur, minimizing a loss of contact between the electrodes.

As the electrolyte fills the polymer membrane, it will take the place of the free volume in the polymer.[19-22] The ionic conductivity will depend on the ability of the electrolyte to penetrate the polymer and fill the free space creating a connected network of the electrolyte material. For this, we investigate the morphology of the polymer through scanning electron microscopy. The surface of the PVDF films shown in **Figure 2**, exhibits a porous polymer surface, and the same is true for PTFE, shown in **Figure 3**. There are clear morphology differences between the two polymer membranes beginning with the size and shape of the pores in the surface of the polymer film.

(a)

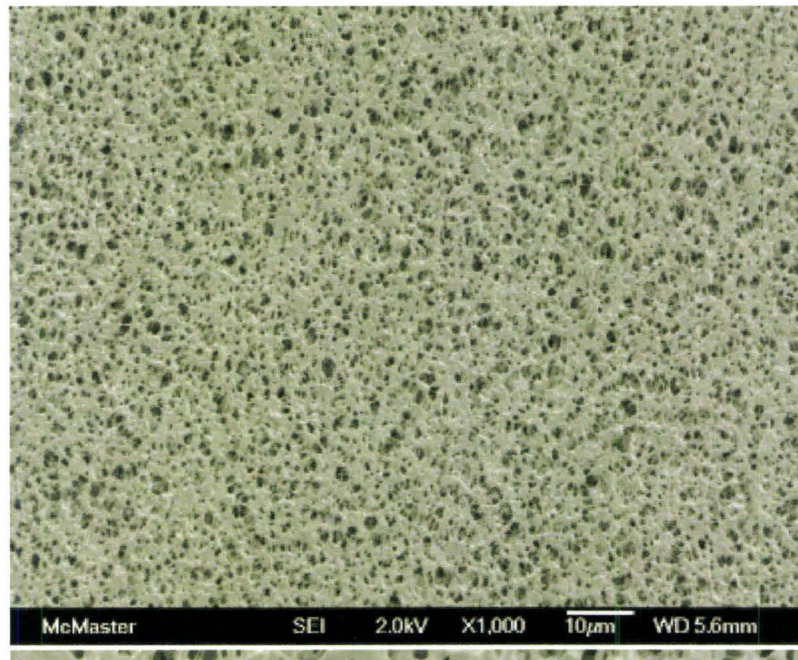

(b)

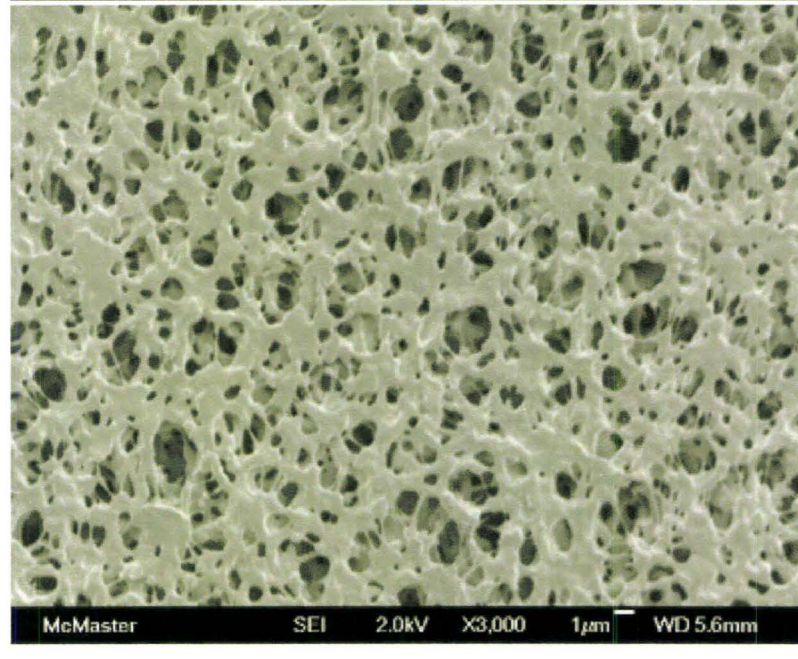

Figure 2 – SEM images of the surface of PVDF at (a) x1000 magnification and (b) x3000 magnification. The polymer surface shows 1 μm pores with large polymer domains that continue beneath the surface of the polymer.

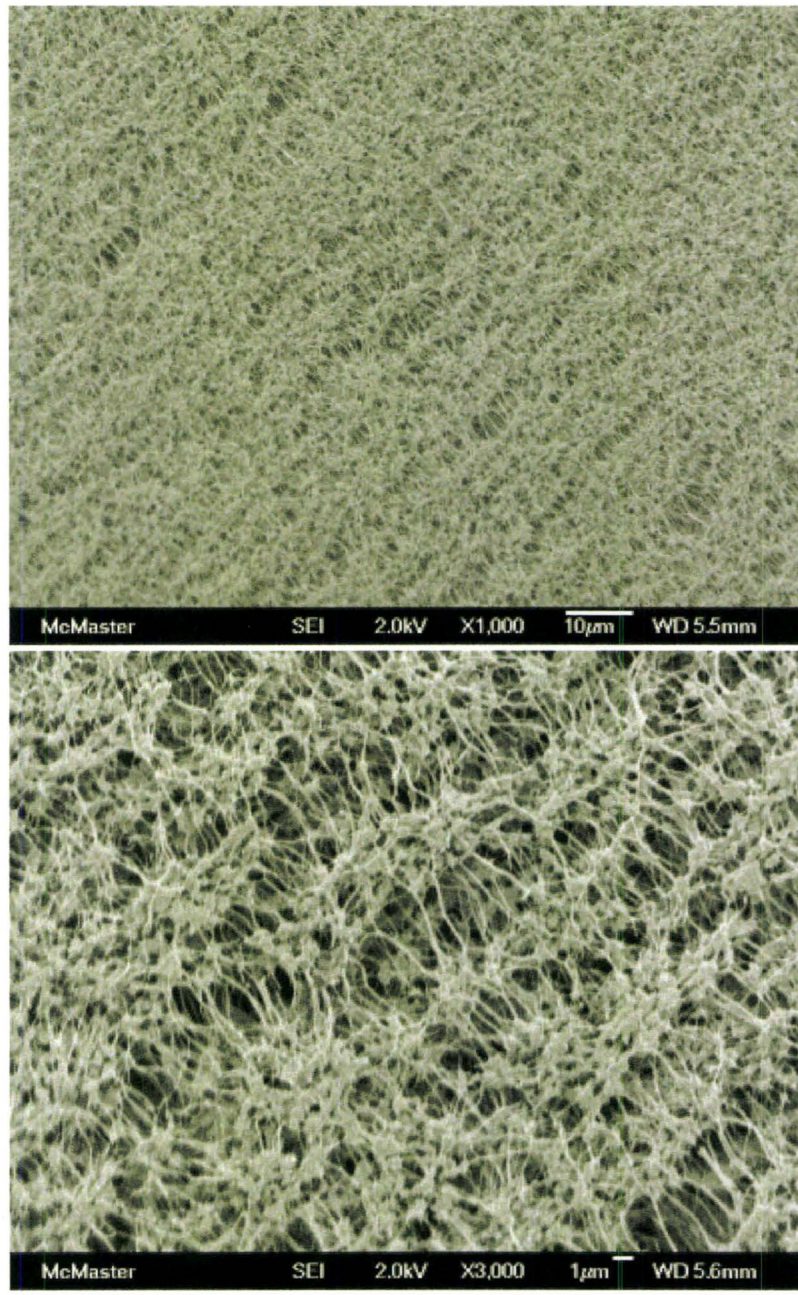

Figure 3 - SEM images of the surface of PTFE at (a) x1000 magnification and (b) x3000 magnification. The polymer surface shows 1 μm pores or larger and has a different polymer morphology than the PVDF polymer.

The SEM images show the morphology of the polymer films that were used to create the polymer composite material. The images of PVDF in **Figure 2,** show a continuous and uniform distribution of the polymer domains and pores throughout the polymer's surface. In **Figure 2b**, the surface is mostly composed of overlapping polymer domains and pores on the 1 μm level. The large polymer domains contribute to the strength and rigid nature of the polymer disc used in the composite preparation. However, the total pore volume at the surface will determine the amount of exposed electrolyte to the catalyst material, which influences the number of ions passing through the electrolyte material. The polymer material must balance mechanical strength with number of pores to ensure that the composite material is strong enough to avoid deformation and provide adequate contact.

The SEM images of PTFE show in **Figure 3** show a different distribution of the polymer domains than in PVDF. On a larger scale the PTFE does not appear to have a more porous surface than PVDF but polymer domains divide into a morphology that resembles a neuron. The surface of PTFE shows 4-5 μm clusters of PTFE connected by fibrous polymer material approximately 3-4 μm long. In gaps between the polymer clusters are the pores of the material for the electrolyte. The larger pores would expose larger portions of the electrolyte to the catalyst increasing the transport of ions across the electrolyte. The important feature of any porous polymer for electrolyte materials is that the polymer must have a path for the electrolyte material to reach both side of the

polymer film without the creation of bottlenecks to the diffusion of ions through the material. .

The resistance of the polymer backbone to chemical attack controls the lifetime of a fuel cell.[5, 23-27] The relative strength of a carbon-hydrogen bond versus a carbon fluorine bond makes the PVDF polymer susceptible to chemical degradation. Unfluorinated sections of a polymer decompose faster, leading to a shorter lifetime for the polymer material.[24] The carbon fluorine bond is stronger than the carbon hydrogen bond by 69 kJ/mol (485 versus 416 kJ/mol).[18] For these reasons, polymers with a fully fluorinated backbone are preferred over unfluorinated materials. However, using PVDF over PTFE as a polymer host is cost effective solution.

In terms of the spectroscopic studies of interest here, the background resonances from the polymer material will overlap with the resonances of the electrolyte for the polymer composite. For the purpose of the solid-state NMR investigation, the partially protonated backbone of PVDF poses a challenge. This is especially problematic if the amount of the electrolyte is small, such that the background could obscure the electrolyte signal. The ^{1}H NMR spectrum of pure PVDF in **Figure 4** shows the proton resonance present in the aliphatic region of the spectrum, which will be observed in the composite samples as well.

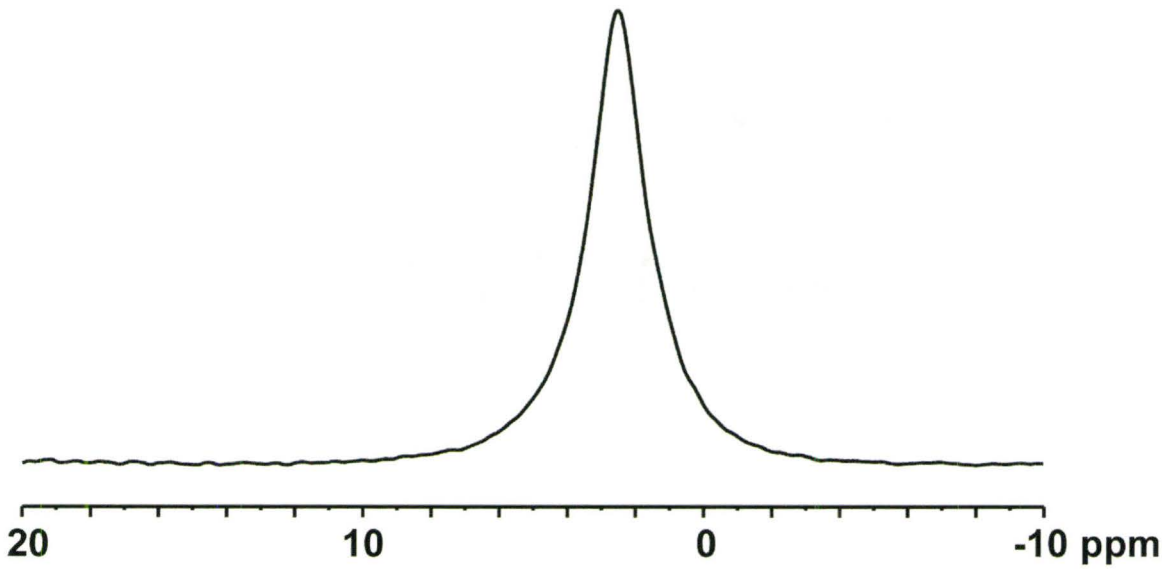

Figure 4 – The ^{1}H NMR spectrum of PVDF at 10 kHz MAS, shows a broad resonance for the $-CH_2-$ protons at 2.5 ppm.

The polymer protons of PVDF provide a method for monitoring the dynamics of the backbone. The initial linewidth of the protons at 2.5 ppm in the ^{1}H NMR spectrum at 298 K is 950 Hz. The motion of the polymer backbone causes the linewidth to reduce as the temperature increases. A plot of the ^{1}H linewidth for PVDF versus temperature in **Figure 5** shows that the protons of the backbone experience local dynamics, which results in line narrowing at higher temperatures. The activation energy for the motion of the polymer backbone in PVDF is 14 ± 2 kJ/mol. By comparison, the activation energy for polyethylene from a ^{13}C NMR 2D exchange study was 103 ± 10 kJ/mol.[28, 29] This activation energy measures the chain dynamics that interchange the domains of amorphous polyethylene to crystalline polyethylene. This activation energy for polyethylene is higher due because it accounts for the energy needed for a phase change

and the dynamics. The low activation energy of PVDF suggests that the backbone fluctuates between different positions easily. The linewidth of the polymer is 350 Hz at 360 K. The wide lineshape of the proton resonance suggests that the protons are not experiencing fast dynamics. However, the motion of the polymer backbone could facilitate the transport of ions in the electrolyte.

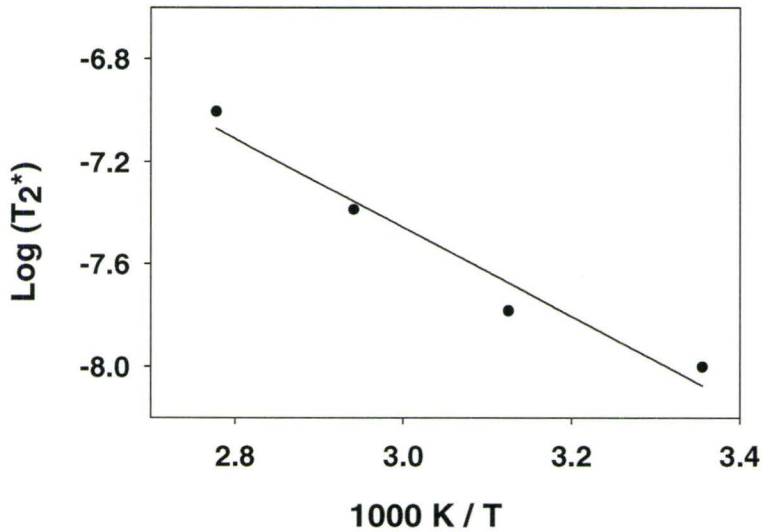

Figure 5 – The plot of T_2* versus temperature, the activation energy of the backbone dynamics is 14 ± 2 kJ/mol from ^{1}H NMR linefitting methods.

7.3 – Polymer composite: Bi-ePA

7.3.1 – Concentration Dependence

The Bi-ePA electrolyte is a good electrolyte candidate because the pure electrolyte has a melting point above the boiling point of water. For an anhydrous fuel cell operation above 100°C is an essential feature. The synthesis of the polymer

composite requires a solution of the electrolyte using a solvent that wets the polymer, swelling the material to increase the uptake of the electrolyte. The amount of electrolyte in the polymer was found to be proportional to the concentration of the stock solution. PVDF was soaked using two stock solutions of Bi-ePA having a concentration of 0.5 M and 1 M in dimethylsulfoxide. The TGA of the two materials are shown in **Figure 6**. The 0.5 M concentration has a larger polymer decay indicating that the material has less electrolyte. The results of the TGA are summarized in Table 1.

Table 1 – TGA results for the PVDF composites, calculated values are marked by an asterisk.

	Pure PVDF / %	0.5 M Electrolyte Solution / %	1 M Electrolyte Solution / %
Polymer Decay	70	60	44
Polymer Remaining	30	25*	19*
Electrolyte	0	15*	37*

The TGA of the pure material helps calculate the amount of electrolyte in the polymer composites. Only 70% of the polymer's mass decays in the TGA of the pure PVDF sample. Using the 70 to 30 ratio and the mass loss of the PVDF in the composite material, it is possible to calculate the total percentage of polymer material in the composite. The remainder of mass after the sum of both polymer contributions is the total mass of the electrolyte.

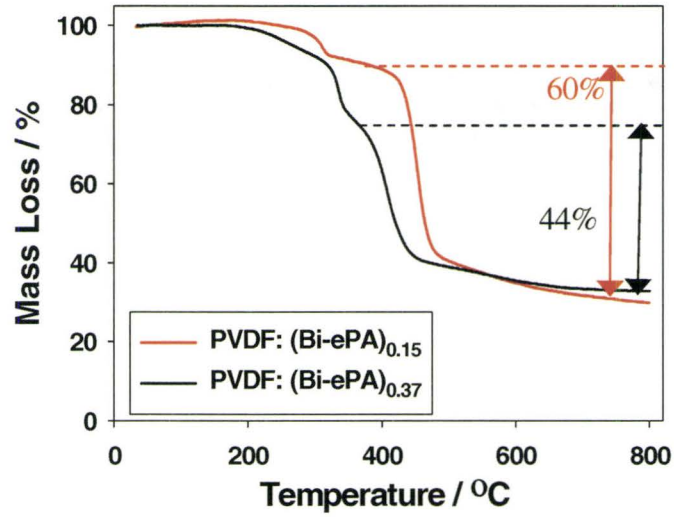

Figure 6 - The TGA of the two PVDF: Bi-ePA samples (0.5 M as red and 1 M as black). The polymer degradation begins near 400°C. The TGA results show that the polymer accounts for a greater portion of the 0.5 M sample. The mass of the electrolyte in the 0.5 M sample is 15 % and 37 % for the 1 M sample.

The TGA of the more concentrated sample in black in **Figure 6**, has 63% of the sample mass as polymer, leaving only 37% as electrolyte. This sample will have the designation PVDF: $(Bi\text{-}ePA)_{0.37}$. This new label incorporates the total amount of electrolyte into the name of the polymer composite. The decay of electrolyte in PVDF: $(Bi\text{-}ePA)_{0.37}$ has two electrolyte plateaus, while the lower concentration sample has only one. The decomposition events of the electrolyte occurs prior to the polymer and their magnitude is dependent on the total concentration of the electrolyte in the material. The first decomposition near 200°C in PVDF: $(Bi\text{-}ePA)_{0.15}$ is very small and is stronger in the more concentrated sample. From this it is clear that the amount of electrolyte in the polymer composites depends on the original stock concentration.

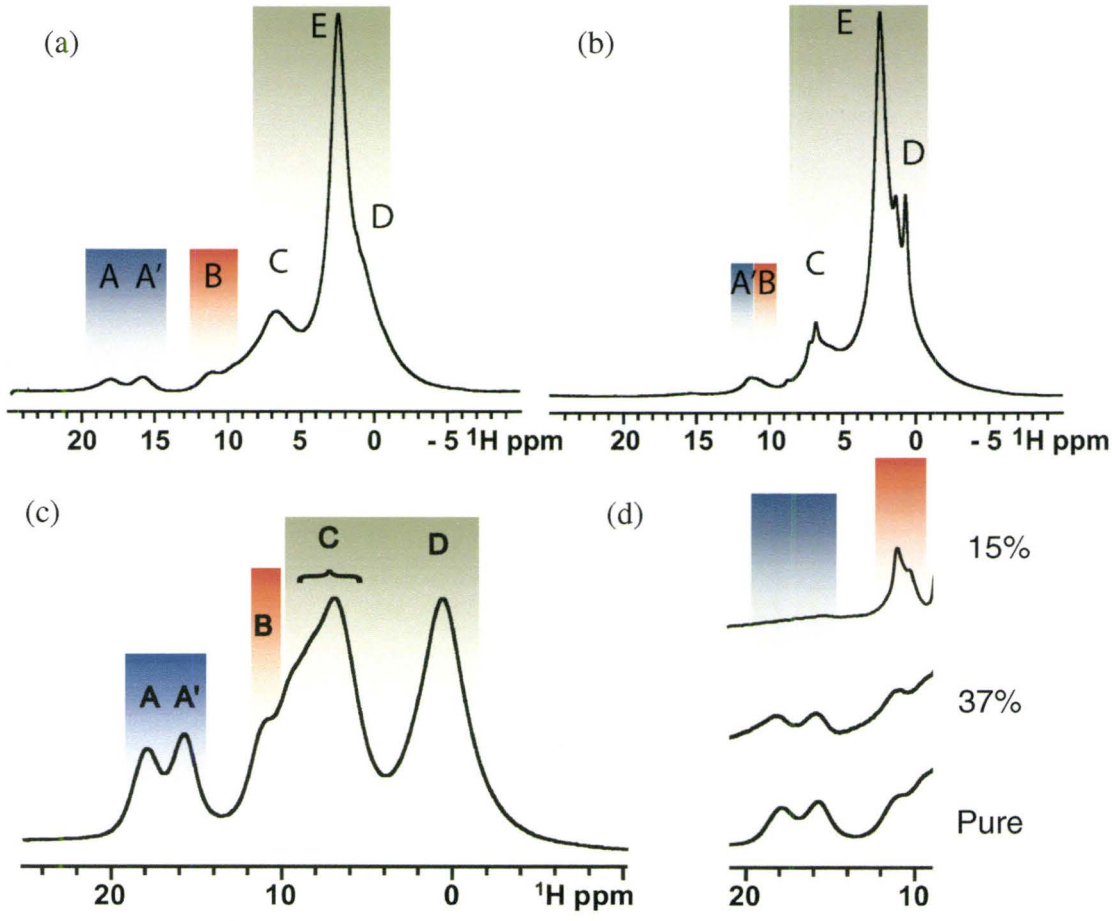

Figure 7 – The ^{1}H MAS NMR spectra of PVDF: Bi-ePA at 25 kHz MAS from stock solution concentrations of (a) 37%, (b) 15%, (c) pure electrolyte, (d) a stack plot of the hydrogen bonding region of the three spectra. The blue regions represent N-H◦◦O hydrogen bonds, red for OH◦◦O, and grey for aromatic or aliphatic resonances.

The spectra of the resulting polymer composite materials are shown in **Figure 7**. The ^{1}H NMR spectra of PVDF: Bi-ePA for these two concentrations are different. The ^{1}H NMR of PVDF: $(Bi\text{-}ePa)_{0.37}$ solution (**Figure 7a**) resembles the 1D spectra of the Bi-ePA solid electrolyte, however the spectrum of the polymer composite from the 0.5 M solution does not (**Figure 7b**). The spectrum of Bi-ePA from Chapter 5 and **Figure 7a** are superimposable in the hydrogen bonding region, suggesting that the electrolyte in the

more concentrated sample has the same bonding motif as the stock electrolyte in the solid-state. The PVDF: $(Bi\text{-}ePa)_{0.15}$ polymer composite has a narrower linewidth for the electrolyte than the higher concentration mixture and the hydrogen bonding resonances are only visible through one resonance near 11.1 ppm. This resonance in the stock electrolyte is from the O-H∞O hydrogen bond of Bi-ePA and in the PVDF: $(Bi\text{-}ePa)_{0.15}$ polymer composite the hydrogen bonding resonances are undergoing exchange. This results from the fast local dynamics of the electrolyte in the pores of the polymer material. As the electrolyte fills the polymer the local motion of the electrolyte decreases. The smaller linewidth of the PVDF resonance in the PVDF: $(Bi\text{-}ePa)_{0.15}$ polymer composite (550 Hz versus 720 Hz) shows that the mobility for the latter composite material is greater than in the more concentrated composite. The mobility of the polymer backbone would require some free volume to accommodate some motion in the backbone of the polymer, while the more concentrated composite does not have as much free volume, restricting the motion of the polymer backbone.

The ^1H-^1H double quantum filter (DQF) spectra of the two PVDF: Bi-ePA composites in **Figure 8**, showed a reduction in the intensity of the resonances. Only resonances of protons that experience strong dipolar couplings are present in the DQF spectra of the polymer composites. The attenuation of the dipolar couplings in the PVDF: $(Bi\text{-}ePa)_{0.15}$ composite are a result of the high degree of local mobility. For the PVDF: $(Bi\text{-}ePa)_{0.37}$ polymer composite, the intensity of the ^1H-^1H DQF resonances decreased versus the regular ^1H MAS spectrum. The original electrolyte material also

experiences a decrease in DQF intensity for each resonance, the DQF signal of the two highest hydrogen bonds is 75 ± 3% of the original MAS signal.

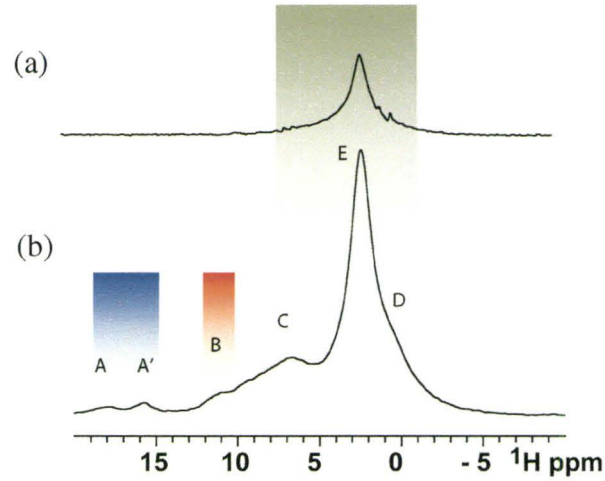

Figure 8 – The ^{1}H-^{1}H DQF spectra of (a) PVDF: (Bi ePa)$_{0.15}$ (b) PVDF: (Bi ePa)$_{0.37}$. The complete decay of the resonance from (a) shows that no strong dipolar couplings remain for the electrolyte.

For the PVDF: (Bi-ePa)$_{0.37}$ polymer electrolyte, the decay of the DQF signal for the same hydrogen bonds is 15 ± 2% of the original signal from the ^{1}H MAS spectrum. This shows that the electrolyte in the polymer composite material has significantly attenuated dipolar couplings compared to the pure electrolyte material. The attenuation of the dipolar couplings is caused by the motion of the polymer, which enhances the motion of the electrolyte.

The PVDF: (Bi-ePa)$_{0.15}$ composite has the higher local proton mobility at room temperature but the signal intensity in the ^{1}H NMR spectrum from the material is significantly less than the PVDF: (Bi-ePa)$_{0.37}$ composite. This can be seen from the

relative intensity of the two PVDF resonances, which acts as an internal standard. By comparison, the ^1H-^1H DQF spectrum of PVDF: $(Bi\text{-}ePa)_{0.15}$ has no observable intensity from the electrolyte than the PVDF: $(Bi\text{-}ePa)_{0.37}$ sample. The ionic conductivity of the polymer composites is used to determine whether the local mobility of the electrolyte actually contributes to the long range transport of ions through the electrolyte material. The ionic conductivity of the two PVDF: Bi-ePA polymer composites in **Figure 9** show that the PVDF: $(Bi\text{-}ePa)_{0.15}$ composite has a significantly lower ionic conductivity.

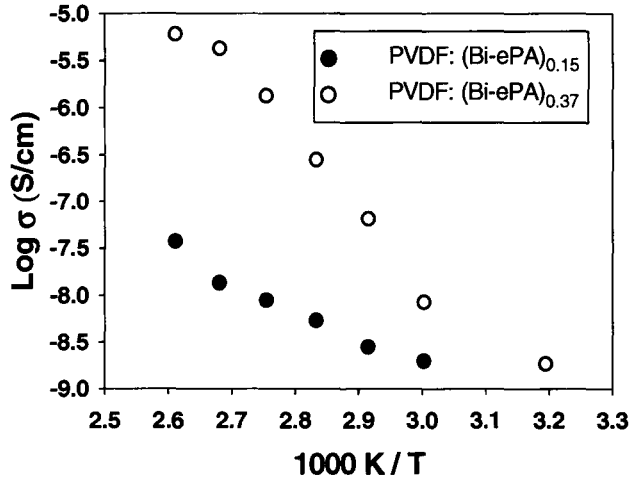

Figure 9 – The ionic conductivity of PVDF: Bi-ePA at two different concentration levels. The lower concentration has solid circles, while the higher concentration has open circles on the graph.

The ionic conductivity of the PVDF: $(Bi\text{-}ePa)_{0.15}$ composite does not scale with temperature as efficiently as the PVDF: $(Bi\text{-}ePa)_{0.37}$ composite. By 110°C, the PVDF: $(Bi\text{-}ePa)_{0.37}$ composite has reached 5.9×10^{-6} S/cm and is two orders of magnitude ahead of the PVDF: $(Bi\text{-}ePa)_{0.15}$ composite. This shows that the lower concentration of the electrolyte in the polymer material cannot transport ions as fast as the higher

concentration composite. This is attributed to the lower number of charge carriers in the PVDF: $(Bi\text{-}ePa)_{0.15}$ composite, which lowers the ionic conductivity. A summary of these findings are illustrated schematically in **Figure 10**.

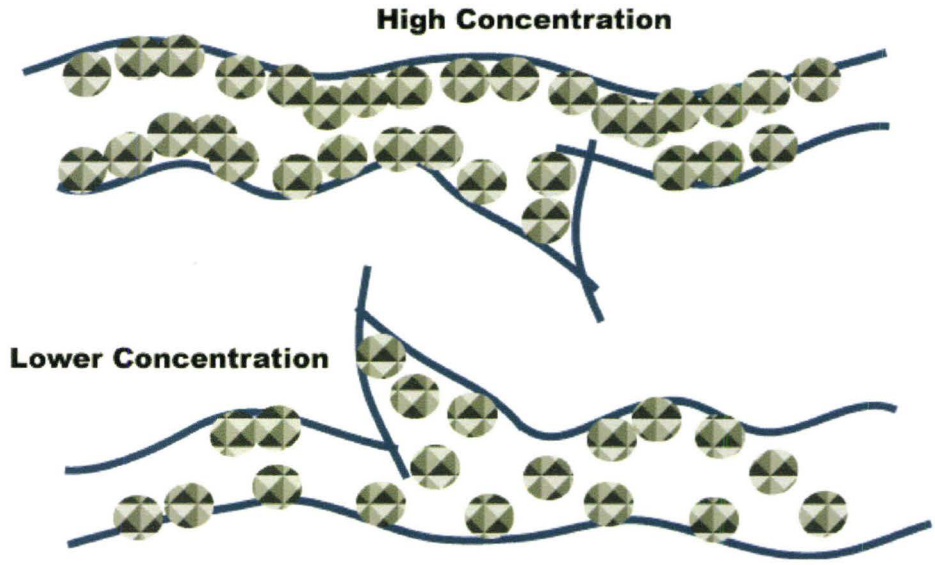

Figure 10 – An illustration of high and low concentration of electrolyte in the PVDF polymer composites. The blue lines represent the polymer and the grey hatched circles are the electrolyte.

The concentration of the electrolyte controls the amount of ion transport and in low concentration ion flow can be interrupted by a lack of a continuous network of the electrolyte. This confirms that the concentration of the electrolyte inside the polymer is extremely important in determining the macroscopic ionic conductivity. The graph in **Figure 9** implies that having more of a less mobile electrolyte is better than having less of a more mobile electrolyte, in cases where the polymer backbone is not active in proton transport. Thus, for the remainder of this chapter the concentrations of the electrolyte solutions used in the synthesis was maintained at 1 M. This concentration of electrolyte

solution is shown to be able to generate an ionic conductivity that is comparable to or better than other anhydrous electrolytes for use in a proton exchange membrane for fuel cells. [30-34]

7.3.2 – PTFE vs. PVDF

The interaction of the electrolyte and the polymer differs between PTFE and PVDF. The SEM images of PVDF: $(Bi\text{-}ePA)_{0.37}$ and PTFE: Bi-ePA in **Figure 11** shows the different morphologies of the two polymer composite materials. In **Figure 11a,** the PVDF composite is not fully saturated with electrolyte material and 1-5 μm pores still exist. The electrolyte in PVDF coats and forms around the polymer clusters observed in the earlier SEM images of **Figure 2**. This might ensure the transfer of protons through the structure but the lack of electrolyte in the free volume of the electrolyte would limit the number of charge carriers available to transfer ions between electrodes, reducing the ionic conductivity of the composite. Large amounts of free volume in the polymer composite could also permit unreacted hydrogen fuel to diffuse through the polymer and react with the oxygen at the cathode.

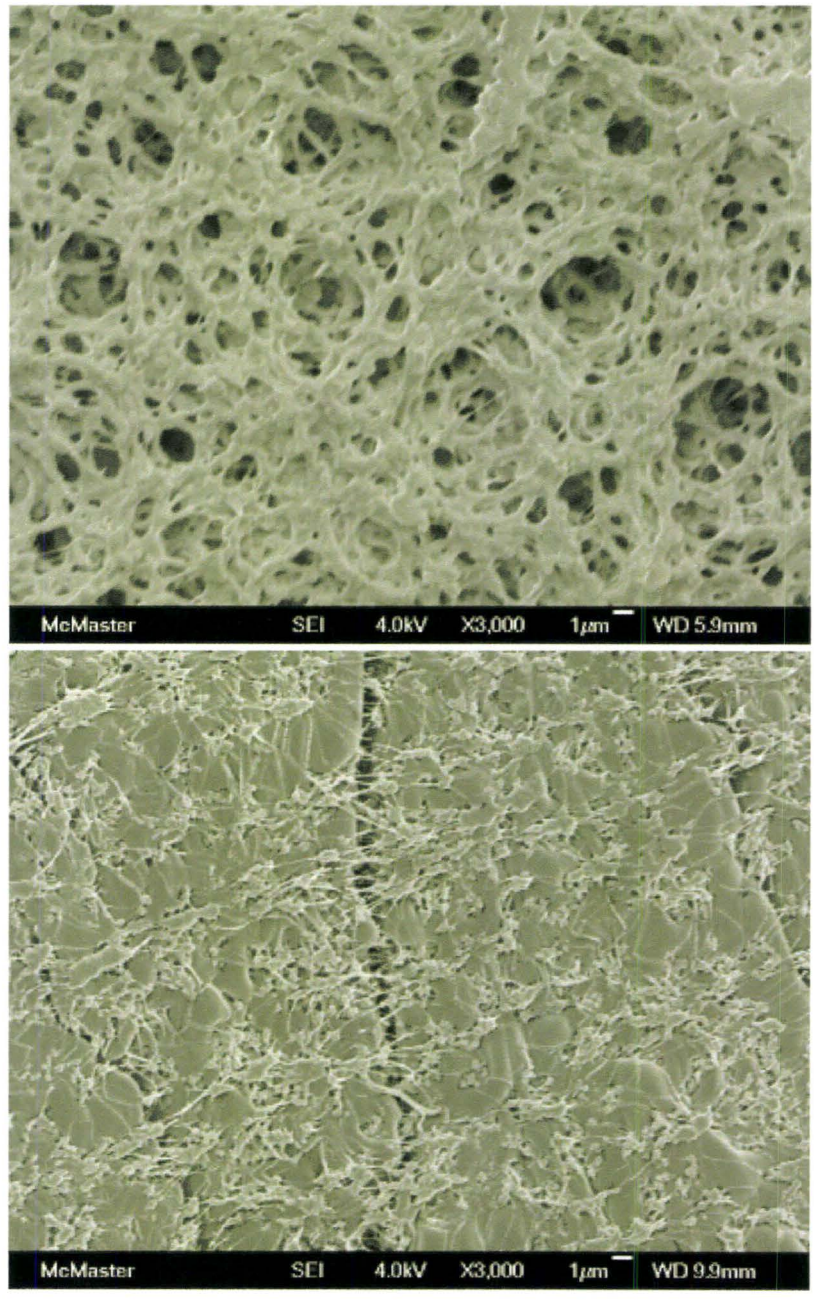

Figure 11 – The SEM images of the polymer composites (a) PVDF: $(Bi\text{-}ePA)_{0.37}$ and (b) PTFE: $(Bi\text{-}ePA)_{0.53}$, collected with x3000 magnification. The SEM images show the difference in morphology for the two materials.

In the SEM image of PTFE: Bi-ePA (**Figure 11b**) the polymer is fully saturated with electrolyte material. The electrolyte material forms large domains with the PTFE fibers included into the solid electrolyte. Thermogravimetric analysis of **Figure 12** reports that the electrolyte material in PTFE: Bi-ePA has 53% of the total weight of the sample. The free space that is available between electrolyte domains is spanned by PTFE fibers that provide support for the composite. Closer inspections of the surface show evidence that the PTFE strands are incorporated beneath the surface of the electrolyte domain. The surface of the PTFE composite is more uniform than the surface of the PVDF composite and would provide more surface area for the catalyst to transfer ions into the electrolyte. The PTFE samples would also prevent hydrogen crossover since the composite is a solid material. The large electrolyte domains would also be able to transport more ions due to the large amount of charge carriers present at the surface of the polymer composite.

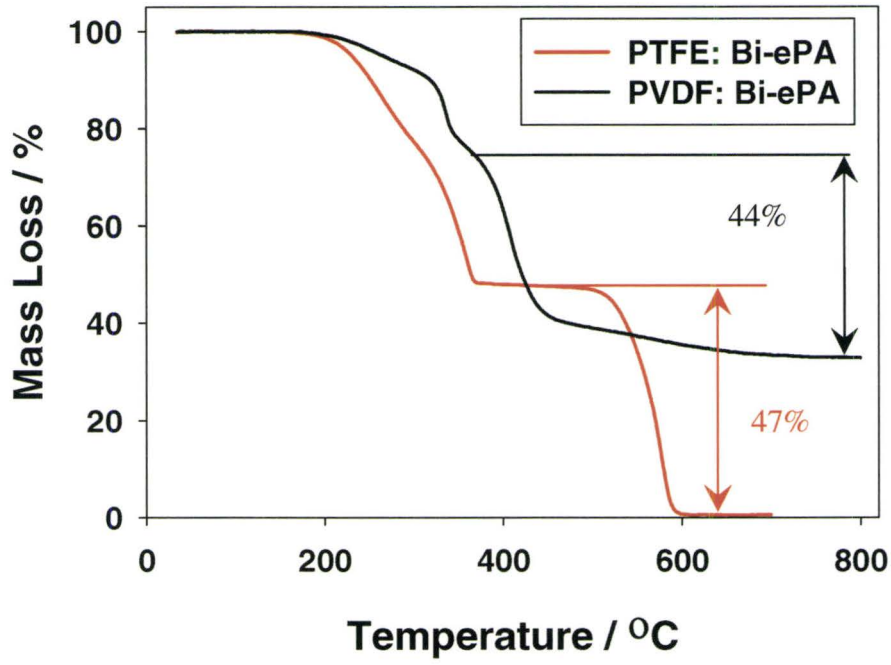

Figure 12 – The TGA traces of PTFE: Bi-ePA (red) and PVDF: Bi-ePA (black). Mass loss of pure PTFE showed a 100% mass loss of its mass. Thus, the total PTFE in the composite is 47%.

The protons of PVDF overlap with the alkyl groups of the model salts from Chapters 5 and 6. The overlap of the PVDF protons crowds the spectrum and obscures the resonances of the electrolyte. By replacing the PVDF with PTFE, the electrolyte material becomes easier to observe in the ^{1}H NMR. This greatly decreases the complexity of spectrum and increases the sensitivity of the experiment. The ^{1}H MAS spectrum of PTFE: $(Bi\text{-}ePA)_{0.53}$ in **Figure 13a** has no resonances relating to the backbone of the polymer and the alkyl resonances are easily observed. In the ^{1}H MAS spectrum the alkyl resonances are beginning to split in to separate resonances, indicating an increase in mobility over the pure electrolyte material.

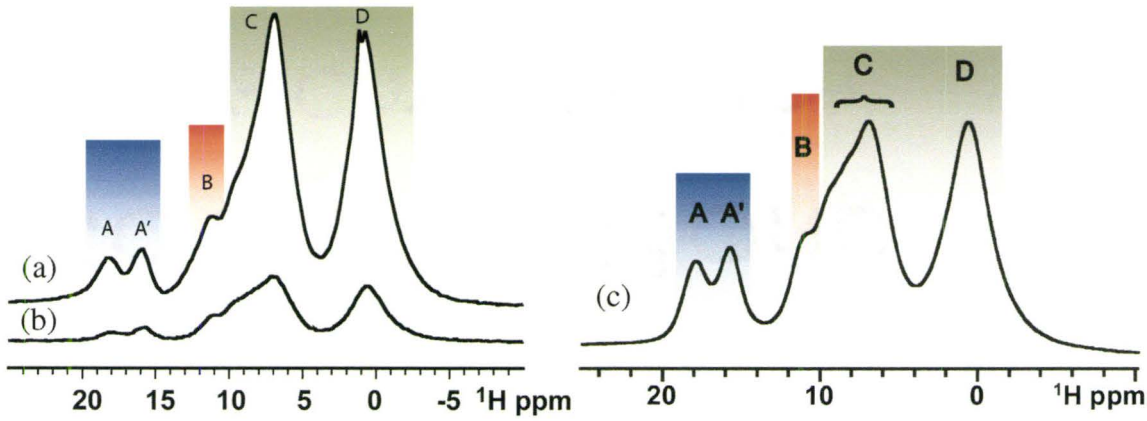

Figure 13 – (a) The ^{1}H MAS spectrum of PTFE: $(Bi\text{-}ePA)_{0.53}$ at 25kHz MAS. The benefit of switching to PTFE is that there are no polymer resonances in the spectrum. (b) The ^{1}H-^{1}H DQF spectrum using $1\tau_R$ of recoupling for PTFE: $(Bi\text{-}ePA)_{0.53}$. (c) The ^{1}H MAS spectrum of the pure electrolyte.

Fitting the lineshape of the PTFE: $(Bi\text{-}ePA)_{0.53}$ protons from the ^{1}H MAS spectrum to the original Bi-ePA pattern, showed that the mobile ethyl resonances comprise 10 % of the total signal for the ethyl protons. A similar result from a study of rubidium methylphosphonate suggested that the alkyl group experiences the onset of dynamics prior to the protons in the hydrogen bonded network.[35] The increased mobility of the ethyl protons within the composite supports the hypothesis that the polymer composite has increased dynamics over the pure electrolyte. The increased dynamics implies that the composite will serve as a better proton conductor than the pristine electrolyte, in addition to offering superior mechanical properties.

In the ^1H-^1H DQF of **Figure 13b** the spins that do not have rigid dipolar coupling do not observed in the spectrum. The remaining protons in the spectrum correspond to spins in the electrolyte material that are not mobile. The distribution and linewidth of the resonances in the rigid portion of the electrolyte resemble the spectrum of the pure electrolyte.

The structure of PTFE: $(Bi\text{-}ePA)_{0.53}$ is similar to that of the pure material because the two spectra are very close and contain the same type and distribution of resonances. The 2D ^1H-^1H double quantum correlation (DQC) spectra of **Figure 14** show that the rigid phase of the polymer composite has the same dipolar contacts as the pure electrolyte material. The dipolar coupling contacts of **Table 2** confirm that the polymer composite has the same local structure as the pure electrolyte that was presented in Chapter 5. Since the mobile phase has the same chemical shift as the rigid spins, then the structure of the mobile phase is simply a more dynamic domain of the electrolyte. The mobile phase of the electrolyte in PTFE: $(Bi\text{-}ePA)_{0.53}$ attenuates the dipolar couplings through fast molecular dynamics but is not strong enough to narrow the linewidth of the resonances significantly. An increase in thermal energy should trigger the growth of the mobile domain within the polymer composite.

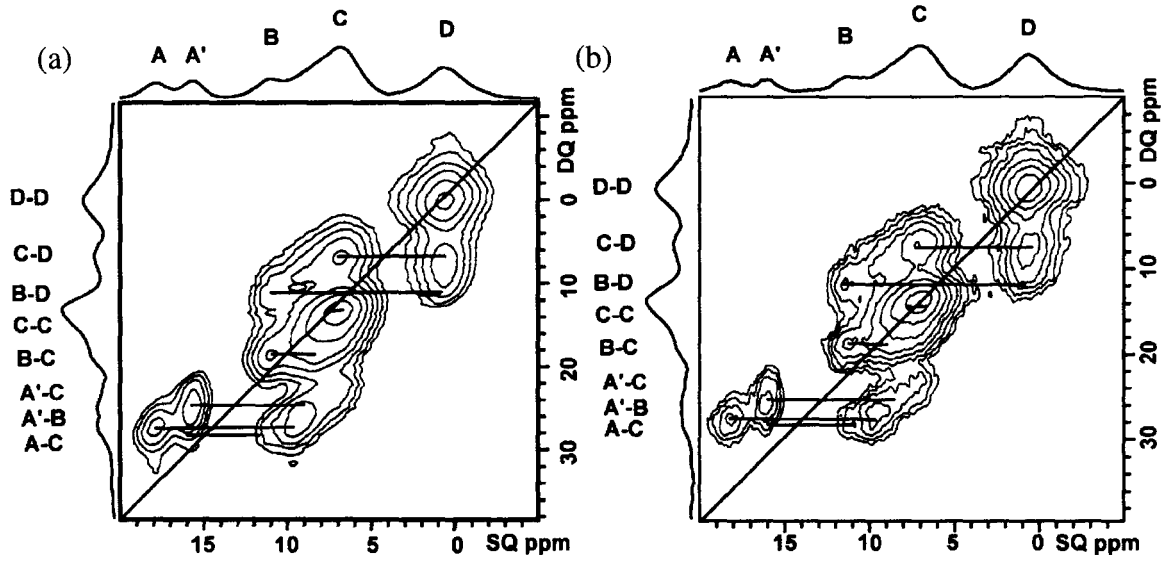

Figure 14 – The 2D ^{1}H-^{1}H DQC spectra of (a) pure Bi-ePA and (b) PTFE: $(Bi\text{-}ePA)_{0.53}$ collected using 1 τ_R of recoupling at 25 kHz MAS. The two materials are remarkably similar and the polymer composite has all of the dipolar coupling contacts of the pure electrolyte.

Table 2 – The hydrogen bonding dipolar contacts from the ^{1}H-^{1}H DQC for the pure electrolyte and PTFE: $(Bi\text{-}ePA)_{0.53}$.

Dipolar Coupling	Pure Electrolyte (ppm)		Polymer Composite (ppm)	
	SQ/SQ	DQ	SQ/SQ	DQ
AC	18.1/9.6	27.7	18/9.6	27.6
A'C	16.0/7.5	23.5	16.0/8.0	24.0
A'B	16.0/11.3	27.3	16.0/11.1	27.1
BC	11.1/7.9	19.0	11.3/7.5	18.8
BD	11.0/0.3	11.4	11.3/0.4	11.7

7.3.3 – Polymer Dynamics

The microscopic structure has a large impact on the mobility of the protons, as observed in the ^1H NMR spectra, whereas impedance spectroscopy characterizes the macroscopic transport of ions and also depends on the morphology of the electrolyte in the polymer. The ionic conductivity of the PVDF: Bi-ePA and PTFE: Bi-ePA are shown in **Figure 15**.

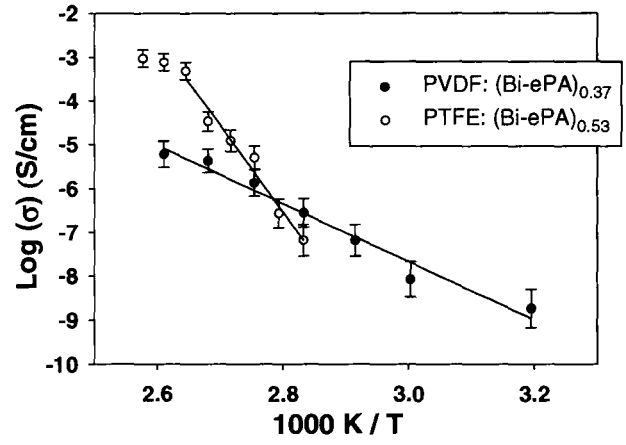

Figure 15 – A plot of the ionic conductivity of PVDF: $(Bi\text{-}ePA)_{0.37}$ (•) and PTFE: $(Bi\text{-}ePA)_{0.53}$ (◦) from impedance spectroscopy. The ionic conductivity of the two polymers scales differently with temperature, indicating a difference in activation energy between the two composite materials. Both linear regression have R values of 0.99.

The ionic conductivity of PTFE: $(Bi\text{-}ePA)_{0.53}$ reaches a maximum conductivity value of 9.5×10^{-4} S/cm at 115°C under dry conditions. The conductivity of the PTFE polymer is two orders of magnitude larger than the PVDF polymer at the highest temperatures. The activation energy for the PVDF polymer is 55 ± 4 kJ/mol, while for the PTFE polymer the activation energy is 160 ± 10 kJ/mol. The ionic conductivity of the PTFE sample is

greater, and thus requires high temperatures to reach the maximum potential for the polymer membrane. The ionic conductivity plateaus near 105°C, this is below the melting point of the electrolyte in the polymer composite at 120°C. This shows that the material is not undergoing a phase transition and the mobility is related to the solid-state dynamics.

The NMR spectra of the two polymer composites in **Figure 13a** (PTFE) and **Figure 7a** (PVDF) have a similar spectrum for the electrolyte material. Thus, the local structure of the electrolyte material is similar. The major factor influencing the ionic conductivity between the two polymer composites is the morphology of the polymer host and the material's response to an increase in temperature. In **Figure 11**, the two SEM images of the polymer composites are radically different, leading to the significant difference in ionic conductivity at high temperatures. The higher concentration of the electrolyte in the PTFE composite (53% for PTFE versus 37% for PVDF) leads to the larger number of charge carriers, creating a large ionic conductivity for the PTFE composite. The stock solutions used to cast the electrolyte into the polymer had the same concentration of electrolyte material, yet the uptake of the electrolyte is different. This shows that the PTFE is better at absorbing the electrolyte material and further comparison of electrolyte materials will use the PTFE polymer in order to obtain the highest ionic conductivity.

7.3.4 – Proton Dynamics

The ability of the electrolyte to transport ions is fundamental for obtaining a high ionic conductivity and depends on the local structure of the electrolyte. In Chapter 5, the ion conduction mechanism of Bi-ePA was discussed. The motion of the phosphonate in the pure electrolyte material occurs prior to the narrowing of the aromatic resonances. The ^1H variable temperature study showed that the hydrogen bonding resonances experienced line narrowing prior to the aromatic protons of the benzimidazole ring. The ^1H NMR study of PTFE: $(Bi\text{-}ePA)_{0.53}$ in **Figure 16a** shows similar trend.

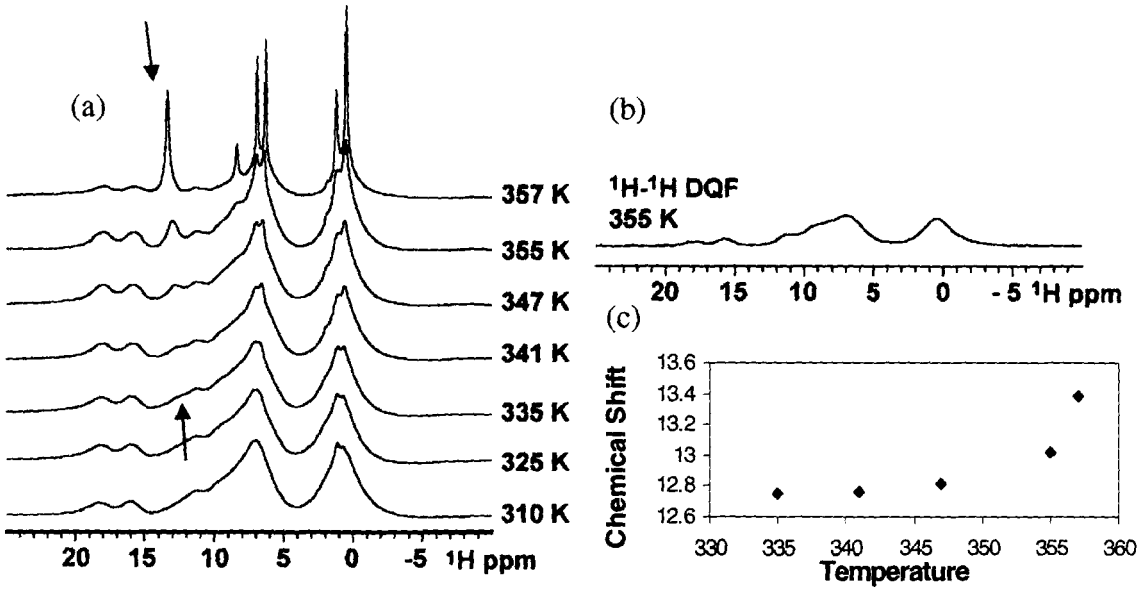

Figure 16 – (a) The ^1H variable temperature spectra of PTFE: $(Bi\text{-}ePA)_{0.53}$, (b) the ^1H-^1H DQF spectrum, (c) chart of the chemical shift trends of the new hydrogen bonding resonance. The new resonance that appears near 12.7 ppm does not have any strong dipolar coupling and there is not seen in the ^1H-^1H DQF spectrum.

The new resonance of **Figure 16a** at 341 K experiences a chemical shift change with temperature towards higher ppm and increases in intensity. Increasing the chemical shift of the indicates that these protons are exchanging with the protons at higher chemical shift. The first appearance of the mobile hydrogen bond is at 335 K with a chemical shift of 12.7 ppm. The average of the A' and B resonances is 13.6 ppm, this shows that the resonance is not fully exchanging between the two sites. As the temperature increases, the new resonance shifts to a higher chemical shift values, indicating that the amount of exchange between the N-H∞O hydrogen bonds is increasing. The chemical shift of the new resonance does not reach the average value for all three resonances in the temperature range of this study. The highest chemical shift observed in the temperature limit of the spectrometer was 13.4 ppm, the trend is shown in **Figure 16c**. This indicates that full exchange between the three sites has yet to be achieved within this temperature range. Thus, the dominant motion creating the exchange of the A' and B hydrogen bonds remains the rotation of the phosphonate.

The increase in intensity of the mobile phase parallels a decrease in the intensity of rigid phase. The remaining resonances that seem unaffected by temperature retain some residual dipolar couplings and are shown in the ^{1}H-^{1}H DQF spectrum (**Figure 16b**). The narrow resonances of the variable temperature plot do not are appear in **Figure 16b** because those resonances experience strongly attenuated dipolar couplings from the molecular motion. By 357 K, the mobile portion of the electrolyte includes 45% of the spins in the sample, indicating that the material is extremely dynamic at high

temperatures, although this is well below the melting point of the pure electrolyte. The onset of the plateau in the ionic conductivity matches the significant change in dynamics observed in the ^{1}H NMR spectra. This implies that the ionic conductivity is driven by the local dynamics observed via solid-state NMR.

The ^{1}H variable temperature MAS and the ^{1}H-^{1}H DQF have shown that both a rigid and mobile phase exists in the polymer composite at high temperatures. In **Figure 17**, a model of the PTFE: $(Bi\text{-}ePA)_{0.53}$ composite is proposed. At low temperatures in the model, the electrolyte surrounds the polymer material. However, at higher temperatures the electrolyte divides into two general domains, a rigid domain and a mobile domain. The mobile domain (shown in red) is responsible for the narrow resonances in the ^{1}H MAS spectra. The rigid domain, (shown in black) corresponds to the protons of the ^{1}H MAS spectra that do not experience line narrowing. This model approximates the range of dynamics of the electrolyte, observed by NMR.

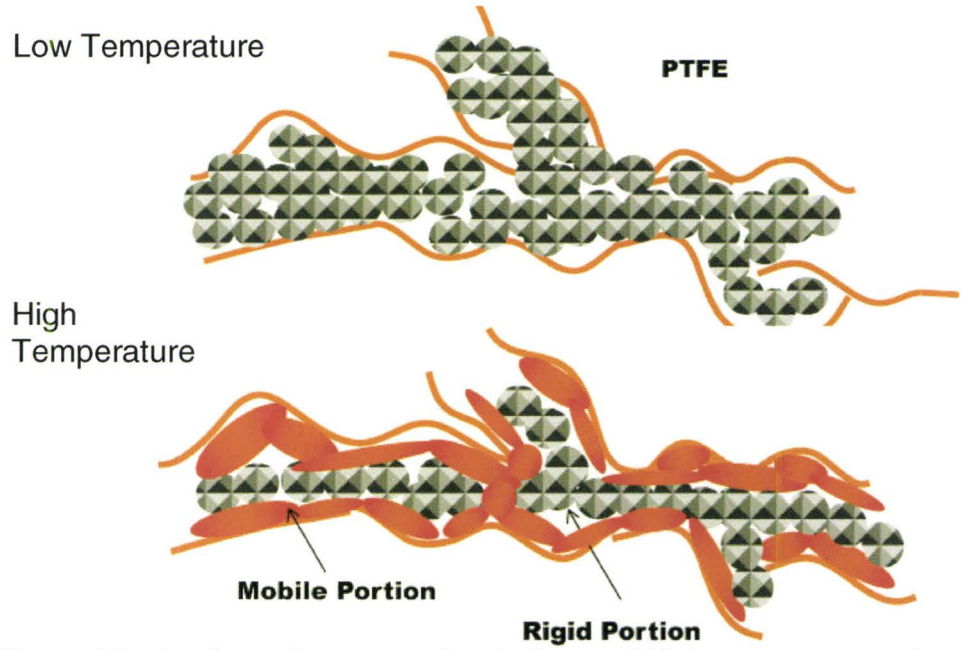

Figure 17 – A schematic representing the low and high temperature regimes in PTFE: $(Bi\text{-}ePA)_{0.53}$. The orange lines represent the polymer, grey hatched circles for the rigid electrolyte, and the red gradient represents the mobile domains of the electrolyte.

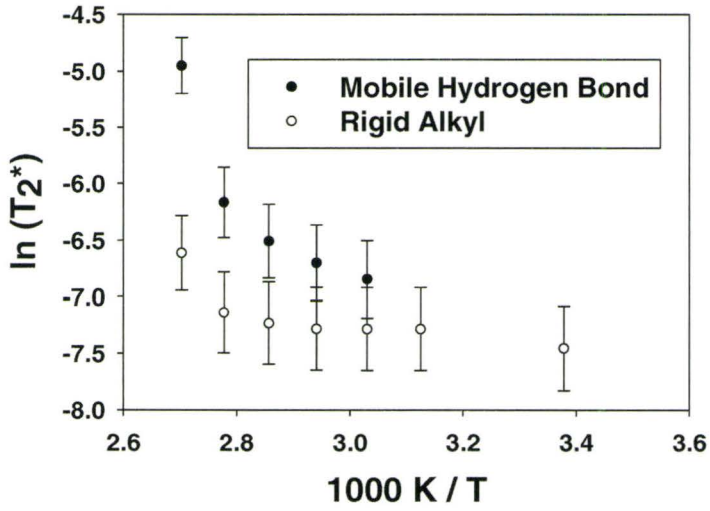

Figure 18 – A plot of the natural logarithm of T_2^* versus 1000 K / T shows the change of the linewidth with temperature for PTFE: $(Bi\text{-}ePA)_{0.53}$. The data exhibits non-linear behavior consistent with the influence of available free volume on polymer back bone dynamics.[36]

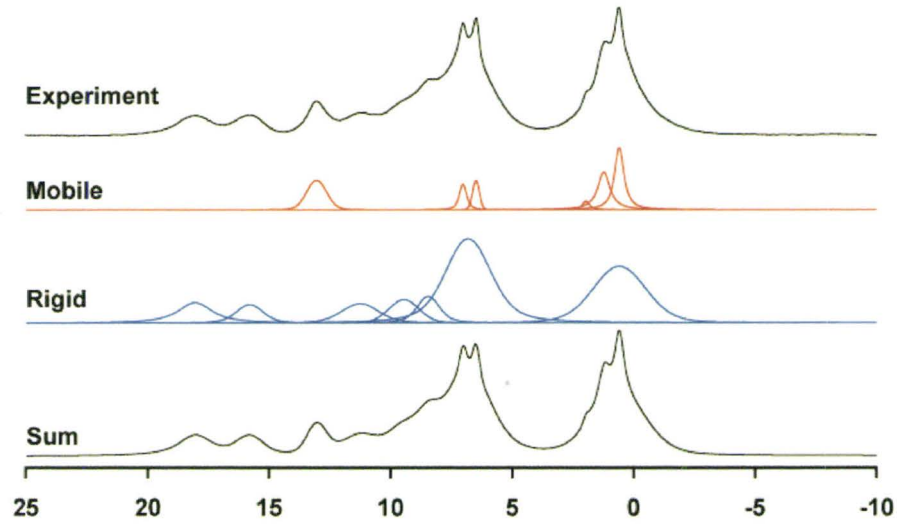

Figure 19 – The fit of the 355 K ^{1}H MAS spectrum of PTFE: $(Bi\text{-}ePA)_{0.53}$. The red lines are for mobile resonances, blue for immobile, and black is the total fit and the experiment. Traces of the methanol solvent occurs at 1.95 ppm.

Line fitting of all the resonances shows that the material exhibits non-Arrhenius behavior with temperature as seen in **Figure 18**, while **Figure 19** shows the quality of the line fitting. The result of the line fitting are summarized in **Table 3**. In amorphous polymer systems above the glass transition temperature, the motion of the polymer cannot be described by an Arrhenius process. Rather the system deviates from linearity and follows more closely the exponential model of Williams-Landel-Ferry (WLF).[36] The model suggests that the free volume of the polymer influences the apparent viscosity, and rates of molecular rearrangement of a material. The non-linear behavior of the line narrowing shows that the nature of the polymer backbone is influencing the dynamics of the electrolyte. The mobile alkyl and aromatic spins create resonances that narrow with temperature and do not experience a change in chemical shift. For the hydrogen bonded protons, the mobile protons coalesce into the new resonances at 12.7 ppm. From the

^{1}H MAS variable temperature experiments it is clear that the dynamics of the material begin by exchanging the A' and B protons. To further investigate the dynamics we turn to multinuclear techniques.

Table 3 – A summary of the line fitting for the ^{1}H spectrum of PTFE: $(Bi\text{-}ePA)_{0.53}$ at 355 K. Fitting of the lineshapes used the Peakfit program with a Voigt profile to determine the area and the linewidth, the fitting used an iterative least squares routine to fine the best fit.

Assignment	Shift (ppm)	Area ± 0.2 %	Full Width Half Max (Hz) ± 10-20 Hz	Type
D	0.57	5.8	230	Mobile
D	1.21	4.8	30	Mobile
Solvent	1.95	0.6	170	Mobile
C	6.46	1.4	160	Mobile
C	7.00	1.7	180	Mobile
A'B	13.02	4.4	480	Mobile
D	0.57	22.6	1280	Rigid
C	6.79	31.9	1110	Rigid
C	8.44	5.0	540	Rigid
C	9.44	5.2	720	Rigid
B	11.24	5.7	880	Rigid
A'	15.79	4.0	640	Rigid
A	18.02	6.9	820	Rigid

7.3.5 – Phosphonate Dynamics

The CODEX pulse sequence is able to determine the rotation rate and geometry of a motion via a change in the chemical shift anisotropy. The technical description of CODEX and the application of the sequence to the materials in this chapter is given in Chapter 2. The exchange curve for PTFE: $(Bi\text{-}ePA)_{0.53}$ is given in **Figure 20**.

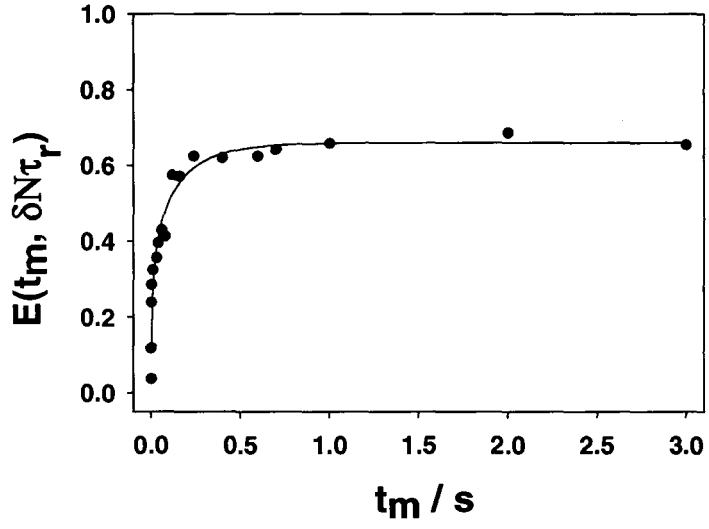

Figure 20 – The ^{31}P CODEX NMR pure exchange curve for PTFE: $(Bi\text{-}ePA)_{0.53}$. The exchange curve best fit a stretched exponential with a very broad distribution of environments for the correlation time of the phosphonate.

The pure exchange curve represent the motion of the phosphonates in the electrolyte. The variable temperature ^1H NMR spectra of PTFE: Bi-ePA showed that the T_2^* does not follow typical Arrhenius behavior. From this it can be inferred that the dynamics of the material are complex and distributed. Due to the distribution of possible correlation times resulting from the polymer environment, a stretched exponential fit was necessary to accurately describe the exchange curve. In **Table 4**, the results of the ^{31}P CODEX

NMR on the PTFE: $(Bi\text{-}ePA)_{0.53}$ polymer composite show the trend of the material with temperature and the distribution of the correlation times.

$$E_{\infty}(t_m, \delta N \tau_R) = A(1 - \exp(-t_m / \tau_c)^B) \quad (7\text{-}1)$$

Table 4 – A summary of the best fits for the ^{31}P CODEX NMR exchange curves.

Temperature / K	A / %	τ_C / s	B
293	66 ± 2	0.210 ± 0.08	0.27 ± 0.04
305	63 ± 2	0.140 ± 0.03	0.51 ± 0.06

The prefactor (A) of the exponential fits depict the geometry of the rotation. For the alkyl phosphonates, a three-fold rotation occurs around the P-C bond. This result echoes the result from the pure electrolyte, which also showed the three-fold motion. Only in the phosphate electrolyte of Chapter 5 did a four-fold motion occur. The correlation times (τ_C) and the exponential parameter (B) show rate of the reorientation and the distribution of correlation times, respectively. The correlation time decreases with temperature as expected for any thermally driven rotation. However, the standard deviation in the correlation time at room temperature is significant and decreases with temperature. The large deviation is a result of the very broad distribution of correlation times in the polymer composite. The exponential parameter for Bi-ePA in the pure electrolyte is one, while for the polymer composite the value is 0.27 ± 0.04. This shows that there is a large range of correlation times for the phosphonate due to different local environments of the polymer architecture. The broad distribution of correlation times increases the standard deviation of the mean correlation time. As the temperature increases, the exponential

parameter increases, indicating that the distribution of correlation times is narrowing, and the dynamics are becoming more uniform within the composite. The increase in the exponential parameter reduces the deviation from the mean for the correlation times for this data set. The increased temperature also increases the motion of the phosphonate resulting in a lower average correlation time, as expected.

7.4 – Summary

There are several important factors that influence the ionic conductivity of the polymer composite. At low concentrations of electrolyte material in the composite there are insufficient charge carriers, and a lack of connectivity among domains. This results in a low ionic conductivity. This was shown by changing the concentration of the electrolyte material in the polymer. The choice of polymer material determines the uptake and binding of the electrolyte into the pores of the polymer. It was determined that PTFE was a superior polymer due to the strong uptake of electrolyte material over PVDF. The concentration of electrolyte adsorbed into the two polymer composites was enhanced by nearly 20% in PTFE than in PVDF. The higher concentration of electrolyte increased the ionic conductivity by two orders of magnitude in the PTFE composite over the PVDF composite. The last major factor studied here is the overall transport properties of the electrolyte. It was found that Bi-ePA in PTFE showed non-Arrhenius behavior that was consistent with backbone motion of the polymer influencing the transport of ions in the electrolyte. This created mobile and rigid domains that varied in

the amount of dynamics observed at higher temperatures. The difference was that the polymer backbone causes a distribution in the rates of motion, this was observed in the ^{31}P CODEX NMR. The distribution of the dynamics decreases with temperature as more sites become involved in the chemical exchange. The high concentration of electrolyte and mobility of the ions at higher temperatures ensures that these materials are viable anhydrous electrolytes for fuel cells. Further testing in a fuel cell environment would determine the overall success of the polymer composite.

7.5 – References

1. N. G. Boyle, V. J. McBrierty and D. C. Douglass, *Macromolecules*, 1983, **16**, 75-80.
2. M. Ciureanu, *J. Appl. Electrochem.*, 2004, **34**, 705-714.
3. Q. Li, R. He, J. O. Jensen and N. J. Bjerrum, *Fuel Cells* 2004, **4**, 147-159.
4. Y. F. Zhai, H. M. Zhang, G. Liu, J. W. Hu and B. L. Yi, *J. Electrochem. Soc.*, 2007, **154**, B72-B76.
5. S. Yu, L. Xiao and B. C. Benicewicz, *Fuel Cells*, 2008, **8**, 165-174.
6. E. Ortiz, R. A. Vargas and B. E. Mellander, *J. Chem. Phys.*, 1999, **110**, 4847.
7. T. Uda and S. M. Haile, *Electrochem. Solid-State Lett.*, 2005, **8**, A245-A246.
8. A. Preisinger, K. Mereiter and W. Bronowska, *Mater. Sci. Forum*, 1994, **166-169**, 511-516.
9. E. Ortiz, R. A. Vargas and B. E. Mellander, *Solid State Ionics*, 1999, **125**, 177-185.
10. A. Sezgin, U. Akbey, R. Graf, A. Bozkurt and A. Baykal, *J. Polym. Sci. Pt. B-Polym. Phys.*, 2009, **47**, 1267-1274.
11. U. Akbey, R. Graf, Y. G. Peng, P. P. Chu and H. W. Spiess, *J. Polym. Sci. Pt. B-Polym. Phys.*, 2009, **47**, 138-155.
12. H. Ye, J. Huang, J. J. Xu, N. Kodiweera, J. R. P. Jayakody and S. G. Greenbaum, *J. Power Sources*, 2008, **178**, 651-660.
13. M. Jithunsa, K. Tashiro, S. P. Nunes and S. Chirachanchai, *Polym. Degrad. Stab.*, 2008, **93**, 1389-1395.
14. P. K. Singh, K. W. Kim and H. W. Rhee, *Synth. Met.*, 2009, **159**, 1538-1541.
15. M. C. Lechmann, D. Kessler and J. S. Gutmann, *Langmuir*, 2009, **25**, 10202-10208.
16. J. E. Benedetti, A. D. Goncalves, A. L. B. Formiga, M. A. De Paoli, X. Li, J. R. Durrant and A. F. Nogueira, *J. Power Sources*, 2010, **195**, 1246-1255.
17. G. J. M. P. van Moorsel, E. R. H. Vaneck and C. P. Grey, *J. Magn. Reson., Ser. A*, 1995, **113**, 159-163.
18. C. E. Housecroft and A. G. Sharpe, *Inorganic Chemistry*, Pearson Education Limited, Harlow, Essex, United Kingdom, 2001.
19. C. S. Coughlin, K. A. Mauritz and R. F. Storey, *Macromolecules*, 1991, **24**, 1526-1534.
20. C. S. Coughlin, K. A. Mauritz and R. F. Storey, *Macromolecules*, 1990, **23**, 3187-3192.
21. K. A. Mauritz and R. F. Storey, *Macromolecules*, 1990, **23**, 2033-2038.
22. K. A. Mauritz, R. F. Storey and S. E. George, *Macromolecules*, 1990, **23**, 441-450.
23. J. Roziere and D. J. Jones, *Annu. Rev. Mater. Res.*, 2003, **33**, 503-555.
24. T. Xie and C. A. Hayden, *Polymer*, 2007, **48**, 5497-5506.
25. C. Chen and T. F. Fuller, *Polym. Degrad. Stab.*, 2009, **94**, 1436-1447.

26. J. Xie, D. L. Wood Iii, D. M. Wayne, T. A. Zawodzinski, P. Atanassov and R. L. Borup, *J. Electrochem. Soc.*, 2005, **152**, A104-A113.
27. T. Kinumoto, K. Takai, Y. Iriyama, T. Abe, M. Inaba and Z. Ogumi, *J. Electrochem. Soc.*, 2006, **153**, A58-A63.
28. K. Schmidtrohr and H. W. Spiess, *Macromolecules*, 1991, **24**, 5288-5293.
29. E. A. Zubova, N. K. Balabaev and L. I. Manevitch, *Polymer*, 2007, **48**, 1802-1813.
30. A. Aslan and A. Bozkurt, *J. Power Sources*, 2009, **191**, 442-447.
31. S. T. Günday, A. Bozkurt, W. H. Meyer and G. Wegner, *J. Polym. Sci. Pt. B: Polym. Phys.*, 2006, **44**, 3315-3322.
32. A. Bozkurt, W. H. Meyer, J. Gutmann and G. Wegner, *Solid State Ionics*, 2003, **164**, 169-176.
33. A. Bozkurt, M. Ise, K. D. Kreuer, W. H. Meyer and G. Wegner, *Solid State Ionics*, 1999, **125**, 225-233.
34. A. Bozkurt and W. H. Meyer, *Solid State Ionics*, 2001, **138**, 259-265.
35. M. Vijayakumar, J. W. Traer, J. F. Britten and G. R. Goward, *The Journal of Physical Chemistry C*, 2008, **112**, 5221-5231.
36. M. L. Williams, R. F. Landel and J. D. Ferry, *J. Am. Chem. Soc.*, 1955, **77**, 3701-3707.

Chapter 8: Summary and Outlook

8.0 – Summary

Solid-state nuclear magnetic resonance (NMR) is a valuable tool for understanding the local environment and dynamics of the hydrogen nucleus. The application of advanced NMR techniques such as ^{1}H dipolar recoupling, variable temperature, multinuclear spectra, and exchange techniques allowed for the in depth investigation of the molecular dynamics of several electrolyte materials. The impetus of this research was understanding the processes involved in the local dynamics that lead to ionic conductivity in anhydrous proton electrolytes for fuel cells. The materials investigated ranged from solid acid electrolyte, model compounds, and novel anhydrous electrolytes.

Anhydrous electrolytes are protic materials that are able to transport hydrogen ions with a minimal amount of hydration and operate at higher temperatures to reduce carbon monoxide poisoning of the catalyst material. Anhydrous electrolytes offer a significant improvement over hydrated electrolytes because they do not require humidification of the fuel. The first electrolyte investigated was the solid acid compound, cesium dihydrogen phosphate (CDP). The mechanism of ion transport in the solid-state was suggested to occur through the phosphate rotation. ^{31}P CODEX NMR shows that the phosphate undergoes a four-fold reorientation near the 100ms timescale at

room temperature. Molecular dynamics studies suggest that the phosphate rotation is the limiting process in the conduction of ion in CDP. The activation energy of the phosphate rotation by ^{31}P CODEX NMR was 74 ± 1 kJ/mol. This is lower than the 95 kJ/mol activation energy for long range transport, from impedance spectroscopy. This confirms that the rate limiting step for the transport of ions in CDP is the rotation of the phosphate. The dehydration temperature of CDP depends on the grain size and level of humidity, meaning that this solid acid has a very limited operating temperature window. Modification of the phosphate to alkyl phosphonate was able to provide ion conduction at lower temperatures and avoid the thermal decomposition. The ^{31}P CODEX NMR for this compound showed that the phosphonate rotation has a correlation time of 34 ± 5 ms and had a activation energy that was 11 ± 3 kJ/mol. With a smaller barrier for rotation, the phosphonate would be able to transport ions at temperatures below 200°C.

Acidified polymers are successful alternatives to hydrated electrolytes. However, they suffer from poor ionic conductivity in the absence of the acid medium. To study these materials several models were used to depict the types of ion transport available to the polymer. The model compounds used the benzimidazole ring and phosphate based anions. The ^{1}H solid-state NMR experiments showed that the dynamics of the materials began at the hydrogen bonds involving the anions. It was found through ^{31}P CODEX NMR that the type of phosphate controlled the geometry of the motion. For a phosphate, it is possible for the four oxygen atoms to exchange, while the alkyl phosphonates were limited to three-fold rotation. The timescale for the reorientations from ^{31}P CODEX

NMR showed that the addition of the methyl group did not hinder the ability of the phosphonate to rotate and the phosphonate retained a similar correlation time for the motion. The rotation rate of the phosphate was 56 ± 3 ms, for the methylphosphonate it was 75 ± 6 ms. The absence of the ring dynamics in the ^{1}H NMR and no observable motion in the ^{13}C CODEX NMR showed that the benzimidazole rings were not contributing to ion transport. This explains, the poor ionic conductivity of the polymer membrane without any liquid acid. The activation energy of methylphosphonate was 7 ± 1 kJ/mol and 3.2 ± 0.3 kJ/mol for ethylphosphonate. The barrier of rotation for the phosphate in CDP was found to be 74 ± 1 kJ/mol. The difference between the two types of activation energies is due to the type of motion involved. The four-fold motion creates a high barrier for rotation, while the three fold motion of the phosphonates has a small barrier. This shows the geometry dependence of the rotation in the solid-state.

Our selection of anhydrous electrolytes moved away from large bulky ring systems towards smaller rings. The smaller ring system like imidazole or triazole may provide a mobile cation and thereby an additional pathway for ion conduction, improving the total ionic conductivity. The ionic conductivity of the model compound using imidazole as the cation was two orders of magnitude larger than its benzimidazole counterpart. The correlation time for phosphonate dynamics from ^{31}P CODEX NMR is 58 ± 4 ms. The rotation of the imidazole ring was detected through ^{13}C CODEX NMR, with a correlation time of 31 ± 9 ms. ^{1}H NMR variable temperature experiments confirmed that resonances belonging to the imidazole narrowed at high temperatures.

The activation of the ring at high temperatures created a second mechanism of ion transport that improved the ionic conductivity.

The mobility of the ions in the model compounds made them viable electrolytes. The creation of a new anhydrous electrolyte material was accomplished by combining an inert polymer host with the model compounds as the electrolyte material. Impedance spectroscopy showed that these new electrolytes could transport ions without the aid of a liquid electrolyte. The maximum ionic conductivity was obtained using the highest ratio of electrolyte to polymer material. From the ^{1}H solid-state NMR experiments, it was proposed that the higher concentrations of the electrolyte created a continuous electrolyte domain. The polymer composites with large electrolyte domains had fewer bottlenecks and more charge carriers to transport ions. These factors contributed to the high ionic conductivity of the material. The ^{1}H variable temperature spectra and the ^{31}P CODEX NMR found that polymer composite was comprised of both rigid and mobile components. Even at high temperatures a significant portion of the rigid phase remained. The ionic conductivity of the ethylphosphonate polymer composite reached $1x10^{-3}$ S/cm at 115°C. This ionic conductivity shows that the polymer composites are a competitive class of electrolytes for anhydrous fuel cells.

8.1 – Outlook

The strong ion dynamics observed in the solid-state NMR spectra and impedance spectroscopy prove that the polymer composites are suitable candidates for hydrogen fuel

cells. The solid-state NMR experiments are able to investigate the structure and dynamics of a material on the molecular level. Proton experiments such as the ^{1}H-^{1}H double quantum correlation spectra are used to assign the resonances of the spectrum and determine the local packing of the structure. From the assignment of the resonances, the variable temperature spectra record the behavior and trends in the material with temperature. Advanced multinuclear experiments like CODEX are able to determine the geometry and rate of a specific motion. This type of characterization enables us to determine the specific contribution of each group to transport of ions in the solid-state. The activation energies from solid-state NMR are a measure of the local dynamics, while impedance spectroscopy provides the characterization of the long range dynamics. With these two techniques, it is possible to determine the mechanism of ion transport.

The polymer composites were shown to transport ions in the solid-state without a liquid electrolyte. These materials are viable in a temperature region where current aqueous electrolytes are not able to operate. Due to the modular nature of the host material, the choice of electrolyte broadens to include any anhydrous electrolyte. Improvement of the electrolyte material through fluorinated ions would improve the chemical resistance of the electrolyte and reduce the probability of degradation. Enhancing the ionic conductivity of the electrolyte is also a priority. New materials with higher ionic conductivities will provide higher open circuit voltages in a fuel cell environment.

The standard fuel cell test center is equipped for testing aqueous based electrolytes in a temperature range below the boiling point of water. These test stations use humidified gases to control the water content of the electrolyte. However, most stations do not have an option to eliminate humidification of the hydrogen and oxygen fuel, nor reach temperatures of 140°C. To fully test the potential of the anhydrous electrolyte a dry fuel source is required with no humidification and the operation temperature must be able to exceed 80°C. These are the major requirements for testing an anhydrous polymer composite. When the test station able to meet these requirements is installed, then it would provide a means to test the polymer composite material in a functioning fuel cell environment as was intended for anhydrous electrolytes. With an anhydrous test center and solid-state NMR it would be possible to study the performance of the material and correlate the results with the local dynamics of the electrolyte.

The goal of this research would be to improve upon the current polymer composites and quantify the mechanism of ion transport in the solid-state. Further study of the current polymer composites with a variable temperature study would provide much information on the timescale and behavior of the distribution of correlation times. The new electrolytes could improve upon the operating range of the electrolyte, different mechanisms of ion transport employed, and study the dependence of the mechanism on concentration of the electrolyte or versus individual ions. All these changes are observable via solid-state NMR and through the general performance of the electrolyte as a fuel cell.

The continued research of these proton conductors will provide insight on the molecular level dynamics and structure of anhydrous electrolytes. The outlined study of new electrolytes and optimization of current electrolytes will provide the material chemist with the knowledge to create better electrolytes for use in hydrogen fuel cells.